THÈSE DE DOCTORAT DE

L'ÉCOLE CENTRALE DE NANTES

ÉCOLE DOCTORALE N° 602
Sciences pour l'Ingénieur
Spécialité : *Génie Civil*

Par
Alexandros STATHAS

Numerical modeling of earthquake faults

Thèse présentée et soutenue à Nantes, le 13/12/2021
Unité de recherche : UMR 6183, Institut de recherche en Génie Civil et Mécanique (GEM)

Rapporteurs avant soutenance :

Samuel FOREST	**Directeur de recherche - CNRS**	MINES ParisTech, Corbeil Essones
Panos PAPANASTASIOU	**Professeur**	University of Cyprus, Chypre

Composition du Jury :

Président :	**Ahmed BENALLAL**	**Directeur de recherche - CNRS**	École Normale Supérieure Paris-Saclay
Examinateurs :	**Stéphanie CHAILLAT**	**Chargé de recherche HDR - CNRS**	ENSTA Paris
	Itai EINAV	**Professeur**	The University of Sydney, Australia
	Nicolas MOËS	**Professeur des universités**	École Centrale de Nantes
Dir. de thèse :	**Ioannis STEFANOU**	**Professeur des universités**	École Centrale de Nantes

Acknowledgment: This work was supported by the European Research Council (ERC) under the European Union Horizon 2020 research and innovation program (Grant agreement no. 757848 CoQuake), http://coquake.com.

CoQuake.com

European Research Council
Established by the European Commission

Institut de Recherche en
Génie Civil et Mécanique

ACKNOWLEDGEMENTS

Me completing successfully this thesis was a result of the beneficial influences of different people, whom I cannot thank enough. First, I sincerely thank my Professor Dr. Ioannis Stefanou for all the help and support during these three years. Him believing in me even when I was doubting myself, and giving me the chance to work on a challenging and stimulating topic away from my comfort zone has changed me in a very positive way (at least I hope so!). I cherish our valuable conversations and him sharing his keen insight and observations during the different stages of this Thesis. Indeed his stance constitutes a luminous example of a mentor for any young researcher aspiring to conduct research in a responsible, efficient and productive manner.

No good journey starts if you're alone... The arrival of my good friend Dr George Tzortzopoulos in France taught me that. George with his tenacity, rigor and good humor is a friend and a coworker that always lifts your mood. He is a source of great inspiration, courage and support. Of course, I could not forget Timos and Andrianna my good friends in France, always available to discuss console and smile. Their emotional and psychological support cannot be described with words.

Coquake, the team That I am proudly member of, consists of many more members, whose contribution I will not leave unnoticed. I thank my friends and coworkers Dr. Filippo Masi for our stimulating discussions, Dr. Philip Braun, Dr. Pravin Badarayani, Dr. Diego Gutiérrez-Oribio, Ahmad Morsel and Abdallah Aoude for the refreshing coffee breaks of which -thankfully- there were plenty. Finally, I thank all my coworkers in the GeM laboratory for creating a suitably calm and amicable research environment.

Nearing the end of this small note, I would like to offer my sincere thanks to the reviewers of my Thesis, Professor Samuel Forest and Professor Panos Papanastasiou, who took the time to read through my manuscript and meticulously review it. I wholeheartedly thank the members of my committee, Professor Ahmed Benallal, Professor Nicolas Moës , Professor Itai Einav and Dr. Stefanie Chiallat. They gave me valuable feedback as well as a stimulating discussion during the defense of my Thesis.

Finally, I extend my thanks towards my family. My mother, father, brother and grandmother, who motivated and supported me during both sad and happy times, always believing in me. Even though they are far, they are close to heart. I am grateful to all those that heard my peeves and kept me company during these three fun and strenuous years.

TABLE OF CONTENTS

Chapter 1

Introduction

Earthquakes are among the deadliest and costly misfortunes that befall humanity. They are severely disrupting natural and man-made environment inflicting devastation that amounts to thousands of deaths and destruction of key facilities (homes, harbors, energy and transportation networks) that reverse or inhibit the economic growth and human activity (see OECD, 2018). Earthquakes can be separated into two categories, those that occur naturally given the seismogenic activity of particular regions (see Kanamori & Brodsky, 2004b) and those that occur due to the human activity (see Elsworth et al., 2016; Rubinstein & Mahani, 2015, among others). Indeed anthropogenic earthquake events (induced or triggered seismicity) have been observed in national and international records over the last 80 years resulting from nuclear tests, filling of dams, extraction of oil and gas, storage of nuclear waste, geothermal energy projects as well as CO_2 sequestration for mitigation of the effects of climate change. All these activities increase the seismogenic activity of a region and although the first two causes produce immediate results, whose risk can be efficiently taken into account, this cannot be said for the rest of the activities given above. In fact the increase in the region seismicity will take time to develop. It strongly depends on the properties of the geological network of faults affected by the operations (see Hincks et al., 2018).

While the increase in regional seismicity is noticeable over a time period, we are still not able to predict successfully the occurrence of an earthquake over a meaningful time scale that would allow for successful reinforcement of the existing infrastructure, preventing catastrophe. Another approach to the same problem would be to mitigate the effects of the earthquake phenomenon by successfully controlling its evolution and the transition of the fault system form stable to unstable seismic slip (see Guglielmi et al., 2015; Raleigh et al., 1976; Stefanou, 2018, 2019). To this end, understanding the mechanical behavior of the fault in conjunction with other physical mechanisms, present during coseismic slip, is of primary importance. In particular, it was recently shown in Stefanou and Tzortzopoulos (2020), Stefanou (2019) that earthquake like frictional instabilities can be controlled provided that some rough boundaries of the friction are known. Therefore, studying the mechanics of faults will allow us to define meaningful upper and lower bounds for the frictional response during an earthquake as well as the expected earthquake acceleration spectra for estimating the radiated energy to the earth's surface.

As shown in Kanamori and Brodsky (2004b), the quantification of the energy released during the earthquake is primarily divided in two parts. The dynamic part, about 5∼10%, is the one that transforms into mechanical waves that reach to the surface. The rest of the energy dissipates inside a narrow zone of intense deformation due to friction, and contributes to a lesser extent in nucleating the fault rupture at the tip of the fault. The region of intense deformation contained inside the adjacent earth blocks forming the edges of the fault is called the fault gouge (see Figure 1.1 and Myers and Aydin (2004)). This is a region of ultracataclastic material, product of the intense friction and fault nucleation taking place during co-seismic slip (see Brantut et al., 2008; Myers & Aydin, 2004; Scholz, 2019; Sibson, 2003b; Sibson & Toy, 2006; Takahashi et al., 2017).

The evolution of the coseismic-slip during an earthquake is governed by the frictional behavior of the fault gouge material under the appropriate temperature and fluid pressure conditions at the prescribed depth inside the seismogenic zone[1]. Performing an experiment to gather data about the in situ behavior is problematic (see Brantut et al., 2008; J. Sulem et al., 2004; Takahashi et al., 2017; Verberne et al., 2015; Verberne et al., 2020). On one hand we lack the capability for large experiments in the suggested temperature and pressure ranges, on the other hand retrieving a sample of fault gouge material from the proper depth while keeping its stress distribution, hydraulic and thermal diffusivity intact is very difficult (see Lee & Delaney, 1987; Mase & Smith, 1987; Rice, 2006a; Sibson, 2003b). Therefore, we have to rely on material retrieved from boreholes at the exhumed parts of the fault, which however might be subjected to erosion for geological times, and are not representative of the material and conditions of seismic faults (see Brantut et al., 2008; F. M. Chester & Chester, 1998a; Myers & Aydin, 2004; Nicchio et al., 2018). Moreover, during specimen extraction the material is disturbed and separated from its initial physico-chemo-mechanical environment, which is affects material parameters crucial dur-

1. In geophysiscs and fault mechanics, the seismogenic zone covers the entire depth of the lithosphere $0 \sim 25$ km. In this depth the temperature and lithostatic pressure allow for elastic and frictional processes to dominate, leading to brittle faulting and seismic events (see Cook et al., 2010; Scholz, 2019).

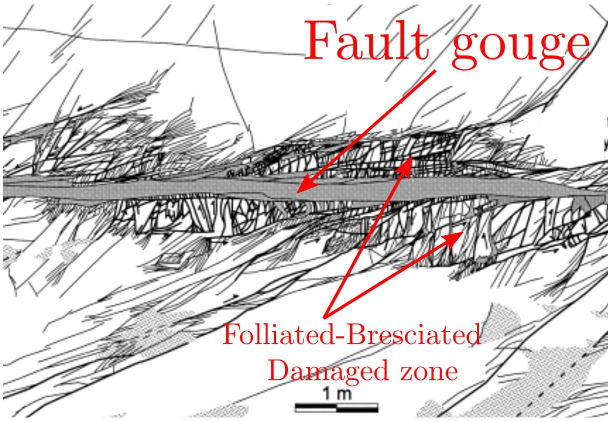

Figure 1.1 – Image of a fault gouge taken by Myers and Aydin (2004)

ing coseismic slip, such as thermal and hydraulic diffusivities.

In recent years sampling of fault gouge material from well monitored faults has become more common (see Carpenter et al., 2011; Ikari et al., 2015; Niemeijer et al., 2016; Tanikawa & Shimamoto, 2009). However, the uncertainty due to the small dimensions of the samples (∼mm) compared to the large scale of the fault (∼km) results to additional limitations to what can be tested experimentally. Apart from the disparity of the dimensions between the samples and physical reality, we need to also take into account the different conditions in terms of stress, temperature, salinity, heterogeneities and asperities distribution, prevalent in the fault gouge region (see Boullier et al., 2009; Brantut et al., 2008; Carpenter et al., 2011; Di Toro et al., 2011b; Rempe et al., 2020; J. Sulem et al., 2004; Takahashi et al., 2017; Verberne et al., 2015; Verberne et al., 2020, among others). Furthermore, as we suggest in chapters 5 and 6, (see also Rice et al., 2014a) , the localization instability travels along the fault gouge and, for this reason, the sample collected might not contain the region of interest for proper characterization of the Principal Slip Zone (PSZ) properties (see Boullier et al., 2009; Collins-craft et al., 2019; Ma et al., 2006; Nicchio et al., 2018; Rice, 2006a). Therefore, experiments performed on such samples do not necessarily reflect the true behavior of the fault gouge during coseismic slip. In light of these facts we need to rely on theoretical models and results obtained from numerical analyses, in combination with experimental observation.

Experimental evidence performed on exhumed fault gouges, points towards a localized mode of failure that is contained is a small region with width of the order of micrometers to milimeters (see Lachenbruch, 1980a; Rice, 2006b; Scholz, 2019; Sibson, 2003b; J. Sulem & Stefanou, 2016a; J. Sulem et al., 2011). This highly localized mode of failure has a lot in common with similar modes observed in experiments on metals (see Benallal et al., 2006; Benallal et al., 2008; Forest, Boubidi, et al., 2001; Hähner et al., 2002; Mazière et al., 2010; Needleman & Tvergaard, 1992; Peirce et al., 1984; Ren et al., 2021; Reyne et al., 2019), where under high strain rates the preferred failure mode is concentrated in a region of a small finite zone of accumulated plastic deformation called a shear band. In metals, a series of criteria have been developed for predicting localization of the uniform shear profile near the highly strained regions of the specimens, based on experiments being conducted over a large range of shearing velocities and temperatures.

Investigating numerically the creation and post yield behavior of a specimen with a shear band is a challenging task due to localization happening on a mathematical plane disturbing the objectivity of the mesh used during the analysis (see Benallal et al., 2006; Benallal, 2005b; Benallal & Comi, 2003; Erlich et al., 1980; Forest, Boubidi, et al., 2001; Moes & Chevaugeon, 2021; Moës et al., 2003; Moës et al., 1999; Moës et al., 2011; Muhlhaus & Vardoulakis, 1988; Needleman, 1988; Papanastasiou & Vardoulakis, 1989; Papanastasiou & Vardoulakis, 1992; I. Vardoulakis & Papanastasiou, 1988; Wu & Freund, 1984; Zervos et al., 2001a; Zervos et al., 2001b). What has been observed is that as we decrease the size of the elements used in the numerical analyses the width of the localized zone becomes progressively smaller without showing any signs of convergence. This mesh dependency of the numerical solution leads to serious problems in the evaluation of the dissipated energy (the energy loss to heat during yielding of the material). In particular localization on a mathematical plane leads to a solution of zero plastic dissipation. This is reflected in the numerical analyses as we progressively increase the number of elements, where the dissipated energy becomes zero corresponding to near vertical stress drop of the friction vs slip diagram, $(\tau - \delta)$ (see Needleman, 1988; Needleman & Tvergaard, 1992; Sluys & de Borst, 1992, and chapter 3, among others). Consequently, the apparent stress-strain response of the system is mesh dependent.

In metals, elaborate material laws have been developed taking into account viscosity, thermal softening and higher order continua in order to tackle the above described problems and obtain more realistic results (see de Borst & Sluys, 1991; Erlich et al., 1980; Ruina, 1983a; Shawki & Clifton, 1989; Sluys & de Borst, 1992; Sluys et al., 1993; W.

Wang et al., 1997; H. Zbib & Aifantis, 1989). These approaches aim at regularizing the localization of plastic strain rate to a profile of finite width. The majority of those material laws have been tried also in the case of geomaterials, even though the frictional softening is attributed to a broader category of natural causes such as flash heating at the asperity contacts (see Rice, 2006a), thermal pressurization (see Lachenbruch, 1980a), thermal decomposition of carbonate minerals (see Alevizos et al., 2014; J. Sulem & Famin, 2009; E. Veveakis et al., 2014) and lubrication due to silica gel formation (see Di Toro et al., 2011b). Nevertheless, there is some degree of similarity between the micro grains in metals and the quarzites present in the grains of geomaterials that allows for application of concepts from metal plasticity to granular geomaterials (see de Borst & Duretz, 2020; Muhlhaus & Vardoulakis, 1988; Platt et al., 2014a; Rice, 2006a; Rice et al., 2014a; Stefanou et al., 2016; J. Sulem et al., 2011; I. Vardoulakis, 2018; E. Veveakis et al., 2014). Moreover, recently, a new approach accounting for the microstructure of granular materials in a Thermodynamical context was proposed in (see Alaei et al., 2021). The authors of this study introduce the notion of grain temperature in conjuction with the inertial number to predict the constitutive behavior of granular materials under various deformations regimes.

What is of interest in all these approaches is the conditions under which a uniform strain rate profile localizes to a profile of finite or infinitesimal width. This is considered by investigating the stability of the original uniform solution (see Benallal & Comi, 2003; Muhlhaus & Vardoulakis, 1988; Papamichos et al., 2017; Papanastasiou & Vardoulakis, 1992; Rice, 1975; J. Sulem & Vardoulakis, 1995, among others, see chapter 3). This is a challenging task by itself if one considers all the possible physical couplings acting at different length and time scales suspected to influence the localization of the shear band and the nonlinearities of the underlying material problem.

Early attempts at describing the frictional behavior and subsequent deformation inside the fault gouge used a model of uniform shearing of a 1D layer coupled with the temperature and pressure diffusion equations (see Lachenbruch, 1980a). This approach, although sufficient for the cases where the fault gouge width is small $\sim 100\ \mu$m, is lacking for larger widths, where a principal slip zone accommodating the majority of the seismic slip can be identified inside the fault gouge (see Mase & Smith, 1987; Rice, 2006a; Rice et al., 2014a). The consideration of the dissipated energy at the adjacent parts of the fault is assumed to happen primarily due to friction inside the PSZ. The question then emerges, whether the principal slip zone can be considered as an interface in the surrounding brittle rock, in which case, the displacement can be said to localize into a mathematical plane, or it has a certain finite width. This question is directly related to the dissipated energy, the multiphysics couplings and the models to be used for its quantification (see Rice, 2006a; Rice et al., 2001).

In Mase and Smith (1987), Rempel and Rice (2006), Rice (2006a, 2006b) the authors studied the evolution of temperature and pore fluid pressure during coseismic slip. During seismic slip, the fault gouge is under intense plastic deformation and thus plastic work is produced. This work is released in the form of heat in the pore fluid and the solid skeleton of the fault gouge material. The difference in the expansivities of the fluid and solid phase, as the pore fluid tends to expand more, leads to an increase in the pore fluid pressure. Considering that the friction of the fault gouge material is dependent on the confining pressure, this leads to frictional weakening of the fault gouge. This procedure is known as thermal pressurization and is the main weakening mechanism considered in this thesis.

Mase and Smith (1987) conducted numerical analyses in order to show the role of thermal pressurization under isothermal drained boundary conditions, they also investigated the role of variable slip velocity time histories during coseismic slip. By prescribing the width of the localized region their analyses investigated the role of thermal pressurization in the frictional strength of the fault. In Rice (2006a) the results of Mase and Smith (1987) were obtained analytically for the case of a fault gouge localized on a mathematical plane. This allowed the researchers to obtain estimates for the dissipation energy during coseismic slip, and to calculate the energy necessary for the nucleation of the fault according to Rice (1973a). The main assumptions in Rice (2006a) are that strain localizes on a mathematical plane, and that the boundaries of the fault gouge are sufficiently far from the mathematical plane, where strain localizes on. Finally, another central assumption is that during the duration of the analysis the localization remains in the same position inside the fault gouge.

The assumptions described above are paramount for the determination of the frictional response, the part of the overall energy budget of the seismic event that dissipates into heat and of the contributing energy to continue the nucleation of the fault. As such they are a subject of vivid discussion.

Evaluation of the assumptions of slip on a mathematical plane

Thickness of strain localization

Experimental results suggest, that in fact the PSZ has a localization width of the order of some micrometers to millimeters (see F. M. Chester & Chester, 1998a; J. S. Chester et al., 2005; Sibson, 2003b). Therefore, it is a major simplification to assume it as being entirelly localized on a mathematical plane. This is also noted in the models presented in (see Andrews, 2002; Platt et al., 2014a; Rempel & Rice, 2006; Rice, 2006a; Rice et al., 2014a; I. Vardoulakis, 1996a, 1996b) since the width of the PSZ is of paramount importance in evaluating correctly the energy budget under pre- and coseismic slip conditions, in answering questions considering the stability of the fault (see Platt et al., 2014a; Rattez, Stefanou, & Sulem, 2018; Rattez, Stefanou, Sulem, Veveakis, et al., 2018a, 2018b, 2018c), its nucleation procedure (see Rice, 1973a) and the energy escaping to the surface in the form of seismic waves (see Kanamori & Rivera, 2006).

The existence of the finite localization width indicates the presence of a characteristic microstructure taking part in the seismic phenomenon, whose behavior needs to be analyzed. In particular, microstructure introduces internal lengths in the material that need to be taken into account when the thickness of the PSZ is calculated. This is important since the estimation of the localization thickness is crucial in evaluating the dissipated energy, the frictional post yield behavior of the fault and the criteria for fault propagation. However, the classical Cauchy continuum used in the majority of engineering applications to describe the mechanical behavior of geomaterials under severe plastic deformation, lacks a characteristic length scale and can be shown to localize into a mathematical plane of zero thickness under specific -post yield- values of the material parameters. Conditions for simulating the microstructure affecting the mechanical behavior vary in the literature. The approaches commonly used are the use of discrete element modeling (DEM) analyses (see Froiio et al., 2006; Rezakhani & Cusatis, 2016, among others) as well as finite element modeling (FEM) by micromorphic continua such as Cosserat continua (see Rattez, Stefanou, & Sulem, 2018; Rattez, Stefanou, Sulem, Veveakis, et al., 2018a, 2018b; J. Sulem et al., 2011; I. Vardoulakis, 2019).

Apart from direct consideration of the microstucture, different regularization approaches have been suggested in the bibliography to avoid strain localization on a mathematical plane. One such approach is to introduce additional physics into the mechanical problem such as heat and pore fluid diffusion processes. Nevertheless, it has been shown in chapter 3 that a Cauchy layer coupled with pressure and temperature diffusion equations does indeed localize into a mathematical plane. Another approach to the problem is the introduction of a characteristic time scale into the model through the use of rate-dependent elasto-viscoplastic Cauchy continuum (see de Borst & Duretz, 2020; Sluys & de Borst, 1992). Again however, we show in chapters 3 and 4 that regularization of the localization width fails. Finally, the combination of a rate dependent Cauchy material with strain rate hardening and multiphysical couplings is shown in Platt et al. (2014a), Rice et al. (2014a) to regularize the problem considering the apparent strain softening due to the frictional weakening mechanism of thermal pressurization. The model used by the authors in Platt et al. (2014a), Rice et al. (2014a) draws its inspiration from the rate and state friction law Dieterich (1992), Rice et al. (2001), Ruina (1983a), however the authors do not solve for the evolution of the state variable during shearing.

The role of inertia as a regularization mechanism

Considering the regularization approaches we discussed above, the question of inclusion of inertia as an additional regularization mechanism into the problem's modeling equations is also considered. On a physical basis, the inclusion of inertia as a regularization mechanism stems form the potential increase of the width of the PSZ. In Rice (2006a) it has been argued that the small diffusion lengths corresponding to the averaged fault gouge material parameters during slip do not activate a wider region of the material and, therefore, inertia of the PSZ is negligible. This was studied in detail in Platt et al. (2014a), where it was found that the dynamic character of the problem does not depend at all on the diffusion lengths, inasmuch as the ambient effective normal stress and the shear velocity. It was subsequently shown that inertia leads to a widening of the localization zone as well as stalling the localization from developing in full. Using a linear perturbation approach it was shown that both for laboratory as well as in situ seismic processes, the range of seismic slip velocities applied, combined with the ambient effective stresses, does not lead to important inertial effects in all depths of the seismogenic zone.

However, the situation might be different at the propagation front as well as the trailing end of the fault. At the fault front velocities are calculated to severely exceed the critical velocity indicating deviation due to inertial effects. Nevertheless, since the front propagates extremely fast the inertia effects might not amount to much since the localization is still at early stages. At the trailing end, the temperature increase due to friction and chemical reactions leads to thermal pressurization decreasing the effective stress at the PSZ. If we consider the current effective stress instead of the ambient, this tends to reinforce the inertial effects leading to a widening of localization and slower friction drops. At shallow depths this mechanism is thought to create self healing pulses although further study is needed (see Platt et al., 2014a).

The discussion above incorporated the inertia on the fault gouge level. However, inertia also plays a role in the evolution of the microstructure (see Da Cruz et al., 2005). It is estimated in Platt et al. (2014a) that the microstructure is one order of magnitude more sensitive to inertial effects if several assumptions considering the size and shape of the grains hold true. This in turn means that inertia effects need to be studied on a case by case basis considering the properties of the fault gauge. This microinertia can be taken into account by introduction of a continuum accounting for the material microstructure such as the Cosserat continuum corresponding to the first order micromorphic theory (see Germain, 2014; I. Vardoulakis, 2019). Brief description of the Cosserat continuum kinematics and balance equations are given in chapter 3. This continuum has the added advantage that its localization width under mechanical strain softening or coupled diffusion conditions remains finite. It is shown through bifurcation analysis in Rattez, Stefanou, and Sulem (2018), Rattez, Stefanou, Sulem, Veveakis, et al. (2018a, 2018b) that introduction of inertia leads to a slight increase of the localization width in a Cosserat medium.

Considering the role of inertia in the strain localization profile during coseismic slip, Platt et al. (2014a), Rice et al. (2014a) have shown through the use of an appropriate characteristic time in the non dimensionalized system of coupled partial differential equations that its influence can be negelected except at the propagation tip. In chapter 5, section 5.2.6 we show that the inertia calculations described in (see Platt et al., 2014a; Rice et al., 2014a) remain still valid for the Cosserat case with multiphysical couplings. Additional information about grain inertia can be given through the use of viscosity in the constitutive description to model the jiggling of the grains (among other complicated phenomena at the microscale) during deformation (see Alaei et al., 2021; Rognon et al., 2015). This, has been modeled in section 5.4. In particular, we incorporated Perzyna viscoplasticity with thermal pressurization in the framework of Cosserat micromorphic theory for the shearing of a Cosserat layer, considering large coseismic slip via an Adaptive Lagrangian Eulerian (ALE) method. This leads to a velocity weakening strain rate hardening model, exhibiting stick slip events qualitatively similar to a rate and state macroscopic friction law (see Dieterich, 1992; Ruina, 1983a).

Influence of propagating strain localization instabilities in the fault's frictional response

The assumption about a stationary PSZ is also a major constraint. As we suggest in chapter 6, the strain localization may be traveling inside the fault gouge. The concept of the traveling strain localization inside the fault gouge has been suggested also in Collins-craft et al. (2019), Platt et al. (2014a), in higher spatial dimensions this traveling mode of strain localization may give rise to eddies forming in the granular media as described in Griffani et al. (2013), Miller et al. (2013), Rognon et al. (2015). It should be noted that similar behavior has been observed in metals in the context of Portevin Le Chatelier shear bands (see Benallal et al., 2006; Benallal et al., 2008; Hähner et al., 2002; Mazière et al., 2010; Ren et al., 2021; Reyne et al., 2019).

In Benallal (2005b), Benallal and Comi (2003) the researchers have shown that in a saturated porous Cauchy continuum the existence of imaginary part in the Lyapunov coefficient. This leads to flutter instabilities inside the medium (see Rice, 1975). The imaginary part of the Lyapunov exponent is responsible for a traveling localization inside the continuum (see also chapters 4 and 5). Traveling shear bands have also been observed in Rice et al. (2014a), where the authors have identified conditions for the existence of the traveling perturbations. The authors note, however, that the existence of these perturbations are only possible in the context of periodic boundary conditions. Furthermore, according to their model such perturbations are only possible for specific values of the rate hardening parameter and the hydraulic diffussivity. In the context of the nonlinear Cosserat continuum used in chapter 5 of this thesis, with perfectly plastic Drucker Prager material law and without the introduction of mechanical strain rate hardening, we observe traveling perturbations in a isothermal drained bounded domain for permeability values that are typically observed in fault gouges.

Furthermore, the effect of heat and pore fluid flow through the boundaries should not be ignored. As we show in chapters 5 and 6, the effect of the boundaries is felt in the fault gouge domain for the range of seismic slip velocities observed in nature. Together with the traveling shear band, boundary effects are responsible for "ventilation" phenomena that result in frictional regain and oscillations in the fault's frictional response.

In chapter 6, we investigate by semi analytical methods the implications of a traveling instability in the pore fluid pressure and temperature profiles of the fault gouge. We extend our analyses from the case of the stationary shear band on an infinite domain described in Platt et al. (2014a), Rice (2006a), Rice et al. (2014a), to the case of a moving shear band on an infinite domain. Then, we take into account the dimensions of the fault gouge and examine the effect of the boundary conditions on the temperature and pore fluid pressure profiles obtained by the traveling strain localization. Next, we examine bounds for the traveling velocity of the shear band inside the fault zone. Under these considerations new bounds for the timescales of thermal pressurization are obtained. A traveling shear band together with the new set of boundary conditions significantly change the frictional behavior of the fault enhancing the frequency content of the acceleration spectra that we can predict (see Aki, 1967; Brune, 1970; Haskell, 1964; Okubo et al., 2019).

Through these analyses it is found that for the typical average seismic slip velocity and seismic slip displacement, the evolution of friction deviates from the available solutions presented in literature (see Lachenbruch, 1980a; Rice et al., 2014a) and from the findings presented in chapters 5 and 6. While at the small shearing analyses (initial stages), the available solutions agree, for large coseismic slip (δ), the solution obtained in chapter 5 for the Cosserat case with strain softening and THM couplings shows a traveling instability developing inside the fault gouge. This behavior presents results that are qualitatively in agreement with those obtained in chapter 6, section 6.4.2.2. The possibility of such an instability has been discussed by Platt et al. (2014a) while evidence of such a behavior were proposed after examination of the Chi-Chi earthquake (see Boullier et al., 2009). Those results could present an alternative answer to the disagreement between the low frequency seismic spectra predicted by the dynamic model concerning the frictional behavior during coseismic slip and the high frequency acceleration spectra inferred by the seismograms observations at the surface (see Madariaga et al., 1998; Tsai & Hirth, 2020).

Scope and structure of the thesis

The scope of this thesis is the quantification of the behavior of a fault during coseismic slip. We investigate the frictional behavior of a fault gouge subjected to shear under the influence of the apparent frictional weakening mechanism of thermal pressurization. We are mainly interested in the role of the microstructure and the assessment of thermal pressurization as a frictional weakening mechanism. In other words we investigate the conditions inside the fault, when an earthquake happens and a seismic slip takes place. Such an analysis can be used for the calculation of the energy balance, stress drop in the material surrounding the fault as well as defining the conditions under which an earthquake nucleates (see Kanamori & Brodsky, 2004b; Rice, 2006a; Viesca & Garagash, 2015).

Due to strain softening, we will see in chapter 3 that strain localizes on a mathematical plane leading to mesh dependent solution for the evolution of friction and the dissipated energy under imposed shear displacement. In order to avoid mesh dependency in numerical analyses, different regularization methods have been proposed in the bibliography. The main approaches considered, are the introduction of viscosity (see de Borst & Duretz, 2020; Kamasamudram et al., 2021; Needleman, 1988; Peirce et al., 1984; Sluys & de Borst, 1992; W. Wang et al., 1997), introduction of multiphysical couplings (see Benallal, 2005a; Benallal & Comi, 2003; Jacquey et al., 2021; Lachenbruch, 1980a; Lee & Delaney, 1987; Mase & Smith, 1987; Platt et al., 2014a; Stefanou & Gerolymatou, 2019, among others) and finally the consideration of the material's microstructure through the use of first order micromorphic Cosserat continua (see De Borst, 1991; de Borst & Sluys, 1991; Forest & Sievert, 2003; Forest, 2019; Forest, Pradel, et al., 2001; Germain, 1973; Muhlhaus & Vardoulakis, 1988; Neff et al., 2014; Papanastasiou & Vardoulakis, 1989; Papanastasiou & Vardoulakis, 1992; Sluys et al., 1993; I. Vardoulakis, 2018; H. Zbib & Aifantis, 1989; H. M. Zbib & Aifantis, 1992; Zervos et al., 2001b, among others). Other approaches for regularization of strain localization in the context of a damage material law, have been proposed based on the level set method with the discontinuous Galerkin method as proposed in Moës et al. (2003), Moës et al. (1999), Moës et al. (2011), Shiferaw et al. (2021) and the novel Lipschitz strain regularization localization method (Liep-field), presented in Moes and Chevaugeon (2021). Numerical techniques for handling the localization of plastic deformation in the context of bounary element methods have also been proposed in Ciardo et al. (2020).

Next, we assess the regularization capability of viscosity, multiphysics and Cosserat continuum to strain localization and mesh dependence. The notion of stability is presented in chapter 2, where the concepts of stability of the solution, fixed loci and bifurcations are discussed in greater detail. Furthermore, we apply the method of Lyapunov stability analysis in an introductory problem. In chapter 3 we apply Lyapunov's first method to the set of regularization approaches under quasistatic loading conditions. We show there, that the proposed regularization methods, the only one capable of efficiently regularizing the ill-posed problem is the consideration of a first order micromorphic Cosserat contiuum.

In chapter 4 we emphasize on the role of viscosity in the regularization of strain localization by considering viscosity and inertia. This problem has been studied in depth in the literature, however, the results are conflicting. In chapter 4, we perform an in depth analysis of the viscosity and inertia regularization approach with the help of Lyapunov stability analysis. We complete our theoretical analysis with numerical examples, proposing a criterion for the conditions under which strain localization becomes noticeable in the numerical results. This useful result allows us to once more justify our selection of the Cosserat continuum as the medium on which to conduct our multiphysical numerical analyses taking the role of the microstructure into account.

In chapter 5 the main numerical results of this thesis are presented. We investigate the frictional response of a mature fault under large coseismic slip. For our analyses we use a linear elastic perfectly plastic first order micromorphic Cosserat continuum coupled with the pressure and temperature diffusion equations. These couplings allow us to investigate the influence of the mechanism of thermal pressurization in the fault's frictional response during coseismic slip. The above problem has also been studied in Rattez, Stefanou, and Sulem (2018), Rattez, Stefanou, Sulem, Veveakis, et al. (2018a, 2018b, 2018c), however, these analyses are mainly constrained to small displacements of 5 mm. In our analyses, we apply realistic seismic slip displacements δ of 1 m under typical seismic slip velocities in the range of $0.1 \sim 1.0$ m/s. The small size of the fault gouge (H = 1 mm) relative to the applied shear displacement, obliges us to consider large displacements during shearing. We do so by using an Adaptive Lagrangian Eulerian method (ALE). Other methods can be used for describing micromorphic continua under in finite strains, as described in Forest and Sievert (2003), Forest (2020a).

Our analyses that advance well beyond the initial stages of seismic slip show a behavior that diverges -spectacularly- from the existing theoretical models of uniform slip (see Lachenbruch, 1980a; Lachenbruch, 1980b) and slip on a mathematical plane (see Mase & Smith, 1987; Platt et al., 2014a, 2014b; Rice, 2006a; Rice et al., 2014a), when the weakening mechanism of thermal pressurization is considered. In particular after the initial velocity weakening behavior observed in our analyses the fault gouge shows signs of *strength regain*, eventually reaching a value of residual shear strength, lower than the fault's initial friction, but not zero as previous analyses show (see Platt et al., 2014a; Rice, 2006a; Rice et al., 2014a). Furthermore, we note that even at the initial stages of the analyses $\delta < 10$ mm, a traveling wave of strain localization makes its appearance. This result although theoretically possible in the Cauchy case (see Benallal, 2005a; Benallal & Comi, 2003; Platt et al., 2014a; Rice et al., 2014a, for flutter instabilities) is observed for the first time in the context of a nonlinear coupled thermal pressurization analysis in Cosserat media. We note here that the phenomenon is similar to the emergence of Portevin Le Chatelier bands in metals during shearing (see Benallal et al., 2006; Benallal et al., 2008; Forest, Boubidi, et al., 2001; Mazière et al., 2010; Ren et al., 2021; Reyne et al., 2019, among others). The periodic motion of the strain localization wave inside the fault gouge results in oscillations of the fault's frictional behavior. In chapter 6 we provide an explanation for the emergence of traveling instabilities and we investigate the conditions for their emergence and the influence of the boundaries in the period of the resulting frictional oscillations.

We continue our investigation of the fault gouge response by introducing viscosity in the material law. We do this in order to model the inertia of the grains and other complex mechanisms of the microstructure inside the fault gouge. The addition of viscosity to our model introduces a rate and state behavior to the model's frictional response. We perform a parametric analysis for the parameters of viscosity, hydraulic compressibility and the material's internal length. We notice that for values of the viscosity parameter close to the corresponding rate parameter, α, of the rate and state model (see Dieterich, 1992; Rice et al., 2001; Ruina, 1983a; Scholz, 2019, among others), the numerical results present apparent jumps, which could lead to multiple stick slip events without the use of any additional internal variable as in the classical rate and state friction model.

We show also that the material length has little to no influence in the numerical results, suggesting that the phenomenon is fully described by the analysis diffusion lengths and viscosity. This is not to say that the material length scale does not affect the analysis. The material length scale provides us with a lower bound to the thickness of the strain localization. This way it ensures that the analyses will not be localizing on a mathematical plane.

Thus, our enhanced model contains both the effect of thermal pressurization and the effect of the rate and state material law. Finally, we compare our theoretical results with the experimental results for the influence of thermal pressurization in the shear response of rocks in a modified rotary shear apparatus found in Badt et al. (2020), Rempe et al. (2020). The results suggest qualitative agreement between the numerical frictional response and the observed friction derived from the experiments.

Nevertheless, the issue of the difference between the established solution of the numerical results and the theoretically predicted response described in Lee and Delaney (1987), Mase and Smith (1987), Platt et al. (2014a, 2014b), Rice (2006a), Rice et al. (2014a) needs to be addressed. In chapter 6 we focus on this issue by questioning the fundamental assumptions of the classical model of slip on a mathematical plane under the influence of thermal pressurization (see Lee & Delaney, 1987; Mase & Smith, 1987; Platt et al., 2014a, 2014b; Rice, 2006a; Rice et al., 2014a).

Following the methodology described in Rice (2006a), we recast the nonlinear boundary value problem as a linear Volterra integral equation of the second kind (see Wazwaz, 2011, among others), by prescribing the localization mode and the trajectory of the strain localization inside the fault gouge domain. We expand the current model by introducing the influence of the boundaries in the frictional response. We consider the case of isothermal drained boundary conditions as in the case of the fully nonlinear numerical analyses of chapter 5. Furthermore, we investigate the influence of a traveling yielding mathematical plane to model the traveling plastic strain wave of chapter 5. In order to solve the weakly singular integral equation of friction accounting for the role of thermal pressurization on the unbounded domain, we make use of the methodology developed in

Mavaleix-Marchessoux et al. (2020). Further results for the smooth kernels in the bounded case were derived based on the work of Tang et al. (2008). We show that under the new assumptions about the boundary conditions and the strain localization mode, the proposed model justifies our numerical results.

Key points

Summarizing, this thesis intends to answer to the following challenging topics in the modeling of fault gouges under seismic slip and seismic slip velocities commonly observed in nature.

- What is the most appropriate method in modeling strain localization in fault gouges under coseismic slip? Which method of strain regularization can avoid strain localization on a mathematical plane and mesh dependency?
- What is the frictional behavior of the fault gouge under large coseismic slip under the influence of thermal pressurization as a frictional weakening mechanism?
- What are the effects of viscosity -grain inertia- in the frictional response of the fault?
- How do the boundary conditions and the strain localization mode affect the predicted frictional response? Is the current model of slip on a mathematical plane adequate in estimating the effects of thermal pressurization?

We answer these questions in the following manner:

- We evaluate different localization approaches common in engineering applications, using the method of Lyapunov stability analysis described in chapters 2, 3, and we prove in chapter 3 that only the Cosserat continuum, which takes the microstructure of the fault gouge into account, can avoid the strain localization on a mathematical plane and mesh dependency.
- We investigate in depth the role of viscosity in the regularization of strain localization in a classical Cauchy continuum. We do so by studying the stability of the homogeneous solution with and without consideration of the inertia terms. Thus, we are able to prove both theoretically and numerically that viscosity in the presence of inertia does not regularize strain localization on a mathematical plane and mesh dependency (see chapter 4).
- In chapter 5, we focus on the main subject of this thesis, which is the numerical

investigation of the fault's frictional response under large coseismic slip. We use the Cosserat continuum and couple its mechanical description of the balance of linear and angular momentum equations with the temperature and pore fluid pressure diffusion equations in order to account for the influence of thermal pressurization in the fault's frictional response. We are interested in the fault's frictional behavior under large coseismic slip and seismic slip rates common in field observations. To do so, we need to account for the influence of large deformations in our analysis. Therefore, we apply an Adaptive Lagrangian Eulerian method (ALE) to our model, changing the mesh dimensions after each converged increment. We investigate the influence of the rate of seismic slip in the frictional response.

- Our results indicate the existence of a lower bound for friction τ_{min} due to the weakening caused by thermal pressurization, which is super-ceded by a frictional residual value τ_{res} due to frictional regain caused by the influence of the boundaries and "ventilation" produced by a periodic wave of traveling strain localization!
- We introduce the effect of grain inertia in our model by adding viscosity in the material description. The numerical results demonstrate a behavior qualitatively similar to the stick slip characteristic jumps of the rate and state model.
- Our results diverge -spectacularly- form the expected behavior discussed in the classical models of friction. These are the model of slip on a mathematical plane under the influence of thermal pressurization as described in Lee and Delaney (1987), Mase and Smith (1987), Platt et al. (2014a), Rice (2006a), Rice et al. (2014a), and the model of slip on a homogeneous deformation profile under adiabatic undrained boundary conditions described in Lachenbruch (1980b).
- The derived experimental results in chapter 5 agree qualitatively well with the experimental results in Badt et al. (2020), Di Toro et al. (2011a), Rempe et al. (2020).
- We explain the divergence between the predictions of the theoretical model and the fully non-linear numerical results of chapter 5. In chapter 6, we identify the sources of this disagreement between the model of slip on a mathematical plane and the numerical results of chapter 5. Firstly, the boundary conditions are assumed at infinity and therefore, their influence is not felt at the overall response of the model. Furthermore, the strain localization mode assumed in the model is stationary corresponding to a divergent instability (Re[s]>0,Im[s=0, see Rice (1975)). It has been shown in Benallal (2005a), Benallal and Comi (2003) among

others, that flutter instabilities also possible (Re[s]>0, Im[$s \neq 0$, see Rice (1975)), and preferred over its stationary counterpart under specific loading conditions. We have confirmed this in the stability analyses of chapter 5. We associate flutter instabilities with a traveling mode of strain localization. Therefore, we conclude that a traveling mode of strain localization should also be applied in the classical model.

- In chapter 6 we account for the influence of the boundaries by deriving the Green's function kernel for the coupled problem of thermal pressurization in the bounded domain. Furthermore, we impose a periodic traveling strain localization profile, by applying a closed trajectory along which the wave of strain localization moves. Inasmuch, we investigate both the unbounded and the bounded case for the fault gouge domain.
- Our results from the expanded model are in qualitative agreement with the numerical results of chapter 5 using Cosserat theory. The existence of oscillations in the frictional response and the residual friction value τ_{res} different than the original zero asymptote are justified. Our results show that the effect of the boundaries is felt inside the suggested seismic slip values for all seismic slip velocities observed in nature (see Boullier et al., 2009; Brantut et al., 2008; Ma et al., 2006). In other words, the influence of the boundary conditions during shearing of the fault gouge cannot be ignored. This can be important for experiments in thermal pressurization, calculation of the fracture energy during earthquake nucleation, evaluation of the transition limit from stable to unstable slip, and also for inference of the earthquake spectral characteristics detected in the surface from the fault gouge properties observed in the field (see Aki, 1967; Brune, 1970; Rice, 1973a, 2006a; Tsai & Hirth, 2020; Viesca & Garagash, 2015).

Chapter 2

Stability and Bifurcation Analysis

Summary

In this chapter we introduce the basic notions of stability of differential equations together with the notions of attracting and repelling fixed points. We use Lyapunov's basic theorems for determination of stability. The methodology of Linear Stability Analysis (LSA) is introduced for determining the stbility of fixed points of non linear differental equations. We explain the concept of Bifurcation and its implications for the fixed points and the different loci in the phase space of non linear differential equation. Finally, we present an application of the bifurcation and linear stability analysis in the 1D mechanical problem of the Overdamped Bead on a Rotating Hoop (OBRH).

2.1 Stability

In this chapter we will present in summary some aspects of the stability and bifurcation theory, which is central in the study of Ordinary Differential Equations (ODEs) and Partial Differential Equations (PDEs). Broadly speaking ODEs and PDEs can be further categorized into linear and non linear differential equations. While for the linear case a general methodology can be applied for their solution using the superposition principle, such a general approach is not yet possible for the non linear differential equations.

Since obtaining a solution in the non linear cases is a rather hard procedure, the interest was shifted in qualitative questions regarding the nature of possible solutions of the non linear differential equation. A solution to a non linear system of differential equations depends on a set of unknowns of the system that constitute its state. Considering the initial conditions of a point-particle at the beginning of observation, we note that we can fully determine its trajectory inside the phase space [1], by integrating its rate of change in time and taking into account the initial conditions, assuming that the trajectory is sufficiently smooth. The great advantage of this approach lies in its compelling geometrical interpretation. However, as the complexity and the order of the systems increase, such an interpretation becomes complicated (see Schneider & Uecker, n.d.; Strogatz, 2000; Wiggins et al., 1990).

In the phase space for a particular system of differential equations we will encounter a set of points whose rate of change at all times of the analysis is zero. This means that they don't move in the phase space and their state remains constant at all times (steady states). We call these sets of points, fixed points (see Figure 2.1). The qualitative questions are the following: Starting from a specific set of initial conditions close to a set of fixed points, does the system remain close to the set of points or it wonders off of it given enough time? Is this behavior the same for points that are close to the vicinity of the prescribed initial conditions? We can answer these questions by considering the stability of the set of fixed points. The theory of stability of ODEs has been developed by Aleksandr Mikhailovich Lyapunov (see Lyapunov, 1992). His methods still find great application in problems of non linear differential equations, where questions of stability

1. By phase space we mean a multidimensional space, whose dimensions are the unknown quantities of the system of differential equations at hand, in which all possible states of the system are represented, each possible state corresponding to a unique point in the phase space (see Arnol'd, 2013, among others.)

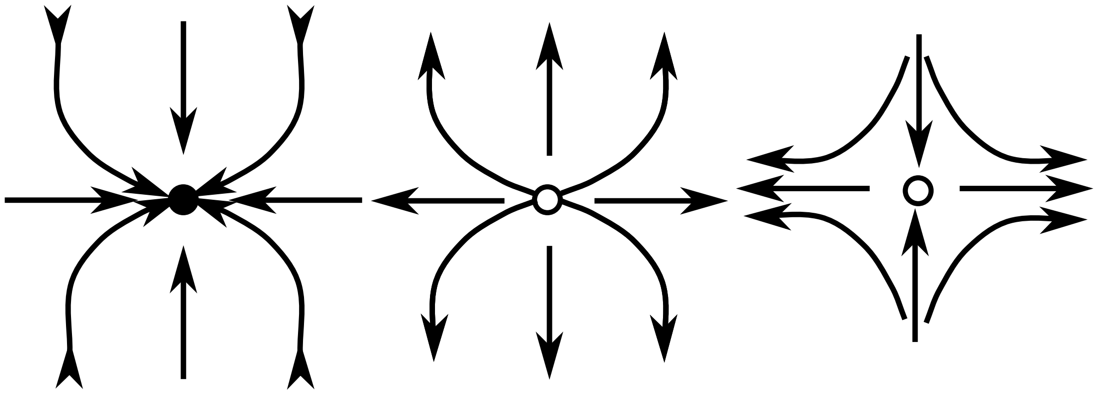

Figure 2.1 – Different types of fixed points in the phase plane. On the left we present an attractor. All trajectories in its vicinity are asymptotically stable, it is a stable fixed point. On the center we present a repeller. It repels all trajectories in its vicinity, consequently, it is an unstable point. Finally, we present a saddle point on the left. It attracts the trajectories in the vertical axis and repels the trajectories in the horizontal axis. It is an unstable fixed point.

of the obtained solutions are of great importance. Lyapunov proposed two methods for investigating the stability of dynamical systems (see Lyapunov, 1992). The first method bases on the linearization of the non linear differential system around a fixed point or set of points. After calculating the eigenvalues of the linearized system we can decide on the stability of the non linear system. This method is well described in Brauer and Nohel (1969), Chambon et al. (2004), Stefanou and Alevizos (2016), Strogatz (2018), among others. We briefly refer to the theorem's of Lyapunov (see Strogatz, 2018) for a stable and an asymptotically stable fixed point.

Lyapunov's theorem

Let's consider the fixed point $x^\star$ of a system $\dot{x} = f(x),\ f(x^\star) = 0$. We say that $x^\star$ is attracting if there is a $\delta > 0$ such that $\lim_{t\to\infty} x(t) = x^\star$ whenever $d_0 = |x(0) - x^\star| < \delta$. In other words any trajectory starting within a distance δ from $x^\star$ will converge to $x^\star$. This does not however tell us anything about how fast or how close to the attracting point is the particle's trajectory at all times. It can be so that the particle initially diverges form the $x^\star$ before it manages to converge (see Figure 2.2).

Lyapunov stability stipulates that nearby trajectories remain close for all times. This means that points that start close to the fixed point at a distance $d_0 < \delta,\ \delta > 0$ will always remain close to the fixed point at distance $d = |x(t) - x^\star| < \varepsilon$ for all positive times, where $\varepsilon > 0$ is a function of δ, $\varepsilon(\delta)$.

We say that $x^\star$ is asymptotically stable if it is both attracting and stable in a Lyapunov sense, i.e. for $|x(0) - x^\star| < \delta,\ |x(t) - x^\star| < \varepsilon(\delta),$ and $\lim\limits_{t\to\infty} |x(t) - x^\star| = 0$ see Figure 2.2.

Finally, we say that $x^\star$ is unstable, if it is not stable. The above theorem constitutes

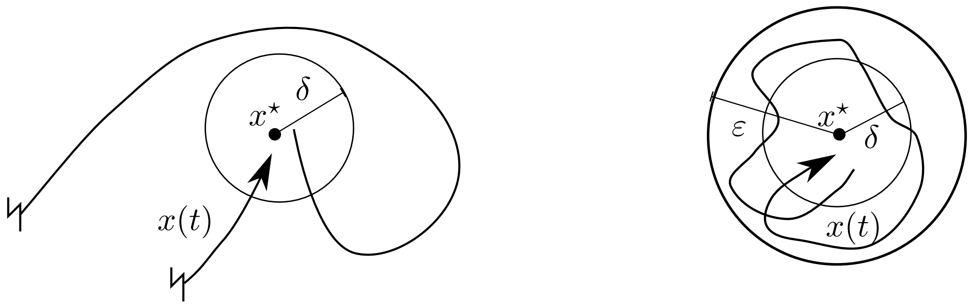

Figure 2.2 – Left: schematic representation of the attracting point. The trajectory starts close to it at distance δ, before it converges to it as $t \to \infty$. Right: A trajectory is stable in a Lyapunov sense, if it remains bounded inside a circle of radius ε for every t. The radius ε depends on the initial distance δ.

the basis of the linearization methodology (see Brauer & Nohel, 1969; Stefanou & Alevizos, 2016; Strogatz, 2000).

Lyapunov's second method for determining stability

While the method of linearization of the non linear system around its fixed points and calculation its stability from the equivalent linear system (Lyapunov's first method) is widely used in literature for a variety of applications. It is, constrained to autonomous systems (see Brauer & Nohel, 1969). By autonomous we mean systems that have time invariant coefficients. This arguably leaves untreated a large volume of systems whose coefficients depend on time, called non-autonomous systems [2].

2. According to Brauer and Nohel (1969), in the cases of non autonomous systems we can prove the asymptotic stability of the the zero solution considering that the eigenvalues of $A_{ij}(t)$, when t tends to ∞ are strictly negative, and that the elements of the characteristic stability matrix $A_{ij}(t),\ (i,j = 1,...)$ are continuous and have only a finite number of local maxima and minima in the interval $T \leq t < \infty$. To prove instability, however, Lyapunov's second method should be used instead

Below, we will present the theorems to prove stability or instability with the help of Lyapunov's second method (direct method, see Brauer & Nohel, 1969). Consider the system of autonomous differential equations:

$$\dot{x}_i = f(x_i), \tag{2.1}$$

where, $f(x_i)$ is derived from an scalar potential V, meaning $f(x_i) = -V,i$, where the comma is to be interpreted as the total derivative of the function V, with respect to its arguments i , $1...n$. Considering the potential function V we give the following definitions:

- The scalar function $V(x_i)$ is said to be positive definite on the set Ω if and only if $V(0) = 0$ and $V(x_i) > 0$ for $x_i \neq 0 \in \Omega$.
- The scalar function V(y) is said to be negative definite on the set Ω if and only if $-V(x_i)$ is positive definite in Ω.

We can determine the stability of this *conservative* system with the help of the following theorems:

- If there exists a scalar function $V(x_i)$ that is positive definite and its total derivative in time (material derivative), $\frac{dV}{dt} \leq 0$ *on some region* Ω *containing the origin*, then the zero solution of $\dot{x} = f(x)$ is stable.
- If there exists a scalar function $V(x_i)$ that is positive definite and its material derivative is negative definite *on some region* Ω *containing the origin*, then the zero solution of $\dot{x} = f(x)$ is asymptotically stable.

The following instability criteria can also be derived:

- If there exists a scalar function $V(x)$, $V(0) = 0$, such that the total derivative at the origin $\frac{V}{dt}\Big\|_{x=0}$) is either positive or negative definite on some region Ω containing the origin, and if there exists in every neighborhood N of the origin $N \subset \Omega$ at least one point α_i, such that $V(\alpha_i)$ has the same sign as the material derivative $\frac{dV}{dt}$, then the zero solution $V(x)$ is unstable.
- If there exists a scalar function V such that in region Ω containing the origin, its material derivative can be given as:

  $$\frac{dV}{dt} = \lambda V(x_i) + W(x_i),$$

  where $\lambda > 0$ is a constant and W is either identically zero, or W is a nonegative or nonpositive function such that in every neighborhood of the origin N, $N \subset \Omega$, there is at least one point α_i such that $V(\alpha_i)W(\alpha_i) > 0$, then the zero solution

$\dot{x}_i = f(x_i)$ is unstable.

Lyapunov's second method is also generalized for non linear, non-autonomous systems, however, their study lies outside the scope of this thesis.

2.1.1 Lyapunov's first method of stability - Linear systems of ODE's

We refer in brief to the theorems on which Lyapunov's first method is based on. We will use as reference a linear first order system of ODE's:

$$\dot{x}_i = A_{ij}x_j, \tag{2.2}$$

where A_{ij} is a rectangular $n \times n$ matrix of constant coefficients, and summation over repeated indices is implied. What is of interest here is the evolution of its solution in time. The solution of the above system of first order linear differential equations of constant coefficients is given by the form $y_i(t) = C_i \exp{(st)}$, where C_i is a vector of constant coefficients. Injecting into the system (2.2), we arrive at the following eigenvalue problem:

$$(A_{ij} - s\delta_{ij})C_j = 0 \tag{2.3}$$

where δ_{ij} is the Kronecker symbol, $\delta_{ij} = 1$ when $i = j$, and $\delta_{ij} = 0$ when $i \neq j$. Apart from the equilibrium -trivial- solution $x_i^\star = C_i^0 = 0$ the above eigenvalue problem has an infinite number of solutions if $\det{[A_{ij} - s\delta_{ij}]} = 0$. The determinant of the characteristic matrix gives rise to the system's characteristic polynomial, whose roots constitute the eigenvalues $s^{(i)}$ of the system. In this case the corresponding vectors $C_j(s^{(i)})$ are the eigenvectors of the system. From algebraic considerations, depending on the multiplicity of the eigenvalues $s^{(i)}$, any linear combination of the eigenvectors is a solution of the linear system described in (2.2). Considering that the characteristic polynomial of degree n has p, $(1 \leq i \leq p)$ distinct eigenvalues of multiplicity $m^{(p)} < n$, (if the eigenvalue k is simple then $m^k = 1$), then the solution of the linear system of ordinary differential equations is described by:

$$x(t) = \sum_{i=1}^{n} \sum_{j=1}^{m^{(i)}} \alpha_{i,j} C_{ij}^{(i)} t^{j-1} \exp{(s^{(i)}t)}, \tag{2.4}$$

where α_{ij} are the coefficients of the Fourier series. From the form of the solution in equation (2.4) we can see that the behavior is defined by the eigenvalues, $s^{(i)}$, which affect the exponential terms. We can prove the following theorems for the solutions of the system in question (see Brauer & Nohel, 1969).

- If all eigenvalues of A_{ij} have non-positive real parts and all those eigenvalues with zero real parts are simple, then the zero solution in system (2.2) is stable.
- If and only if all eigenvalues of A_{ij} have negative real parts, the zero solution in system (2.2) is asymptotically stable.
- If one or more eigenvalues of A_{ij} have a positive real part, the zero solution in system (2.2) is unstable.

While the method of finding the eigenvalues of the characteristic stability matrix $A_{ij},\ (i,j = 1,... \in \mathcal{N})$ was known before Lyapunov, the important contribution of his work, lies in the conditions he imposed concerning when such a linearization is applicable.

2.1.2 Lyapunov's first method of stability -Non-linear systems of ODE's

Unlike the linear case, where the fixed point (zero solution) is unique, in the case of non linear systems of ordinary differential equations, $\dot{x}_i = f(x_i)$, with $f(x_i)$ a non linear function of y_i, there can be multiple fixed points. The discussion of the previous section 2.1.1 can be extented to the case of non linear systems , considering a linearization of the non linear system in the neighborhood of its fixed points. We will express the solution $x_i(t)$ at the fixed point constant value x_i^0 and its perturbation $\tilde{x}_i(t)$, $x_i(t) = x_i^0 + \tilde{x}_i(t)$. Then applying the above form of the solution to the non-linear system of ODE's we obtain:

$$\dot{\tilde{x}}_i(t) = f(x_i^0 + \tilde{x}_i(t)) = f(x_i^0 + \tilde{x}_i(t)) - f(x_i^0), \tag{2.5}$$

where we have used the fact that $\dot{x}_i^0 = 0$ and $f(x_i^0) = 0$. Considering that the perturbation $\tilde{x}_i(t)$ is small, the difference in the right part of equation (2.5), can be written in the form of a Taylor series expansion as:

$$\dot{\tilde{x}}_i(t) = A_{ij}\tilde{x}_j(t) + g(\tilde{x}_i(t)), \tag{2.6}$$

where $A_{ij} = \frac{\partial f_i}{\partial x_j}\Big\|_{x=x_i^\star}$ is the linearized matrix of coefficients of the non linear system near the fixed point $x_i^\star$. The function $g(\tilde{x}_i(t))$ is a continuous function with $p(0) = 0$ and $\lim\limits_{x_i \to 0} = \frac{||g(\tilde{x}_i)||}{||\tilde{x}_i||} = 0$, where $||\cdot||$ is the the Eucledian norm $\sqrt{x_1^2 + ... + x_n^2},\ i = 1...n$. According to Brauer and Nohel (1969) the stability of the linearized system can be determined as follows:

- If all eigenvalues of A_{ij} have negative real parts, the solution $\tilde{x}_i = 0$ of equation (2.6) is asymptotically stable.
- If one or more eigenvalues of A_{ij} have a positive real part, the solution $\tilde{x}_i = 0$ of equation (2.6) is unstable.

We note here that in the case of the linearized systems the eigenvalues need to be strictly negative. We cannot draw any conclusion in the case of zero eigenvalues among the negative ones, since then the linearized system does not correspond to the original non linear case.

The above conditions can be used for determining the stability of a nonlinear system. This is the method of Linear Stability Analysis (LSA), as it is based on the linearization of $f(x_i)$. In section 2.2.1, we give an example of a linear stability analysis using the one dimensional mechanical system of the Overdamped Bead on a Rotating Hoop (OBRH) as described in Strogatz (2000).

When the order of the differential equation increases or equivalently the number of the system equations increases, the dynamics describing the particle flow in the phase space start to become more complicated (see Strogatz, 2000; Wiggins et al., 1990). The geometrical loci, which tend to attract or repel the solution trajectories are not only fixed points, but can be shown to correspond to limit cycles, spheres or even more complex mathematical structures called strange attractors (see Strogatz, 2000). An example of non linear systems performing oscillations approaching a limit cycle are the Duffing and Mathieu equations in the case of two dimensional phase space (see Strogatz, 2000; Wiggins et al., 1990). Increasing further the dimensionality of the system chaotic phenomena [3] become possible and the topology of the fixed surfaces, becomes increasingly complicated to be effectively described by a geometrical approach (see Strogatz, 2000; Trefethen et al., 2017; Wiggins et al., 1990).

In the case of partial differential equations dynamic behaviors of the same form as in the case of the ODEs is also present. We can still examine qualitative characteristics of

3. With the term chaotic we refer to those dynamical systems, whose behavior is strongly dependent on the knowledge of their initial conditions. Small perturbations at the measurement of the initial conditions can lead to wildly different behaviors of the system, making the dynamic system of ODEs inherently unpredictable.

the solution of non linear PDEs, with application of the first method of Lyapunov stability analyses. Examples can be found in chapters 3, 4 and 5 of the present thesis. In the case of non linear partial differential equations, the homogeneous solution can deviate towards different possible geometrical loci indicating a periodic or aperiodic behavior is time (see Strogatz, 2000, and chapters 3, 4, 5) and space (see Hähner et al., 2002; Mazière et al., 2010; Turing, 1990; E. Veveakis et al., 2014, and chapter 5).

In this thesis, as we will see in chapters 3, 4 and 5 we are interested in the conditions under which a fixed stable point corresponding to the homogeneous state of deformation of a solid becomes unstable, leading to the change of the solution to a localized profile of strain. When a fixed point changes its character from an attractor to a repeller (and vice versa) or when a fixed point appears to or disappears from the phase space, we say that the fixed point undergoes a bifurcation. In the next section, we refer to situations, where the fixed points or loci of a non linear differential equation may change abruptly depending on specific parameters of the solution.

2.2 Bifurcation analysis

During the evolution of a non linear phenomenon, fixed points and other attracting or repelling loci of the non linear partial differential equation that governs it, may change as time progresses. We refer to the sudden creation, destruction and even change of the stability of the fixed geometrical loci of the original non linear differential equation (see Figure 2.3). This happens when some of the terms of the original equation gradually change in relative size. Thus the solution is subjected to sudden and abrupt changes in its behavior (see Stefanou & Alevizos, 2016; Strogatz, 2000; J. Sulem & Vardoulakis, 1995). One example of such a behavior can be seen in the case of an Overdamped Bead on a Rotating Hoop (OBRH) presented below (see Strogatz, 2000, and Figure 2.4).

2.2.1 Example of bifurcation and linear stability analysis

The governing equation of the system depicted in Figure 2.4 is given by:

$$mr\ddot{\phi} = -br\dot{\phi} - mg\sin\phi + mr\omega^2 \sin\phi\cos\phi. \tag{2.7}$$

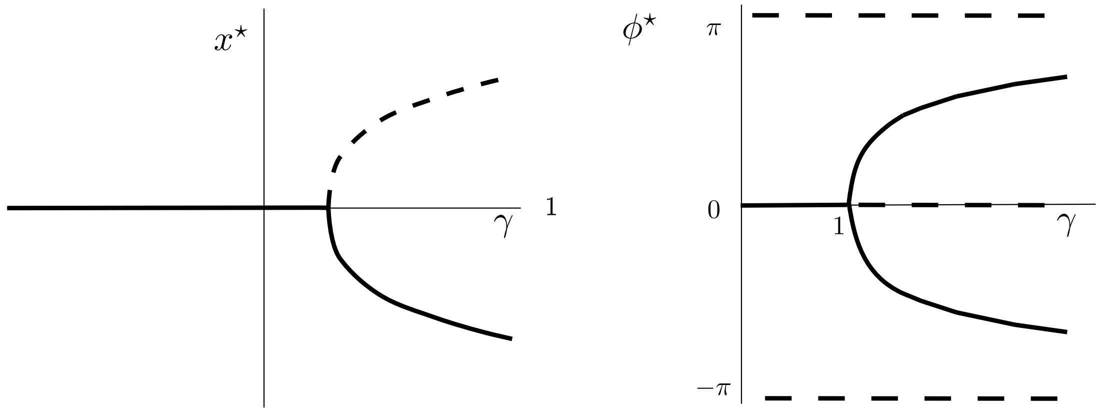

Figure 2.3 – Left: Saddle node bifurcation diagramm of the fixed points based on the bifurcation parameter γ. After the original stable branch gets destroyed two new symmetric branches take its place. One is a stable equilibrium branch (continuous thick line), while the other is unstable (dotted line), any trajectory found close to it will eventually drift towards the stable equilibrium branch. Right: Supercritical pitchfork bifurcation corresponding to the equilibrium paths of the OBRH system. Here after the bifurcation parameter takes its critical value two stable equilibrium branches are found, while the traditional stable branch corresponding to the position at the base of the hoop becomes unstable

Considering that the system is overdamped we can neglect the inertia term $mr\ddot{\phi}$. Consequently, the nonlinear ordinary differential equation of second order reduces to a non linear ordinary equation of first order. The modified equation can then be written as:

$$b\dot{\phi} = mgsin\phi \left(\frac{r\omega^2}{g} cos\phi - 1 \right). \tag{2.8}$$

Inspecting the equation we can establish that there exist two fixed points where $\sin\phi = 0$, namely, $\phi^\star = 0,\ \phi^\star = \pi$. We observe that if the hoop is rotating around its vertical axes fast enough $\gamma = \frac{r\omega^2}{g} > 1$, then two extra fixed points occur where $\phi^\star = \pm\cos^{-1}(g/r\omega^2)$.

We call the parameter γ, the bifurcation parameter of the system, as it determines the appearance, disappearance or change of stability of the fixed points of the system (equilibrium points) in the phase space. In the right part of Figure 2.3, we plot the angles of the fixed points from the center of the rotating hoop ϕ, in relation to the bifurcation parameter γ. We observe that at $\gamma = 1$, when the hoop is spinning fast enough, a bifurcation occurs. The initial stable fixed point at the base of the hoop $\phi = 0$, becomes unstable and two other stable fixed points make their appearance! The bifurcation is named -after its shape- as a pitchfork bifurcation. Thus, we establish that a supercritical pitchfork bifurcation occurs at $\gamma = 1$. We can check the nature of the new fixed points (attractors, repellers or half stable fixed points in the case of the 1D example), by performing a linear stability analysis, LSA, as described in the previous section 2.1.1. More specifically, by taking the first derivative of the nonlinear ODE with respect to the solution variable at the position of the fixed points. For the new fixed points we get:

$$b\frac{\partial\dot{\phi}}{\partial\phi}\Big|_{\phi=\phi^\star} = -mr\omega^2 \sin^2\phi^\star < 0, \tag{2.9}$$

which denotes that the fixed points that occur when the hoop is spinning sufficiently fast are stable fixed points.

On the right part of the Figure 2.3 we can see the stable and unstable equilibrium paths based on the previous analysis. The solid lines denote the asymptotically stable fixed points, while dashed lines denote the unstable fixed points. Noice that for the 1D problem at hand, one can determine the stability of the fixed points graphically, by plotting the phase space of equation 2.8. However, this is not possible for systems of higher dimensionality.

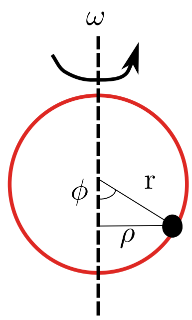

Figure 2.4 – An example of a non-linear mechanical system, bead on a rotating hoop. The angle ϕ is considered big enough during the phenomenon so that its $\sin\phi$, $\cos\phi$ cannot be simplified.

2.3 Key points

In this chapter we presented briefly the core notions of linear stability and bifurcation analysis. We introduced the notion of Lyapunov stability analysis, the existence of fixed points in the phase space for a non-linear system of ODEs and the evaluation of their stability properties (attractors or repellers in the 1D cases discussed in the example). We expanded in brief the notion of stability analysis in the non linear systems and provided the conditions under which the stability of the non linear system and its linearization correspond to each other, leading to the methodology of Linear Stability Analysis (LSA).

Next, we discussed the change of the properties of the fixed points and their existence in the phase space, when the response of the non linear system undergoes a bifurcation. We applied bifurcation analysis and Linear stability analysis in the case of a simple example (the OBRH system).

The above notion of stability and bifurcation will be used extensively in chapters 3, 4 and 5 we deal with the bifurcation and loss of stability of the homogeneous deformation profile in solids with different material models. The loss of stability of the homogeneous deformation is the cause of strain localization. The loss of stability can depend on several material parameters, which ar taken as bifurcation parameters.

Chapter 3

Strain localization and mesh dependency

Summary

Strain localization is a central topic in geomechanics as it is often related to failure and other important physical phenomena and geological processes. In this chapter we apply the method of Linear Stability Analysis (LSA) to evaluate the regularization properties of material laws and constitutive models commonly used in literature. We first show the inherent pathology of classical, Cauchy rate-independent continuum that leads to mesh sensitivity and we present methods for alleviating/regularizing this problem. These methods involve the use of theories that result in the introduction of characteristic time and length scales into the system. We then investigate the conditions under which, the homogeneous deformation loses stability leading to strain localization. One-dimensional examples are used to illustrate each regularization approach and show the main results of our analyses.

3.1 Introduction

Strain localization is a phenomenon which is found throughout natural and man-made structures. It is characterized by non-linearity as well as different characteristic time and spatial scales ranging from the near instantaneous fracture of brittle materials to the vast geological time required for the formation of intricate patterns in the earth strata. Strain softening is responsible for mesh dependence in numerical analyses involving the Cauchy continuum, which is observed in a vast variety of applications in solid mechanics, dynamics, biomechanics, geomechanics and rock mechanics. Therefore, numerical techniques that correctly regularize strain localization are of great importance in the analysis and design of engineering products and systems.

Another term that equivalently describes strain localization is the concept of "wave trapping" as explained in Erlich et al., 1980; Shawki and Clifton, 1989; Wu and Freund, 1984. According to this, the strain level at which the shear tangent modulus becomes zero propagates at zero speed, hence the strain wave becomes "trapped" Wu and Freund, 1984. An adiabatic shear band formation criterion has been proposed in Erlich et al., 1980. In Shawki and Clifton, 1989; Wu and Freund, 1984, the authors propose various general power laws for the regularization of strain localization. They couple their mechanical model of a generalized Arrhenius law with thermal softening while they constrain themselves to mechanical strain hardening to avoid "wave trapping" on a mathematical plane.

On a mathematical level, strain localization is understood as a bifurcation from the initial homogeneous deformation state of the structure to another equilibrium path. This automatically raises questions concerning the uniqueness of the reference homogeneous solution and its stability. We consider as solution $u(x,t)$ to a Boundary Value Problem (BVP), the function that satisfies the differential equation, while it respects the initial conditions at time $t = 0$ and the boundary conditions (BC's) at all times t. When (at a specific time $t = T < \infty$) the solution $u(x,t)$, depending on the boundary conditions and the forcing terms of the equation, becomes independent of time t, then the solution has reached a stable equilibrium namely $u(x,t) = u^\star(x), \forall t > T$. We say then that the solution of the problem has reached a steady state $u^\star(x)$.

In analyses involving geomaterials, which are the main focus of this chapter, depending on the type of continuum and the constitutive law used, perturbations $\tilde{u}(x,t)$ from the steady state $u^{\star}(x)$ may grow overtaking the behavior of the problem. In the case of homogeneous deformation (the specimen deforms under constant strain along its height (see left part of Figure 3.2), growing perturbations from the homogeneous steady state solution lead to localization of the strain profile (see Rice, 1975, 1976; J. Sulem & Vardoulakis, 1995). For a Cauchy continuum, the question of stability of the steady state solution of the homogeneous deformation is decided from the conditions needed such that the determinant of the acoustic characteristic tensor of the problem is equal to zero according to Rice (1976), Rudnicki and Rice (1975) among others.

Let us consider the uniform shearing of a 1D layer in the general case of a non linear material law with different multiphysical couplings (see right part of Figure 3.1). This a common application in different disciplines, however, in this chapter we will focus on the application in geomechanics. This application justifies also the selection of the material parameters used throughout the chapter (see Tables 3.1, 3.3). In this chapter we will investigate the conditions for bifurcation from the homogeneous reference solution under quasistatic conditions only. We will also assume that the layer under shear lies initially in static-equilibrium. In this case the reference homogeneous solution is a steady state $u^{\star}(x)$. We call a deviation $\tilde{u}(x,t)$ from the reference steady state, a perturbation. In the analysis of BVPs by the Finite Element (FE) method such a perturbation from the initial nominal solution, arises due to the introduction of geometrical or material imperfections, variation of the initial guess of the integration algorithm or simply by the accumulation of numerical error during the integration procedure. Based on the stability consideration between the steady state $u^{\star}(x)$ and the perturbed one $\tilde{u}(x,t) = u^{\star}(x,t) + \tilde{u}(x,t)$, the perturbed solution may become prevalent.

As mentioned above, we are interested on the conditions under which such a change in the behavior of the problem may arise. More precisely, we will answer to the following questions: When does the reference steady state becomes unstable? When do new fixed points leading to localized deformation profiles make their appearance, depending on the variation of some material parameters? What is the localization width of the perturbed solution? We will answer these questions with the help of the Linear Stability Analysis (LSA) introduced in the previous chapter 2.

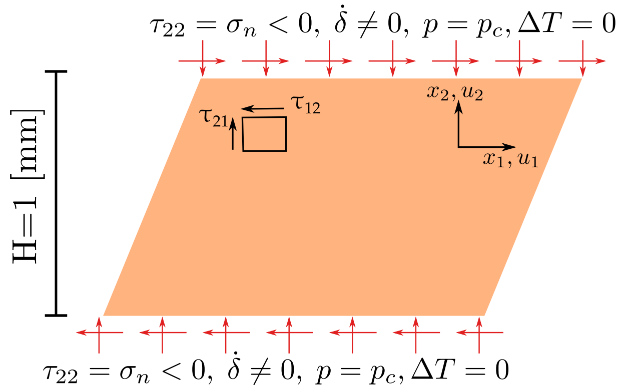

Figure 3.1 – Simple shear of a 1D Cauchy layer. Homogeneous deformation of a Cauchy non linear layer under 1D simple shear, the boundary conditions refer to the general case, when also multiphysical couplings are present.

The above questions are important, since for a perturbed solution to provide meaningful information about the problem in question, it must give ubiquitous results for specific quantities of the mathematical problem, such as the energy, and not break more general and fundamental fundamental physical laws (see for example the discrete nature of material in the micro- and nano- scales, the barrier of the speed of light in Einstein's theory of general and special relativity, etc). These are tests for instance, that an analysis based on classical mechanics must hold up to. However, often the perturbed solutions obtained by numerical solutions fail to these tests. This is when the underlying numerical model reaches its limits and new assumptions about finer scales and more precise description of the problem's constituents needs to be included.

A prime example of such a case is the localization on a mathematical plane in the predicted post bifurcation regime of numerical analyses involving geomaterials, which in the absence of viscosity can take place in infinite rate (see section 3.2.1, Figure 3.3). Moreover, localization on a mathematical plane, renders the solution obtained from numerical methods, such as the FE method, mesh dependent. In addition, experimental evidence in materials suggests that localization in nature does not occur on a mathematical plane, rather it involves a small zone of finite thickness that accommodates the majority of the deformation (see Chambon et al., 2004; F. M. Chester and Chester, 1998a; Muhlhaus and Vardoulakis, 1988; Sibson, 2003a; I. Vardoulakis and Sulem, 1995 among others).

To remedy this inconsistency between experiments and analytical and numerical predictions, two main approaches are often found in the literature. The first approach seeks to incorporate a modified constitutive law including the effects of viscosity (see de Borst & Duretz, 2020; Sluys & de Borst, 1992; Sluys et al., 1993; W. Wang et al., 1996; W. Wang et al., 1997, and section 3.3, also described in greater detail in chapter 4). Furthermore, the addition of multiphysical, Thermo-Hydro-Chemo-Mechanical (THMC) couplings (see Lachenbruch, 1980b; Mase & Smith, 1987; Platt et al., 2014a; Rice, 2006a; J. Sulem & Famin, 2009; J. Sulem & Stefanou, 2016a, among others) in order to avoid strain localization on a mathematical plane have been considered. This is further explored in section 3.4. The other approach starts from the introduction of micromorphic continua, which, as we show in section 3.5, introduce characteristic length scales to the mathematical problem (see De Borst, 1991; de Borst & Sluys, 1991; Germain, 1973; Rattez, Stefanou, Sulem, Veveakis, et al., 2018b; Sluys et al., 1993; J. Sulem et al., 2011; I. Vardoulakis, 2009, among others).

When analyzing the localized strain profile of the perturbed solution with the help of FE analyses, care must be taken so that the profile of strain localization remains constant (and thus objective) upon mesh refinement. Considering that the solution indicates strain localization on a mathematical plane, then upon mesh refinement localization will always be constrained in one element. This is problematic for two reasons. Firstly it is not possible in nature for deformation to localize upon a mathematical plane. Experiments performed in the laboratory and observations in nature clearly show that deformation is accommodated in a narrow zone of several hundred micrometers (see Needleman & Tvergaard, 1992; Sibson, 2003a, among others). We know that nature in small scales is discontinuous. Especially geomaterials such as sand, exhibit granular characteristics at length scales observed by the naked eye. Secondly, localization on a mathematical plane corresponds to zero dissipation, when the material is clearly undergoing plastic deformation and its temperature increases due to plastic work (see Alaei et al., 2021; Needleman & Tvergaard, 1992; Rognon et al., 2015). This result also translates to the numerical analyses. As we refine the mesh of the analysis we note that localization on the smallest mesh dimension gradually reduces the dissipated energy to zero. Thus we cannot get an objective estimation of the dissipated energy in such cases. This is a big problem especially in fault mechanics where the dissipated energy is crucial for evaluating the stability and nucleation of the fault, and estimating the energy traveling in the form of seismic waves to the surface (see Kanamori & Rivera, 2006; Rice, 1973b). Therefore, care must be taken so that the perturbed solution leads to a mesh objective strain profile.

Before selecting the appropriate continuum theory for our analyses in fault mechanics, we investigate the regularization properties of several constitutive properties in the framework of the classical Cauchy continuum. We start with an elasto-viscoplastic rate independent material law in section 3.3. We then consider a classical Cauchy continuum with an elastic perfectly plastic material law with the influence of THM couplings (see section 3.4) and comment on strain localization and mesh dependency. Finally, we present a Cosserat micromorphic continuum model with an elastic plastic strain softening material law in section 3.5. We compare the obtained numerical results in terms of their stress-strain diagrams and localization profiles in order to evaluate their regularization properties. This comparizon shows that the Cosserat micromorphic continuum is the only appropriate model for understanding the behavior of a fault gouge under coseismic slip, like the one studied in chapter 5.

The numerical results presented here, are based on non linear quasistatic analyses. We apply linear stability analysis under quasistatic conditions (neglecting the inertia terms), since we consider the influence of inertia is not important during shearing of the fault gouge under coseismic slip (see Platt et al., 2014a; Rice et al., 2014a, and the Inroduction). The influence of inertia is important, however, when the regularization properties of the elasto-visco plastic material law are discussed (see de Borst & Duretz, 2020; Needleman, 1988; Sluys & de Borst, 1992; W. Wang et al., 1997). We will study this claim in chapter 4, where the LSA methodology will be applied in the study of a material law incorporating viscoplasticity and inertia.

Finally, we investigate in this chapter a mechanism of a traveling shear band instability in the case of a elasto-viscoplastic material with strain hardening and strain-rate softening. The last mechanism creates a traveling instability in the medium named the Portevin - Le Chatelier (PLC) traveling localization phenomenon. In chapter 5, section 5.3.3, we have identified a similar mechanism in the case of an elastic perfectly plastic Cosserat continuum with THM couplings. Here, we make use of a conceptually simpler model, that incorporates the notion of a propagating strain localization wave inside the continuum layer.

3.2 Cauhy elasto-plasticity with strain softening

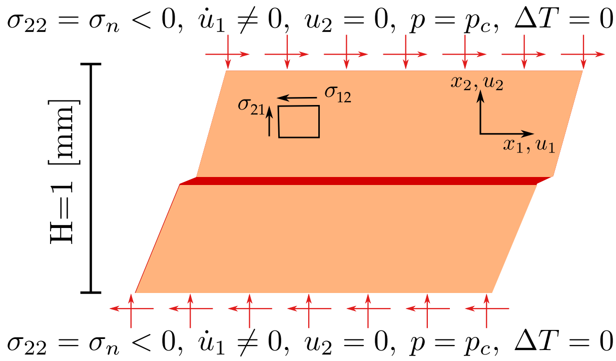

Figure 3.2 – Simple shear of a 1D Cauchy layer. The boundary conditions refer to the general case, when also multiphysical couplings are present. Strain localization of the solution after bifurcation from the homogeneous steady state takes place.

In this section we investigate with the help of the LSA the preferred localization mode for the case of a linear elastic plastic strain softening Cauchy continuum. The general PDEs of the problem in 1D showing the body in equilibrium with its inertial forces are:

$$\frac{\partial \sigma_{12}}{\partial x_2} = \rho \ddot{u}_1, \quad \frac{\partial \sigma_{22}}{\partial x_2} = \rho \ddot{u}_2, \tag{3.1}$$

where σ_{ij} are the Cauchy stress tensor components, ρ is the material density and u_i represents the displacement in the direction i. We use the dot symbol $\dot{()}$ to refer to derivation w.r.t time. When the body is in a steady state:

$$\frac{\partial \sigma^\star_{12}}{\partial x_2} = 0, \quad \frac{\partial \sigma^\star_{22}}{\partial x_2} = 0, \tag{3.2}$$

We apply the perturbed displacement fields $u_1 = u_1^\star + \tilde{u}_1,\ u_2 = u_2^\star + \tilde{u}_2$ and stress fields $\sigma_{ij} = \sigma^\star_{ij} + \tilde{\sigma}_{ij}$, respecting the BC's in the BVP, $u_1\Big\|_{x=0} = u_1\Big\|_{x=H} = 0$, $\sigma_{22}\Big\|_{x=0} = \sigma_{22}\Big\|_{x=H} =$ 200 MPa (see Figure 3.2). The perturbed system of partial differential equations reads:

$$\frac{\partial \tilde{\sigma}_{12}}{\partial x_2} = \rho \ddot{\tilde{u}}_1, \quad \frac{\partial \tilde{\sigma}_{22}}{\partial x_2} = \rho \ddot{\tilde{u}}_2. \tag{3.3}$$

In this example we will consider the simple example of simple shear of the 1D layer. For elastoplasticity, the yield criterion involving the shear stress tensor under the 1D simple shear assumption can be written as:

$$F(\sigma_{12}, \gamma^p) = \sigma_{12} - \tau_0(\gamma^p), \tag{3.4}$$

where σ_{12} is the shear stress and γ^p is the accumulated plastic strain $\gamma^p = \int_0^t \dot{\varepsilon}_{12}^p dt$. The constitutive relations for the stresses taking part in the equilibrium equations can be written as:

$$\begin{aligned}\tilde{\sigma}_{12} &= 2G\frac{h}{1+h}\tilde{\varepsilon}_{12},\\ \tilde{\sigma}_{22} &= K\tilde{\varepsilon}_{22},\end{aligned} \tag{3.5}$$

where G, K are the shear and bulk moduli of the 1D material and h is the softening parameter indicating the slope of post yielding branch of the material. The form of the perturbation used is not at random. Since in our application the BC's were prescribed $(u_1\Big\|_{x=0,H} = u_2\Big\|_{x=0,H} = 0)$, (Dirichlet boundary conditions), the values of the perturbation at the boundaries need to be zero. From Fourier analysis of the PDE problem, we know that every solution of the problem can be expressed as a series of sine and cosine terms. Equations 3.3, 3.5 define a system which have solutions of the form $\tilde{u}_i = u_i \exp(st + ikx_2)$, $i = 1, 2$, with $g_i \neq 0$. Therefore, replacing the general solution in (3.5) we obtain:

$$\begin{bmatrix} -\frac{Gh}{1+h}k^2 - \rho s^2 & 0 \\ 0 & -Mk^2 - \rho s^2 \end{bmatrix} \begin{bmatrix} u_1 \\ u_2 \end{bmatrix} = \begin{bmatrix} 0 \\ 0 \end{bmatrix} \tag{3.6}$$

Consequently, the determinant of the above system has to be equal to zero, leading to:

$$s = -ikv_p\sqrt{\frac{M}{\rho}}, \text{ or equivalently} \tag{3.7}$$

$$s = \pm ikv_s\sqrt{\frac{h}{1+h}}, \tag{3.8}$$

where $v_p = \sqrt{\frac{M}{\rho}}$ and $v_s = \sqrt{\frac{G}{\rho}}$ are the longitudinal and shear wave velocities respectively. The variable s is also called the Lyapunov coefficient.

Therefore, the initial stable homogeneous deformation steady state becomes unstable and the trajectories of the solution will be repelled from the steady state of the homogeneous deformation towards another fixed point, when Re[s]>0. This happens when we take $h < 0$. In this case the real part of the Lyapunov coefficient $\mathrm{Re}[s]$ is greater than zero and the perturbation grows away from the homogeneous deformation state. Additionally we can investigate which perturbation increases the fastest in the medium. This will give us the new localization profile. In this case we note that the Lyapunov coefficient s is proportional to the wavenumber k and therefore, inversely proportional to the wavelength $\lambda = \frac{2\pi}{k}$ namely, $s \sim \frac{1}{\lambda}$ (see Figure 3.3). We establish therefore, that the infinitesimal wavelength ($\lambda \to 0$) increases the fastest. Therefore, considering h as the bifurcation parameter, when h changes sign from hardening to softening the solution will diverge from its state of homogeneous deformation to a state where strain localizes on a mathematical plane.

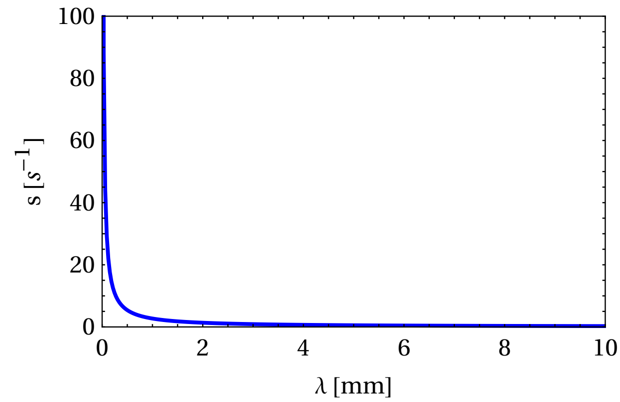

Figure 3.3 – Plot of the Lyapunov Coefficient over a range of different wavelengths. The infinitesimal wavelength presents the higher Lyapunov coefficient which tends to ∞.

3.2.1 Numerical example

We present here a numerical application of the above LSA analysis with the help of Finite elements. We will study the simple shear of a 1D Cauchy layer (see Figures 3.1, 3.2) with a linear elastic plastic strain softening material with prescribed boundary conditions and the material law of equation (3.10). The parameters used in the numerical analyses are shown in Table 3.1. They correspond to typical values of geomaterial parameters for rock.

Where, by H_c we denote the softening parameter used for the evolution of $\tau_0(\gamma^p)$. The strain softening parameter h used in the theoretical analysis of equations (3.10),(3.5) can the be derived as: $h = \tau_0\Big\|_{\gamma^p=0} H_c$. We use a linear relation of the form:

$$\tau_0(\gamma^p) = \tau_0|_{\gamma^p=0}(1 + H_c\gamma^p) \tag{3.9}$$

In what follows we will use linear finite elements with reduced integration. We can confirm the calculations above with the help of a numerical analysis shearing only one element and convergence analyses (see Stathas & Stefanou, 2019a).

Parameters	Values	Units
K	$\frac{1}{3}10^2$	GPa
G	10	GPa
$\tau_0\|_{\gamma^p=0}$	10^{-1}	GPa
H_c	-0.25	-

Table 3.1 – Material parameters

In order to show that in a quasi static analysis the classical Cauchy continuum with plastic softening localizes on a mathematical plane, we perform a series of numerical analyses, where we progressively increase the number of elements. In order to provoke the numerical solution to localize, we introduce a material imperfection in a small region in the middle of the specimen. In each of the analyses performed the imperfection has a size of two elements.If the solution does not localize on a mathematical plane then the width of the strain localization will be always the size of two elements. However, we show that the numerical solution indeed localizes on the smallest possible mesh dimension of one element as plastic strain localizes on a mathematical plane. In Figure 3.4 on the left, we present the frictional response of the layer with respect to the displacement on top of the layer. We note the characteristic kink and subsequent slope reduction of the frictional response at the post yielding branch of the $\sigma_{12}-\delta$ diagram, indicating that strain localizes in one element. On the right part we present the localization profiles at the end of the analyses. We notice that localization is always trapped in only one element. This leads to even smaller localization width as the mesh becomes progressively finer confirming the theoretical results of the previous paragraph. The reduction on the localization width is directly reflected in the decrease of the slope of friction displacement curves $\sigma_{12} - \delta$.

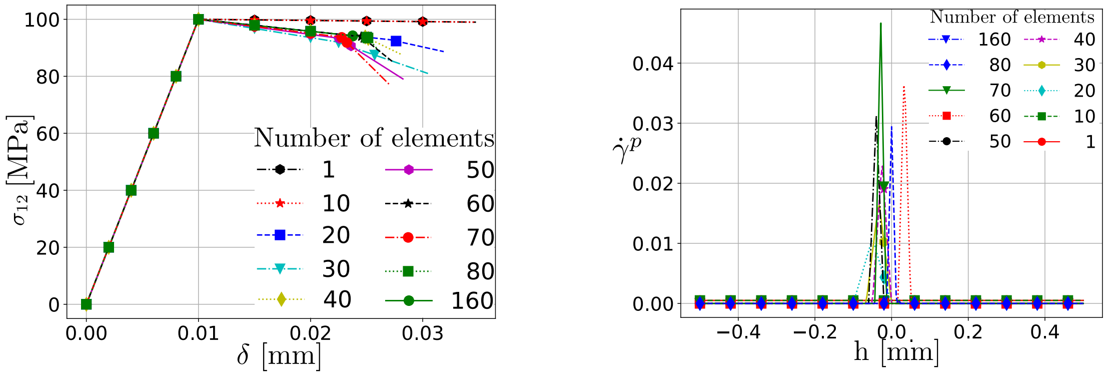

Figure 3.4 – Simple shear of an infinite layer for different number of elements. Left: Frictional strength σ_{12} vs horizontal displacement on top of the layer δ. The analysis of one element does not localize and can be used as a way of validating w.r.t. the theoretical prediction of homogeneous deformation. As element number increases localization drives the slope steeper. On the right: Localization width profiles for different number of elements. We interpret localization as the rate of increase of the plastic deformation ($\dot{\gamma}^p$). The analysis for one element does not localize. The characteristic peak at the profiles of the plastic strain-rate indicate that the solution localizes in one element.

3.3 Cauchy elato-vicoplsticity with strain softening and strain-rate hardening

In this section we investigate with the help of the LSA the preferred localization mode for the case of a linear elastic, visco-plastic strain softening and strain-rate hardening Cauchy continuum. We use the Perzyna approach for considering elasto viscoplasticity as described in Appendix A, the yield criterion involving the deviatoric part of the stress tensor under the 1D simple shear assumption can be written as:

$$F(\sigma_{12}, \gamma^p) = \sigma_{12} - \tau_0(\gamma^p), \tag{3.10}$$

Following the Perzyna Plasticity approach the viscoplastic strain-rate can be defined as:

$$\dot{\gamma}^{vp} = \frac{F}{\eta F_0}\frac{\partial F}{\partial \sigma_{ij}}, \tag{3.11}$$

Considering that we apply simple shear on the BVP, the only plastic strain is the $\gamma^{vp} = 2\varepsilon^{vp}_{12}$. Making use of the Perzyna constitutive relation and differentiating it with respect to time we arrive at the relationship $\ddot{\lambda} = \frac{\dot{F}}{\eta F_0}$. For a complete elasto-visco-plastic formulation of Perzyna or consistency type in 3D we refer to the Appendix A. According to the viscoplastic rate form of the constitutive equation, due to the additive decomposition between the elastic and plastic part of strain, we obtain:

$$\dot{\sigma}_{12} = G(\dot{\gamma} - \dot{\gamma}^{vp}), \tag{3.12}$$

where due to the form of the yield criterion, the viscoplastic multiplier is equal to the viscoplastic strain-rate $\dot{\lambda} = \dot{\gamma}^{vp}$. Multiplying by $\frac{\partial F}{\partial \sigma_{12}}$ the equation (3.12) and applying the consistency condition $\dot{F} = 0$ we obtain the following relation for the viscoplastic strain-rate:

$$\dot{\lambda} = \frac{1}{h+1}\dot{\gamma} + \frac{\eta F_0}{h+1}\ddot{\lambda}. \tag{3.13}$$

Inserting equation (3.13) into equation (3.12), we derive the material description for an elasto-viscoplastic solid under 1D shear:

$$\dot{\sigma}_{12} = \frac{hG}{1+h}\dot{\gamma} + \frac{\eta F_0}{h+1}\ddot{\gamma}^{vp}, \quad \dot{\sigma}_{22} = M\dot{\varepsilon}_{22}, \tag{3.14}$$

where we have taken advantage of the relation $\ddot{\lambda} = \ddot{\gamma}^{vp}$. Replacing the material equations (3.14) into the equilibrium equation (3.3), we arrive at the following PDE describing the BVP in question (see also Appendix A for a more general formulation):

$$Gh\frac{\partial^2 \tilde{u}_1}{\partial x^2} - \frac{\partial^2 \tilde{u}_1}{\partial t^2}\frac{(3+\bar{h})G}{v_s^2} + \bar{\eta}^{vp}G\left(\frac{\partial^3 \tilde{u}_1}{\partial t \partial x^2} - \frac{1}{v_s^2}\frac{\partial^3 \tilde{u}_1}{\partial t^3}\right), \tag{3.15}$$

where $v_s = \sqrt{\frac{G}{\rho}}$, $\bar{\eta}^{vp}G = \eta F_0$. Next, we consider the following normalized quantities: $\bar{u}_1 = \frac{\tilde{u}_1}{u_c}$, $\bar{t} = \frac{t}{t_c}$, $\bar{x} = \frac{x}{x_c}$. Replacing in the above equation (3.15) we arrive at the normalized form of the equation:

$$\left(\frac{v_c^2}{v_s^2}\frac{\partial^3 \bar{u}_1}{\partial \bar{t}^3} - \frac{\partial^3 \bar{u}_1}{\partial \bar{x} \partial \bar{t}}\right)\frac{\bar{\eta}^{vp}}{t_c h} + \frac{v_c^2}{v_s^2}\frac{3+h}{h}\frac{\partial^2 \bar{u}_1}{\partial \bar{t}^2} - \frac{\partial^2 \bar{u}_1}{\partial \bar{x}^2} = 0, \tag{3.16}$$

where $v_c = \frac{x_c}{t_c}$ is a characteristic velocity of the problem. This equation is the normalized elasto-visoplastic partial differential equation of equilibrium which we will study in full in the next chapter 4. Replacing the general solution of the form $\tilde{u}_i = u_i \exp(st + ikx_2)$, $i = 1, 2$ in the above equation, and considering the form of the perturbation fields respecting the BC's, we arrive at the following expression for the system of PDEs:

$$\begin{bmatrix} -hk^2 - \left(\frac{3+h}{v_s^2}\right) + \eta^{vp}\left(-sk^2 - \frac{1}{v_s^2}s^2\right) & 0 \\ 0 & -Mk^2 - \rho s^2 \end{bmatrix} \begin{bmatrix} u_1 \\ u_2 \end{bmatrix} = \begin{bmatrix} 0 \\ 0 \end{bmatrix} \tag{3.17}$$

In this chapter, based on the normalized quantities, assuming that the terms of viscosity are larger than the ones of inertia, we can neglect the inertia terms and study the stability of the quasistatic viscous case. We are allowed to make such a simplification based on asymptotic and physical considerations as presented in (see also Stefanou & Gerolymatou, 2019). The inertia quantified by the density term ρ, lies inside the $v_s = \sqrt{\frac{G}{\rho}}$ term. Assuming $\rho = 0$ we are left with the following system:

$$\begin{bmatrix} -hk^2 + \eta^{vp}sk^2 & 0 \\ 0 & -Mk^2 - \rho s^2 \end{bmatrix} \begin{bmatrix} u_1 \\ u_2 \end{bmatrix} = \begin{bmatrix} 0 \\ 0 \end{bmatrix} \tag{3.18}$$

We seek conditions for which the above system admits multiple solutions. This happens when its determinant becomes zero (see Chambon et al., 2004; Rice, 1975; Stefanou & Alevizos, 2016; J. Sulem & Vardoulakis, 1995, among others).

$$s = \pm ikv_p, \text{ or} \tag{3.19}$$

$$s = -\frac{h}{\eta^{vp}}. \tag{3.20}$$

Thus, we establish that the real part of the Lyapunov coefficient is greater than zero (Re[s]>0). We note here, however that in this case the Lyapunov coefficient s does not depend on k (see Figure 3.5). All perturbations from the homogeneous reference state grow away with the same rate. In the case of strain-rate dependency in the form of an elasto-viscoplastic material law, Needleman (1988) notes that strain localization follows the profile of the material imperfection used for the perturbation from the nominal homogeneous solution. In this sense, localization does not happen anymore on a mathematical plane, but on the width of the imperfection. Although this is a method to restore the mesh objectivity of the numerical solution, this approach does not provide us with a framework of correctly choosing the imperfection width. In other words, the imperfection width is not tied to a fundamental material parameter and as a consequence we are forced to decide on it a priori. Furthermore, an imperfection in nature, can have different origins and we cannot possibly account for all of them in the sense that the quasistatic viscosity

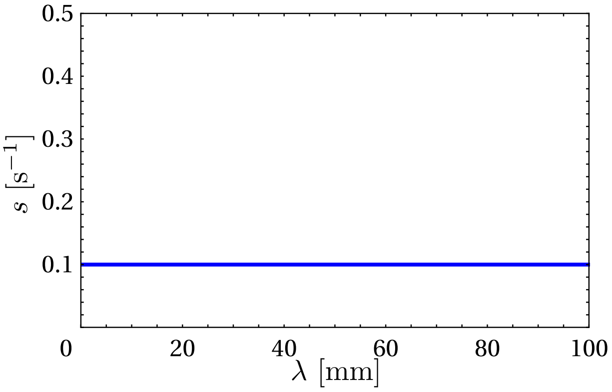

Figure 3.5 – Plot of the Lyapunov Coefficient over a range of different wavelengths. The Lyapunov coeffixient is uniform over the whole range of wavelengths. All the perturbations increase by the same amount no strain localization mode is preferred.

regularization model is indifferent to the size (scale) of the imprefections. In this sense, the problem is still not regularized.

3.3.1 Numerical example

In order to illustrate the above theoretical findings, we perform non linear finite element analyses, in which we increase progressively the number of finite elements while adding a material imperfection in the middle of the specimen. The width of the imperfection is set to 2 elements wide. In Figure 3.6 we present the results of our analyses fotr the simple shear of an elasto viscoplastic layer.

On the left part of Figure 3.6 we present the shear stress σ_{12} vs horizontal displacement on top of the layer δ. The analysis of one element does not localize and can be used as a way of validating w.r.t. the theoretical prediction. As element number increases localization drives the slope steeper. The exact moment when localization happens depends on the viscosity parameter η along with imperfection size and the number of elements. On the right part of the Figure we present the localization width profiles for different number of elements. We interpret localization as the rate of increase of the plastic deformation γ^p. The localized zone is always two element wide in accordance with the imperfection width. In this sense the results are dependent in the choice of the imperfection length and thus mesh dependent due to the absence of a characteristic material parameter.

We continue our study of the classical Cauchy elasto viscoplastic continuum under qua-

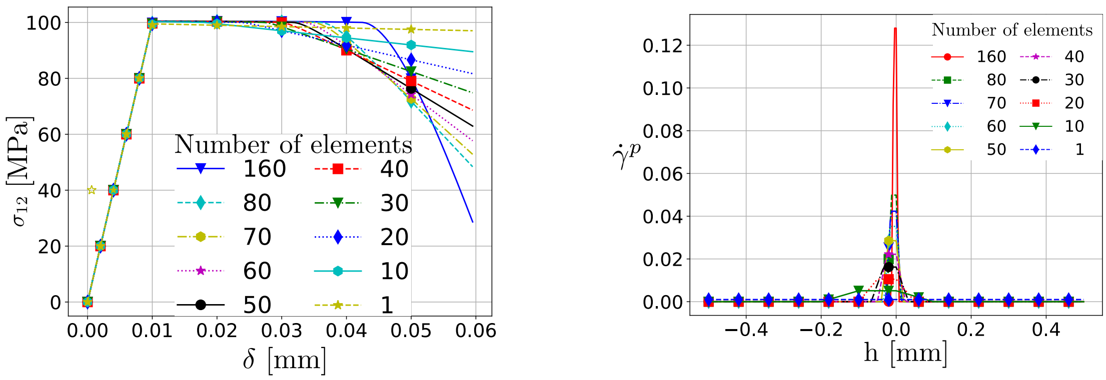

Figure 3.6 – Simple shear of an infinite layer for different number of elements. Left: Frictional strength τ vs horizontal displacement on top of the layer δ. On the right: Localization width profiles for different number of elements.

sistatic conditions by exploring the influence of a smaller viscosity parameter η in the results. We present these results in Figure 3.7. On the left part of the Figure 3.7, we show the $\sigma_{12} - \delta$ diagrams for a small viscosity parameter η, by varying the mesh size and the imperfection length of the specimen. While initially the results follow the localization width, dictated by the imperfection size, we note that in later parts of the analysis, the perturbation grows enough so that localization inside the imperfection can be observed, thus localization on the width of one element ensues. This happens because the numerical simulation introduces perturbations by itself due to small numerical errors in the finite element discretization and small errors in the residual during the Newton-Raphson procedure for the numerical solution of the resulting nonlinear algebraic equations.

The influence of the viscosity parameter on the time when localization on a mathematical plane takes place is shown on the right part of Figure 3.7. For small values of $\eta \leq 0.02$ s, the results between the rate independent and the rate dependent cases exhibit localization on the smallest possible mesh dimension almost immediately. Increasing further the viscosity parameter η we note that we improve the convergence of the solution tied to the localization on the smallest mesh dimension. Increasing the viscosity value to $\eta = 2$ s leads to localization being constrained to the width of the initial imperfection, Finally, for very large values of the viscosity parameter $\eta = 20$ s we show that the analysis does not localize at all within the prescribed range of the applied slip displacement δ values.

The localization of strain in one element in the numerical solution is a result of the growth of small perturbations inside the already weakened region due to imperfection. When the viscosity parameter is high, strain localization on a mathematical plane is delayed since it takes time for the numerical errors to accumulate and provoke the localization inside the imperfection. Nevertheless, from a theoretical standpoint (see equation (3.20)) both strain localization of the imperfection width and inside it, increase with the same velocity as time progresses (same Lyapunov coefficient s). This means that eventually the strain localization inside the localization width will become prevalent and strain will localize on a mathematical plane. The time it takes for strain localization to accumulate in one element inside the imperfection is related to the characteristic localization time as defined in chapter 4.

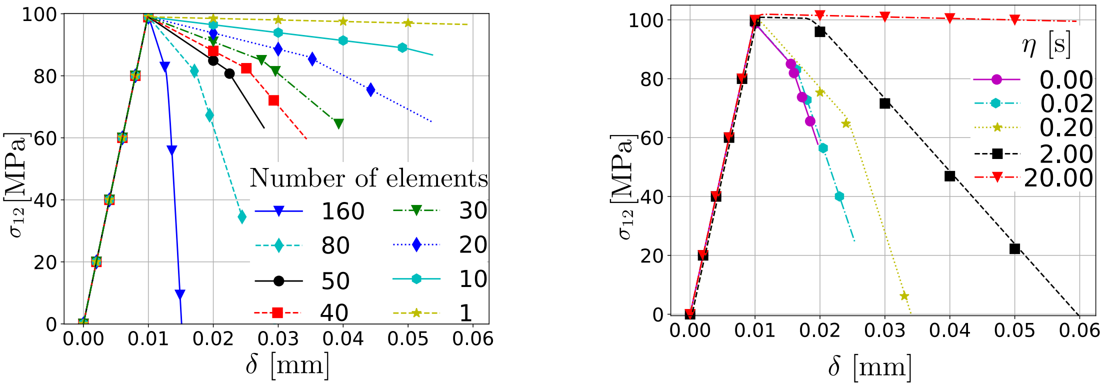

Figure 3.7 – Simple shear of an infinite layer for different number of elements. Left: Frictional strength τ vs horizontal displacement on top of the layer δ. The analysis of one element does not localize and can be used as a way of validating w.r.t. the theoretical prediction. On the right: Influence of the viscosity parameter η on the localization profiles of an elasto-viscoplastic material with strain softening and strain-rate hardening. The imperfection size and the number of finite element is kept constant for all the analyses. Localization on a mathematical plane vs localization on the imperfection width vs no localization at all, can be discerned from observing the difference in slope between the analyses.

3.4 Strain localization in a Cauchy linear elastic, perfectly plastic material with multiplysical couplings

In nature phenomena rarely happen in isolation. This means that different physical processes may happen simultaneously and affect the outcome of the overall procedure. The coexistence of different physical phenomena in same or different space and time scales and the way they interact is a subject of vivid discussion (see Alaei et al., 2021; Alevizos et al., 2014; T. J. Burns, 1985; Chambon et al., 2004; Forest & Sievert, 2003; Forest, Pradel, et al., 2001; Jacquey et al., 2021; Lachenbruch, 1980a; Lee & Delaney, 1987; Mase & Smith, 1987; Masi et al., 2021; Neff et al., 2014; Rattez, Stefanou, Sulem, Veveakis, et al., 2018b; Rezakhani & Cusatis, 2016; Rice, 2006a; Rice et al., 2014a; Stefanou, 2019; Stefanou & Gerolymatou, 2019; Stefanou et al., 2010; Strogatz, 2000, among others). We expect that phenomena coexist and interact when their characteristic time (or characteristic length in spatial homogenization applications) are of the same order of magnitude, if the identified phenomena differ by more than one order of magnitude in their characteristic evolution time then they don't interact across different scales (Principle of separation of scales).

In the case of shearing of faults, researchers have proposed the introduction of different weakening mechanisms in the evolution of friction during coseismic slip. Apart from the classical mechanical softening approach, we note the introduction of frictional weakening mechanisms due to melt formation under flash heating (see Rice, 2006a), fine particle generation due to comminution breakage of grains (see Collins-Craft et al., 2020; Rattez, Stefanou, & Sulem, 2018), thermal decomposition of minerals (see J. Sulem & Famin, 2009; J. Sulem & Stefanou, 2016a) and lubrication due to shearing of silicate minerals causing water release (see Di Toro et al., 2011b). The main frictional weakening mechanism we will be investigating in the later chapters of this thesis 5 and 6, is thermal pressurization (see Platt et al., 2014a; Rattez, Stefanou, & Sulem, 2018; Rattez, Stefanou, Sulem, Veveakis, et al., 2018b; Rempel & Rice, 2006; Rice, 2006a; Rice et al., 2014a, among others). During thermal pressurization the part of the fault gouge under yield (Principal Slip Zone, PSZ), releases heat during the production of plastic work (dissipation). The release of heat to the surroundings of the PSZ causes the temperature of the nearby pore fluid to increase. This leads to a constrained expansion of the fuid volume at the pores of the solid, which increases the pore fluid pressure and decreases the effective stress of the fault gouge material. Considering that the friction of the material at the fault gouge is sensitive to the effective confining pressure, this leads to a frictional weakening of the fault gouge.

In this section, we model the 1D simple shear of a 1D Cauchy layer with THM couplings under isothermal drained boundary conditions in order to show the effects of coupled processes as far it concerns strain localization. The introduction of more physics into the localization problem such as the coupling of the mechanical behavior of the specimen with the heat and pore fluid diffusion equations has two opposing effects. On the one hand it introduces apparent softening to the model due to the effect of thermal pressurization (see chapters 5 and 6), on the other hand it is believed that the diffusion terms will help diffuse plastic strain as pressure and temperature diffuse inside the medium, expanding the localized zone.

We apply this fairly complex model in the hopes that strain localization will not happen again on a mathematical plane and that the localization width can be predicted based on the introduced diffusion lengths. This constitutive model accounting for the diffusion phenomena present during shearing of the fault gouge has the same multiphysical couplings as the model of chapter 5. However, in chapter 5 the use of the Cosserat micromorphic continuum takes also into account the influence of the fault's microstructure in the localization width.

The Cauchy linear elastic perfectly plastic material model with temperature and pressure diffusion couplings discussed in this section, will be also used to further our understanding of the fault's frictional behavior under large coseismic slip in chapter 6, where we investigate the influence of thermal and pressure diffusion mechanisms in the context of traveling waves of strain localization in bounded and unbounded domains. In chapter 6 we remove the pathology of the Cacuchy continuum regarding strain localization on a mathematical plane by the ad-hoc introduction of a Dirac discontinuity in the plastic shear strain field.

In this section we introduce the mathematical description of a material with multiphysical couplings of pressure and temperature. We derive the non linear material behavior and apply the LSA in order to derive the characteristic matrix of the BVP at hand (see right part of Figure 3.2). The total strains of the problem can be formulated as:

$$\dot{\varepsilon}_{ij}^{tot} = \dot{\varepsilon}_{ij}^{e} + \dot{\varepsilon}_{ij}^{p} + \dot{\varepsilon}_{ij}^{th} \tag{3.21}$$

The relationship between the total stresses of the porous medium (σ_{ij}^{tot}), the effective stresses of the material (σ'_{ij}) and the pore fluid pressure ($p^f > 0$) is given by the Terzaghi principle,

$$\sigma_{ij} = \sigma'_{ij} - p^f \delta_{ij}, \tag{3.22}$$

where $\sigma_{ij}, \sigma'_{ij}$ are negative in compression. For the yield criterion, we adopt a simplified version of a more general pressure dependent yield criterion:

$$F(\sigma_{12}, \gamma^p) = \sigma_{12} - \tau_0(1 - H_c\gamma^p) - p' \tan\phi, \tag{3.23}$$

where $\gamma^p = 2\epsilon^p_{12}$ is the engineering plastic strain and $p' = \frac{\sigma'_{11}+\sigma'_{22}+\sigma'_{33}}{3}$ the effective mean stress, negative in compression. We choose the corresponding plastic potential as:

$$G = \sigma'_{12} - \tau_0(1 - H_c\gamma^p) - p' \tan\psi, \tag{3.24}$$

where ψ is the dilation angle, which in our case is taken to be zero. Due to the form of the yield condition (equal to the plastic flow rule) no plastic deformation takes place, except for $\dot{\varepsilon}^p_{12}$. The equations of the stress increment perturbations of the 3D material are given as:

$$\tilde{\sigma}^{tot}_{11} = \frac{E}{(1+\nu)(1-2\nu)}(1-\nu)\left(\tilde{\varepsilon}^{tot}_{11} - \alpha\tilde{T} + \nu\left(\tilde{\varepsilon}^{tot}_{22} - \alpha\tilde{T}\right) + \nu\left(\tilde{\varepsilon}^{tot}_{33} - \alpha\tilde{T}\right)\right) - \tilde{p}^f, \tag{3.25}$$

$$\tilde{\sigma}^{tot}_{22} = \frac{E}{(1+\nu)(1-2\nu)}(1-\nu)\left(\tilde{\varepsilon}^{tot}_{22} - \alpha\tilde{T} + \nu\left(\tilde{\varepsilon}^{tot}_{11} - \alpha\tilde{T}\right) + \nu\left(\tilde{\varepsilon}^{tot}_{33} - \alpha\tilde{T}\right)\right) - \tilde{p}^f, \tag{3.26}$$

$$\tilde{\sigma}^{tot}_{33} = \frac{E}{(1+\nu)(1-2\nu)}(1-\nu)\left(\tilde{\varepsilon}^{tot}_{33} - \alpha\tilde{T} + \nu\left(\tilde{\varepsilon}^{tot}_{11} - \alpha\tilde{T}\right) + \nu\left(\tilde{\varepsilon}^{tot}_{22} - \alpha\tilde{T}\right)\right) - \tilde{p}^f, \tag{3.27}$$

$$\tilde{\sigma}^{tot}_{12} = \tilde{\sigma}^{tot}_{21} = 2G\frac{h}{h+1}\tilde{\varepsilon}^{tot}_{12} - K\frac{\tilde{\varepsilon}_{22} - 3\alpha\tilde{T}}{h+1}\tan\phi \tag{3.28}$$

For simple shear the following holds true: $\dot{\tilde{\varepsilon}}^{tot}_{11} = \dot{\tilde{\varepsilon}}^{tot}_{33} = 0$ and also $\dot{\tilde{\varepsilon}}^{tot}_{13} = \dot{\tilde{\varepsilon}}^{tot}_{23} = \dot{\tilde{\varepsilon}}^{tot}_{31} = \dot{\tilde{\varepsilon}}^{tot}_{32} = 0$. We prescribe the horizontal displacement under isothermal drained boundary conditions at the edges of the model, see Figure 3.2. From the problem's boundary conditions in 1D we can also deduce at all times that: $\tilde{\sigma}^{tot}_{11} = \tilde{\sigma}^{tot}_{33} = 0$ while $\tilde{\sigma}^{tot}_{22}|_{x=-\frac{h}{2}} n_1 = -\tilde{\sigma}^{tot}_{22}|_{x=\frac{h}{2}} n_2 = 0$ due to prescribed tractions at the boundary ($n_1 = -n_2$ are the outward normal vectors to the line domain at the boundary points). The fact that we prescribed the normal at the boundary means that the material is able to expand in the vertical direction therefore $\dot{\epsilon}_{22} \neq 0$. The linearized equations of energy and mass balance read respectively:

$$\frac{\partial \tilde{T}}{\partial t} = c_{th}\tilde{T}_{,ii} + \frac{1}{\rho C}\tilde{\sigma}_{ij}\dot{\varepsilon}^p_{ij} + \frac{1}{\rho C}\sigma_{ij}\dot{\tilde{\varepsilon}}^p_{ij}, \tag{3.29}$$

$$\frac{\partial \tilde{p}^f}{\partial t} = c_{hy}\tilde{p}^f_{,ii} + \frac{\lambda^*}{\beta^*}\frac{\partial \tilde{T}}{\partial t} + \frac{1}{\beta^*}\frac{\partial \tilde{\varepsilon}^{tot}_v}{\partial t}, \tag{3.30}$$

where $\varepsilon_v = \varepsilon_{11} + \varepsilon_{22} + \varepsilon_{33}$ denotes the volumetric part of the total strain ε_{ij}. Taking into account the above kinematical hypotheses:

$$\frac{\partial \tilde{T}}{\partial t} = c_{th}\tilde{T}_{,22} + \frac{1}{\rho C}\tilde{\sigma}_{12}\dot{\varepsilon}^p_{12} + \frac{1}{\rho C}\sigma_{12}\dot{\tilde{\varepsilon}}^p_{12}, \tag{3.31}$$

$$\frac{\partial \tilde{p}}{\partial t} = c_{hy}\tilde{p}_{,22} + \frac{\lambda^*}{\beta^*}\frac{\partial \tilde{T}}{\partial t} + \frac{1}{\beta^*}\frac{\partial \tilde{\varepsilon}^{tot}_{22}}{\partial t}. \tag{3.32}$$

In the above we assume that in the total strain perturbation $\tilde{\varepsilon}^{tot}_{12}$ is equivalent to the perturbation of the plastic strain $\tilde{\varepsilon}^p_{12}$. Finally the stress components read:

$$\tilde{\sigma}^{tot}_{22} = M\left(\tilde{\varepsilon}^{tot}_{22} - (1+2\nu)\alpha\ \tilde{T}\right) - \tilde{p}^f, \tag{3.33}$$

$$\tilde{\sigma}^{tot}_{12} = 2G\frac{h}{h+1}\tilde{\varepsilon}^{tot}_{12} - K\frac{1}{h+1}\left(\tilde{\varepsilon}_{22} - 3\alpha\tilde{T}\right)\tan\phi, \tag{3.34}$$

where $M = \frac{E(1-\nu)}{(1+\nu)(1-2\nu)}$, $K = \frac{2G(1+\nu)}{3(1-2\nu)}$ are the longitudinal and bulk moduli respectively. And the quasi-static equilibrium equations can be written as:

$$\frac{\partial \tilde{\sigma}_{22}}{\partial x_2} = 0, \quad \frac{\partial \tilde{\sigma}_{12}}{\partial x_2} = 0. \tag{3.35}$$

The above linearized system accepts solutions of the form: $\tilde{u}_1, \tilde{u}_2, \tilde{T}, \tilde{p} = \{u_1, u_2, T, p\}\exp(st + ikx)$. Thus we arrive at the system matrix:

$$\begin{bmatrix} Mk^2 & 0 & -M(1+2\nu)\alpha ki & -ki \\ -\frac{K}{1+h}(ik)^2\tan\phi & \frac{2Gh}{h+1}(ik)^2 & \frac{3\alpha K}{h+1}\tan\phi & 0 \\ -\frac{1}{\rho C}\frac{K}{h+1}(ik)^2 & \frac{1}{\rho C}\frac{2Gh}{h+1}ik\dot{\varepsilon}^{HS}_{12} & c_{th}(ik)^2 - s + \frac{3\alpha K}{h+1}\tan\phi & 0 \\ \frac{1}{\beta^*}iks & 0 & \frac{\lambda^*}{\beta^*}s & c_{hy}(ik)^2 - s \end{bmatrix} \begin{bmatrix} u_2 \\ u_1 \\ T \\ p \end{bmatrix} = 0, \tag{3.36}$$

where the exponent (HS) indicates the reference homogeneous solution. For the above solution to not have zero amplitude, the determinant of the above system needs to be zero. In the general case, applying Krammer's rule, we can see (by multiplication of the diagonal terms) that the characteristic polynomial is of order $n = 6$. There are no known analytical solutions for polynomial of order greater than $n = 4$ (see Arfken & Weber, 1999; Brown, Churchill, et al., 2009). For typical parameters for geomaterials (see Table 3.2), the corresponding Lyapunov coefficient is unbounded ($s \sim \frac{1}{\lambda^2}$,see Figure 3.8).

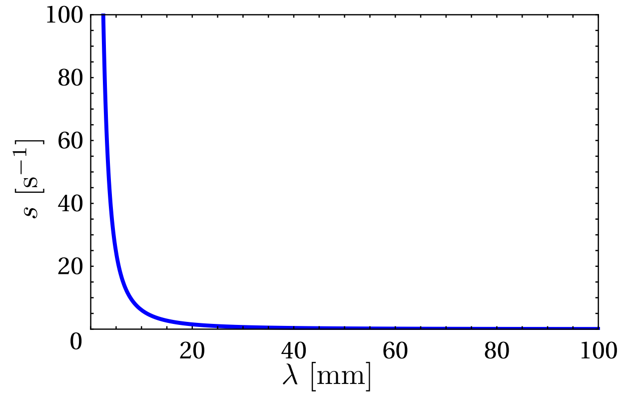

Figure 3.8 – Plot of the Lyapunov Coefficient over a range of different wavelengths. The Lyapunov coefficient is unbounded for the infinitesimal wavelength, it drops asymptotically to zero with a rate $\sim \frac{1}{\lambda}$ as we increase the wavelength. The preferred mode of strain localization is on a mathematical plane.

In Benallal and Comi (2003), the authors study the problem of strain localization in a fluid saturated inelastic Cauchy porous medium in the quasistatic regime. The authors find conditions for which localization on a mathematical plane is the preferred localization mode. They also provide conditions under which a traveling localization mode will become prevalent. Furthermore, based on the form of the characteristic polynomial the authors were able to provide conditions under which they can distinguish between localized and diffused failure modes in fluid saturated inelastic Cauchy porous media. The problem of strain localization in an inelastic Cauchy continuum, where both thermal and pressure couplings are considered has been studied in its general form in Benallal (2005b).

Finally, the case of multiphysical couplings and viscosity has been studied in Jacquey et al. (2021), Stefanou and Gerolymatou (2019). It is shown that under particular choice of the viscosity parameter, regularization of strain localization in a region of finite width is possible. However, the region in which the plastic strain localizes is very small and therefore, the heat production will lead to underwhelming temperature increases that do not correspond to experimental results and field observations (see Bizzarri & Bhat, 2012; Blanpied et al., 1995; Boullier et al., 2009; Brantut et al., 2008; Forest, Boubidi, et al., 2001; Kanamori & Brodsky, 2004b; Needleman & Tvergaard, 1992). Furthermore, the resulting small localization width, neglects the existence of the microstructure of the material. The material microstructure poses a lower bound to the thickness of the fault gouge (see Eremeyev, 2018; Forest, 2020a, 2020b; Ren et al., 2021; Reyne et al., 2019; J. Sulem et al., 2011, among others).

3.4.1 Numerical example

We proceed in an application of shearing of a 1D layer of a linear elastic perfectly plastic Cauchy medium coupled with the equation of pressure and temperature diffusion. In what follows, we will consider an introductory simplified model of 1D shear of a geometrial with THM couplings. The material starts initially in a stress state of $\sigma_{11} = \sigma_{22} = \sigma_{33} = 200$ MPa, corresponding to a fault gouge lying inside the seismogenic zone $\sim$ 14 km under the surface. We prescribe the horizontal displacement in the boundaries of the gouge under isothermal drained boundary conditions for the diffusion equations. The material parameters to be used in the subsequent numerical application are:

Parameter	Value	Unit
ρ	0	kg/m^3
c_{th}	1	mm^2/s^2
c_{hy}	10	mm^2/s^2
E	10	GPa
ν	0.	-
α	10^{-5}	/°C
ρC	2.8	MPa/°C
λ^*	7.4 10^{-5}	/°C
β^*	8.2 10^{-5}	MPa^{-1}

Table 3.2 – Material parameters of a Cauchy continuum with multiphysical couplings.

In Figure 3.9, we present the shear stress σ_{12}, horizontal displacement δ behavior of a Cauchy continuum coupled with the pore fluid pressure and temperature equations described in equation (3.28). Our numerical analyses localize on a mathematical plane upon mesh refinement. Our numerical results indicate that localization happens once the material enters the yielding region. In the right part of Figure 3.9, we can readily see that localization takes place upon the smallest element mesh dimension indicating that the material localizes on a mathematical plane as expected by the theoretical analysis of the previous section. This result, in which, strain localizes on a mathematical plane, is contrary

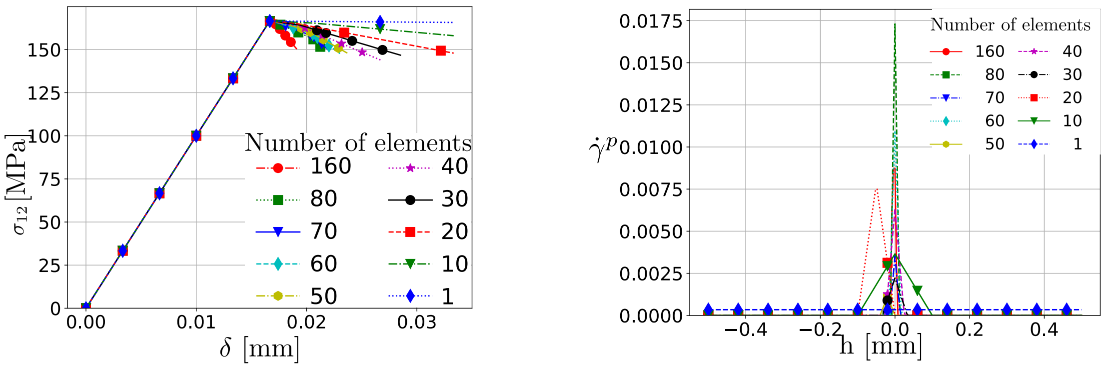

Figure 3.9 – Simple shear of an infinite layer for different number of elements. Left: Frictional strength τ vs horizontal displacement on top of the layer δ. On the right: Localization width profiles for different number of elements. We interpret localization as the rate of increase of the plastic deformation $\dot{\gamma}^p$.

to experiments and observations that clearly show that strain localization should posses a finite width, which is constrained by a characteristic length of the material. The above numerical findings guide us, once more, towards the use of higher order micromorphic continua for the correct determination of the width of the principal slip zone. In chapter 5 we use a Cosserat micromorphic continuum for the determination of the principal slip zone of a fault during coseismic slip. This continuum will help us model the frictional response of a fault gouge during coseismic slip, where the values of the seismic slip as well as those of the velocity of the seismic slip are typical of those observed in the field (see Rice, 2006a; J. Sulem et al., 2004, among others).

3.5 Cosserat elasto-plasticity with strain softening

In this section we will present an example showing the regularizing properties of a Cosserat continuum by making use of the LSA (see Figure 3.10). The theory of micromorphic continua is a general continuum theory that can be used to model heterogeneous systems with microstructure (see Eringen, 1968; Forest & Sievert, 2003; Forest, 2020a, 2020b; Germain,

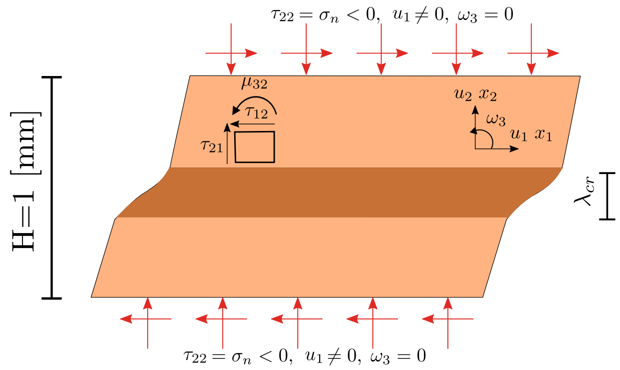

Figure 3.10 – Localization profile of a Cosserat layer under 1D simple shear.

1973; Stefanou & Gerolymatou, 2019; J. Sulem & Vardoulakis, 1995; I. Vardoulakis, 2018, 2019). The Cosserat continuum belongs to a special case of micromorphic continua in which the microstructure is considered to be made of rigid particles that can rotate in the level of the microstructure as the macrocontinuum deforms.

Cosserat kinematics

We introduce the kinematic field of the deformation tensor γ_{ij}. We define its symmetric part $\gamma_{(ij)}$ as the macroscopic strain ε_{ij} while its antisymmetric part $\gamma_{[ij]}$ is the difference between macroscopic rotation Ω_{ij} and the microscopic rotation tensor ω_{ij}. We also take into account the gradient of the microscopic rotation tensor κ_{ij}.

$$\gamma_{ij} = \gamma_{(ij)} + \gamma_{[ij]} = u_{i,j} - \omega_{ij} = u_{i,j} + \epsilon_{ijk}\omega_k, \tag{3.37}$$

$$\gamma_{(ij)} = \varepsilon_{ij} = \frac{1}{2}\left(u_{i,j} + u_{j,i}\right), \tag{3.38}$$

$$\gamma_{[ij]} = \frac{1}{2}\left(u_{i,j} - u_{j,i}\right) - \omega_{ij} = \Omega_{ij} - \omega_{ij}, \tag{3.39}$$

$$\kappa_{ij} = \omega_{i,j} \tag{3.40}$$

where, $i, j = 1...3$ sre the indices of the 3D space and by $(,)$ we denote the spatial derivative. The symbol ϵ_{ijk} is the Levi-Civita permutation tensor.

A comprehensive study of the energetics of the arbitrary generalized micromorphic continua and the kinematic properties and their work conjugate quantities can be found in (see Germain, 1973). Here we focus on the shearing of a 1D Cosserat layer, we derive the system of the PDEs incorporating the material behavior, we find the conditions under which multiple solutions to the system of PDEs become possible and the homogeneous reference solution becomes unstable. Finally, we examine the strain localization profile of the localized solution.

For simple shear in 1D conditions linear and angular momentum balance leads to:

$$\frac{\partial \tau_{12}}{\partial x_2} = \rho \ddot{u}_1,\ \frac{\partial \tau_{22}}{\partial x_2} = \rho \ddot{u}_2,$$
$$\frac{\partial \mu_{32}}{\partial x_2} + \tau_{21} - \tau_{12} = I \ddot{\omega}^c_3, \tag{3.41}$$

where $\tau_{ij}, \mu_{ij},\ i,j = 1...3$ are the components of the stress and generalized stress tensor. We note that in the case of a Cosserat material both the stress and the generalized stress tensor are not symmetric. This is also true for their work conjugate quantities. In the case of homogeneous deformation at steady state ($u^\star_i(x),\ i = 1,2,\ \omega^\star_3(x) = 0$), the asymmetry of the stress tensor $\tau^\star_{[ij]}$ is zero. In this case the Cosserat moments (generalized forces) are also zero $\mu^\star_{32} = 0$. Therefore, in this state, the Cosserat continuum is equivalent to the classical Cauchy continuum (see right part of Figure 3.2). Applying a perturbation to the initial stable configuration leads to the following system of perturbed PDEs:

$$\frac{\partial \tilde{\tau}_{12}}{x_2} = \rho \ddot{\tilde{u}}_1, \quad \frac{\partial \tilde{\tau}_{22}}{\partial x_2} = \rho \ddot{\tilde{u}}_2$$
$$\frac{\partial \tilde{m}_{32}}{\partial x_2} + \tilde{\tau}_{21} - \tilde{\tau}_{12} = I \ddot{\tilde{\omega}}^c_3 \tag{3.42}$$

For elastoplasticity, the simplified yield criterion we present in equation (3.10), is adapted to Cosserat as follows:

$$F(\tau_{12}, \gamma^p) = \tau_{(12)} - \tau_0(\gamma^p), \tag{3.43}$$

where $\tau_{(12)}$ is the symmetric part of the τ_{21} stress, which participates to the linear momentum equilibrium equation and $\gamma^p = 2\int_0^t \dot{\gamma}^p_{(12)} dt$. Applying the elastoplastic analysis of the previous section, and assuming an associative flow rule we arrive at the following relations for the material incremental behavior under mechanical softening:

$$
\begin{aligned}
&\tilde{\tau}_{12} = 2G\frac{h}{1+h}\tilde{\gamma}_{(12)} + 2\eta_1 G\tilde{\gamma}_{[12]} = G\frac{h}{1+h}\frac{\partial \tilde{u}_1}{\partial x_2} + 2G_c\tilde{\omega}_3,\\
&\tilde{\tau}_{22} = M\tilde{\gamma}_{22} = M\frac{\partial \tilde{u}_2}{\partial x_2},\\
&\tilde{\mu}_{32} = 4GR^2\tilde{\kappa}_{32} = 4\eta_1 GR^2\frac{\partial \tilde{\omega}_3}{\partial x_2},
\end{aligned}
\tag{3.44}
$$

where η_1 indicates the stress asymmetry and R is the characteristic length, which we call Cosserat radius. We note here that any ratio of the material coefficients can be used for the derivation of a characteristic length (see Mindlin, 1963). We note again that due to the prescribed boundary conditions of the BVP, the general solution is given by $[\tilde{u}_1, \tilde{u}_2, \tilde{\omega}_3]^{\mathrm{T}} = [g_1, g_2, g_3]^{\mathrm{T}} \exp{(st + ikx_2)}$. The system of PDEs can then be written as:

$$
\begin{bmatrix}
-G\frac{h}{h+1}k^2 - \rho s^2 & 0 & 2\eta_1 Gik\\
0 & -Mk^2 - \rho s^2 & 0\\
-2\eta_1 Gik & 0 & -4\eta_1 GR^2k^2 + 4\eta_1 G
\end{bmatrix}
\begin{bmatrix} g_1\\ g_2\\ g_3 \end{bmatrix} = 0,
\tag{3.45}
$$

where the influence of the rotational moment of microinertia I was neglected. When the determinant of the above system becomes zero, the amplitudes of the general solution are different than zero, (see Chambon et al., 2004; Rice, 1975; Stefanou & Alevizos, 2016; J. Sulem & Vardoulakis, 1995, among others). Considering that I is equal to zero for simplicity we obtain:

$$
s = \mathrm{i}kv_p \quad \text{or} \tag{3.46}
$$

$$
s = \pm \mathrm{i}kv_s\sqrt{\frac{h}{h+1}}\sqrt{\frac{\eta_1\left(1+\frac{1}{k^2R^2}\right)+\frac{h+1}{h}}{\frac{\eta_1}{k^2R^2}+1}}. \tag{3.47}
$$

The system is unstable when $Re[s] > 0$ or, equivalently when $h < 0$ (softening) and $\eta_1\left(1+\frac{1}{k^2R^2}\right)+\frac{h+1}{h} > 0$. The latter condition leads to a critical wavelength λ_{cr}:

$$
\lambda > \lambda_{cr} = 2\pi R\sqrt{-\frac{1+h}{h} - \eta_1}. \tag{3.48}
$$

The wavelength of the perturbation has to be larger than this critical value for localization to occur, see Figure 3.11. We note here that λ_{cr} is proportional to the Cosserat internal length, R. If $R \to 0$ we retrieve the same condition for strain localization with the 1D example presented in section 3.2 for a Cauchy continnum.

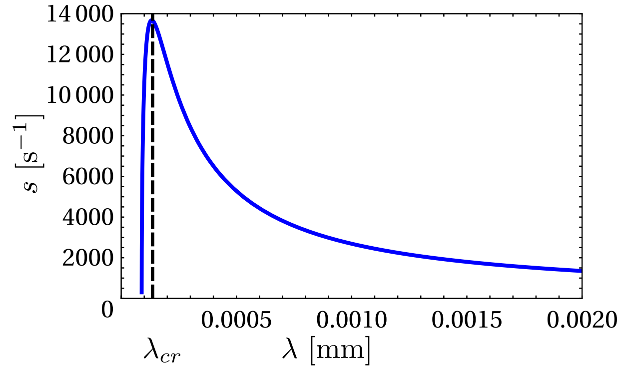

Figure 3.11 – Plot of the Lyapunov Coefficient over a range of different wavelengths for a Cosserat elastoplastic continuum. The Lyapunov coefficient is positive and bounded over a region where $\lambda > \lambda_{cr}$. This means that the strain in the case of the Cosserat continuum cannot localize on a mathematical plane.

3.5.1 Numerical analysis

In the case of a Cosserat linear elasto- plastic strain softening material under quasi static conditions, it has been shown with the help of a Lyapunov stability analysis in Muhlhaus and Vardoulakis (1988) and also numerically in de Borst and Sluys (1991) that strain localization will lead to mesh independent results. The parameters used in the case of a Cosserat material are presented in Table 3.3. In the analyses presented here, no matter the discretization of the specimen's mesh, localization will always happen on a width dictated by the fastest growing wavelength of the stability analysis. This is larger than the infinitesimal wavelength ($\lambda_{cr} > 0$). We present these results in Figure 3.12, On the left part of Figure 3.12, we see that the shear stress displacement diagrams $\tau_{21} - \delta$ present a converging response. This is also true for the localization profiles of the analyses performed with increasing number of elements (decreasing mesh size). The localization profile converges to a specific width controlled by the fastest growing wavelength derived from the Lyapunov stability analysis. By H_c we denote the softening parameter used for the evolution of $\tau_0(\gamma^p)$. We use a linear relation of the form:

$$\tau_0(\gamma^p) = \tau_0|_{\gamma^p=0}(1 + H_c\gamma^p) \tag{3.49}$$

Parameters	Values	Units
K	$\frac{1}{3}10^2$	GPa
G	10	GPa
G_c	10	GPa
$\tau_0\|_{\gamma^p=0}$	10^2	MPa
H_c	-2	-
R	0.01	mm

Table 3.3 – Intact material parameters

Where $\dot{\gamma}^p = 2\dot{\gamma}^p_{(12)}$ and $h = H_c\tau_0\Big\|_{\gamma^p=0}$ according to equations (3.43)(3.44). We establish

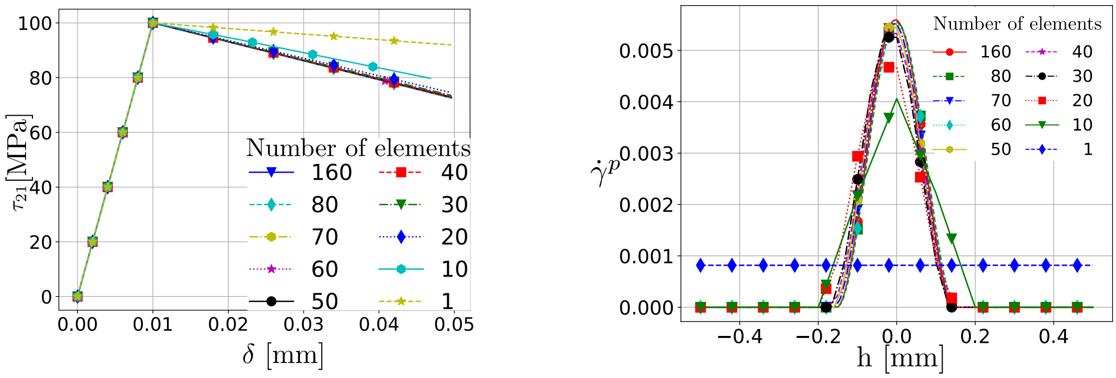

Figure 3.12 – Simple shear of an infinite layer for different number of elements. Left: Frictional strength τ vs horizontal displacement on top of the layer δ. The analysis of one element does not localize and can be used as a way of validating w.r.t. the theoretical prediction. Adding more elements into the model results to the slope during plastic softening remaining the same due to localization being bounded by the material constant λ_{cr}. On the right: Localization width profiles for different number of elements. We interpret localization as the rate of increase of the plastic deformation $\dot{\gamma}^p$. The analysis for one element does not localize. We notice that localization converges to a value bounded by the material constant λ_{cr}.

here, that indeed localization in Cosserat elasto-plastic strain softening materials is independent from the mesh size and the imperfection width. This result extends also in the case of rate dependent Cosserat material with strain softening and strain-rate hardening. In the next section, we investigate another configuration for rate dependency that results in a traveling instability. Our motivation for this numerical investigation lies in the numerical results obtained in chapter 5 and the Appendix C. We see in chapter 5 that traveling waves of strain localization are present in the results of the numerical analyses. Moreover, in appendix C we have identified conditions for traveling instabilities to occur, in the case of Cauchy elasto-viscoplastic continua with strain softening and strain-rate hardening. It has been shown in W. Wang et al. (1997) that a traveling instability can develop in the elasto viscoplastic Cauchy continua with strain hardening and strain-rate softening. We investigate under which conditions such a traveling instability can develop in the simple Cosserat mechanical models of our analyses. The results are presented in the next section.

3.5.2 Portevin Le Chatelier phenomenon in Cosserat elasto-viscoplasticity with strain hardening and strain-rate softening.

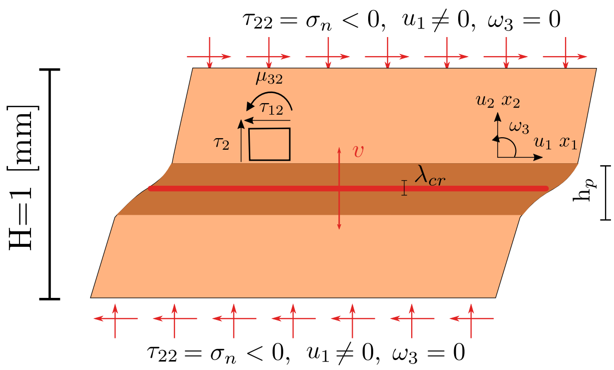

Figure 3.13 – Localization profile of a Cosserat layer under 1D simple shear. The material law is elasto-viscoplastic with strain hardening and strain-rate softening. In this case a traveling localization emerges (in red) whose width is λ_{cr}. This shear band travels inside the Cosserat layer with velocity v, along a region of the layer which is plastified, and has a width of h_p.

In the post bifurcation regime of Cosserat micromorphic continua, the case of linear elasto-viscoplastic strain hardening, strain-rate softening materials present special interest. Such materials, exhibit a particular kind of instability when the Portevin Le-Chatelier (PLC) phenomenon takes place. This instability mode refers to a localized plastic strain-rate profile that travels inside the medium as shearing evolves (see Figure 3.13). In the framework of metal plasticity on classical Cauchy continua, it has been studied extensively, and has been tied to the existence of limit cycles and the Hopf-Andropov bifurcation (see Hähner et al., 2002; Mazière et al., 2010; W. Wang et al., 1997). We emphasize here, however, that in this configuration of strain hardening and strain-rate softening care must be taken such that the dissipation of the material at all times is positive ($D \geq 0$), i.e. the system does not produce energy. For the 1D case studied here (see Figure 3.14) the dissipation is given by:

$$\begin{aligned} D &= \tau_{12}\dot{\gamma}_{12}^{vp} = (\tau_{12}^1 + \tau_{12}^2)\dot{\gamma}_{12}^{vp}, \\ &= \eta^{vp}(\dot{\gamma}_{12}^{vp})^2 + \tau_y\dot{\gamma}_{12}^{vp} + h\gamma_{12}^{vp}\dot{\gamma}_{12}^{vp} \geq 0, \end{aligned} \tag{3.50}$$

where we separate the influence of the visocity and plasticity components $\tau_{12}^1,\ \tau_{12}^2$ respectively. We note further that, $h > 0$ is the strain hardening modulus, and $\eta^{vp} < 0$ is the strain-rate softening parameter and $\dot{\gamma}_{12}^{vp} \geq 0$ the viscoplastic strain internal variable. Solving the inequality we show that the viscoplastic strain rate should obey:

$$\dot{\gamma}_{12}^{vp} \leq \frac{\tau_y + h\gamma_{12}^{vp}}{|\eta^{vp}|}. \tag{3.51}$$

at all times.

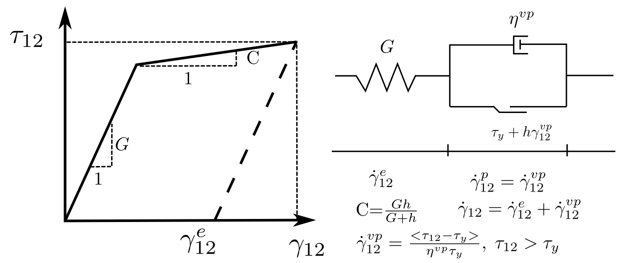

Figure 3.14 – Elasto-viscoplastic material configuration and description in 1D.

In Figure 3.15 we obtain similar results for the case of an elasto-viscoplastic Cosserat continuum with strain softening and strain-rate hardening. In Figure 3.15 the localization profile along the 1D dimensional domain is plotted for different times during the analysis. We note that the localization travels along the layer. Moreover the phenomenon is periodic as the traveling shear band is reflected in the boundaries. We note that after the first period the subsequent profiles appear at the same positions as before on top of the profile at past times. The question of traveling instabilities in the framework of a Cauchy continuum with multiphysical couplings has been addressed in Benallal (2005b), Benallal and Comi (2003). There, the authors identified regimes for which traveling instabilities may occur. However, the numerical difficulties of our current algorithm to achieve convergence obstruct us from a detailed analysis in exploring instabilities of this kind in the Cauchy framework.

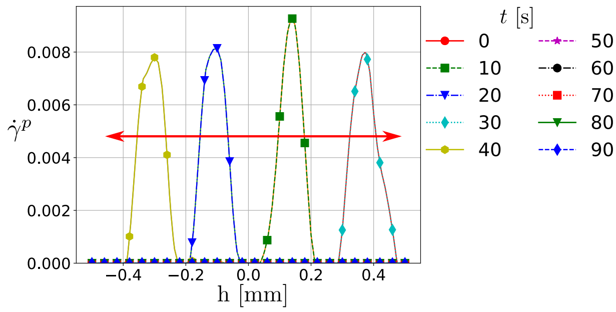

Figure 3.15 – Evolution of the shear band inside the layer as a function of time. The shear band travels inside the layer.

3.6 Key points

In this chapter different material models were investigated together with different continuum descriptions, in order to evaluate their ability in assuring mesh independent results for the prediction of the width of the localization zone (principal slip zone) under quasistatic conditions. It has been shown that under strain softening only the Cosserat continuum is able to assure mesh independent results and a mesh independent localization width. In particular introduction of multiphysical couplings in the case of a classical Cauchy continuum was shown to not regularize the problem. This leads us to consider the Cosserat continuum for the estimation of localization width and the dissipated energy in chapter 5 of the Thesis. Viscoplasticity was also considered in its ability to regularize localization in the case of a Cauchy continuum. On the base of a simple example, it has been shown that in quasistatic analyses such a claim is unfounded. However, the ability of viscoplasticity to assure mesh independent results in the presence of inertia terms is still a matter of vivid discussion. We discuss further this topic in the next chapter 4.

Chapter 4

The role of viscous regularization in dynamical problems, strain localization and mesh dependency

Summary

Strain softening is responsible for mesh dependence in numerical analyses concerning a vast variety of fields such as solid mechanics, dynamics, biomechanics and geomechanics. Therefore, numerical methods that regularize strain localization are paramount in the analysis and design of engineering products and systems. This is also the case in fault mechanics. In this chapter we revisit the elasto-viscoplastic, strain-softening, strain-rate hardening model as a means to avoid strain localization on a mathematical plane ("wave trapping") in the case of a Cauchy continuum. Going beyond previous works (de Borst and Duretz, 2020; Needleman, 1988; Sluys and de Borst, 1992; W. Wang et al., 1997), we assume that both the frequency ω and the wave number k belong to the complex plane. Therefore, a different expression for the dispersion relation is derived. We prove then that under these conditions strain localization on a mathematical plane is possible. The above theoretical results are corroborated by extensive numerical analyses, where the total strain and plastic strain rate profiles exhibit mesh dependent behavior.

4.1 Introduction

Going beyond and expanding on existing results of chapter 3, we revisit, in this chapter, the role of viscosity for the regularization of the classical Cauchy continuum in the presence of inertia. Considerable amount of research has been made on viscous regularization of localization under both quasi-static and dynamic conditions (see Loret and Prevost, 1990; Needleman, 1988; Sluys and de Borst, 1992). In particular, for the quasi-static case, it is noted that the elasto-viscoplastic Cauchy medium based on a power law for the viscoplasticity description, will exhibit strain localization on a mathematical plane, except if a particular procedure for the time integration takes place see Needleman, 1988. Furthermore, it is mentioned in Sluys and de Borst, 1992 that the regularizing properties of the elasto-viscoplastic medium are present only in the context of dynamical analyses, due to the regularizing role of the higher order inertial terms, which are naturally introduced. Moreover, for the dynamic case, a conclusion taken from Needleman, 1988; Sluys and de Borst, 1992 is that the selection of a consistency or Perzyna yield condition for the viscoplastic model is preferred over a power law based on the fact that the third order terms of the Partial Differential Equation (PDE), gradually vanish in the latter as strain softening occurs.

As it has been already presented in Abellan and de Borst, 2006 and in particular in de Borst and Duretz, 2020 the formulation of the elasto-viscoplastic material model, specifically the position of the damper element into the idealized viscoplastic configuration, is of great importance. It has been shown in de Borst and Duretz, 2020 that a solution localizes into a mathematical plane once the configuration of the viscosity dashpot, the plasticity element and the elastic spring are in series. The present chapter addresses stability and localization questions for the parallel configuration as studies are not conclusive yet. Hence the elasto-viscoplastic model with strain softening, which involves a parallel connection between the plasticity element and the dashpot, is examined at present using bifurcation and Lyapunov stability analysis. In particular, we examine in detail the stability of the reference solution of uniform deformation of the elasto-viscoplastic problem. This will help us then to choose in the next chapters, the appropriate continuum for modeling the shear behavior of a fault gouge.

In previous works (de Borst and Duretz, 2020; Needleman, 1988; Sluys and de Borst, 1992; W. Wang et al., 1997), the question of localization of the deformation was addressed by looking at the propagation velocity of localization. In particular it is mentioned in Sluys and de Borst, 1992 that the original ill-posed problem of strain-softening plasticity presents imaginary wave speeds corresponding to standing waves, which cannot extend the localization zone. As mentioned above, this is thought to be remedied by the introduction of viscosity. It is also stated in these works that to properly test the conditions under which strain localization is present in the non-linear elasto-viscoplastic problem, we would require a closed form analytical expression for the solution, which until now is impossible. Since no analytical known way exists in solving the softening, rate-dependent plasticity problem, the focus was shifted in the derivation of the dispersion relationships. Namely, in the previous, it was assumed that if every mode has a real velocity, then the corresponding part of the deformation will propagate and, therefore, it will not concentrate in only one element of the model as it would be the case with a standing wave.

An additional argument that is presented in Sluys and de Borst, 1992; W. Wang et al., 1996, is the dispersive character of the partial differential equation, which is assumed to further regularize the problem as the deformation front widens due to the different velocity of the deformation modes. In all these works, the dispersion relation was derived based on the assumption that the circular frequency ω and consequently, the wave velocities c are real, while the wavenumber k is complex: $k = k_r + k_i i,\ k_r, k_i = \alpha \in \mathbb{R}$, indicating spatial attenuation of the derived deformation modes, thus leading to characteristic localization length $l = \frac{1}{\alpha}$. However, we find no reason to strictly assume $\omega \in \mathbb{R}$, which makes an important difference in the analysis. The concept of imaginary frequency can be shown to correspond to the real and negative square of the wave velocity c, which leads to divergence growth according to Benallal and Comi, 2003; A. Bernard et al., 2001; Chambon et al., 2004; Deschamps et al., 1997; Gerasik and Stastna, 2010; Mainardi, 1984, 1987; Marion, 2013; Rice, 1975, 1976; Stefanou and Alevizos, 2016 (see also equation (4.22) in section 4.2.3.2). In a physical context imaginary frequencies ω are important in the description of physical phenomena as shown in the kinematic theory developed by Hayes, 1970 and Poeverlein, 1962.

In this chapter we depart from this main assumption by assuming both $\omega, k \in \mathbb{C}$, thus considering the problem in its general form. Furthermore, due to application of the Lyapunov analysis we are interested in the magnitude of the imaginary part of ω, $\omega_i = \mathrm{Im}[\omega]$, which controls the evolution of the amplitude of the perturbations and therefore, the stability of the reference homogeneous deformation state. We argue that if the amplitude of the mode with zero wavelength increases faster than that of the others, then this mode will dominate the deformation profile and strain localization on the mathematical plane will be possible. Theoretical proofs are presented at first showing this phenomenon and also, the emergence of traveling waves of strain localization in some cases. The theoretical results are corroborated then by numerical analyses where the total strain and plastic strain profiles exhibit mesh dependent behavior. These analyses provide counter examples to viscous regularization in dynamical problems.

4.2 The elasto-viscoplastic wave equation

4.2.1 Problem description

Let us consider a body under homogeneous small deformation lying at rest. The equilibrium equation of a homogeneous deformation profile is given as:

$$\sigma^{\star}_{ij,j} = 0, \tag{4.1}$$

where $\sigma^{\star}_{ij}$ is the developed stress field (for the mathematical definitions see section 3.2 in 3.2).Considering a perturbation $\tilde{u}_i$ to the reference displacement field $u^{\star}_i$ of homogeneous deformation, we find a relationship between the perturbed stress and displacement $\tilde{u}$ fields, according to the conservation of linear momentum:

$$(\sigma^{\star}_{ij} + \tilde{\sigma}_{ij})_{,j} = \rho\ddot{\tilde{u}}_i, \tag{4.2}$$

$$\tilde{\sigma}_{ij,j} = \rho\ddot{\tilde{u}}_i, \tag{4.3}$$

where ρ is the density of the material. Both displacement and stress variations are arbitrary respecting only the boundary and loading conditions such that $\tilde{u}_i = 0, \tilde{\sigma}_{i,j}n_j = 0$ at the boundary of the body, where displacement and loading conditions are specified, respectively. In order to continue with the bifurcation analysis of the problem we need to look first at the elasto-viscoplastic constitutive law we take into account.

4.2.2 Elasto-viscoplastic constitutive relations

As mentioned in section 4.1 a variety of yield criteria and flow rules are available for modeling viscoplasticity. Here we use the von Mises yield criterion with strain-hardening (softening) and the Perzyna viscoplasticity approach (see J.-P. Ponthot, 1995; W. Wang et al., 1997). In the Appendix A, we present also an alternative formulation for viscoplasticity, the consistency approach (see Heeres et al., 2002; W. M. Wang et al., 1996, 1997). We show that the linearized descriptions of these two alternatives to rate dependent viscoplasticity match leading to the same linearized stability differential equation and the same conclusions for their stability.

4.2.2.1 von Mises yield criterion Perzyna approach

In an elasto-viscoplastic formulation the following relations hold as given in De Borst, 1991; W. M. Wang et al., 1996; W. Wang et al., 1996; W. Wang et al., 1997:

$$F(\sigma_{ij}, \bar{\epsilon}^{vp}) = 0, \tag{4.4}$$

$$\dot{\varepsilon}_{ij} = \dot{\varepsilon}^{e}_{ij} + \dot{\varepsilon}^{vp}_{ij}, \tag{4.5}$$

$$\dot{\sigma}_{ij} = M^{e}_{ijkl}\left(\dot{\varepsilon}_{kl} - \dot{\varepsilon}^{vp}_{kl}\right), \tag{4.6}$$

$$\dot{\varepsilon}^{vp}_{ij} = \dot{\lambda}\frac{\partial F}{\partial \sigma_{ij}} = \left(\frac{F}{\eta F_0}\right)^{n} \frac{\partial F}{\partial \sigma_{ij}}, \; n = 1, \tag{4.7}$$

$$\bar{\epsilon}^{vp} = \int_0^t \dot{\bar{\epsilon}}^{vp} dt, \tag{4.8}$$

where $F = F(\sigma_{ij}, \bar{\epsilon}^{vp})$ is the yield function incorporating the effects of strain hardening through the use of the accumulated deviatoric viscoplastic strain $\bar{\epsilon}^{vp}$.The effects of strain rate hardening are taken into account by the viscosity coefficient η applied in the definition of the viscoplastic strain rate $\dot{\bar{\epsilon}}^{vp}$, respectively. The viscoplastic multiplier $\dot{\lambda}$ is given directly by the Perzyna viscoplasticity law defined above. The von Mises yield criterion with strain-hardening (softening) for the Perzyna approach reads (see W. M. Wang et al., 1996; W. Wang et al., 1996; W. Wang et al., 1997):

$$F(\sigma_{ij}, \bar{\varepsilon}^{vp}) = \sqrt{3J_2(\sigma_{ij})} - (F_0 + h\bar{\epsilon}^{vp}), \tag{4.9}$$

where F_0 is the initial yield strength of the material, h is a parameter indicating strain hardening of the material ($h < 0$ indicates strain softening) with increasing accumulated plastic strain and The rate of the accumulated plastic strain is defined as $\dot{\bar{\epsilon}}^{vp} = \sqrt{\frac{2}{3}\dot{\varepsilon}^{vp}_{ij}\dot{\varepsilon}^{vp}_{ij}}$. From the above definitions we conclude that $\bar{\epsilon}^{vp} = \lambda, \dot{\bar{\epsilon}}^{vp} = \dot{\lambda}$. We define the viscoplastic potential $\Omega(\sigma_{ij}, \lambda, \dot{\lambda})$ as:

$$\Omega(\sigma_{ij}, \lambda, \dot{\lambda}) = F(\sigma_{ij}, \lambda) - F_0 F^{-1}(\dot{\lambda}\eta) = 0 \tag{4.10}$$

The time derivatives of the yield condition and the viscoplastic potential in this case are the following:

$$\dot{F} = \frac{\partial F}{\partial \sigma_{ij}}\dot{\sigma}_{ij} + \frac{\partial F}{\partial \lambda}\dot{\lambda}, \tag{4.11}$$

$$\dot{\Omega} = \frac{\partial \Omega}{\partial \sigma_{ij}}\dot{\sigma}_{ij} + \frac{\partial \Omega}{\partial \bar{\lambda}}\dot{\lambda} + \frac{\partial \Omega}{\partial \dot{\lambda}}\ddot{\lambda} = 0. \tag{4.12}$$

Now the consistency condition is valid for the visocplastic potential: $\dot{\lambda}\Omega = 0\ \dot{\lambda} \geq 0,\ \Omega \leq 0$, where during plastic loading $\dot{\Omega} = 0$.

Alternatively one can define the concistency von Mises yield condition (inserting an extra term $g\dot{\bar{\epsilon}}^{vp}$ in the yield condition, $g > 0$ indicating hardening) and assume that after the material reaches the yield limit the viscoplastic strain-rate is given by solving the corresponding consistency condition ($\dot{\lambda}F = 0,\ F = 0,\ \dot{\lambda} > 0$, see Appendix A). The results between Perzyna and consistency viscoplasticity criteria are the same as far as monotonic loading is applied and non-holonomic behavior of the material is excluded, provided that we assign $g = \eta F_0$ in the yield criterion. In the case of stress reversal and subsequent unloading, however, the results between the consistency approach and the Perzyna model will be different due to the elasto-viscoplastic component that the Perzyna model predicts during unloading (see Heeres et al., 2002).

In what follows the principal results of the elasto-viscoplastic bifurcation analysis are presented. A full derivation of the elasto-viscoplastic constitutive relations for both Perzyna and concistency viscoplasticity criteria is presented in the Appendix A. Applying equation (4.9) to equations (4.6) and (A.1.10) of the Appendix A, we arrive at the relationship for the stress rate $\tilde{\sigma}_{ij}$:

$$\tilde{\sigma}_{ij} = M^e_{ijkl}\left(\tilde{\varepsilon}_{kl} - \frac{C}{-h+C}\tilde{\varepsilon}_{kl} + \frac{hb_{kl}}{-h+C}\dot{\tilde{\lambda}}\right), \tag{4.13}$$

where in order to simplify the notation we have replaced accordingly:

$$
\begin{aligned}
&\frac{\partial \Omega}{\partial \dot{\lambda}} = h, \\
&C = \frac{\partial \Omega}{\partial \sigma_{ij}} M^e_{ijkl} \frac{\partial \Omega}{\partial \sigma_{kl}}, \\
&b_{kl} = \frac{\partial \Omega}{\partial \dot{\lambda}} \frac{\partial \Omega}{\partial \sigma_{kl}}.
\end{aligned} \tag{4.14}
$$

4.2.3 Derivation of the perturbed equation

We proceed now in deriving the general linearized perturbed equation of equilibrium for the given material law under monotonic loading. Inserting equation (4.13) into equation (4.3) and taking into account the spatial derivative of equation (4.7), we obtain:

$$
M^e_{ijkl} \left(\tilde{\varepsilon}_{kl,j} - \frac{C}{-h+C} \tilde{\varepsilon}_{kl,j} + \frac{h}{-h+C} \dot{\tilde{\varepsilon}}_{kl,j} - M^{e^{-1}}_{ijkl} \rho \dddot{\tilde{u}}_i \right) = \rho \ddot{\tilde{u}}_i, \tag{4.15}
$$

This equation describes the spatio-temporal evolution of perturbations from the reference solution of homogeneous deformation in 3D.

4.2.3.1 Shearing of a viscous Cauchy layer

We constrain our analysis to the study of 1D problems, since they constitute the simplest case to study localization and the regularization effects coming from the above material law. In this way direct parallels can be drawn between our work and the main bulk of literature on the subject de Borst and Duretz, 2020; Needleman, 1988; Sluys and de Borst, 1992; W. M. Wang et al., 1996. For the shearing of an 1D layer we assume that the shearing is coaxial to the direction of x_1 and that the body deforms in the direction x_1. Therefore $\tilde{u}_i = [0, \tilde{u}_2]^T = [0, \tilde{u}]^T$. Since we are in a state of 1D deformation, only the derivatives along the 1D axis, x_1, survive, therefore we set $\frac{\partial \tilde{u}_2}{\partial x_1} = \frac{\partial \tilde{u}}{\partial x}$. Taking into account the appropriate material constant $M^e_{ijkl} = D^e_{2121} = G$, we proceed in deriving the perturbed linear momentum equation for the shearing of an 1D elasto-viscoplastic layer:

$$
G\bar{h} \frac{\partial^2 \tilde{u}}{\partial x^2} - \frac{\partial^2 \tilde{u}}{\partial t^2} \frac{(3+\bar{h})G}{v_s^2} + \bar{\eta}^{vp} G \left(\frac{\partial^3 \tilde{u}}{\partial t \partial x^2} - \frac{1}{v_s^2} \frac{\partial^3 \tilde{u}}{\partial t^3} \right) = 0, \tag{4.16}
$$

where $v_s = \sqrt{\frac{G}{\rho}}$ and $\bar{\eta}^{vp} G = \eta F_0 = g$.

This coincides with the elasto-viscoplastic equation derived by de Borst and Duretz, 2020; Sluys and de Borst, 1992; W. M. Wang et al., 1996, 1997. However, the equation derived above describes the evolution of a perturbation from the initial homogeneous deformation state. It will not be used as a description of the total behavior of the material as it neglects the material behavior in unloading and we are not interested in the solution of the elasto-plastic problem but only at the stability of the homogeneous deformation state, in order to draw conclusions about strain localization(see Lemaitre et al., 2020).

Here we note that the equation (4.16) has time independent coefficients (autonomous system, see Brauer and Nohel, 1969). Thus, incorporating a linear law for strain softening and strain rate hardening allows us to investigate stability according to Lyapunov's first method (Lyapunov, 1992; Mawhin, 2005). Incorporation of more general material laws including non-linear effects in strain softening and strain rate hardening would result in a non autonomous system. As such stability of the solution for the wavenumbers (k_r) and wavelengths (λ) of interest should be studied using Lyapunov's second (global) method. However, such an investigation lies outside the scope of this chapter. Here we investigate the capability of a simple elasto-viscoplatic law with linear strain softening and linear strain-rate hardening as the one described in de Borst and Duretz, 2020; W. Wang et al., 1997, to regularize the width of the localization in dynamical elasto-viscoplastic analyses.

As mentioned in W. Wang et al., 1997, this equation contains two components, a classical elastoplastic wave equation plus the higher order rate-dependent terms. The nature of this differential equation is defined by the higher order derivatives. It is also stated in Sluys and de Borst, 1992 that, in the limit of high viscosity $\bar{\eta}^{vp} \rightarrow \infty$, only the rate terms contribute, since they travel with the elastic wave velocity. In this case, the implied deformation pulse will travel with the corresponding elastic wave velocity as predicted in Loret and Prevost, 1990 and Needleman, 1988.

4.2.3.2 Normalizing the 1D elasto-viscoplastic wave equation.

We consider $\bar{u} = \frac{u}{u_c}$, $\bar{t} = \frac{t}{t_c}$, $\bar{x} = \frac{x}{x_c}$, where $u_c,\ t_c,\ x_c$ are the characteristic displacement, time and length, respectively. Applying these definitions to equation (4.16) we obtain:

$$\left(\frac{x_c^2}{v_s^2 t_c^2}\frac{\partial^3 \bar{u}}{\partial \bar{t}^3} - \frac{\partial^3 \bar{u}}{\partial \bar{x}^2 \partial \bar{t}}\right)\frac{\bar{\eta}^{vp}}{t_c \bar{h}} + \frac{x_c^2}{v_s^2 t_c^2}\frac{3+\bar{h}}{\bar{h}}\frac{\partial^2 \bar{u}}{\partial \bar{t}^2} - \frac{\partial^2 \bar{u}}{\partial \bar{x}^2} = 0. \tag{4.17}$$

Introducing the characteristic velocity $v_c = \frac{x_c}{t_c}$, the result is written as:

$$\left(\frac{v_c^2}{v_s^2}\frac{\partial^3 \bar{u}}{\partial \bar{t}^3} - \frac{\partial^3 \bar{u}}{\partial \bar{x}^2 \partial \bar{t}}\right)\frac{\bar{\eta}^{vp}}{t_c \bar{h}} + \frac{v_c^2}{v_s^2}\frac{3+\bar{h}}{\bar{h}}\frac{\partial^2 \bar{u}}{\partial \bar{t}^2} - \frac{\partial^2 \bar{u}}{\partial \bar{x}^2} = 0. \tag{4.18}$$

The above equation is linear and has solutions of the form:

$$\bar{u}(\bar{x},\bar{t}) = A \exp\left[i(\bar{k}\bar{x} - \bar{\omega}\bar{t})\right], \tag{4.19}$$

where $\bar{k}, \bar{\omega} \in \mathbb{C}$ and $A \in \mathbb{R}$ is a constant indicating the wave amplitude. Finally, inserting the non-dimensional solution (4.19) into the normalized equation (4.18) we arrive at:

$$\bar{k}^2 v_s^2(\bar{h}\bar{t}_c - i\bar{\eta}^{vp}\bar{\omega}) - v_c^2\bar{\omega}^2[(3+\bar{h})\bar{t}_c - i\bar{\eta}^{vp}\bar{\omega}] = 0. \tag{4.20}$$

It is worth emphasizing that the choice of assuming both $\bar{\omega}, \bar{k} \in \mathbb{C}$ is not studied extensively in the literature. However, examples of the notion can be found in Mainardi, 1984, 1987; Marion, 2013.

Replacing $V = \frac{v_c}{v_s}$, $T = \frac{\bar{\eta}^{vp}}{t_c}$ and solving the above for $\bar{k}$ we obtain:

$$\bar{k}_{1,2} = \pm\sqrt{\frac{V^2\bar{\omega}^2(3+\bar{h} - iT\bar{\omega})}{(\bar{h} - iT\bar{\omega})}}. \tag{4.21}$$

The above equation can be also derived directly by use of a Fourier transform on equation (4.18). Expanding $\bar{k}, \bar{\omega}$ in imaginary and real parts, $\bar{k} = \bar{k}_r + \bar{k}_i i$, $\bar{\omega} = \bar{\omega}_r + \bar{\omega}_i i$ as explained in Hayes, 1970; Maugin, 2007; Poeverlein, 1962 indicates that in our analysis the dependence of the amplitude of the solution has both a spatial and a temporal component. In particular the non-dimensional solution can be written as:

$$\bar{u}(\bar{x},\bar{t}) = \exp\left(-\bar{k}_i\bar{x} + \bar{\omega}_i\bar{t}\right)\exp[i(\bar{k}_r\bar{x} - \bar{\omega}_r\bar{t})], \tag{4.22}$$

where, without loss of generality, the amplitude constant in front of the exponential terms of solution (4.22) is set to unity. The first factor in the right hand side of equation (4.22) indicates a quantity that increases or decreases based on the relationship between ($\bar{\omega}_i\bar{t}$ and $\bar{k}_i\bar{x}$). In this chapter, we define that an observer moving along $\bar{x}$ with a velocity c_i, such that the amplitude profile $\exp\left(-\bar{k}_i\bar{x}+\bar{\omega}_i\bar{t}\right)$ remains constant, is moving with the *amplitude velocity*:

$$c_i = \frac{\bar{\omega}_i}{\bar{k}_i}. \tag{4.23}$$

Conversely the second factor of equation (4.22) indicates the classical wave solution. An observer moving with a velocity c_r such that the phase $\exp\left[i(\bar{k}_r\bar{x}-\bar{\omega}_r\bar{t})\right]$ remains constant is said to be moving with the *phase velocity* Marion, 2013; Pain and Beyer, 1993; Sluys and de Borst, 1992:

$$c_r = \frac{\bar{\omega}_r}{\bar{k}_r}. \tag{4.24}$$

According to the definition of Lyapunov for continuous dynamical systems Mawhin, 2005; Rattez, Stefanou, and Sulem, 2018, for an equilibrium solution to be unstable, the amplitude of the initial perturbation must increase in time. According to Lyapunov stability analysis, a partial solution of the partial differential equation (4.18) is given by $\bar{u}(\bar{x},\bar{t}) = \exp\left(\bar{s}\bar{t}+i\bar{k}\bar{x}\right)$, where $\bar{s}$ is the Lyapunov exponent $\bar{s} = -i\bar{\omega}$. From this we conclude that the important term whose sign determines the stability of the reference solution, corresponding to homogeneous deformation (4.19), is the imaginary part of $\bar{\omega}$, i.e. $\bar{\omega}_i$. Therefore, for the perturbation to grow in amplitude, the term $\exp\left(-\bar{k}_i\bar{x}+\bar{\omega}_i\bar{t}\right)$ must be increasing as the wave travels. Localization on a mathematical plane will happen if we can find appropriate $\bar{\omega}_i, \bar{k}_i$ terms for the amplitude to be constantly increasing the fastest for the smallest possible wavelength $\bar{\lambda} \rightarrow 0$ ($\bar{k}_r = \frac{2\pi}{\bar{\lambda}} \rightarrow \infty$).

4.3 Dispersion analysis

4.3.1 Solution of the dispersion equation

Equation (4.21) consists of two multivalued functions $\bar{k}_1(\bar{\omega}), \bar{k}_2(\bar{\omega})$ in the complex set $\bar{\omega} \in \mathbb{C}$. Introduction of branch cuts along selected points of unambiguous value is needed for their study on the values of their argument $\bar{\omega}$ Arfken and Weber, 1999.
Noticing the square powers of V^2, $\bar{\omega}^2$ inside the root, equation (4.21) can be simplified

yielding:

$$\bar{k}_{1,2}(\bar{\omega}) = \pm V \left(\frac{3+\bar{h}}{\bar{h}}\right)^{\frac{1}{2}} \bar{\omega} \left(\frac{3+\bar{h}}{T} i + \bar{\omega}\right)^{\frac{1}{2}} \left(\frac{\bar{h}}{T} + \bar{\omega}\right)^{-\frac{1}{2}}. \tag{4.25}$$

Each of the two solutions contains right and left propagating waves based on the sign combinations of $\bar{\omega}_r, \bar{k}_r$. The second solution $\bar{k}_2(\omega)$ presents the exact same points of interest as the first. The difference lies in the -1 factor between the two solutions. This factor according to the Euler identity can be written as $e^{i\pi} = -1$ and ,therefore, indicates a change in the argument of the second solution. Figure 4.1 shows 3D plots of $\bar{k}_1(\bar{\omega}),\ \bar{k}_2(\bar{\omega})$. The colors on the right of Figure 4.1 are changed indicating a change of the argument from the upper half of the imaginary plane to the lower half of it, meaning that the two solutions $\bar{k}_{1,2}(\bar{\omega})$ behave differently when it comes to the spatial amplification/attenuation coefficient $\bar{k}_i$. In particular, $\bar{k}_1(\bar{\omega})$ predicts only attenuation waves, while $\bar{k}_2(\bar{\omega})$ consists of amplification waves. This change indicates that the waves in Figure 4.1 travel in the same direction with opposite imaginary part of $\bar{k}(\bar{\omega})$. To us the propagation direction of the wave is not important because of spatial symmetry of the solution (4.21).

In the next section the points of interest of the $\bar{k}_1(\bar{\omega})$ are presented and their behavior is explained in the form of branch cuts and poles. As discussed previously, the same behavior is valid for $\bar{k}_2(\bar{\omega})$. We choose to draw further conclusions in the form of plots over line from the combination of the two solutions $\bar{k}_{1,2}(\bar{\omega})$. In particular, we focus on the positive real parts of the solutions $\bar{k}_{1r}(\bar{\omega}), \bar{k}_{2r}(\bar{\omega}) > 0$ as well as the positive imaginary parts of the solutions $\bar{k}_{1i}(\bar{\omega}), \bar{k}_{2i}(\bar{\omega}) > 0$. Thus, we investigate the function $\bar{k}(\omega) = |\bar{k}_r(\bar{\omega})| + i|\bar{k}_i(\bar{\omega})|$ as shown later in Figure 4.4.

4.3.2 Poles and zeros

Studying equation (4.25), the following points can be readily specified in the above form:

- The third factor indicates a zero at the origin: $\bar{\omega}^{\mathrm{O1}} = 0$.
- The fourth factor becomes zero at position: $\bar{\omega}^{\mathrm{O2}} = -\frac{3+\bar{h}}{T} i$.
- The last factor indicates the presence of a pole at: $\bar{\omega}^{\mathrm{P1}} = -\frac{\bar{h}}{T} i$.
- The value of the function at complex infinity $\bar{\omega}^{\mathrm{P2}} \to \infty$ is found to be infinite in a complex sense, $\lim_{\bar{\omega} \to \bar{\omega}^{\mathrm{P2}}} \bar{k}_1(\bar{\omega}) \to \infty$.

For the purposes of our analysis the behavior of the dispersion function at the poles $\bar{\omega}^{\mathrm{P1}}$, $\bar{\omega}^{\mathrm{P2}}$ is very important as it will be shown to promote localization on a mathematical plane. Because of the fractional powers of the second and third term, equation (4.25) is a

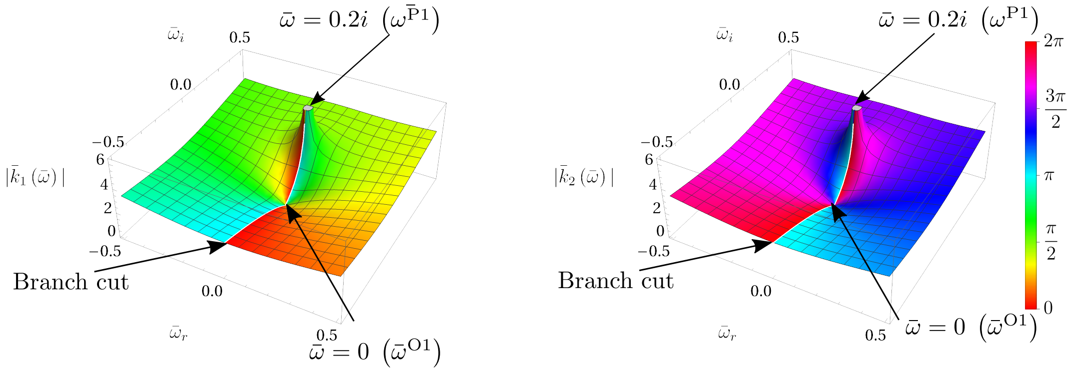

Figure 4.1 – On the left: Complex 3D plot of the $\bar{k}_1(\bar{\omega})$ solution (4.21). On the right: Complex 3D plot of the $\bar{k}_2(\bar{\omega})$ solution (4.21). Values on vertical axis indicate the solution's magnitude, where the coloring indicates the argument of the function. Along the branch cut discontinuity, the difference in color indicates the jump in the argument of $\bar{k}_1(\bar{\omega})$.

multivalued equation, since it is affected by the values of the argument. In order to remove the ambiguity from the function we need to constrain it in such a way that each value of the function corresponds to only one argument. For this we introduce *branch cuts*. A branch cut is a discontinuity in the function that is defined by arbitrarily joining the two points defined as branch points. The branch points are defined as points of unambiguous value, where the argument of the function is exactly known for a particular value of the function and the values corresponding to other points in a region sufficiently close to the branch point depends on the argument of the complex number inserted in the function. Two such points for the complex function $f(\bar{\omega}) = \bar{\omega}^{\frac{1}{2}}$ are $\bar{\omega} = 0$, and $|\bar{\omega}| \to \infty$, $\bar{\omega} \in \mathbb{C}$, because for these particular numbers the value of the function is always zero and infinity respectively. However, around them the value of the function depends on the argument of the complex number (see below).

We can translate this result to other points in the complex plane, namely to $\bar{\omega}^{\mathrm{O2}}$, $\bar{\omega}^{\mathrm{P1}}$. In a region close and around $\bar{\omega}^{\mathrm{O2}} = -i\frac{3+\bar{h}}{T}$ the complex number with starting point $\bar{\omega}^{\mathrm{O2}}$ that follows the curve surrounding $\bar{\omega}^{\mathrm{O2}}$ changes its argument by $2\pi i$. However, the factor $\left(\frac{3+\bar{h}}{iT} - \bar{\omega}\right)^{\frac{1}{2}}$ only changes by πi, meaning that there is a sign difference between the starting and the end position along the closed curve at the same point. Similarly, the same happens in the region near the pole $\bar{\omega}^{\mathrm{P1}}$, where for every $2\pi i$ that the relative complex number starting at $\bar{\omega}^{\mathrm{P1}}$ changes following the surrounding curve, the factor $\left(\frac{\bar{h}}{iT} - \bar{\omega}\right)^{-\frac{1}{2}}$ changes by $-\pi i$. However at complex infinity ($\bar{\omega} \to \infty$), both previous points are entailed by the curve at infinity. Therefore, the total change in the argument is $\pi i - \pi i = 0$. This means that, $\bar{\omega}^{\mathrm{P2}}$ it is not a branch point (it does not belong to the branch cut). The simplest cut is the one that follows the line defined by the two branch points as shown in Figure 4.2. Since the point at complex infinity is not a branch point then it can be expected to be an isolated singular point, namely a pole of n-order or an essential singularity Arfken and Weber, 1999; Brown, Churchill, et al., 2009. In this case it can be proven to be a simple pole as shown in Appendix B

Introducing the mapping $\bar{\omega} = \frac{1}{z}$ we notice $\bar{\omega} \to \infty$ can be written as $\frac{1}{z}$ when $z \to 0$. The properties of this mapping are explained in Brown, Churchill, et al., 2009 and in the Appendix B.

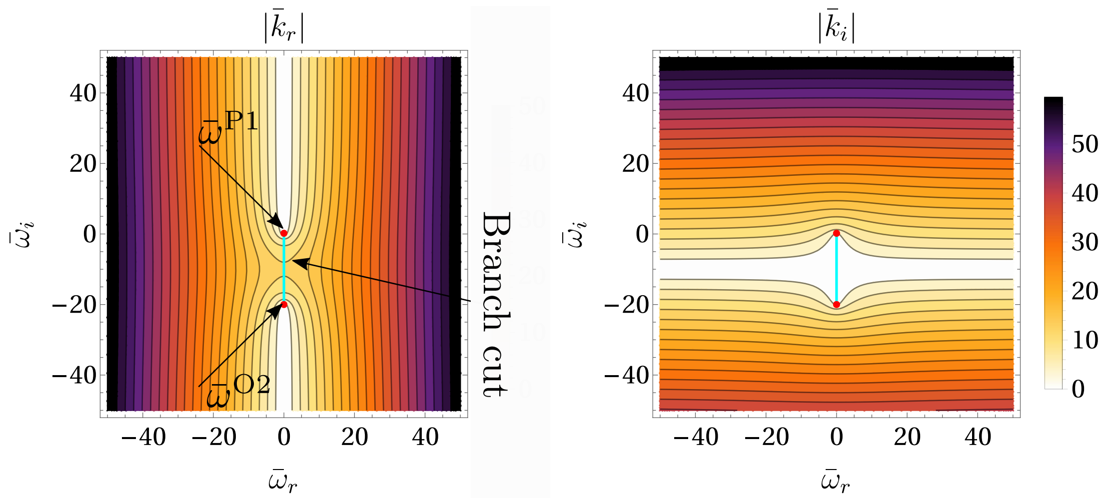

Figure 4.2 – Contours of the solution (4.21) indicating with red color the position of the branch points and with cyan the branch cut line that connects them.

The plots showing the poles and zeros of the function $\bar{k}_1(z)$ with the mapping are shown in Figure 4.3. On the right part of the Figure the region around the poles and infinity is shown while on the left a detail is presented where the zero value $\bar{\omega}^{\mathrm{O2}}$ - that due to the mapping is found closer to the origin - is shown.

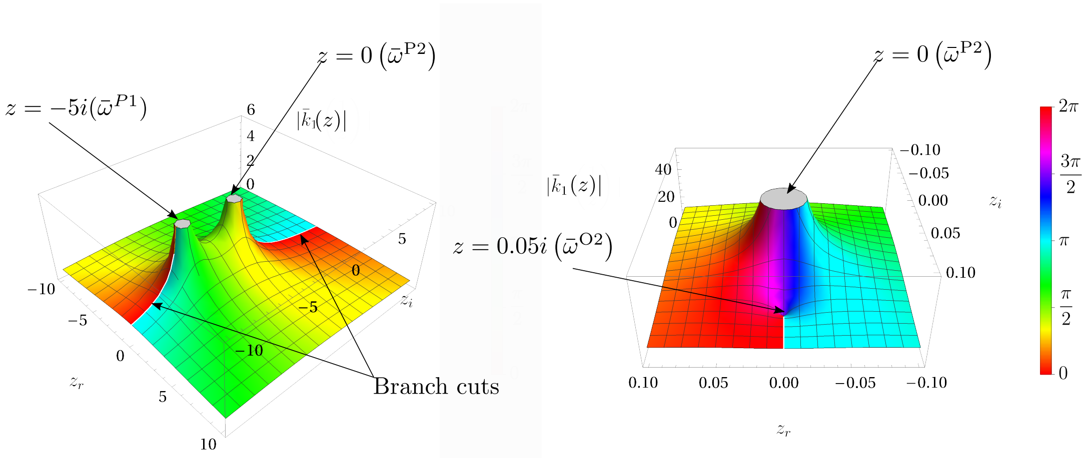

Figure 4.3 – Complex 3D plot of the $\bar{k}_1(z)$ where $z = \frac{1}{\bar{\omega}}$. On the left part of the Figure the behavior in the region near $\bar{\omega}$ infinity $\bar{\omega}^{\mathrm{P2}}$ and the pole at $\bar{\omega}^{\mathrm{P1}}$ is presented.We notice the two poles lying at positions $\bar{\omega}^{\mathrm{P2}}:\ z = 0$ and $\bar{\omega}^{\mathrm{P1}}$ lying at $\omega^{\mathrm{P1}} : z^p = -5i$ respectively. On the right the region close to the pole at infinity $z = 0$ is plotted. We notice the existence of the zero $\bar{\omega}^{\mathrm{O2}}$ that due to the mapping now lies at $z = 0.05$ extremely close to $z = 0$, inside the unit circle.

4.3.3 Localization on a mathematical plane

Localization will happen when the amplitude of a particular perturbation mode as shown in equation 4.22 is found to be continuously increasing faster than the rest. If this happens for the perturbation of the smallest possible wavelength $\bar{\lambda} \to 0$ that corresponds to $\bar{k}_r \to \infty$ then localiazation on a mathematical plane takes place.

As stated in the previous paragraphs without loss of generality we focus on the positive real and imaginary parts of the function $|\bar{k}(\bar{\omega})| = |\bar{k}_r| + |\bar{k}_i|i$. $|\bar{k}(\bar{\omega})|$ has the same poles $\bar{\omega}^P$ and zeros $\bar{\omega}^O$ as the original $\bar{k}(\bar{\omega})$ with the added simplification that only the positive argument values of both functions $\bar{k}_1(\bar{\omega}), \bar{k}_2(\bar{\omega})$ are plotted. This simplifies our analysis with regards to the sign of $\bar{k}_i$, which contributes to the exponential growth of the amplitude, but it is not crucial for the time evolution of the perturbation which is determined by $\bar{\omega}$.

First we focus to the pole value at $\bar{\omega}^{\mathrm{P1}}$ which is shown in the left 3D plot of Figure 4.4. There the pole $\bar{\omega}^{P1}$ and the first zero $\bar{\omega}^{O1}$ are shown. The pole lies at the value $\bar{\omega}^{\mathrm{P1}} = -\frac{\bar{h}}{T}i$ with $\bar{h} < 0$, corresponding to a real and positive Lyapunov exponent $\bar{s} = i\bar{\omega} = \frac{\bar{h}}{T} > 0$.

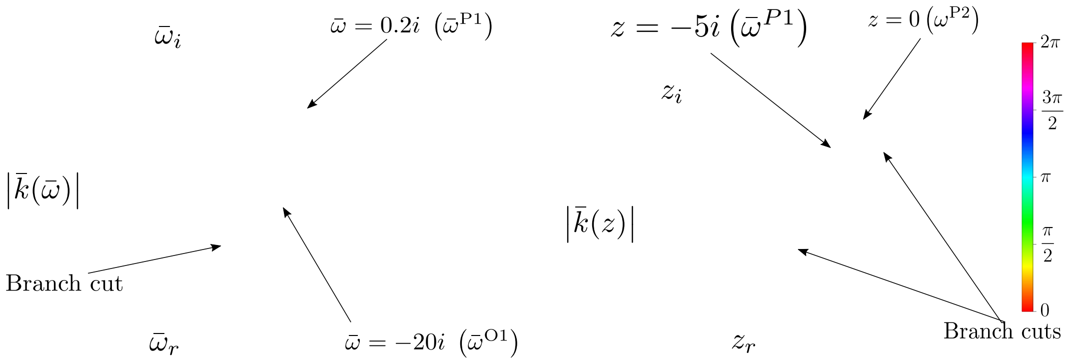

Figure 4.4 – Complex 3D plot of the $\tilde{k}(\bar{\omega})$ combination of the two solutions. This envelope incorporates all the waves that travel to the positive part of the axis together with the highest spatial amplification coefficient. On the left: Complex 3D Plot of $\bar{\tilde{k}}(\bar{\omega}) = |\bar{k}_r| + i|\bar{k}_i|$ for values of $\bar{\omega}_r$, $\bar{\omega}_i$ close to the pole value $\bar{\omega}^{\mathrm{P1}} = 0.2i$. On the right: Complex 3D Plot of $\bar{\tilde{k}}\left(\frac{1}{z}\right) = |\bar{k}_r| + i|\bar{k}_i|$ for values of $\bar{\omega}_r$, $\bar{\omega}_i$ close to infinity, when $z^{\mathrm{P2}} = 0$, $\left(\frac{1}{z}\right) \to \infty$ and the pole value $\bar{\omega}^{\mathrm{P1}} = 0.2i \to z^{P1} = -5i$

Since for $\bar{k}_r(\bar{\omega}) \to \infty$ when $\bar{\omega} = \bar{\omega}^{\mathrm{P1}}$, we conclude that localization on a mathematical plane is possible ($\bar{\lambda} = \frac{2\pi}{\bar{k}_r} \to 0$), while in this case the rate of increase of the perturbation amplitude is bounded. This is a new result that the analysis in the complex frequency domain allowed us to obtain, and wouldn't have been possible without this consideration. Note also that other localization criteria (see Rice, 1976; Rudnicki and Rice, 1975) are not applicable to the problem at hand.

The imaginary frequency $\bar{\omega}_i$ of the pole $\bar{\omega}^{P1}$, where $\bar{k}_r$ tends to infinity, indicates the growth rate of the perturbation with infinitesimal wavelength. Its inverse is called here, "*characteristic growth time of the perturbation*" ($T^{\star}$).

The perturbation growth coefficient for viscoplastic media is bounded in contrast to rate-independent media where the perturbation growth coefficient is infinite when the conditions for strain localization are met ($\bar{s} \approx \frac{1}{\lambda}$). However, in both cases strain localization happens on a mathematical plane and, therefore, this analysis shows that viscoplasticity does not regularize this problem even in the presence of inertia terms.

The behavior of $|\bar{k}(\bar{\omega})|$ at $\bar{\omega} \to \infty$ meaning $\bar{\omega} = \bar{\omega}^{P2}$ cannot be captured in this plot. For this reason we perform a change of variables in $\bar{\omega}$, replacing with $\bar{\omega} = \frac{1}{z}$. Now the

non-dimensional material parameters	M1 stable	M2 unstable
$\bar{V} = \frac{v_c}{v_s}$	0.25	0.25
$\bar{T} = \frac{g}{t_c G}$	0.15	0.15
$\bar{h} = \frac{h}{G}$	0.03	-0.03

Table 4.1 – Non-dimensional material parameters used for the numerical analyses

value of $\bar{\omega}$ at infinity corresponds to $z = 0$. The function $\bar{k}(z)$ is plotted on the right of Figure 4.4, where we capture the value at $\bar{\omega}^{\mathrm{P2}} \to \infty$ when $z = 0$ ($\bar{\omega}^{P2}$) and at the pole $\bar{\omega}^{\mathrm{P1}} = \frac{1}{z^{\mathrm{P1}}}$.The second zero value is also captured in the line plots of Figures 4.6 and 4.7 with the help of the transformation $\bar{k}(z)$. In this case $\bar{k}(z)$ tends to infinity. Therefore ω^{P2} also constitutes a localization point.

4.3.4 Characterization of the waves in the complex plane

Having qualitatively described the behavior of the solutions of the dispersion equation we proceed with assigning specific values to the dimensionless parameters according to the material parameters taken from de Borst and Duretz, 2020. These values are presented in Table 4.1 and describe the case of a viscoplastic material obeying the von Mises yield criterion with strain-hardening ($h > 0$) and strain-rate hardening ($g > 0$), M1, as well as the case of strain-softening ($h < 0$) and strain-rate hardening ($g > 0$), M2.

We focus our attention on the case M2. By standing waves here we refer to profiles stationary in space whose values, however, depend on time due to the exponential growth coefficient $\bar{\omega}_i$. The contours of the real $|\bar{k}_r|$ and imaginary parts $|\bar{k}_i|$ of the combination of solutions near the pole ω^{P1} are presented in Figure 4.5. We can define three cases for an 1D elasto-viscoplastic medium expanding to infinity in both directions around the origin:

4.3.4.1 Case 1: Standing waves

We focus our attention on the line where $\mathrm{Re}[\bar{\omega}] = \bar{\omega}_r = 0$ (see also Figure 4.5, Case 1). In this case standing waves are present in the medium. The amplitude of these standing waves is dependent on the values of $\bar{k}_i, \bar{\omega}_i$. When $\bar{k}_i > 0$, while $\bar{\omega}_i = 0$, the amplitude of the standing wave decreases with the distance from the origin as shown in equation (4.22). However, if $\bar{\omega}_i > 0$, then the value of the amplitude of the oscillations at fixed

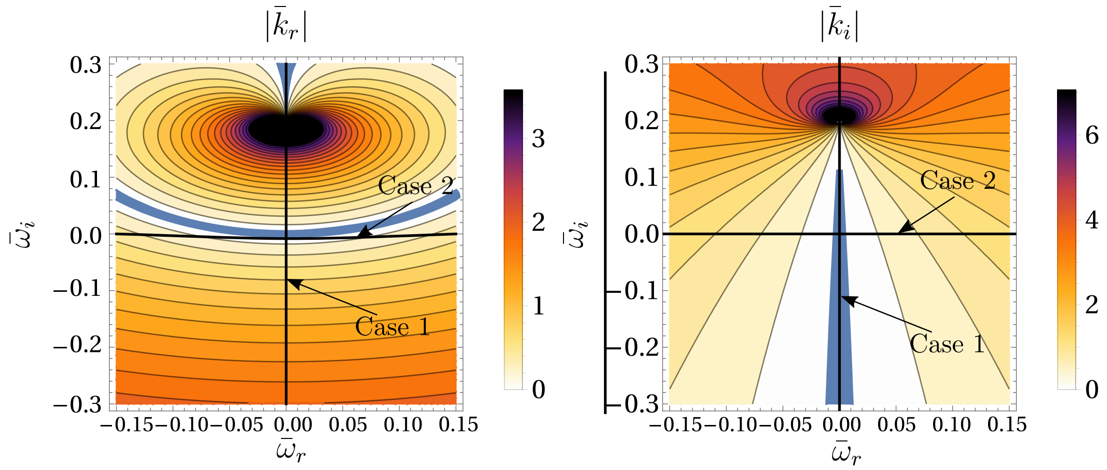

Figure 4.5 – Contourplot of $\bar{k}_r$, $|\bar{k}_i|$ for values of $\bar{\omega}_r$, $\bar{\omega}_i$ close to the pole value $\bar{\omega}^P = -0.2i$. The contour closer to $\bar{k} \to 0$ is presented with blue color.

positions, will grow exponentially with time. Thus strain localization will happen inside a length $\bar{\lambda} = \frac{2\pi}{\bar{k}_r}$.

Along the imaginary axis ($\bar{\omega}_r = 0$), there is only one position where $\bar{k}_r \to \infty$. This is the pole at $\bar{\omega}^{\mathrm{P1}}$ which constitutes a branch point of the dispersion relation (4.20) (see also Figure 4.6-asymptote). In this point $\bar{k}_r(\bar{\omega}^{\mathrm{P1}}) \to \pm\infty$ as well as $\bar{k}_i(\bar{\omega}^{\mathrm{P1}}) \to \pm\infty$. We notice that the value of $\bar{\omega}_i$ at the pole is a cutoff value. There are no higher values of $\bar{\omega}_i$ for which standing waves are possible since $\bar{k}_r = 0$ for $\bar{\omega}_i > \bar{\omega}^{\mathrm{P1}}$(see also Figure 4.6). For a perturbation from the initial homogeneous state to grow with time we are interested only in $\bar{\omega}_i > 0$. Therefore the behavior of $\bar{k}_r$ for $\bar{\omega}_i < 0$ is of no consequence for the stability of the homogeneous deformation, since all these modes will eventually die-off with time. From the above, we conclude that since the infinitesimal wavelength $\bar{\lambda} = \frac{2\pi}{\bar{k}_r} \to 0$ for the highest possible value of $\bar{\omega}_i$ strain localization on a mathematical plane is inevitable. We emphasize again that classical approaches as described in de Borst and Duretz, 2020; W. Wang et al., 1997 neglect the existence of the imaginary frequencies and therefore, are unable to find the pole $\bar{\omega}^{P1}$, failing to predict localization on a mathematical plane. Note that other localization criteria (see Rice, 1976; Rudnicki and Rice, 1975), are also not applicable to the problem at hand due to the introduction of rate dependency (elasto-viscoplasticity).

Next, we investigate the influence of $\bar{k}_i$ to the evolution of the amplitude of the perturbation. Looking at Figure 4.7 and considering the solution branch of equation (4.21) we notice that $\bar{k}_i \to \infty$ for $\bar{\omega} = \bar{\omega}^{\mathrm{P1}}$. Therefore, a standing wave with solution parameters $(\bar{\omega}, \bar{k})$ defined the same as the pole $\bar{\omega}^{\mathrm{P1}}$ will exhibit localization on a mathematical plane as distance $\bar{x}$ from the origin increases.

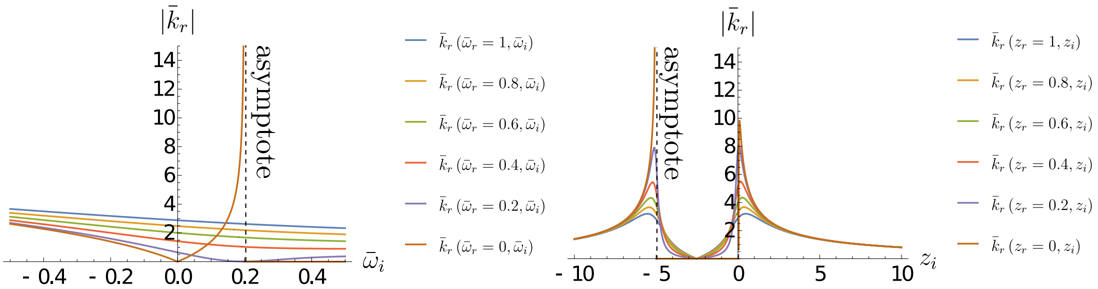

Figure 4.6 – Left: Evolution of $\bar{k}_r$ with respect to $\bar{\omega}_i$ for parameter values $\bar{\omega}_r$ close to the pole value $\bar{\omega}^{\mathrm{P1}} = 0.2i$ indicating traveling waves around the pole $(\bar{\omega}_r \neq 0)$. Right: $|k_r|$ along the lines of $\bar{\omega}_r = const$ for a range of values of $\bar{\omega}_i$ close to infinity.For $\bar{z}_r = 0$ the imaginary axis $\bar{\omega}_i$ is parallel to the imaginary axis z_i. Therefore The detail around $z_i = 0$ is indicative of the behavior of function $\bar{k}(\bar{\omega})$ as $\bar{\omega}_r = 0,\ \bar{\omega}_i \to \infty$.

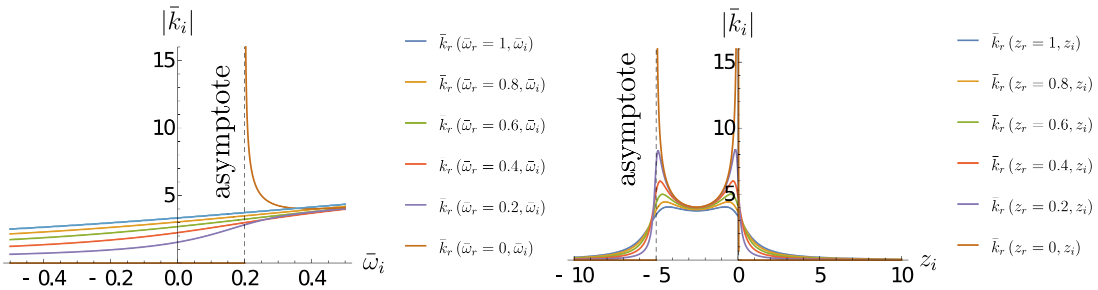

Figure 4.7 – Evolution of $\bar{k}_i$ with respect to $\bar{\omega}_i$ for parameter values $\bar{\omega}_r$ close to the pole value $\bar{\omega}^{\mathrm{P1}} = 0.2i$ indicating traveling waves around the pole $(\bar{\omega}_r \neq 0)$. Left: $|\bar{k}_i(\bar{\omega})|$ along the lines of $\bar{\omega}_r = const$ for a range of values of $\bar{\omega}_i$, detail around the pole region $\bar{\omega}^{\mathrm{P1}}$. Right: $|\bar{k}_i(\frac{1}{z})|$ along lines of constant z_r. For $z_r = 0$ the imaginary axis $\bar{\omega}_i$ is parallel to the imaginary axis z_i. Therefore The detail around $z_i = 0$ is indicative of the behavior of function $\bar{k}(\bar{\omega})$ as $\bar{\omega}_r = 0,\ \bar{\omega}_i \to \infty$.

4.3.4.2 Case 2: Traveling waves of zero temporal attenuation

Another important case seen in bibliography Abellan and de Borst, 2006; de Borst and Duretz, 2020; Sluys and de Borst, 1992; W. Wang et al., 1996; W. Wang et al., 1997 is that of the traveling waves where the imaginary part of angular frequency is zero $\bar{\omega}_i = 0$ (see Figure 4.5, Case 2). Therefore the Lyapunov exponent is also zero $(s = -i\bar{\omega}_i = 0)$. In this case the amplitude growth is dependent only on $\bar{k}_i$: $\bar{u}(\bar{x},\bar{t}) = \exp(-\bar{k}_i\bar{x})\exp[(\bar{k}_r\bar{x} - \bar{\omega}_r\bar{t})]$. The parameter $\bar{k}_i$ corresponds to the parameter α in de Borst and Duretz, 2020; Sluys and de Borst, 1992; W. Wang et al., 1996; W. Wang et al., 1997 and its inverse $l = \alpha^{-1}$ is thought to constitute a critical length that is supposed to regularize the problem, damping the waves of higher wavenumber $\bar{k}_r$ and therefore avoiding strain localization on a mathematical plane. Here we show that in fact depending on the solution branch of equation (4.21) the contribution of $\bar{k}_i$ to the solution's behavior can instead be positive, indicating amplification of perturbations of higher wavenumber $\bar{k}_r$. We focus our attention on Figure 4.8. We follow the red line corresponding to $\bar{\omega}_i = 0$. We notice that the dispersion relation predicts $\bar{k}_r = 0$ for $(\bar{\omega}_r, \bar{\omega}_i) = (0, 0)$. As we move away from the origin along the direction of $\bar{\omega}_r$ we notice a quasi-linear increase of the wavenumber $\bar{k}_r$. Figure 4.8 shows that $|\bar{k}_r|$ increases monotonically and tends to infinity for $|\bar{\omega}_r| \to \infty$. The latter can be proven mathematically (see Appendix B). From this we establish that perturbations whose wavelength tends to zero $\bar{\lambda} \to 0$ are admissible. Next we proceed on examining the rate of increase of their amplitude with respect to distance $\bar{k}_i$.

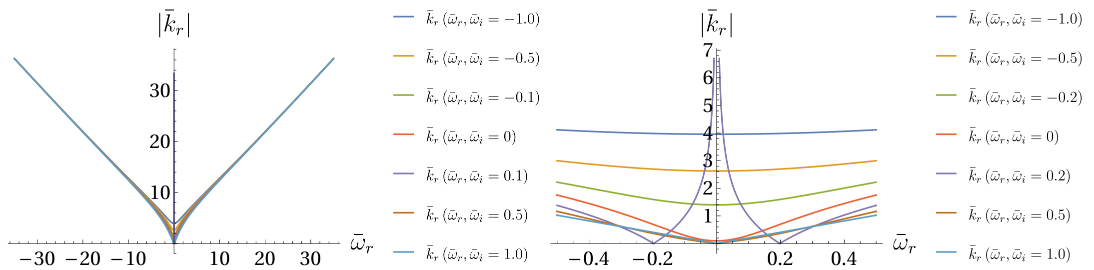

Figure 4.8 – Dispersion curves $(\bar{\omega}_r, \bar{k}_r)$ for different values of parameter $\bar{\omega}_i$ along the line of zero temporal coefficient $\bar{\omega}_i = 0$ (case 2). With red color and the value passing from the pole $\bar{\omega}^{\mathrm{P1}} = 0.2i$ purple color. Detail of the dispersion for low values of $\bar{\omega}_r$ is shown on left.

Figure 4.9 shows that for $\bar{\omega}_r$ tending to infinity, the value of $|\bar{k}_i|$ increases monotonically and tends to a ceiling value $\bar{k}_i \to c \ \in \mathbb{R}$. The latter can be proven mathematically (see Appendix B). Therefore, when $\bar{k}_r(\omega) \to \infty$, $\bar{k}_i < 0$ takes its maximum absolute value (see Figures 4.8, 4.9), we notice that the amplitude of the perturbation of zero wavelength $\bar{\lambda}$ is increasing the fastest as the perturbation travels through the medium. Therefore, strain localization on a *traveling mathematical plane* will happen.

We note here, that the original approach of de Borst and Duretz, 2020; Sluys and de

Borst, 1992; W. Wang et al., 1996; W. Wang et al., 1997 does not take into account the possibility of a positive value for $\bar{k}_i$. In all the previous works the attenuation coefficient $\bar{\alpha} = \bar{k}_i$ is considered negative. Thus spatial amplification of the highest wavenumber $\bar{k}_r$ (infinitesimal wavelength $\bar{\lambda} \to 0$) is not considered in these works.

4.3.4.3 Case 3: The general case of traveling waves,

Based on Figure 4.5 and the diagrams of Figures 4.6, 4.7, 4.8 and 4.9 very general cases of traveling waves can be examined. In Figures 4.6 and 4.7 we examine the evolution of $\bar{k}_r$, $\bar{k}_i$ with respect to the imaginary part of the frequency $\bar{\omega}_i$, by considering the real part of the angular frequency $\bar{\omega}_r$ as a parameter.

We already presented case 1 of standing waves $\bar{\omega}_r = 0$ where the influence of the pole leads to strain localization due to $\bar{\omega}_i > 0$ for $\bar{k}_r(\bar{\omega}) \to \infty$ as seen on the left diagram of Figure 4.6. For the rest of the values of the parameter $\bar{\omega}_r$, the wavenumber $\bar{k}_r$ is bounded. Therefore, no strain localization on a mathematical plane will take place in these cases.

In Figures 4.8 and 4.9 temporal amplification $\bar{\omega}_i$ is introduced as a parameter, keeping $\bar{\omega}_r$ as the independent variable. Figure 4.8 is indicative of the dispersion relation of the medium. Away from $\bar{\omega}_r = 0$ the dispersion relation $\bar{\omega}_r, \bar{k}_r$ becomes linear for all values of $\bar{\omega}_i$ and the resulting traveling waves have a common phase velocity. We notice here that as $\bar{\omega}_r \to \infty$, $\bar{k}_r(\bar{\omega}_r, \bar{\omega}_i) \to \infty$. For the waves with the same value for the parameter $\bar{\omega}_i > 0$ this means that the growth of their amplitude in time is the same. For large real angu-

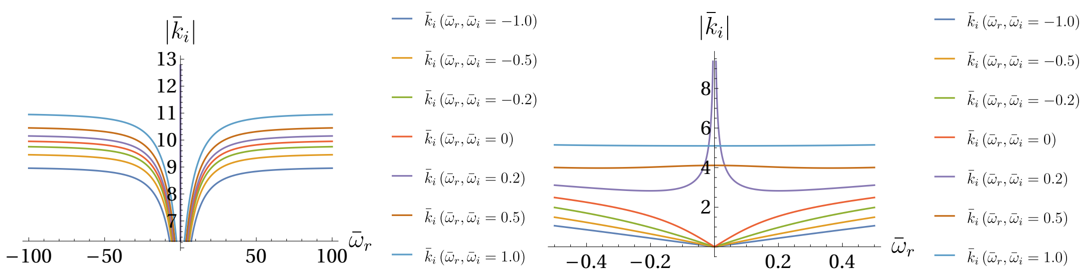

Figure 4.9 – Evolution of $\bar{k}_i$ for different values of temporal coefficient $\bar{\omega}_i$ including the case zero temporal attenuation/amplification $\bar{\omega}_i = 0$ to the pole value $\bar{\omega}^{\mathrm{P1}} = 0.2i$. For traveling waves around the pole ($\bar{\omega}_r \neq 0$) the spatial attenuation coefficient $\bar{k}_i$ is reaching an upper bound. Figure on left presents the curve of $|k_i|$ along the lines of $\bar{\omega}_i = const$ for a range of values of $\bar{\omega}_r$ while Figure on right presents a detail around the pole region $\bar{\omega}^{\mathrm{P1}}$.

lar frequencies $\bar{\omega}_r$ the spatial amplification coefficient $|\bar{k}_i|$ presents a ceiling value. This result is already proven for $\bar{\omega}_i = 0$ (see Appendix B). The ceiling value depends on the parameter value ω_i, namely it increases as the parameter $\bar{\omega}_i$ increases. The ceiling value of the amplification coefficient $\bar{k}_i$ corresponds to a wavenumber $\bar{k}_r$ that tends to infinity $\bar{k}_r \to \infty$. This result shows that in the general case of traveling waves with infinitesimal wavelength $\bar{\lambda} = \frac{2\pi}{\bar{k}_r} \to 0$, strain localization on a traveling mathematical plane will happen due to the combination of $\bar{k}_i < 0$ and $\bar{\omega}_i > 0$, provided that $\bar{k}_r \to \infty$.

In the above we focused mainly on limit cases related to strain localization in a elasto-viscoplastic strain-softening ($h < 0$), strain rate-hardening medium ($g > 0$). For a more general, qualitative description of a traveling monochromatic pulse, we refer to Appendix C.1. In this Appendix we refer also to the connection between strain localization and the interplay between phase and amplitude velocities.

4.3.4.4 Behavior of the pole at infinity $\omega^{\mathbf{P2}}$

Based on the behavior close to infinity, $\bar{\omega} \to \infty$ or $z \to 0$, we get $\bar{k}(\bar{\omega}) = \bar{k}(\frac{1}{z}) \to \infty$. In contrast to real infinity that can be either positive or negative or indeterminate based on whether we approach the value of z from above or below zero, complex infinity (∞) is indeterminate as at the pole value $\bar{\omega}^{P2}$ the limit along each direction surrounding the pole indicates differences in the real and imaginary parts of $\bar{k}(\bar{\omega})$. Since around a simple pole like $\bar{\omega}^{\mathrm{P2}}$, where $\bar{\omega}_r^{\mathrm{P2}} \to \infty$, $\bar{\omega}_i^{\mathrm{P2}} \to \infty$ the argument of a complex function changes by a full 2π radians, the two limiting cases for the value of $\bar{k}(\bar{\omega}^{\mathrm{P2}})$ are $\mathrm{Re}[\bar{k}] = \bar{k}_r \to \infty, \mathrm{Im}[\bar{k}] = \bar{k}_r \to 0$ and $\mathrm{Re}[\bar{k}] = \bar{k}_r \to 0, \mathrm{Im}[\bar{k}] = \bar{k}_r \to \infty$. Since $\bar{k}_r \to \infty$ when $\bar{\omega} = \bar{\omega}^{\mathrm{P2}}$, we conclude again, that localization strain on a mathematical plane is possible. Since, localization on a mathematical plane happens for values of $\bar{\omega} \to \infty$, the rate of increase of the perturbation amplitude as given by the Lyapunov exponent $\bar{s} = -i\bar{\omega}_i$ is unbounded.

4.3.4.5 Influence of the pole $\bar{\omega}^{P1}$

By expanding the solution space allowing for complex $\bar{\omega}_i$ we allow a connection with the Lyapunov exponent $\bar{s}$ used in stability analyses. The new solution space is richer regarding the perturbations we can introduce in the visco-elastoplastic medium. Some key characteristics retained by the solution from the definitions already found in the literature, is the exclusion of standing waves of infinitesimal length that grow with an infinite Lyapunov coefficient as in the case of the pure ill-posed rate-independent plasticity problem.

The introduction of the parameter $T = \frac{\bar{\eta}^{vp}}{t_c}$ allows for the existence of a zero value on the imaginary axis. This zero in turn plays the role of the branch point, forcing the argument of the pole $\bar{\omega}^{P2}$ at infinity to turn by $\pi/2$ thus nullifying the real part of $\bar{k}(\bar{\omega})$ along the imaginary axis. If that zero was not there, then the point at infinity would be a branch point, therefore strain localization on a mathematical plane would happen for infinite $\bar{\omega}_i$ as in the case of a strain-softening rate-independent material.

The visco-elastoplastic medium discussed here under the expansion of its dispersion equation solution negates the instantaneous localization of deformation, however as dictated by the pole $\bar{\omega}^{P1}$ amplification of the infinitesimal wavelength perturbation is still possible. In other words, the value of the Lyapunov exponent $\bar{s} = -i\bar{\omega}_i$ becomes bounded due to viscoplasticity but this is not true for the value of the wavenumber $\bar{k}_r$. Our approach of treating the problem of stability in the complex domain shows that localization on a mathematical plane is possible due to the existence of the pole $\bar{\omega}^{P1}$, which the classical approach described in de Borst and Duretz, 2020; Sluys and de Borst, 1992; W. Wang et al., 1996; W. Wang et al., 1997 fails to predict.

4.3.4.6 Comparison to case M1 (stable configuration)

For case M1 we note that $\bar{h} = 0.03 > 0$. In this case the points of interest of the dispersion relation (4.25) change leading to different behavior than the one previously presented. The relationships for the determination of zeros and poles of the function remain the same (see section 4.3.2).

For these numerical values, the pole $\bar{\omega}^{\mathrm{P1}}$ is reflected due to the change of sign of $\bar{h}$ around the Real axis. This however is not true for the he zero $\bar{\omega}^{\mathrm{O1}}$ since the sign of $(-3+h)$ does not change (provided that $|\bar{h}| < 1$). This change will move the branch cut defined on the imaginary axis below the origin $\bar{\omega}^{\mathrm{O1}}$. Since now the pole lies on $\bar{\omega}_i < 0$ the perturbations of infinitesimal length corresponding to it $\bar{\lambda} \to 0, \bar{k}_r \to \infty$ are attenuated with time, therefore strain localization on a mathematical plane is not possible in this case.

4.4 Numerical analysis

In this section, two sets of numerical analyses are performed in order to verify the stability and possible strain localization of the elasto-viscoplastic strain softening ($h < 0$), strain-rate hardening ($g > 0$) wave equation. Two sets of analyses were performed. In the first set, a 1D model of an elasto-viscoplastic infinite string was used on which, the linear differential equation of third order (equation (4.18)) is numerically solved for a variety of initial conditions. We comment on the displacement profiles that develop with time and we verify the theoretical findings of section 4.3. In the second set, we proceed in numerically solving the fully non-linear problem. The difference between these two sets of analyses, lies in the fact that in the second case unloading is allowed to take place. Therefore, we can investigate its influence on the strain localization profiles. The non linear numerical analyses show also strain localization and mesh dependency.

4.4.1 Linearized model: Model description

To model the infinite string a large length and the Sommerfeld open boundary conditions were used. The latter can be used since the partial differential equation in question is linear and by use of the Fourier transform can be shown to have partial solutions in the form of $A\exp(i(\bar{\omega}\bar{t} - \bar{k}\bar{x}))$. Three modes of inducing the perturbation from the reference homogeneous state were examined making use of non zero initial conditions for the string displacement. This is achieved by varying the shape of the perturbation with three different ways: an initial pinch of the string at the middle, a cosine pulse centered in the middle as well as a Gaussian distribution centered at the middle.

Two sets of parameters were used for the analyses, where the sign of the hardening parameter $\bar{h}$ varies between positive or negative in order to compare between strain-hardening and a strain-softening material as shown in Table 4.1. The material parameters used in the unstable case are those provided by de Borst and Duretz, 2020. The numerical analyses were performed using the method of Finite Differences. In particular a central difference scheme was used for the spatial discretization of the PDE problem, the domain of length $L = 15$m is discretized into 250 segments, resulting in a coupled system of ODE's which was solved by the algorithm IDA of the Mathematica^{TM} software package Wolfram Research, 2020.

4.4.1.1 Pinching

We present in Figure 4.10 the behavior of the string after an initial pinching -application of initial displacement conditions at the middle node of the discretized domain. Mesh convergence analysis has shown that, in the unstable case M2, the localization width is equal to the mesh size. Therefore, the elasto-viscoplastic formulation does not regularize the underlying problem as presented in the introduction and the solution is mesh dependent. This is in accordance with the theoretical results presented in subsections 4.3.4.1, 4.3.4.2, 4.3.4.3. We note also that the strain hardening material of the M1 case does not lead to strain localization as expected (see section 4.3.4.6).

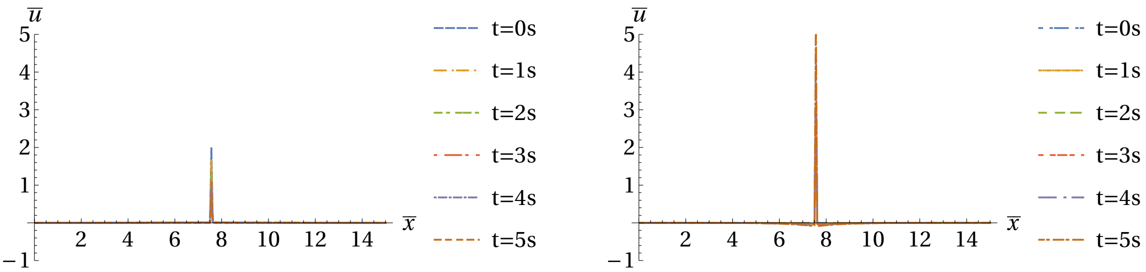

Figure 4.10 – Evolution of the pinching perturbation at different times. Left: strain hardening material case M1. On the right: strain softening material case M2.

4.4.1.2 Monochromatic cosine pulses

The behavior of the string after application of cosine initial conditions for the two sets of parameters (see Table 4.1) is presented in Figure 4.11. Again we notice a localization of deformation for the case of strain softening. In order to verify the theoretical prediction,

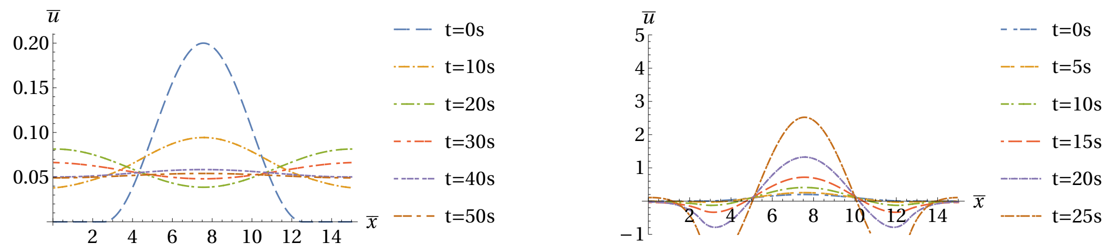

Figure 4.11 – Evolution of the cosine perturbation at different times. Left: strain hardening material case M1. On the right: strain softening material case M2.

that the elasto-viscoplastic medium with strain softening localizes on a mathematical plane under dynamic loading conditions, we superpose three different cosine perturbations in the medium by varying the width of each perturbation as shown in Figure 4.12. The perturbation wavelengths are $\bar{\lambda}$: 1, 5, 10, corresponding to perturbation widths of 0.5 ,2.5 , 5. In Figure 4.12, the position of the perturbations from left to right is $\bar{x} = 3.75 \rightarrow \bar{\lambda} = 10$, $\bar{x} = 7.5 \rightarrow \bar{\lambda} = 1$ and $\bar{x} = 11.24 \rightarrow \bar{\lambda} = 5$ respectively. Figure 4.12 shows that localization is accumulating faster for the smallest perturbation length, verifying the theoretical findings of section 4.3.

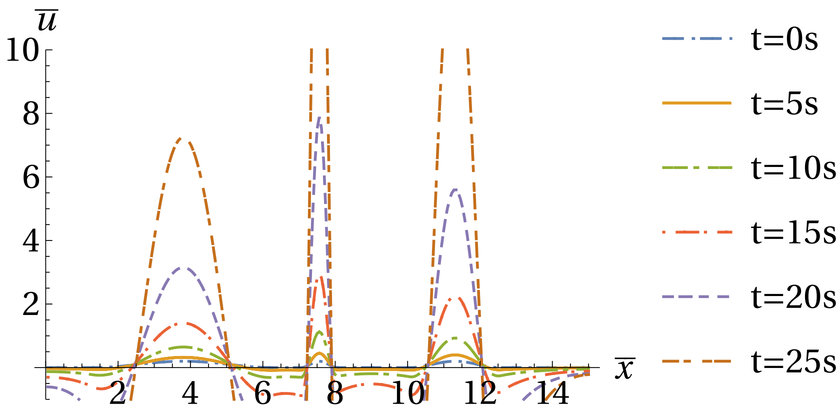

Figure 4.12 – Evolution of the different wavelength cosine perturbations. Faster strain localization is observed for the smallest wavelength.

4.4.1.3 Centered Gaussian initial condition

In Figure 4.13 we present the behavior of the string after a gaussian perturbation of the initial conditions -application of initial gaussian displacement conditions centered at the middle node of the discretized domain. In the strain softening case M2, we notice that the localization of the deformation is contained into a narrow band of finite length, dependent on the width of the initial perturbation as shown on the right of Figure 4.13.

We emphasize, that the lower bound of localization is a result of the mesh discretization. Further increase of the mesh will lead to narrower bands as expected by theory mesh dependency. In Figure 4.14 we compare among the perturbation profiles at different times for Gaussian perturbations of varying width. As in the previous case, the narrowest perturbation localizes the fastest.

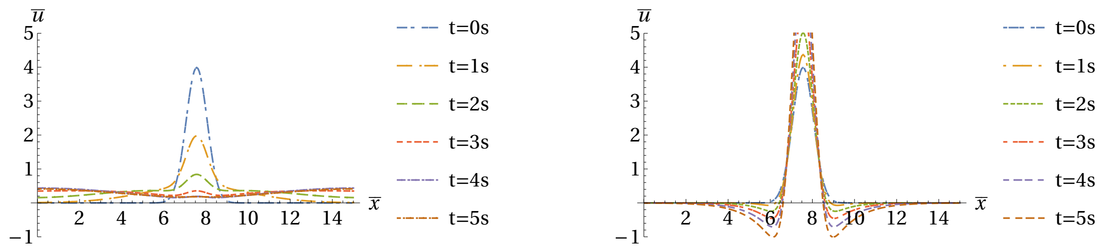

Figure 4.13 – Evolution of the Gaussian perturbation at different times. Left: strain hardening material case M1. On the right: strain softening material case M2.

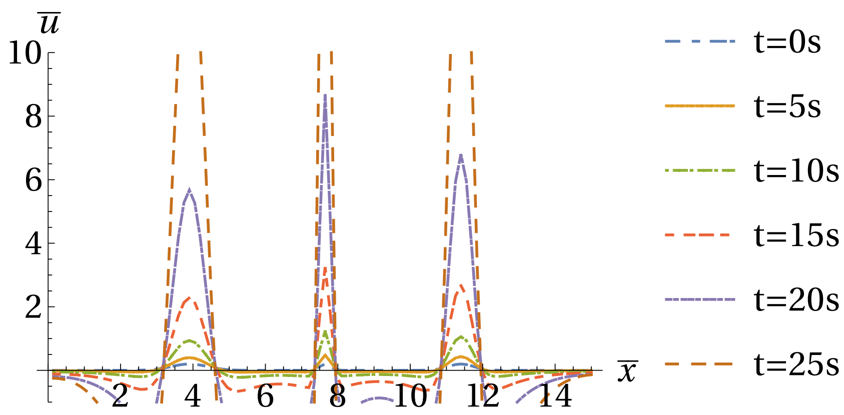

Figure 4.14 – Evolution of different Gaussian perturbations varying in their width. Faster strain localization is observed for the smallest wavelength.

4.4.2 Fully non-linear problem

In order to model the effect of viscous regularization on the strain localization and possible mesh dependence in fully nonlinear cases without neglecting the effect of unloading, a series of dynamic numerical analyses was performed using the finite element analysis program ABAQUS (Smith, 2009). The fully implicit Newmark scheme was used. The parameters used for the Newmark scheme correspond to the trapezoidal rule ($\alpha = 0, \ \beta = \frac{1}{4}, \ \gamma = \frac{1}{2}$) in order to avoid numerical damping.

The use of a User Material Subroutine (UMAT) was favored in order to incorporate the Perzyna elasto-viscoplastic constitutive material law into ABAQUS. The material parameters leading to mesh independent solution were taken from de Borst and Duretz, 2020, see Table 4.2. These values are quite low for real physical applications, but they are used following de Borst and Duretz, 2020 in order to allow direct comparisons. Configuration D1 corresponds to a set of material parameters that seems to lead to regularization

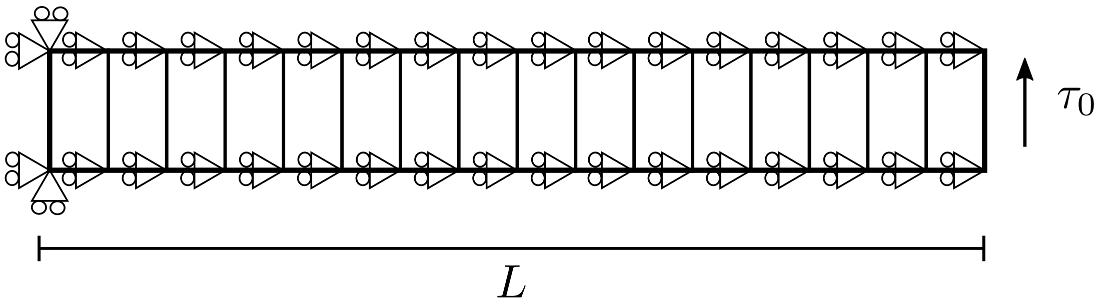

Figure 4.15 – 2D model of a layer subjected to shear.

of strain localization and therefore to mesh independent results. However, as it will be shown, this is not always the case. Configuration D2 corresponds to a set of parameters leading to strain localization and ,therefore, to mesh dependent results. Care was taken to remove additional viscosity from the analysis except for the one strictly prescribed by the material. The analyses were performed using 2D solid, reduced integration elements CPE4R.

analyses	D1	D2	
mesh independence	Yes	No	Units
ρ	1250	1250	$\frac{kg}{m^3}$
G	20000	20000	Pa
h	-200	-1000	Pa
c	20	20	Pa
$\eta^{vp} = \frac{g}{F_0}$	50	25	s

Table 4.2 – Material parameters used for the ABAQUS numerical analyses. The first set of parameters is taken from de Borst and Duretz, 2020.

We study the pure shear of a 1D layer of length L (see Figure 4.15). This is an example used in the available literature de Borst and Duretz, 2020; W. Wang et al., 1996; W. Wang et al., 1997 and, therefore, we can compare directly the observed behavior in our analyses to the one mentioned by other researchers. In order to avoid bending, we block displacements along the length of the model. A shear traction $\tau_0 = 14$ Pa is applied instantaneously on top of the model and it propagates towards the fixed end at the base of the layer. We extract our results after the pulse has returned to the free end of the model. For the duration of the analysis the time increment is kept smaller than $\Delta t = 0.001$ s, which is smaller than the time Δ_{CFL} needed for the elastic wave to traverse the smallest element dimension of the mesh as specified by the Courant-Friedrichs-Lewy (CFL) crite-

analyses (D1, D2) element number	Δt [s]
25	0.001
50	0.001
100	0.001
200	0.001
400	0.0002
800	0.0002

Table 4.3 – Time increment Δt measured in seconds, used for the ABAQUS numerical analyses, such that the CFL yield criterion is satisfied for each mesh discretization.

rion. Considering the length of the model $L = 1$ m, and the material parameters of Table 4.2 leading to the elastic shear wave velocity $c_g = \sqrt{\frac{G}{\rho}} = 4\ \frac{m}{s}$, for a mesh discretization of 200 elements, we obtain: $\Delta t_{\mathrm{CFL}} = \frac{1}{200*4} = 0.00125$ s. The time increment selected for all analyses is given in Table 4.3.

To investigate whether an analysis is mesh dependent or not we plot the profiles over the length of the model of the engineering total shear strain γ_{12} and shear plastic strain rate $\dot{\gamma}^p_{12}$ for different number of elements. Results are given at the end of the analysis for time $t = 0.5$ s.

From Figure 4.16, we establish that the solution obtained with the parameters of D1 de Borst and Duretz, 2020 is mesh independent as the total strain γ_{12} and the plastic shear strain rate $\dot{\gamma}^p_{12}$ profiles are spread over the model length and converge upon mesh refinement. From the analysis of de Borst and Duretz, 2020 we can extract the so called "material length scale" of the problem, which is equal to $l = \frac{2\eta^{vp}c}{\sqrt{\rho G}} = 0.4$ m, (based on a yield function and Perzyna material law of the form $F = \tau_{12} - c - h\gamma^p_{12}$, $\dot{\gamma}^p_{12} = \dot{\lambda} = \frac{F}{\eta^{vp}c}$ respectively). This is in close agreement with the total strain and plastic strain profiles we present in Figures 4.16. It should be noted, however, that the above relation of de Borst and Duretz, 2020 does not take into account the softening slope of the material. To this end the relation available in W. M. Wang et al., 1996 can be used instead.

However, for the same material parameters of configuration D1 but for L=10 m the response of the model is completely different. We present the profiles of total shear strain and normalized plastic shear strain $\gamma_{12}, \dot{\bar{\gamma}}^p_{12}$ in Figure 4.17. The results are taken at time

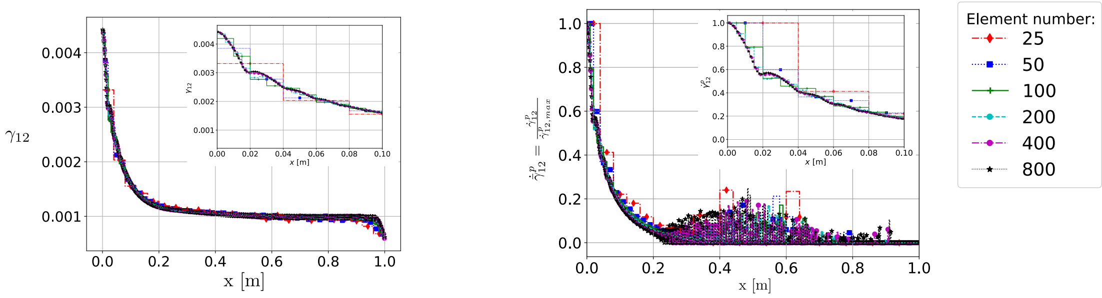

Figure 4.16 – On the left: Total shear strain γ_{12} profiles at the end of the analysis for different mesh discretization of the model for the material set D1. On the right: Normalized plastic shear strain rate, $\bar{\dot{\gamma}}^p_{12}$, profiles with respect to the maximum plastic shear strain rate over the model, $\dot{\gamma}^p_{12,max}$, at the end of the analysis for different mesh discretization, for the material parameters set D1. The response converges to a mesh independent solution as the number of elements increases. The results agree well with the material length defined by de Borst and Duretz, 2020. In both plots a detail near the region of interest 0.1 m is plotted. The response was plotted without averaging between the mesh nodes (i.e. the stress computed at the Gauss points is shown).

$t = 4.0$ s after the stress pulse is reflected and has passed the middle of the bar for a second time. To maintain a constant mesh density near the base of the cantilever, where the highest strain gradients are observed, we apply the same uniform mesh as in the analyses of 1 m, in the 1 m region close to the cantilever support. We vary then the mesh in the rest of the cantilever by progressively increasing the element size to reduce calculation cost. Again the time increment of the analyses is kept smaller than the one specified by the CFL criterion for the smallest elements in the mesh (see Table 4.3). We notice that strain and plastic strain localize on one element and the solution does not show any signs of converging upon mesh refinement. The profiles show narrower localization for finer discretizations as expected by the theoretical analysis in section 4.3.

As we discuss later in section 4.4.3, we change the specimen's length such that the characteristic growth time of the perturbation $T^\star$ is smaller than the time the stress wave takes to complete a round trip along the specimen's height. Thus the localization can grow sufficiently to be noticeable in the results. In section 4.3.3, we define the characteristic growth time $T^\star$ as the inverse of the pole frequency $\bar{\omega}^{P1}$, found in section 4.3. Therefore, according to the above results we can conclude that the analyses with the material set parameters D1 constitute a counterexample, about the beneficial role of viscous regularization in strain localization and mesh dependency. We emphasize here that the only thing that changed in the analysis is the length of the specimen from 1 m to 10 m.

Finally, we present in Figure 4.18 another set of material parameters (see Table 4.2, D2) that lead again to a mesh dependent behavior. Again we change the specimen's material parameters such that the analysis time is larger than the characteristic growth time ($T^{\star}$) of the perturbation, in order for the localization instability to grow sufficiently. The results are taken at time $t = 0.36$ s after the pulse of initial stress is reflected and has passed the middle of the bar for a second time. Mesh dependence is again observed. Thus we have shown with two different counter examples (increase of the specimen's length and change of the material parameters) that viscous regularization does not lead to mesh independent results.

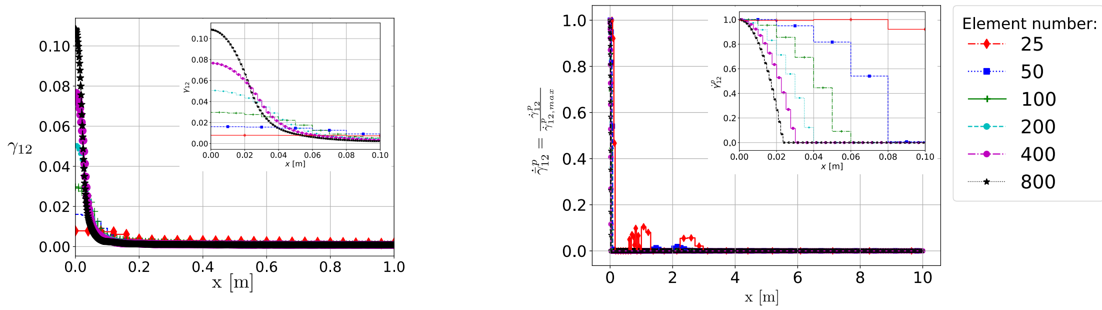

Figure 4.17 – On the left: Total shear strain γ_{12} profiles at time equal to 4s for different mesh discretizations of the model for the material set D1 (increased length to 10 m). Mesh dependence of the solution is observed. On the right: Normalized plastic shear strain rate, $\dot{\bar{\gamma}}^{p}_{12}$, profiles with respect to the maximum plastic shear strain rate over the model, $\dot{\gamma}^{p}_{12,max}$, at time t equal to 4 s for different mesh discretizations, for the material set D1 (increased length to 10 m). The response localizes to a mesh dependent solution as the number of elements increases. In both plots a detail near the region of interest 0.1 m from the support is plotted. The response was plotted without averaging between the mesh nodes (i.e total strain and plastic strain rate are computed at the Gauss points).

4.4.3 Discussion on the conditions for observing strain localization and mesh dependency

The difference observed in localization behavior of the analyses can quantitatively be explained with the use of the theoretical findings of section 4.3. For the material parameters of the configuration D1 the position of the pole lies in $\bar{\omega}^{P1} = 0.2$ s^{-1}, (see also equation

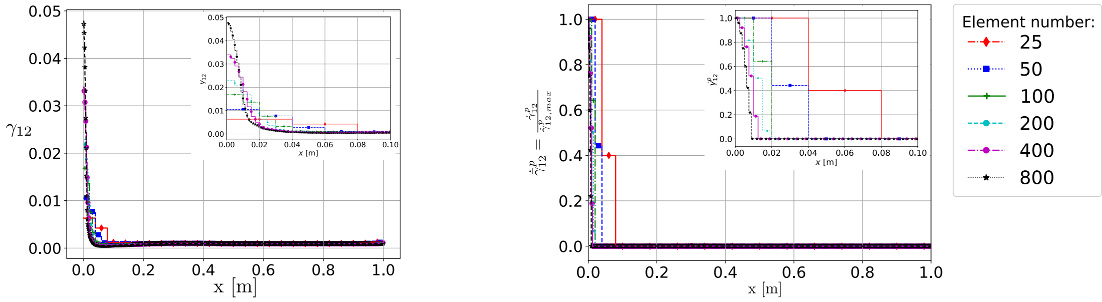

Figure 4.18 – On the left: Total shear strain γ_{12} profiles at time equal to 0.36s for different mesh discretization of the model for the material set D2. Mesh dependence of the solution is observed. On the right: Normalized plastic shear strain rate, $\bar{\dot{\gamma}}^{p}_{12}$, profiles with respect to the maximum plastic shear strain rate over the model, $\dot{\gamma}^{p}_{12,max}$, at time t equal to 0.36 s for different mesh discretizations, for the material set D2. The response localizes to a mesh dependent solution as the number of elements increases. In both plots a detail near the region of interest 0.1 m from the edge of the support is plotted. The response was plotted without averaging between the mesh nodes (i.e total strain and plastic strain rate are computed at the Gauss points).

(4.22), Figure 4.5 and section 4.4.1). This corresponds to a characteristic time for the perturbation to grow $T^{\star} = 5$ s. This is much larger than the time of 0.5 s which is required for reaching steady state when $L = 1$ m. Consequently, strain localization on a mathematical plane and, therefore, mesh dependency in numerical analyses cannot appear because they don't have enough time to be noticeable. In our opinion this is why mesh dependency was not observed in previous works.

If we keep the material parameters the same and increase the length of the specimen we can increase the duration of the simulation without changing the dynamic character of the analysis. We provide, therefore, time to the increasing perturbation to grow. This is precisely what happens when $L = 10$ m. In this case the analysis time for the pulse to return at the free end of the for the 1D layer is 5 s, as a result strain localization has enough time to grow and appear in the numerical results, see Figure 4.17.

Another way for observing mesh dependency is by changing the material parameters instead of the length of the specimen. The parameter set D2 corresponds to a characteristic frequency increase $\bar{\omega}^{P1}$ to the value of 2 s^{-1}, leading to a characteristic time of 0.5 s for the perturbation to grow. This is equal to the analysis time the shear pulse takes to make a full trip back and forth for the 1D layer of length 1 m. Therefore, in case D2, localization has more than enough time to develop and becomes visible before the system reaches its steady state (end of transient regime), see Figure 4.18.

Summarizing, comparing the total time of the dynamic analysis $t^\star$ and the characteristic growth time of the perturbation $T^\star$, taken from calculating the inverse of the characteristic frequency $T^\star = \frac{1}{\bar{\omega}^{P1}}$, we have shown that viscoplasticity will lead to localization on the mathematical plane when $t^\star > T^\star$. In the dynamic analyses localization on a mathematical plane is progressive. Therefore, only conclusions about the necessary time needed for the localization mode to grow can be drawn.

According to our calculations, we have shown that viscoplasticity does not regularize the problem irrespective of any considerations for the magnitude of strain softening $h < 0$ and strain rate hardening $g > 0$ moduli. In other words based on our theoretical developments, and the counter-examples presented in this section, viscoplasticity does not regularize strain localization neither does it remedy mesh dependency. Nevertheless, viscoplasticity slows down the growth of the underlying instabilities and, therefore, the occurrence of mesh dependency

4.5 Key points

In this chapter we investigated the regularization properties of elasto-viscoplasticity regarding strain localization and mesh dependency under the presence of inertia. Even though for quasi-static cases it is well-known that elasto-viscoplasticity of Perzyna or consistency type do not regularize strain localization (Needleman, 1988; Sluys and de Borst, 1992) in the dynamical case the situation was not clear.

Our approach is both theoretical and numerical. After deriving the equilibrium equation of the model under strain-softening ($h < 0$), strain-rate hardening ($g > 0$) elasto-viscoplasticity, we study the Lyapunov stability of states of uniform/homogeneous deformation. In order to avoid unnecessary complexity we focus on a 1D shearing example. Our mathematical analysis differs from previous ones (see de Borst and Duretz, 2020; Needleman, 1988; Sluys and de Borst, 1992; W. Wang et al., 1997) by considering the frequency $\bar{\omega}$ to be a complex number in addition to the complex wavenumber $\bar{k}$. This is an important point for investigating the stability of the homogeneous, reference state as it enables the study of perturbations that can grow with time (see also Lemaitre et al., 2020; Rice, 1976). It is also naturally justified by Lyapunov stability analyses presented in chapters 2 and 3.

Next, we proceed in finding the dispersion relationship between the complex wave number $\bar{k}$ and the complex frequency $\bar{\omega}$ for an arbitrary perturbation. The dispersion equation presents a pole, which is responsible for strain localization on a mathematical plane and thus for mesh dependency. More specifically, the wavenumber becomes infinite, $\bar{k}_r \to \infty$, and the wavelength, $\bar{\lambda} \to 0$, for strain-softening, strain-rate hardening, which means that localization on a mathematical plane is indeed possible in this system (see section 4.3.4). We have also made an extensive discussion about the possibility of traveling waves in the medium (see section 4.3.4) and their relation to strain localization and wave attenuation. Several qualitative observations of the poles of the dispersion equation are provided in section 4.3.4. The analysis is completed by some additional observations about the behavior of propagating sinusoidal monochromatic pulses and their relation with strain localization and phase c_r and amplitude c_i velocities (see Appendix C.1).

We juxtapose our theoretical findings with 1D numerical analyses of an infinite layer. In particular, in section 4.4.1, we investigate the effects of the perturbation mode on the localization mode. The perturbation is introduced in different shapes via various initial conditions. The theoretical relationship between the width of the perturbation and its rate of increase is confirmed. We also confirm that the smallest perturbations propagate the fastest leading to strain localization and mesh dependency. Based on these results we conclude that the elasto-viscoplastic model with strain softening and in the presence of inertia effects is unable to restrict the classical Cauchy continuum from localizing on a mathematical plane.

However, our analysis up to this stage, is based on a linearized version of the problem that does not take unloading into consideration. For this purpose, we perform fully nonlinear, dynamic numerical analyses using the ABAQUS commercial Finite Element software (Smith, 2009) with a strain-softening, strain-rate hardening, Perzyna elasto-viscoplastic user material (UMAT). An implicit Newmark scheme was employed. Special attention was given to avoid any artificial numerical damping in order to guarantee that the right partial differential equations are solved. The results are consistent with the theoretical findings of sections 4.2 and 4.3 and the numerical results of section 4.4.1 and show that mesh dependent solutions are indeed possible. It is worth noticing that for given material parameters the duration of the excitation has to be long enough in order to allow the instability to grow enough and be visible before the system reaches a steady state. This is why strain localization was not identified in previous works.

Our theoretical analyses show that viscoplasticity and inertia do not regularize strain localization and mesh dependency, irrespective of the magnitude of strain softening and strain rate hardening. These results can be important for any computational method in the analysis and design of engineering products and systems in a vast variety of applications in the fields of solid mechanics, dynamics, biomechanics and geomechanics. Our numerical analyses confirm the theoretical findings and provide counter-examples showing that viscosity and inertia do not regularize strain localization and mesh dependency.

Based on the results of this chapter, we conclude that the only way to obtain reliable information from numerical analyses, where strain softening is a key factor of the model is to abandon the Cauchy continuum. To this end, in the next chapters we will choose the Cosserat micromorphic continuum. More specifically, in chapter 5, which contains the main findings of this thesis, we will use the Cosserat micromorphic continuum for simulating the role of the microstructure during the shearimg of a mature fault gouge, where thremal pressurization is the only weakening mechanism introducing apparent strain softening in our model.

Chapter 5

Numerical investigation of fault friction under thermal pressurization during large coseismic slip

Summary

In this chapter, we study the role of thermal pressurization in the frictional response of a fault under large coseismic slip. We investigate the role of the seismic slip velocity, mixture compressibility, characteristic grain size and viscosity parameter in the frictional response of the coupled Thermo-Hydro Mechanical problem, taking into account the fault's microstructure. Starting from the mass, energy and momentum balance for Cosserat continua we derive the equations of our model, which is closed using perfect plasticity and Perzyna viscoplasticity. We investigate both the rate independent as well as the rate dependent frictional response and compare with existing models found in literature, namely the rate and state friction law (Dieterich, 1992,Ruina, 1983b). We show that our model is capable of predicting strain rate hardening and velocity softening without the assumption of a state variable. We observe traveling instabilities inside the layer that lead to oscillations in the fault's frictional response like in the case of Portevin Le Chatelier (PLC) effect. This behavior is not captured by existing numerical analyses presented in Rattez, Stefanou, and Sulem (2018), Rattez, Stefanou, Sulem, Veveakis, et al. (2018a, 2018b) and go beyond the established models of uniform shear (Lachenbruch, 1980b) and shear on a mathematical plane (Rice, 2006b), which predict a strictly monotonous behavior during shearing. Experimental analyses, which have managed to insulate thermal pressurization from other weakening mechanisms (Badt et al., 2020), corroborate our numerical results.

5.1 Introduction

In this chapter we focus on the role of thermal pressurization as the main culprit behind frictional stress drop (apparent strain softening). We do so by considering the energy, mass moment, angular moment balance and Thermo-Hydro-Mechanical (THM) couplings, that account for the friction drop during coseismic slip (Rattez, Stefanou, and Sulem, 2018; Rattez, Stefanou, Sulem, Veveakis, et al., 2018b). This problem was first analyzed in Lachenbruch, 1980b using a classical Cauchy continuum in the case of homogeneous deformation inside the PSZ. However, the stability of the proposed homogeneous solution is not guaranteed and growing perturbations of the plastic strain field are possible due to the apparent softening introduced to the model from thermal pressurization. More specifically, we show in chapter 3 that, the general solution of a homogeneous deformation in the case of apparent softening under THM couplings is unstable. Furthermore, the solution is shown to localize on a mathematical plane of zero thickness. This leads to mesh dependent results in the case of finite element analyses.

Rice (2006a), expanding on the solution of Mase and Smith (1987), presented a solution to the above problem for a strain localization profile concentrated on a plane of zero thickness taking into account the mass and energy balance equations for the THM couplings. It was later shown by Rice et al. (2014b) and platt2014stability through the use of a strain rate hardening friction law that the solution for a localization profile of finite thickness lies between the two solutions tending to the solution of localization on a mathematical plane as shear velocity $\dot{\delta}$ (apparent softening) and seismic slip displacement δ increases.

Strain regularization directly affects the width of the PSZ, where the majority of the stored elastic and potential energies of the fault dissipate, directly affecting the energy budget of the earthquake phenomenon. Failure in avoiding strain localization on a mathematical plane leads to mesh dependent results and therefore wrong estimations of the dissipated energy. In the general case of a two way coupling in the system of balance equations, introduction of strain rate hardening to the apparent strain softening problem of thermal pressurization has been shown to not regularize the problem of strain localization (see chapter 3). Another way of regularizing the problem is taking into account the microstructure of the material in the fault gauge (Muhlhaus & Vardoulakis, 1988; I.

Vardoulakis, 2018)). This can be done through the modeling of the PSZ with a higher order micromorphic continuum (see Forest, Pradel, et al., 2001; Germain, 1973, among others). One such continuum is the Cosserat continuum, that introduces characteristic lengths to the problem thus avoiding strain localization on a mathematical plane. In the work of Rattez, Stefanou, and Sulem, 2018; Rattez, Stefanou, Sulem, Veveakis, et al., 2018b the influence of the Cosserat radius and THM couplings in the strain localization width of the PSZ was investigated with the use of linear stability analyses and nonlinear finite element analyses. The nonlinear finite element analyses have shown that apparent softening is increasing while the localization width is decreasing, as the seismic slip velocity increases. However, the investigated slip distance in these analyses was very limited, and only a rate independent constitutive law was used.

In this chapter we expand on the above mentioned works by investigating the role of seismic slip velocity in the apparent frictional softening and the formation of shear bands (PSZ) inside a fault that is subjected to large coseismic slip observed in earthquakes. Moreover, we investigate both the rate independent and rate dependent cases. In agreement with Platt et al. (2014a), Rattez, Stefanou, and Sulem (2018), Rattez, Stefanou, Sulem, Veveakis, et al. (2018b), Rice et al. (2014a), the PSZ is modeled together with THM couplings to illustrate the role of thermal pressurization in the evolution of the fault's frictional response.

Large displacements were taken into account for the analyses presented in this chapter since the seismic slip is three (3) orders of magnitude larger that the dimensions of the PSZ. Therefore, an adaptive Lagrangian Eulerian method (ALE) was used in order to apply large displacements. We find that after sufficient slip δ has occurred, the PSZ tends to regain part of its strength. The percentage of the regained strength is dependent on the fault's slip velocity $\dot{\delta}$ as well as the height of the PSZ. The increase of friction in the later parts of the analysis is attributed to the existence of a traveling instability inside the PSZ, which indicates the existence of a limit cycle. The analyses agree qualitatively with the recent experimental results ot Badt et al. (2020) and can capture important aspects of the rate and state model, namely strain rate hardening and velocity weakening.

This chapter is structured as follows. In section 5.2 we proceed with the formulation of the shear band model subjected to large coseismic slip (~ 1 m). In section 5.3 we elaborate further on the effect of the seismic slip velocity on the shear strength of the fault as well as the localization profiles of the principal slip zone. From the non-linear analyses performed, we monitor the evolution of the solution after the onset of bifurcation from the homogeneous displacement field. We notice therefore, a traveling instability inside the medium, which is connected with the appearance of a limit cycle (Strogatz, 2000) in the later stages of the analysis. This limit cycle is responsible for the oscillatory behavior of the fields inside the shear band. This behavior naturally enhances the frequency content of the near fault earthquake spectra (see Aki, 1967; Brune, 1970; Haskell, 1964; Tsai and Hirth, 2020) since the frictional response is no longer monotonically decreasing. The traveling shear band instability discussed in this chapter is also found in metals when similar thermal diffusion mechanisms are considered (see Hähner et al., 2002; Mazière et al., 2010). We continue our analysis introducing rate dependence in our model through the use of Perzyna type viscoplasticity. This enhances our model with strain rate hardening in the case of velocity stepping, while retaining the strain softening response at later stages of the analyses. These characteristics of the response are similar to the response of a rate and state friction law (see Dieterich, 1992; Rice et al., 2001; Ruina, 1983a), largely adopted in the fault mechanics community, without the need of introducing an additional state variable. Finally, we present a comparison of the numerical results of this chapter with the experimental findings in Badt et al. (2020), where thermal pressurization was studied in the absence of other weakening mechanisms.

5.2 Problem description

5.2.1 The role of the microstructure in strain localization

In this section we summarize the THM equations that govern the behavior of the PSZ taking into account the role of the microstructure. Here we consider the microstructure of the medium to be made of rigid particles with six degrees of freedom inside the medium, three translations u_i and three rotations $\omega_i,\ i = 1, ...3$. The need to switch from a classical Boltzman Cauchy continuum to a Cosserat micromorhic continuum of first order, stems from the beneficial effects of regularization of strain localization. In a strain softening elastoplastic material, such as in the case of geomaterials, it has been proven in both quasistatic and dynamic regimes (I. Vardoulakis, 1996a) that strain localizes in a mathematical plane, thus rendering the solutions derived from numerical analyses mesh dependent, affecting the amount of the calculated dissipated energy (see chapter 3).

Strain regularization of the corresponding elasto-plastic strain softening medium is of paramount importance. Several researchers have tried to regularize the above problem with the introduction of viscosity effects (see Needleman, 1988; W. Wang et al., 1997, among others), however, numerical analyses in chapters 3, 4 suggest that viscous regularization is not capable of regularizing the problem neither in quasi-static or dynamic conditions. Therefore, the only other way of regularizing the problem without postulating an ad-hoc material law is with the use of higher order micromorphic continua such as the Cosserat continuum, which account for the size of the microstructure (see de Borst & Sluys, 1991; Forest & Sievert, 2003; Forest, Boubidi, et al., 2001; Forest, Pradel, et al., 2001; Muhlhaus & Vardoulakis, 1988; I. Vardoulakis, 2018).

5.2.1.1 Cosserat kinematics

We present here, in a more general formulation of the Cosserat continuum kinematics we introduced in chapter 3. We consider the kinematic field of the deformation tensor γ_{ij}. We define its symmetric part $\gamma_{(ij)}$ as the macroscopic strain ε_{ij} while its antisymmetric part $\gamma_{[ij]}$ is the difference between macroscopic rotation Ω_{ij} and the microscopic rotation tensor ω_{ij}. We also take into account the gradient of the microscopic rotation tensor κ_{ij}.

$$\gamma_{ij} = \gamma_{(ij)} + \gamma_{[ij]} = u_{i,j} - \omega_{ij} = u_{i,j} + \epsilon_{ijk}\omega_k, \tag{5.1}$$

$$\gamma_{(ij)} = \varepsilon_{ij} = \frac{1}{2}\left(u'_{i,j} + u'_{j,i}\right), \tag{5.2}$$

$$\gamma_{[ij]} = \frac{1}{2}\left(u'_{i,j} - u'_{j,i}\right) = \frac{1}{2}\left(u_{i,j} - u_{j,i}\right) - \omega_{ij} = \Omega_{ij} - \omega_{ij}, \tag{5.3}$$

$$\kappa_{ij} = \omega_{i,j} \tag{5.4}$$

where ϵ_{ijk} is the Levi-Civita permutation tensor.

5.2.1.2 Linear and angular momentum balance equations

As is the case with Cosserat strains γ_{ij}, the Cosserat stress tensor τ_{ij} is also not symmetric. The gradient of micro rotations introduces also Cosserat moments (also called couple stresses) μ_{ij} to the balance equations. In contrast to Cauchy continua, τ_{ij} can be decomposed into a symmetric, $\tau_{(ij)} = \sigma_{ij}$, and a non-zero antisymmetric $\tau_{[ij]}$ part. The balance equations can then be written as:

$$\tau_{ij,j} - \rho \frac{\partial^2 u_i}{\partial t^2} = 0,$$
$$\mu_{ij,j} - \epsilon_{ijk}\tau_{jk} - \rho I \frac{\partial^2 \omega_i}{\partial t^2} = 0, \tag{5.5}$$

where ρ and I are, respectively, the density and microinertia, which are considered isotropic here.

5.2.2 Energy balance equation

The conservation of energy in a quasi-static transformation, where the material yields producing heat in the form of plastic work, namely dissipation, is expressed, assuming Fourier's law, as:

$$\rho C \left(\frac{\partial T}{\partial t} - c_{th} T_{,ii} \right) = \sigma_{ij}\dot{\epsilon}_{ij} + \tau_{[ij]}\dot{\gamma}_{[ij]} + \mu_{ij}\dot{\kappa}_{ij}, \tag{5.6}$$

where $c_{th} = \frac{k_T}{\rho C}$, k_T are defined as the thermal diffusivity and thermal conductivity of the medium respectively. We neglect the advective derivative, since the porosity of the solid skeleton, χ, of the fault gouge is very small, leading to small fluid velocities resulting from Darcy's law, (see Rattez, Stefanou, Sulem, Veveakis, et al., 2018b, for the full derivation).

5.2.3 Mass balance equation

In the case of porous media as the one discussed here, the medium consists of both a fluid phase and a solid phase (insoluble to the fluid), which we consider to communicate perfectly in whole. Meaning no effects of tortuosity and no distinction between principal and secondary pore fluid network will be taken into account. The two phases communicate with each other by acting forces to one another due to different deformation properties (see Coussy, 2004; Puzrin & Houlsby, 2001; Stefanou et al., 2016). Finally, the local form of the mixture mass balance equation is given according to Rattez, Stefanou, Sulem, Veveakis, et al. (2018b):

$$\frac{\partial p}{\partial t} = c_{hy} p_{,ii} + \frac{\lambda^*}{\beta^*}\frac{\partial T}{\partial t} - \frac{1}{\beta^*}\frac{\partial \epsilon_v}{\partial t}, \tag{5.7}$$

where $c_{hy} = \frac{\chi}{\eta^f \beta^*}$ is the hydraulic diffusivity expressed with the help of the porosity of the solid skeleton χ and the pore fluid viscosity η^f, while $\beta^* = n\beta^f + (1-n)\beta^s$, $\lambda^* = n\lambda^f + (1-n)\lambda^s$ are the mixture's compressibility and expansivity respectively (see I. Vardoulakis, 1986). Finally, $\beta^{(s,f)}$ and $\lambda^{(s,f)}$ are the compressibilities and thermal expansivities per unit volume of the respective fluid and solid phase.

During shearing of a fault, friction at the principal slip zone (PSZ) is responsible for the dissipation of the elastic unloading energy into heat. The plastic work produced that way contributes to the energy equation (5.6). Temperature increase leads to pressure increase according to mass balance equation (5.7). In what follows the Terzaghi theory of effective stress is assumed to hold true.

5.2.4 Cosserat thermo-elastoplasticity

The general constitutive equations in elasticity for a centrosymmetric Cosserat material relating stresses and Cosserat moments to Cosserat strains and curvatures are given by I. Vardoulakis (2018):

$$\begin{aligned} \tau_{ij} &= C^e_{ijkl}\gamma_{kl}, \\ \mu_{ij} &= M^e_{ijkl}\kappa_{kl}. \end{aligned} \tag{5.8}$$

The elastic stiffness tensors C^e_{ijkl}, M^e_{ijkl} are derived from

$$C^e_{ijkl} = \left(K - \frac{2}{3}G\right)\delta_{ij}\delta_{kl} + (G + G_c)\,\delta_{ik}\delta_{jl} + (G - G_c)\,\delta_{il}\delta_{jk}, \tag{5.9}$$

$$M^e_{ijkl} = \left(L - \frac{2}{3}M\right)\delta_{ij}\delta_{kl} + (M + M_c)\,\delta_{ik}\delta_{jl} + (M - M_c)\,\delta_{il}\delta_{jk}. \tag{5.10}$$

We notice that additionally to the elastic moduli used by the Cauchy media (K, G) denoting isotropic compression and shear moduli respectively, four additional constants are added G_c, L, M, M_c referring to the anti-symmetric part of Cosserat deviatoric stresses, the spherical part of Cosserat moments, the symmetric and anti-symmetric deviatoric parts of the Cosserat moments respectively. The rate independent elastoplastic constitutive relations for the coupled THM problem are given as follows:

$$\dot{\tau}_{ij} = C^{ep}_{ijkl}\dot{\gamma}_{kl} + D^{ep}_{ijkl}\dot{\kappa}_{kl} + E^{ep}_{ijkl}\dot{T}\delta_{kl} \tag{5.11}$$

$$\dot{\mu}_{ij} = M^{ep}_{ijkl}\dot{\kappa}_{kl} + L^{ep}_{ijkl}\dot{\gamma}_{kl} + N^{ep}_{ijkl}\dot{T}\delta_{kl}. \tag{5.12}$$

The superscript (^{ep}) denotes the elastoplastic matrices during loading, whose detailed expressions are given in Appendix D.

5.2.5 Large displacements

Since our analyses reach displacements far greater than the 1D model's geometrical dimensions, we need to take into account large changes in the volume of the element along with rotations of the reference frame. Our application involves pure shearing of the layer and therefore, the displacement derivatives with respect to x_1 axes are zero. We notice that the displacement parallel to the x_2 direction is expected to be small. This is because no additional loading will be applied in the vertical direction during shearing, while from the plastic potential we have that for a mature fault the dilatancy angle is very low $\beta \sim 0$ as discussed in Rice, 2006a; J. Sulem and Stefanou, 2016a. The thermal expansion and compressibility coefficients are also very small so that in the observed temperature and pressure range their effects are minimal. Therefore, the deformation tensor F_{ij} can be written in matrix form as:

$$F = \begin{bmatrix} \frac{\partial x_1}{\partial X_1} & \frac{\partial x_1}{\partial X_2} \\ \frac{\partial x_2}{\partial X_1} & \frac{\partial x_2}{\partial X_2} \end{bmatrix} = \begin{bmatrix} 1 + \frac{\partial u_1}{\partial X_1} & \frac{\partial u_1}{\partial X_2} \\ \frac{\partial u_2}{\partial X_1} & 1 + \frac{\partial u_2}{\partial X_2} \end{bmatrix} \approx \begin{bmatrix} 1 & \frac{\partial u_1}{\partial X_2} \\ 0 & 1 \end{bmatrix}, \tag{5.13}$$

where X_i, x_i are the reference and current configuration coordinates, respectively. From the above we establish that $\det F \approx 1$. Therefore no large volume changes are expected to take place during the shearing phase of the analysis. This conclusion is supported also by the numerical findings in which the volumetric strain is adequately small $\epsilon_v < 0.005$. To account for any effects that large displacements may introduce to our model we have also run a series of analyses based on an Arbitrary Lagrangian Eulerian (ALE) method, (see Donea et al., 2004), where at every iteration we update the new mesh position. The change in the mesh is kept at every converged increment otherwise the cumulative change is discarded and the procedure starts anew.

The question of the plastic work due to large rotations of the microstructure can be covered with the help of the ALE approach considering an additive decomposition of the curvature tensor into an elastic and a plastic part. A more general description of the Cosserat continuum in elasto-plasticity under large deformations can be found in Forest and Sievert (2003), Forest (2020a). There, the authors adopt the multiplicative decomposition for the deformation tensor F_{ij} into the elastic and plastic parts $F^e_{ij},\ F^p_{ij}$, while again the additive decomposition for the curvature tensor κ_{ij} is pursued.

5.2.6 Normalized system of equations.

Equations (5.5), (5.6), (5.7) constitute the nonlinear system that describes the behavior of the fault. We define the following dimensionless parameters, $\bar{x} = \frac{x}{\mathrm{H}_0},\ \bar{t} = \frac{t}{t_0}$, $\bar{u}_i = \frac{u_i}{u_0},\ \bar{\tau}_{ij} = \frac{\tau_{ij}}{\tau_0},\ \bar{\mu}_{ij} = \frac{\mu_{ij}}{\mu_0},\ \bar{T} = \frac{T}{T_0},\ \bar{p} = \frac{p}{\tau_0}$, where $\mathrm{H}_0,\ t_0,\ \tau_0,\ \mu_0,\ T_0,\ p_0$ are characteristic length, time, stress, moment, temperature and pressure quantities, respectively. Furthermore, we note that there are specific relations between the characteristic moment $\mu_0,\ \mathrm{H}_0,\ \tau_0$ based on their dimensions i.e. $\mu_0 = \tau_0 \mathrm{H}_0$.

The non-linear, normalized equations of the problem are given then as:

$$
\begin{aligned}
&\bar{\tau}_{ij,j} - I_1 \frac{\partial^2 \bar{u}_i}{\partial \bar{t}^2} = 0,\\
&\bar{\mu}_{ij,j} - \epsilon_{ijk}\bar{\tau}_{jk} - I_2 \frac{\partial^2 \omega_i}{\partial \bar{t}^2} = 0,\\
&\frac{\partial \bar{T}}{\partial \bar{t}} = \frac{c_{th} t_0}{\mathrm{H}_0^2}\frac{\partial^2 \bar{T}}{\partial \bar{x}^2} - \frac{\tau_0}{T_0}\left(\bar{\sigma}_{ij}\dot{\varepsilon}_{ij} + \bar{\tau}_{ij}\dot{\gamma}_{ij} + \bar{\mu}_{ij}\dot{\kappa}_{ij}\right),\\
&\frac{\partial \bar{p}}{\partial t} = \frac{c_{hy} t_0}{\mathrm{H}_0^2}\frac{\partial^2 \bar{p}}{\partial \bar{x}^2} + \frac{\lambda^*}{\beta^*}\frac{T_0}{p_0}\frac{\partial \bar{T}}{\partial \bar{t}} - \frac{1}{\beta^* p_0}\frac{\partial \varepsilon_v}{\partial \bar{t}},
\end{aligned}
\tag{5.14}
$$

where, $I_1 = \rho \frac{u_0 \mathrm{H}_0}{t_0^2 \tau_0}$ and $I_2 = \frac{\rho I}{t_0^2 \tau_0}$. We consider the following characteristic dimensions and their relations, in order to investigate properly the effect of each term in the behavior of the system:

$$
\mathrm{H}_0 = u_0 = R,\ \tau_0 = p_0 = \sigma_n - p^{init},\ T_0 = \frac{(\sigma_n - p^{init})\beta^*}{\lambda^*},\ t_0 = \frac{R}{V}, \tag{5.15}
$$

where R is the Cosserat radius of the continuum particles, $\sigma_n,\ p^{init}$ are the normal stress (constant during the analysis) and the initial pore fluid pressure, respectively, and V is the constant shear velocity applied at the boundaries of the layer. Here we emphasize that different scaling parameters may be chosen for the non dimensionalization of the system. In particular in J. Sulem et al., 2011 the authors chose to scale time with the help of the thermal diffusivity ($t_0 = \frac{R^2}{c_{th}}$).

Another candidate for time non dimensionalization are the characteristic timescales found in the homogeneous shear solution defined by Lachenbruch, 1980b or the shear on a plane defined by Mase and Smith, 1987. These solutions involve parameters such as the diffusivities $c_{th},\ c_{hy}$ in the normalization of time. However, as explained in Platt et al. (2014a), Rice (2006a), Rice et al. (2014a), these quantities can significantly change during shearing of the fault gouge. We will apply here the time scaling chosen in Rice et al., 2014b, $t_0 = \frac{\rho C \mathrm{H}_0}{f\Lambda\dot{\delta}}$. Apart from not containing the diffusion parameters itself, this scaling has the advantage that it keeps the inertia effects independent of the diffusion parameters of the system. Application of this scaling in the system of equations (5.14), indicates the influence of the layer's height in the numerical analyses. We will make use of this later in section 5.3.4. Applying the scaling to the non dimensionalized system of equations (5.14) we obtain:

$$
\begin{aligned}
&\bar{\tau}_{ij,j} - I_1\frac{\partial^2 \bar{u}_i}{\partial \bar{t}^2} = 0,\\
&\bar{\mu}_{ij,j} - \epsilon_{ijk}\bar{\tau}_{jk} - I_2\frac{\partial^2 \omega_i}{\partial \bar{t}^2} = 0,\\
&\frac{\partial \bar{T}}{\partial \bar{t}} = \frac{c_{th}\rho C}{\mathrm{H}_0 f\Lambda\dot{\delta}}\frac{\partial^2 \bar{T}}{\partial \bar{x}^2} - \frac{\tau_0}{T_0}\left(\bar{\sigma}_{ij}\dot{\varepsilon}_{ij} + \bar{\tau}_{ij}\dot{\gamma}_{ij} + \bar{\mu}_{ij}\dot{\kappa}_{ij}\right),\\
&\frac{\partial \bar{p}}{\partial t} = \frac{c_{hy}\rho C}{\mathrm{H}_0 f\Lambda\dot{\delta}}\frac{\partial^2 \bar{p}}{\partial \bar{x}^2} + \frac{\lambda^*}{\beta^*}\frac{T_0}{p_0}\frac{\partial \bar{T}}{\partial \bar{t}} - \frac{1}{\beta^* p_0}\frac{\partial \varepsilon_v}{\partial \bar{t}},
\end{aligned}
\tag{5.16}
$$

where $I_1 = \frac{\rho}{\tau_0}\left(\frac{f\Lambda\dot{\delta}}{\rho C}\right)^2,\ I_2 = \frac{I}{\rho\tau_0}\left(\frac{f\lambda\dot{\delta}}{C\mathrm{H}_0}\right)^2$. We observe that the height of the layer influences the diffusion terms of the system (5.16), and the rotational inertia of the microstructure. Increase of the layer's height H decreases the efficiency of the diffusion terms, further intensifying thermal pressurization.

Platt et al. (2014b), Rice et al. (2014b) investigated the role of inertia in the localization width of the principal slip zone in the constant seismic slip velocity analyses. They concluded that inertia does not significantly affect the width of the localized zone except at the propagation tip where the inertial number is significantly high and the localization profiles widen. Additionally, the role of the microstructure (inertia of the grains) was investigated in the linear perturbation analyses in J. Sulem et al., 2011. It is found that for the in situ observed seismic slip velocities up to ~ 1 m/s, the localization width does not change significantly compared to the case where inertia is neglected.

For the nominal parameter values used in our analysis (see Table 5.2) and a maximum seismic slip velocity $\dot{\delta} = 1$ m/s, using the scaling for time ($t_0 = \frac{R^2}{c_{th}}$), assuming spherical particles of radius R we can deduce the effect of the inertia terms on the above non dimensionalized, non-linear system of partial differential equations,

$$I_1 = \rho\frac{\dot{\delta}^2}{\tau_0} = 1.810^{-5} \ll 1, \text{and } I_2 = \frac{8\pi\rho^2\dot{\delta}^2 R^3}{15\tau_0} = 7.810^{-17} \ll 1 \tag{5.17}$$

For lower values of δ these parameters are even smaller. Therefore we establish that both the inertia of the gouge as well as the inertia of the grains are negligible for the nominal parameters used in this analysis and the corresponding terms can safely be omitted. We note here that this result is independent of the choice between the two proposed scaling alternatives presented in this section.

5.2.7 Linear stability analysis

In what follows we refer to the shearing of a 1D layer under constant shear slip velocity at the boundaries as discussed in Lachenbruch, 1980b; Rice, 2006b. From now on, in order to reduce notation complexity we remove the $(^{-})$ sign from the normalized unknowns. We apply a perturbation $\tilde{\phi}(x_l,t) = [\tilde{\tau}_{ij}(x_l,t),\ \tilde{\mu}_{ij}(x_l,t),\ \tilde{T}(x_l,t),\ \tilde{p}(x_l,t)]$ to the homogeneous solution $\phi^*(t) = [\tau^*_{ij}(t),\ \mu^*_{ij}(x_l,t),\ T^*(t),\ p^*(t)]$. Applying the perturbed solution $\phi^* + \tilde{\phi}$ to the above system of equations we obtain the linearized perturbed system,

$$\tilde{\tau}_{ij,j} = 0,$$

$$\tilde{\mu}_{ij,j} - \epsilon_{ijk}\tilde{\tau}_{jk} = 0, \tag{5.18}$$

$$\frac{\partial \tilde{T}}{\partial t} = \frac{c_{th}t_0}{x_0^2}\tilde{T}_{,ll} - \frac{\tau_0}{T_0}\left(\sigma^*_{ij}\tilde{\epsilon}_{ij} + \tau^*_{[ij]}\tilde{\gamma}_{[ij]} + \mu^*_{ij}\tilde{\kappa}_{ij}\right), \tag{5.19}$$

$$\frac{\partial \tilde{p}}{\partial t} = \frac{c_{hy}t_0}{x_0^2}\tilde{p}_{,ll} + \frac{\lambda^*}{\beta^*}\frac{T_0}{p_0}\frac{\partial \tilde{T}}{\partial t} - \frac{1}{\beta^* p_0}\frac{\partial \tilde{\varepsilon}_v}{\partial t}. \tag{5.20}$$

We note here that we consider only perturbations of the plastic deformation and curvature tensors in order for equation (5.19) to be valid. We inject the constitutive relations of equation (D.1.19) into the linearized system (5.20), expressing the total linearized strains $\tilde{\gamma}_{ij}$ and curvatures $\tilde{\kappa}_{ij}$ with respect to the perturbed displacements $\tilde{u}_i$ and Cosserat rotations $\tilde{\omega}^c_i$ as presented in Rattez, Stefanou, and Sulem, 2018:

$$C^{ep}_{klmn}(\tilde{u}_{m,nl} + \epsilon_{mnq}\tilde{\omega}^c_{q,l}) + E^{ep}_{klmn}\tilde{T}_{,l}\delta_{mn} + D^{ep}_{klmn}\tilde{\omega}^c_{m,nl} - \tilde{p}_{,l}\delta_{kl} = 0, \tag{5.21}$$

$$\begin{aligned} &M^{ep}_{klmn}\tilde{\omega}^c_{m,nq} + L^{ep}_{klmn}(\tilde{u}_{m,nq} + \epsilon_{mnq}\tilde{\omega}^c_{q,l}) - \epsilon_{klm}(C^{ep}_{lmnq}(\tilde{u}_{n,q} + \epsilon_{nqr}\tilde{\omega}^c_r) \\ &+ E^{ep}_{lmnq}\tilde{T}\delta_{nq} + D^{ep}_{lmnq}\tilde{\omega}^c_{n,q} - \tilde{p}\delta_{lm}) = 0, \end{aligned} \tag{5.22}$$

$$\frac{\partial \tilde{T}}{\partial t} = \frac{c_{th}t_0}{x_0^2}\tilde{T}_{,ll} - \frac{\tau_0}{T_0}\left(\tau^*_{ij}(\tilde{u}_{i,j} - \epsilon_{ijk}\tilde{\omega}_k) + \mu^*_{ij}\tilde{\omega}_{i,j}\right), \tag{5.23}$$

$$\frac{\partial \tilde{p}}{\partial t} = \frac{c_{hy}t_0}{x_0^2}\tilde{p}_{,ll} + \frac{\lambda^*}{\beta^*}\frac{T_0}{p_0}\frac{\partial \tilde{T}}{\partial t} - \frac{1}{\beta^* p_0}\frac{\partial \tilde{u}_{k,k}}{\partial t}. \tag{5.24}$$

We note here, that in order to obtain equation (5.23), we neglect the perturbations of the elastic deformation and curvature fields in comparison to their plastic counterparts. We assume shearing under constant shear slip velocity $\dot{\delta}$, and therefore, the layer is sheared under linear in time Dirichlet boundary conditions. Moreover, we assume shearing of the layer under isothermal and drained boundary conditions for the temperature and pressure diffusion equations. We introduce a perturbation $[\tilde{u}_i, \tilde{\omega}_i, \tilde{T}, \tilde{p}] = [u_0, \omega_0, T_0, p_0]\exp(s\bar{t})\exp(ik\bar{x}_j n_j)$, $k = \frac{2\pi}{\lambda}$ that satisfies the boundary conditions therefore $\lambda = \frac{h}{2\pi N}$, where N is an integer satisfying the boundary conditions.

In this chapter we are mainly interested in the shearing of a 1D layer (see Figure 5.1). In this context only the derivatives along the x_2 axis survive, therefore, the above system is reduced as follows:

$$C^{ep}_{2222}\tilde{u}_{2,22} + D^{ep}_{2232}\tilde{\omega}^c_{3,22} + E^{ep}_{2222}\dot{T}_{,2} - \tilde{p}_{,2} = 0, \tag{5.25}$$

$$C^{ep}_{1212}(\tilde{u}_{1,22} + \epsilon_{123}\tilde{\omega}^c_{3,2}) + D^{ep}_{1232}\tilde{\omega}^c_{3,22} = 0, \tag{5.26}$$

$$\begin{aligned} &M^{ep}_{3232}\tilde{\omega}^c_{3,22} + L^{ep}_{3212}(\tilde{u}_{1,22} + \epsilon_{123}\tilde{\omega}^c_{3,2}) + C^{ep}_{2112}(\tilde{u}_{1,2} + \tilde{\omega}^c_3) - C^{ep}_{1221}(\tilde{u}_{2,1} - \tilde{\omega}^c_3) \\ &+ D^{ep}_{2132}\tilde{\omega}^c_{3,2} + D^{ep}_{1232}\tilde{\omega}^c_{3,2} = 0, \end{aligned} \tag{5.27}$$

$$\frac{\partial \tilde{T}}{\partial t} = \frac{c_{th}t_0}{x_0^2}\tilde{T}_{,22} - \frac{\tau_0}{T_0}\left(\tau^*_{21}(-\tilde{\omega}_3) + \tau^*_{12}(\tilde{u}_{2,1} + \tilde{\omega}_3) + \mu^*_{32}\tilde{\omega}_{3,2}\right), \tag{5.28}$$

$$\frac{\partial \tilde{p}}{\partial t} = \frac{c_{hy}t_0}{x_0^2}\tilde{p}_{,22} + \frac{\lambda^*}{\beta^*}\frac{T_0}{p_0}\frac{\partial \tilde{T}}{\partial t} - \frac{1}{\beta^* p_0}\frac{\partial \tilde{u}_{2,2}}{\partial t}. \tag{5.29}$$

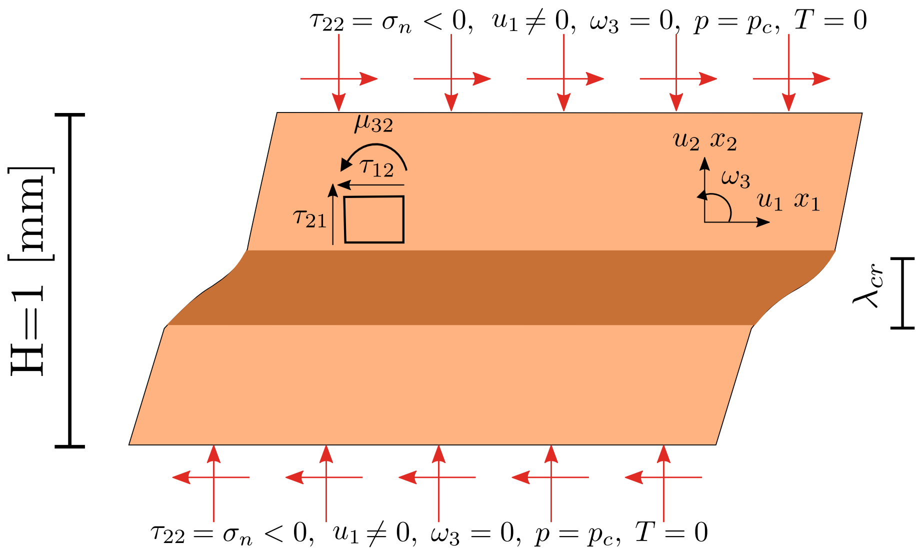

Figure 5.1 – 1D consolidated Cosserat layer under shear.

5.2.8 Traveling instabilities

In this section, we advance beyond the linear stability analyses carried out in Rattez, Stefanou, Sulem, Veveakis, et al. (2018b), as we are mainly concerned with the behavior of the imaginary part of the complex eigenvalues defining the Lyapunov coefficient (s). In the context of Lyapunov stability analysis the eigenvalues with positive real part show that the system is unstable. Moreover, if the eigenvalue in question is complex then the instability is characterized as a flutter instability see (Brauer and Nohel, 1969). In partial differential equations though, the appearence of imaginary parts in s is associated to the nucleation of traveling waves as presented in Platt et al. (2014b), Rice et al. (2014b) and chapter 4. More specifically, by assuming a perturbation $\tilde{\phi}$ of complex frequency $\omega = \omega_r + \omega_i i$ and complex wavenumber $k = k_r + k_i i$,

$$\tilde{\phi} = \phi_0 \exp[i(\omega\bar{t} - k\bar{x})]. \tag{5.30}$$

The Lyapunov coefficient $s = i\omega$ can then be expressed as $s_r = \text{Re}[s] = \text{Re}[i\omega] = -\omega_i$, $s_i = \text{Im}[s] = \text{Im}[i\omega] = i\omega_r$ leading to:

$$\tilde{\phi} = \phi_0 \exp(-\omega_i\bar{t} + k_i\bar{x}) \exp[i(\omega_r\bar{t} - k_r\bar{x})] = \exp(s_r\bar{t} + k_i x) \exp[i(s_i t + k_r\bar{x})]. \tag{5.31}$$

From the above expressed form of the perturbation we observe that in case of a complex Lyapunov coefficient, traveling perturbations appear in the medium, as the second factor or equation (5.31) becomes a sinusoidal.

The existence of the traveling perturbations together with the special kind of drained, isothermal, Dirichlet (essential) boundary conditions of the PDE system leads to reflections of the traveling perturbation inside the fault gouge and may lead to the appearance of a limit cycle. Characterization of the bifurcation leading to the appearance of the limit cycle as a Hopf (subcritical, supercitical) or global bifurcation in this system of 4 PDEs lies outside the scope of this thesis. We note here that the applied boundary conditions are extremely important for the behavior of the instability. In the case of adiabatic undrained boundary conditions the spatial profiles of pressure and temperature do not allow for a reflection of the traveling instability at the boundaries and therefore, the perturbation stations in one of the boundaries of the model.

The existence of a limit cycle, and the traveling instability is a characteristic of the Portevin Le Chatelier effect found in metals (see Hähner et al., 2002; Mazière et al., 2010; W. Wang et al., 1997, among others). In these cases the systems of PDEs in question are kept intentionally small, by two equations namely, the balance law, the diffusion equation and an a priori assumption of the plastic strain rate λ profile see (Hähner et al., 2002). Consequently the identified limit cycle in these works, is attributed to the diffusion mechanisms present in the medium and the inherent coupling between balance and diffusion equations.

The perturbed linearized system depends on time due to the energy and mass balance equations. The Lyapunov exponent is then introduced in the system due to the first derivative of temperature and pressure, indicating that the polynomial characterizing the stability of the system is of second order. In this chapter we are interested in the conditions under which linearized stability analyses provides us with complex roots of positive real part, that indicate a traveling instability as explained above. We note that from the linear stability analysis of the previous system around the solution of homogeneous deformation, such a condition is not possible. This, however, is not guaranteed as one ventures more into the perturbed equilibrium path.

Assuming a correspondence exists between the apparent softening and a mechanical softening parameter, we expect flutter instabilities to be present once the system starts exhibiting a softening behavior. In addition to mechanical softening (if present), in our analyses apparent softening is expected due to the terms of thermal pressurization and the Terzaghi theory of effective stress.

In Figure 5.2 we present the effect of the softening parameter h on the localization length λ_r of the maxima of the real and imaginary parts (s_r, s_i) of the Lyapunov coefficient s. We note that the value of the real part of Lyapunov coefficient s_r is negative for perturbations of zero wavelength, therefore no localization on a mathematical plane can occur, independently of the softening parameter h. This is to be expected in the case of a Cosserat continuum due to the introduction of an internal length. Initially for small values of softening the wavelengths corresponding to the maxima of s_r, s_i to not match. The wavelength corresponding to the growing perturbation exhibits an unbounded positive real part and zero imaginary part for the Lyapunov coefficient. This means that at the initial stages of the analysis the instability is not traveling in the medium. However, as yielding continues and thermal pressurization leads to more pronounced softening, the imaginary part catches up with the real part, meaning that both the maxima of the real and imaginary parts of the Lyapunov coefficient s occur for the same perturbation wavelength. This leads to a traveling instability inside the layer (see Figure 5.2) and section 5.3.

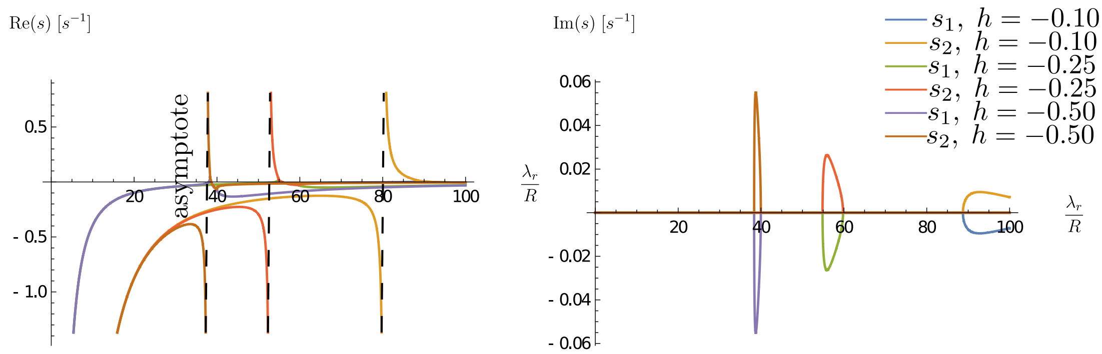

Figure 5.2 – On the left: Real part of the two roots of the characteristic polynomial for different values of the hardening parameter h. There is always a critical wavelength value λ_{cr} greater than zero, for which the Lyapunov exponent tends to infinity. On the right: Imaginary parts of the roots for the same softening values. As softening intensifies, positive real values of s with non zero imaginary part appear on a $\lambda_r \neq 0$, leading to a traveling perturbation of a non zero critical wavelength.

For the value of the softening parameter $h = -0.50$ that produces the traveling perturbation of finite width, we further examine the effect of a non negative imaginary part in the wavenumber $k = k_r + k_i i$. The imaginary part of k is responsible for the change of the perturbation amplitude with space. In a bounded problem such as the one discussed here, its effect is not important as the amplitude will remain bounded with distance. It is of interest, however, to examine whether traveling instabilities are possible in the more general context. For a given value of the softening parameter h and treating k_i as a parameter, the plots of the real and imaginary part of the roots of the characteristic polynomial $s_{1,2}$ are shown in Figure 5.3. In the left part of Figure 5.3, we notice that localization on a mathematical plane is avoided for any k_i, since for $\lambda_r = 0$ the real part of the Lyapunov coefficient s tends to $-\infty$. This is in contrast with viscous regularization, where it was recently shown that strain localization on a mathematical plane is always possible (see chapters 3, 4). This behavior is owed to the internal length introduced in the Cosserat continuum that regularizes effectively strain localization.

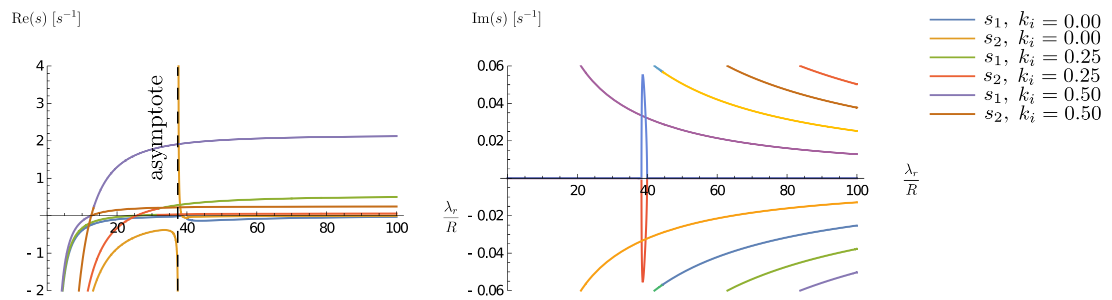

Figure 5.3 – On the left: Real part of the two roots of the characteristic polynomial for different values of the attenuation coefficient k_i. The two roots start negative and eventually they pass to positive values for the real part of s. The wavelength each root changes its sign as well as the maximum value reached are characteristics of the value of k_i. On the right: Imaginary parts of the roots for the same softening values and values of the attenuation coefficient k_i. For $k_i \neq 0$, the magnitude of the imaginary part of the roots Im$[s_1, s_2]$ starts from ∞ when $\lambda_r = 0$ and slowly attenuates. This is in high contrast to the behavior exhibited when $k_i = 0$. The perturbation increasing the fastest is the one lying on $k_i = 0$.

On the right part of Figure 5.3 we notice that the behavior of the imaginary part of the roots s_1, s_2 is symmetric around $k_i = 0$, as expected. Therefore, we focus our attention to values of $k_i > 0$. The roots present a positive real part for a range of values of λ_r (see Figure 5.3). For $k_i \neq 0$ the positive real part is bounded and obtains its maximum value as λ_r tends to ∞. The wavelength value, where the real part of the Lyapunov exponent changes sign from negative to positive, as well as the maximum positive value depend on the value of the parameter k_i (see left part of Figure 5.3). The maximum value of the imaginary part of $s_{1,2}$ is obtained for $\lambda_r \to 0$ and then it slowly attenuates as $\lambda_r \to \infty$. We conclude that traveling perturbations of unbounded increasing amplitude and finite width are possible in the case $(s_r > 0, s_i \neq 0, k_i = 0)$.

5.3 Numerical Analyses

A 1D model of a Cosserat layer was used, where shear displacement was applied to the boundaries of the layer, while rotations were blocked at both ends. Figure 5.1 describes the model in more detail. The layer was discretized using 80 finite elements, with quadratic shape functions for the displacement field u_i and linear shape functions for the rotations ω_i. Reduced integration scheme was used for the displacement field compared to full for the rotation field (see Godio et al., 2016). These element parameters were taken as a result of a mesh convergence investigation of different shape functions and number of Gauss points that was performed in a previous work in order to find the optimal mesh description (see Stathas & Stefanou, 2019a). The mesh characteristics are summarized in Table 5.1. The Cosserat material properties used to describe a mature fault in the seismogenic zone are summarized in Table 5.2, where a relatively high value for the friction coefficient μ has been used with respect to the values provided in Rempel and Rice (2006), Rice (2006a), Rice et al. (2014a) and path averaged values for λ^*, β^* were considered, as proposed in Rice, 2006b; Rice et al., 2014a.

	u_i	ω_i
Element type	Quadratic	Linear
Integration scheme	Reduced	Full
Number of elements	80	

Table 5.1 – Mesh properties of the problem.

To illustrate the role of seismic slip velocity in the post peak behavior of the fault, we apply two different shear velocity-stepping programs to the model at hand. First we implement a three step procedure described in section 5.3.1 which includes, consolidation of the layer to the stresses and pressure at a depth representative of the seismogenic zone (7 km) followed by slow shear of the layer and then by fast shear for a shear slip of 10 mm at each stage. The second program in section 5.3.2 involves initial consolidation and then shear with constant slip velocity, $\dot{\delta}$, ranging from as slow as 0.01 m/s to 1.0 m/s for a total of 100 mm of seismic slip δ.

Parameters	Values	Properties	Parameters	Values	Properties
K	$20.\ 10^3$	MPa	μ	0.5	-
G	$10.\ 10^3$	MPa	β	0	-
G_c	$5.\ 10^3$	MPa	λ^*	$13.45\ 10^{-5}$	$/^o$C
L	10^3	MPa mm^2	β^*	$8.2\ 10^{-5}$	MPa$^-$1
M	1.5	MPa mm^2	ρC	2.8	MPa$/^o$C
M_c	1.5	MPa mm^2	c_{hy}	12.0	mm^2/s^2
R	0.01	mm	c_{th}	1.0	mm^2/s^2
σ_n	200	MPa	α_s	10^{-5}	$/^o$C
p_0	66.67	MPa	χ	$12.\ 10^{-15}$	m^2

Table 5.2 – Material parameters of a mature fault at the seismogenic depth (see Rattez, Stefanou, & Sulem, 2018; Rice, 2006b).

A second series of analyses were also run, where the seismic slip displacement is set to 1 m and the seismic slip velocity to 1 m/s - typical values observed in nature during large coseismic slip. These analyses go far beyond the previous limit of 5 mm presented in Rattez, Stefanou, and Sulem (2018), Rattez, Stefanou, Sulem, Veveakis, et al. (2018a), and allow us to observe new and interesting phenomena. The higher seismic slip displacement, allows us a deeper understanding of the phenomenon of thermal pressurization since it is shown that a traveling instability is formed inside the gouge due to the existence of a limit cycle in later parts of the analysis (see Figure 5.16). This behavior is new compared to previous analyses on the same mechanism of thermal pressurization done with simpler models (see Lachenbruch, 1980b; Rice, 2006b; Rice et al., 2014b) and it resembles behavior specified in other analyses with different physical mechanisms taken into account, such as the comminution of grains and evolution of the microstructure (see Collins-Craft et al., 2020).

Finally, in section 5.3.4, we illustrate here the effect of the boundaries in the traveling velocity v of the PSZ inside the shear band, by considering two different shear bands of height 1 mm and 2 mm respectively subjected to the same seismic slip displacement δ=1 m with seismic slip velocity $\dot{\delta}$=0.5 m/s. We note, based on the scaled system of equations (5.16), that the two configurations described here, differ only in the diffusion terms. Namely, the thicker layer diffuses pressure and temperature slower, exhibiting more pronounced apparent softening due to thermal pressurization.

5.3.1 Shearing of a mature fault under low slip ($\delta = 10$ mm) and velocity stepping

To better understand the effects of the applied shearing rate $\dot{\delta}$ in thermal pressurization and the overall effects of the boundary, as mentioned above, we proceed with the application of a velocity stepping shearing procedure. After consolidation (see Table 5.3), the layer is sheared with varying slip velocity $\dot{\delta}$ in two steps. At each step a target displacement δ of 5 mm at each end is reached for a total of 10 mm at the end of the analysis. The shear velocity $\dot{\delta}$ during the first shear step is 0.01 m/s. For the second (final) step we ran different analyses under different applied constant shear velocity. The range of shear velocity values spans from 0.01 m/s to 1 m/s.

STEP		Slip δ mm	Slip velocity $\dot{\delta}$ m/s
0	Consolidation	-	-
1	Shear	5	0.01
2	Shear	5	0.01 0.1 1.0

Table 5.3 – Loading program for the analyses performed using the three step procedure.

We intent to investigate the effect of the shearing rate on the frictional response of the layer. We investigate the predictions of our model concerning the apparent softening in the layer's frictional response subjected to isothermal (ΔT=0) drained (Δp=0) boundary conditions. In Figure 5.4 we compare the different shear stress τ seismic slip displacement δ responses for the different velocities applied at the final step of the analyses and we show the profiles of strain localization rate $\dot{\gamma}^p$ over the layer's height. We observe that the increase of slip velocity $\dot{\delta}$ has a weakening effect on the $\tau - \delta$ diagram as observed also by Rattez, Stefanou, and Sulem, 2018; Rattez, Stefanou, Sulem, Veveakis, et al., 2018b. This happens due to the fact that a fast increase in the heat production term of equation 5.6 leads to an increase in the thermal pressurization term of equation 5.7, which in turn increases pressure and intensifies weakening due to the application of Terzaghi principle $\sigma^{eff} = \sigma_n + p$, ($p > 0$ water pressure, $\sigma^{eff}, \sigma_n > 0$ in tension). The increase of slip velocity leads also to narrower localization zones, which are in agreement with the steeper post-peak response observed in τ, δ diagrams.

Finally, we investigate the influence of the boundary conditions of pressure and temperature to the behavior of the problem. Their influence to the frictional response is of great importance as they control the effect of diffusion on leading temperature and pressure

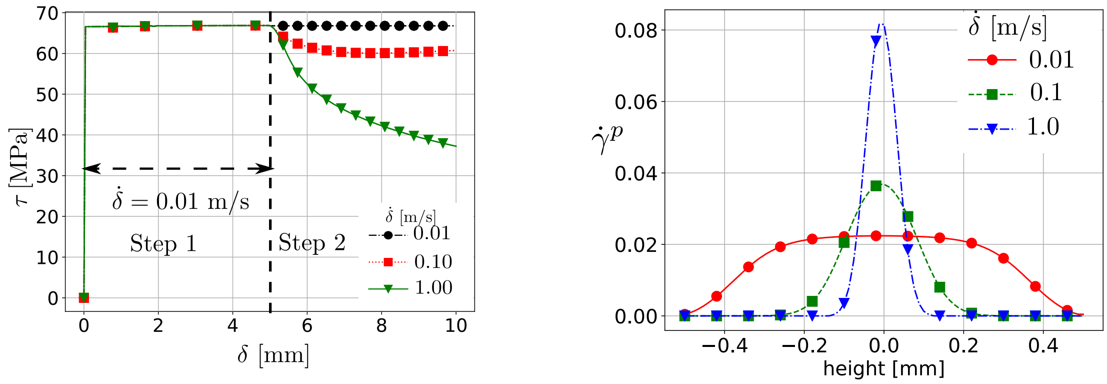

Figure 5.4 – Left: $\tau - \delta$ response of the layer for different slip velocities $\dot{\delta}$ applied (velocity stepping). We observe that as the shearing rate increases, the softening behavior becomes more pronounced as a result of smaller localization widths due to the smaller characteristic diffusion time. Right: Profiles of strain localization rate inside the layer for different slip velocities $\dot{\delta}$ applied at the end of the analysis. Higher shearing velocities correspond to more localized plastic strain rate $\dot{\gamma}^p$ profiles.

increase $(\Delta T, \Delta p)$ away from the localized zone. On the left part of Figure 5.5 we present the curves of $\tau - \delta$, for slip velocity $\dot{\delta}$ at the final step of the analysis of 1 m/s, for Adiabatic-Undrained ($q_T = q_p = 0$), Isothermal-Drained ($\Delta T = \Delta p = 0$), Isothermal-Undrained ($\Delta T = q_p = 0$) and Adiabatic-Drained conditions ($q_T = \Delta p = 0$). We observe that undrained boundary conditions influence the response the most as they tend to follow on the solution of uniform adiabatic undrained shear Lachenbruch, 1980b for small slip velocities $\dot{\delta} = 0.01$ m/s. The difference at the peak strength between drained and undrained conditions has to do with the frequency our algorithm saves the output as well as the time increment used by the analysis (automatic time stepping). Furthermore, on the right of Figure 5.5 we present the plastic strain-rate profiles $\dot{\gamma}^p$ for different boundary conditions applied at the end of the analysis. We observe that for the given seismic slip of 10 mm, localization width is dependent on the seismic slip velocity applied and not on the boundary conditions.

Based on the above results, we conclude that the true response of the fault gouge is very much dependent on the applied boundary conditions. Normally a kind of Robin boundary condition should be employed to better approximate the physical conditions. However, since this interaction between fluxes and essential boundary conditions is not yet sufficiently documented in the existing literature, the isothermal ($\Delta T = 0$), drained ($\Delta p = 0$) boundary conditions are closer to the real conditions due to the highly damaged

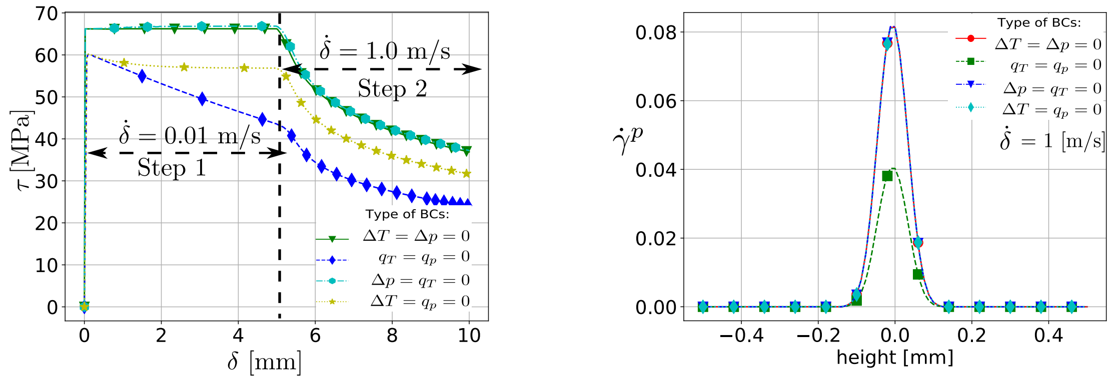

Figure 5.5 – Left: $\tau - \delta$ response of the layer for different boundary conditions applied. An envelope is created between Isothermal drained ($\delta T = \Delta p = 0$) and Adiabatic-Undrained ($q_T = q_p = 0$) conditions. At the slow slip part of the analysis in the case of adiabatic undrained boundary conditions, thermal pressurization is present from the beginning. In this case, the initial stress at the start of the fast shear is lower and thus the stress drop is smaller. Right: Profiles of strain localization rate inside the layer for different boundary conditions. Since Cosserat material parameters and coseismic slip velocity $\dot{\delta}$ remain the same in all cases, the localization width does not change.

regions encapsulating the fault gouge.

The thermal diffusivity of the fault gouge and the surrounding damaged zone (surrounding folliations) presents less variations than the corresponding hydraulic diffusivities. Thermal diffusivity of the fault gouge material is of the same order of magnitude as the diffusivity of the damaged zone (see for instance Tanaka et al., 2007). For the much more crucial hydraulic diffusivity parameter (see Aydin, 2000), the hydraulic diffucivity ratio between the mature fault gouge and the surrounding folliated rock can be shown to differ up to 4 orders of magnitude, with diffusivity of the folliated rock being greater than that of the gouge. Furthermore, according to in situ observations (see Ingebritsen & Manga, 2019) of increased water discharge to aquifiers, the ratio is expected to increase even more during coseismic slip. Therefore, we can estimate the ratios of thermal, r_{th}, and hydraulic, r_{hy}, diffusivities between the fault gouge material and the nearby damaged material:

$$r_{th} = \frac{c_{th}^{rc}}{c_{th}^{fg}} \sim 1, \quad r_{hy} = \frac{c_{hy}^{rc}}{c_{hy}^{fg}} \sim 10^4 \tag{5.32}$$

These parameters, further justify our choice of setting the boundary conditions in the rest of the chapter to isothermal $\Delta T = 0$ drained $\Delta P = 0$.

5.3.2 Shearing of a mature fault under moderate slip ($\delta = 100$ mm), and variable slip velocities

To better illustrate the dependence of the fault behavior to the velocity of seismic slip $\dot{\delta}$, we run a second part of analyses for the case of isothermal drained conditions ($\Delta T = \Delta p = 0$) in which the intermediate part of slow shear velocity has been omitted and the fault model is immediately subjected to fast slip velocity rates after initial consolidation. Furthermore, the target seismic displacement δ has been increased to 100.0 mm. We aim that way to examine in more detail the fault's response under displacement scales commonly observed in nature at variable slip rates. Fast slip rates would correspond to the fault gouge being in the center of the fault rupture area. For the numerical steps of the simulations see Table 5.4

STEP		Height h mm	Slip δ mm	Slip velocity $\dot{\delta}$ m/s
0	Consolidation	1	-	-
1	Shear		100.0	$\{0.01, 0.05, 0.1, 0.25, 0.50, 0.75, 0.90, 1.0\}$
0	Consolidation	1	-	-
1	Shear		1000.0	1.0
0	Consolidation	1	-	-
1	Shear		1000.0	0.5
0	Consolidation	2	-	-
1	Shear		1000.0	0.5

Table 5.4 – Loading program for the analyses performed using the two step procedure.

In Figure 5.6 we present the shear stress τ with seismic slip on top of the layer δ response for the point on top of the layer. We plot the $\tau - \delta$ response for different values of seismic slip velocity. It can be clearly seen from the results that two behaviors are present depending on the shear velocity. If the slip velocity is low, then the layer accommodates the heat produced from the plastic work during yielding of the material and both heat and pressure diffuse efficiently away from the yielding zone, which has a comparatively large localization width l_{loc} as shown in Figure 5.7. As slip velocity increases the post peak softening response is seen in larger parts of the analysis before eventually diffusion dominates and peak shear strength is restored. However, shear strength is only partially restored for the analyses of large shear velocities.

In the left part of Figure 5.6 the response of the layer obtained from the numerical

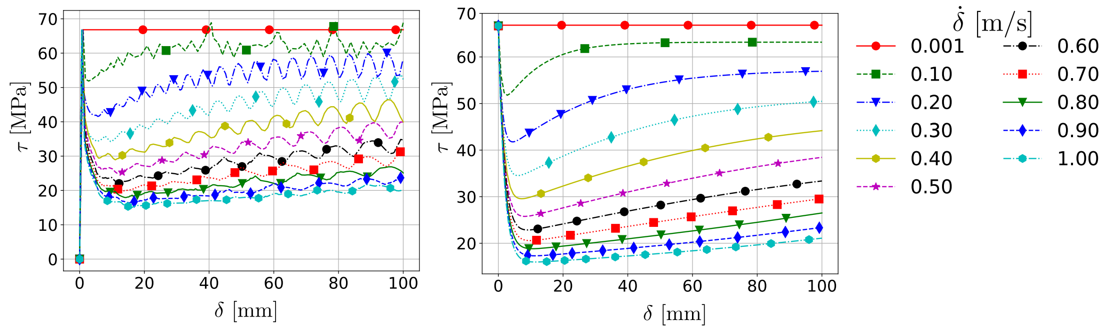

Figure 5.6 – Left: $\tau - \delta$ response of the layer for different velocities. Isothermal, drained boundary conditions $\Delta T = \Delta p = 0$ are applied. Frictional strength regain is observed due to the diffusion at the boundaries. The frictional response presents oscillations due to the traveling plastic strain rate instability. A smaller residual friction value is achieved. Right: Fitted $\tau - \delta$ response of the layer for different velocities. Isothermal, drained boundary conditions $\Delta T = \Delta p = 0$ are applied. All analyses at the start reach the peak strength $\tau = 66.67$ MPa. As slip δ progresses an increase of the residual shear stress τ takes place.

analyses of first row of Table 5.4 is presented. We notice the existence of oscillations in the frictional response for all velocities apart from the very small ($\dot{\delta} = 0.01$ m/s). The oscillations start during the apparent softening branch of the analysis frictional response. They are affected by the boundaries of the model, namely in the case of undrained, adiabatic boundaries the shear band travels to one of the boundaries and then persists at this position, while for isothermal drained conditions an oscillatory response is present.

In the right part of Figure 5.6 we present the $\tau - \delta$ fit of the numerical results. The fit is used to simplify conceptually the results and highlight the main findings of the numerical analyses. The fit contains the initial frictional weakening and subsequent frictional regain due to the diffusion at the boundaries of the model. Furthermore, the effect of the oscillations is highlighted. The fit passes through the middle of the oscillations of the numerical analyses. Thus, we conclude that due to the oscillations, friction is not fully restored to its initial value. There exists a residual value of friction at the later stages of the slip. For the fitted curves $\tau - \delta$, we employ a function composed of an exponential decay and a logistic curve.

$$\tau(\delta, \dot{\delta}) = a(\dot{\delta}) \exp\left[-b(\dot{\delta})\delta\right] + \frac{c(\dot{\delta})}{d(\dot{\delta}) + \exp\left[-f(\dot{\delta})(\delta - g(\dot{\delta}))\right]}, \tag{5.33}$$

where $\alpha(\dot{\delta}),\ b(\dot{\delta}),\ c(\dot{\delta}),\ d(\dot{\delta})$ are the interpolation parameters, dependent on $\dot{\delta}$.

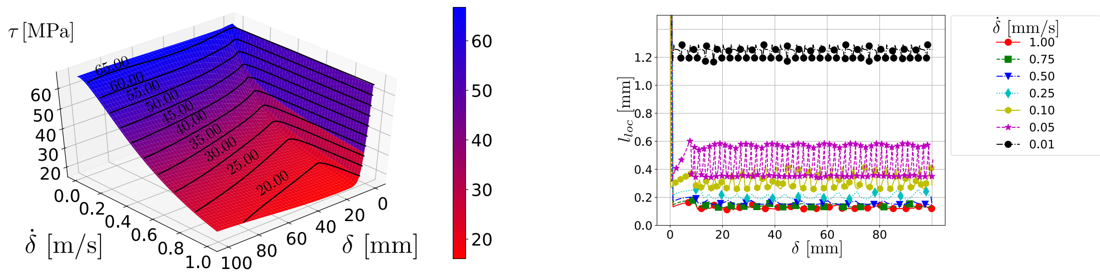

Figure 5.7 – Left: 3D fitted surface of τ with slip distance δ and velocity $\dot{\delta}$. Right: $l_{loc} - \delta$ response of the localization width inside the layer for different boundary shear velocities applied at the boundaries.We notice that the localization width is oscillating for the small to intermediate range of shear velocities $\dot{\delta} = 0.01 - 0.25$ m/s. This is due to the interaction between the diffusion lengths of pressure and temperature.

On the left part of Figure 5.7, we present the frictional surface that corresponds to the fit of the previous paragraph. Through the use of two dimensional interpolation of the results of Figure 5.6, we are able to estimate the frictional response of the fault gouge over a region of low to moderate seismic slips ($\delta = 0 \sim 0.1$ m) and seismic slip velocities ($\dot{\delta} = 0.1 \sim 1$ m/s).

On the right part of Figure 5.7, we present the evolution of the shear band width for the different seismic slip velocities. In order to estimate the localization width in each case a curve according to equation (5.34) described in Rice, 2006b was selected for fitting.

$$
\begin{aligned}
\dot{\gamma}^p =& A + \frac{B}{\sqrt{1\pi}D} \exp\left[-\frac{1}{2}\left(\frac{y-C}{D}\right)^2\right] \\
l_{loc} =& 2\sqrt{2\ln(2)}D
\end{aligned}
\tag{5.34}
$$

It is clear that large velocities lead to narrower localization widths l_{loc}. We observe that for large velocities localization width is not monotonously decreasing, but rather it exhibits some noise as shearing progresses. This goes beyond the results of Rattez, Stefanou, and Sulem (2018), Rattez, Stefanou, Sulem, Veveakis, et al. (2018b), where the localization width was shown to progressively decrease until it remains constant. This behavior has to do with the fact that the instability exhibited here by the material is a traveling wave instability. This can be seen in the $\tau, \bar{\gamma}_{21}$ response, where a periodic increase and loss of strength is observed in the post peak response for all velocities above 0.01 m/s.

This jerky behavior, which is a characteristic of a Portevin Le Chatelier effect can be responsible for higher frequency instabilities during seismic slip and enhance the frequency content of an earthquake event as discussed in Aki, 1967; Brune, 1970; Haskell, 1964; Tsai and Hirth, 2020. The observed behavior is primarily due to the applied isothermal drained boundary conditions. In the case of adiabatic undrained conditions the shear band can be shown to travel towards a boundary, where it is trapped for the duration of the analysis and the results obtained in this case are closer to those derived in the case of uniform shear (Lachenbruch, 1980b).

5.3.3 Shearing of a mature fault for large slip $\delta = 1$ m and co-seismic slip velocity $\dot{\delta} = 1$ m/s.

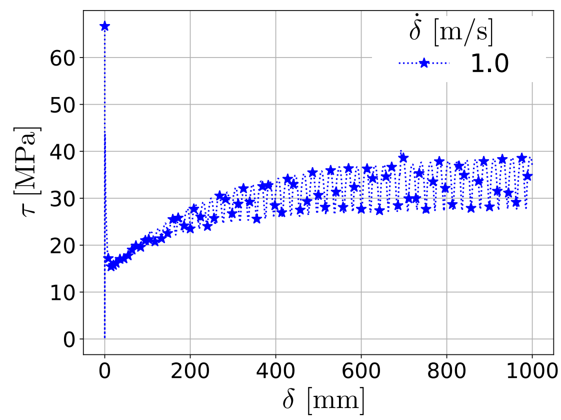

Figure 5.8 – Left: Evolution of τ with slip distance δ. We observe that after sufficient time has passed the oscillations have stabilized in amplitude and frequency partially recovering the layer's initial shear strength. The steady state reached around which the oscillations take place is reached after a slip of 1.0 m. The value of friction at the steady state is a result of the interplay between the rate of work dissipated into heat and the diffusion properties of the fault gouge.

In order for the observed oscillations to fully develop in amplitude for the analyses with high slip rate $\dot{\delta}$ we apply a very large shear displacement. Figure 5.8, presents the τ, δ response for a slip velocity $\dot{\delta}$ of 1 m/s and an applied slip $\delta = 1$ m. As can be seen from the above analysis the shear strength of the layer is eventually oscillating around a new residual strength value, which is smaller than the original peak strength.

Left part of Figure 5.9 shows the profiles of plastic strain rate $\dot{\gamma}^p$ and accumulated plastic strain γ^p at the end of the analysis. It is clear that the shear band travels across the material since the accumulated plastic strain profile is larger in width than the localization width of the instability. This is one major difference compared to small slip rates, which our analyses under large displacements allowed to highlight (see Figure 5.6).

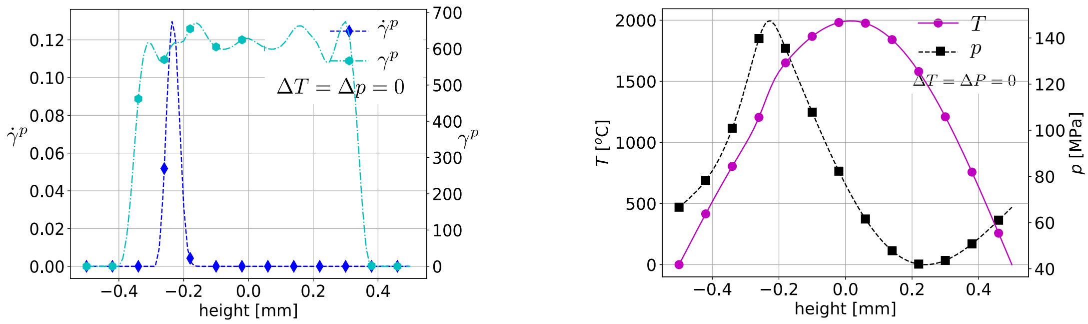

Figure 5.9 – Left: Profiles of shear strain rate and accumulated plastic shear strain $\dot{\gamma}^p, \gamma^p$ at the end of the analysis for applied slip $\delta = 1$ m and slip rate $\dot{\delta}$ =1 m/s. Since the two profiles differ, we conclude that the localization oscillates inside the layer. Localization does not travel the whole of the layer due to the boundary conditions applied. Right: Profiles of pressure and temperature p, T at the end of the analysis for applied slip $\delta = 1$ m and slip rate $\dot{\delta}$ =1 m/s. Diffusion at the boundaries leads to extremely high values of temperature ΔT =2000 ^{o}C.

Finally, the right part of Figure 5.9 presents the profiles of temperature T and pressure p at the end of the analysis. We observe that the temperature reached is much higher than the one required for the onset of melting for the minerals present in the seismogenic zone Rice, 2006b. This has to do with the relatively high friction coefficient μ used in our analyses. A moderate value of μ=0.25 would roughly halve the temperature observed. This does not preclude though other mechanisms, such as chemical effects Alevizos et al., 2014; J. Sulem and Famin, 2009; J. Sulem and Stefanou, 2016a; E. Veveakis et al., 2014, that might become dominant after thermal pressurization becomes impossible.

A cycle of friction during the oscillation of the shear band inside the fault gouge is separated in two stages: First the band travels inside the medium which corresponds to a weakening phase of the frictional response. The weakening phase takes place as the band travels across a hot region of the layer in which case according to equation (5.20) the pressure increases as ΔT is positive. Next, as the band travels inside the fault gouge expanding the yield zone, it approaches the boundaries. Close to the boundaries, temperature and pressure diffusion are more efficient. In particular, near the boundary, temperatures are lower as dictated by the parabolic profile of temperature T (see Figure 5.9) due to diffusion. The high diffusion gradients result in the cooling of the region, where the shear band is present. This in turn leads to a decrease in the applied pressure, therefore, the layer regains part of its strength. During each cycle the yield region is slightly increasing and the oscillations grow in period, since the yield zone is progressively expanding, and in amplitude, since the cooling effect becomes more pronounced and the temperature gradients become steeper.

5.3.4 Effect of the layer's height on the oscillations behavior

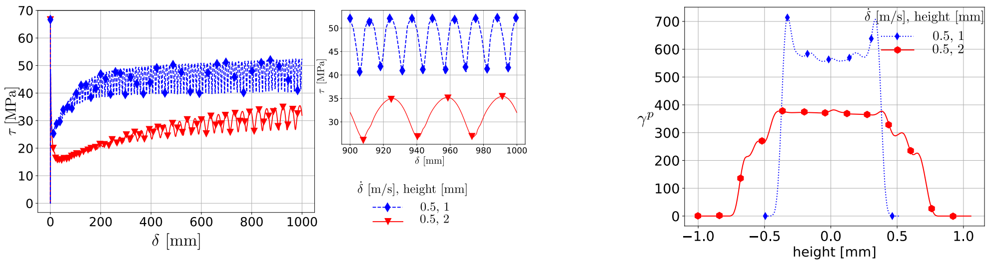

Figure 5.10 – Left: Frictional strength evolution of two layers of width 1 mm (dashed , blue, diamond curve) and 2 mm (solid, red, triangle curve) under the same seismic slip velocity $\dot{\delta} = 0.5$ m/s. Right: Profiles of accumulated plastic strain rate at the end of the two analyses. Yielding has not yet fully developed in the case of thickness of 2 mm.

In order to investigate how the boundaries affect the evolution of the traveling instability and of the frictional behavior inside the medium we compare the response between two layers of different height, 1 mm and 2 mm respectively, under a constant seismic slip velocity of 0.5 m/s (see Figure 5.10). We notice that the two layers exhibit the same response during the initial stages of thermal pressurization, however, the layer of thickness 2 mm reaches an overall lower minimum and a lower value for the residual shear strength. These values are essentially controlled by the diffusion processes. In the case of 1 mm, diffusion to the boundaries is more efficient and the layer regains more of its strength. Furthermore, diffusion is affected by the traveling instability inside the medium. In the case of the wider layer, from the period of the frictional strength oscillations (see inset of left part of Figure 5.10) we deduce that it takes almost twice the time for the traveling instability to cross through the layer. Therefore, temperature and pressure diffuse slower over the height of the layer. The period of the oscillations depends mainly on the distance between the layer's boundaries.

The oscillations in the frictional response of the layer are dependent both in period and in amplitude on the height of the layer. Oscillations of higher amplitude occur in the case of the shorter layer height, where the plastic zone has more time to develop and the diffusion gradients close to the boundary are steeper. It is of paramount importance to take into account the slopes of τ w.r.t. δ both at the beginning and at the oscillation phase since they are vital for the instability nucleation in the various stick and slip models (see Dieterich, 1992; Rice, 1973c; Ruina, 1983b). For high velocities ($0.5 \sim 1$ m/s) the slope at the beginning is the steepest and controls the energy balance (and the radiated energy), in contrast, for relatively small velocities ($0.1 \sim 0.3$ m/s, see Figure 5.6) the trend might be different leading to radically different instability conditions. By calculating the radiated energy from an earthquake and having an accurate value for the seismic slip velocity $\dot{\delta}$, we can estimate the width of the fault gouge during the earthquake.

We note here that based on the discussion of section 5.2.6, applying a scaling that takes both into account the effect of coseismic velocity $\dot{\delta}$ and the characteristic height of the layer H_0, allows us to verify the above results. In essence we note that keeping the velocity constant an increase in the layer's height affects only the diffusion terms. In particular the characteristic diffusion time t_0 doubles in the case of the thicker layer, indicating that the frictional regain due to the boundary effects will take more to develop. Note also that doubling the height of the layer leads to the doubling of the period in the thicker layer, indicating that the phenomenon is dependent on the diffusion properties of the fault gouge and its boundaries, and not on the internal length of the microstructure (Cosserat radius R).

5.4 Introduction of viscosity - rate and state phenomenology

Until now, a characteristic that is absent in the rate independent version of our model is the immediate positive frictional increase due to a sudden increase in the shearing velocity ($\alpha > 0$ in the context of a rate and state friction model, see Dieterich (1992), Rice et al.

(2001), Ruina (1983a), Ruina (1983b)). Adopting rate and state friction as a reference, as shown in Figure 5.11, this means that our model misses some necessary physics at the microscale like a creep mechanism at the asperity scale level and a notion of a state variable describing the contact behavior over time. This can be remedied by the introduction of viscosity in the present model which will lead to a strain rate hardening (or softening) description. The THM coupled model discussed here with the introduction of viscosity, can replicate the immediate effects of rate and state model, without the introduction of extra material parameters or the notion of an internal state variable indicating the contact history.

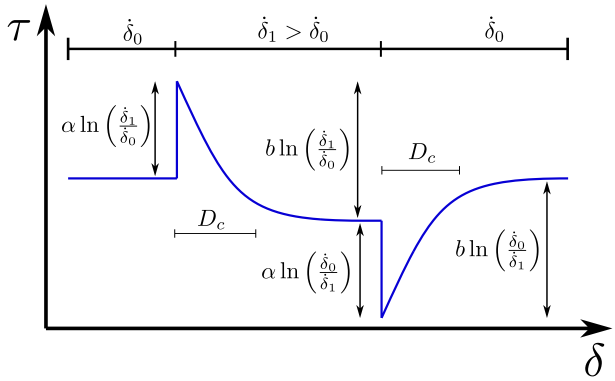

Figure 5.11 – Rate and state phenomenology (image taken from Tzortzopoulos et al., 2021).

Another important difference between our model and the general rate and state frictional response is the absence of a state variable ψ indicating the state of the contacts in the region of interest. As a result our model does not exhibit memory effects as well as the lower bound for the frictional response is not achieved by reaching the steady state w.r.t. ψ_{ss}, rather it is a function of the THM-couplings i.e. how efficient diffusion leads temperature and pressure away from the localized yielding region. It should be emphasized however that the role of the state variable ψ is ambivalent, in the sense that rate and state formulations do not necessarily respect the basic thermodynamic principles, since they mostly result from fittings to experimental results. Furthermore, we still lack data in the pressure and temperature ranges usually expected at the seismogenic depth, therefore, the parameters used in these laws are crucial concerning the prediction of the frictional evolution during a seismic event Rice, 2006a; Rice et al., 2001. Recently, emphasis has been given into the thermodynamically consistent derivation of granular material constitutive laws (see Alaei et al., 2021). These novel constitutive material formulations, lead to thermodynamically consistent models with the introduction of granular inertia effects, that successfully capture the rate and state behavior observed in the laboratory experiments under the laboratory observed temperature range.

In this section we investigate the role of viscosity in the frictional behavior of the fault during coseismic slip. We assume a Perzyna elasto-viscoplastic material introducing strain rate hardening effects through the use of a viscosity parameter η. A velocity stepping procedure is followed in which the fault is initially slipping with a small seismic slip velocity ($\dot{\delta}_0 = 0.01$ m/s) for a small seismic slip displacement ($\delta = 10$ mm). Then an immediate increase in the seismic slip rate is enforced in the model ($\dot{\delta} = 1.0$ m/s) to expose the rate dependence (see Dieterich, 1992; Rice et al., 2001; Ruina, 1983a). We continue shearing until the seismic slip $\dot{\delta}$ reaches a value of 100 mm. Then, we perform a series of parametric analyses to determine the influence of the viscosity parameter η (s), mixture compressibility β^* (MPa^{-1}), Cosserat radius R (mm) and the seismic slip velocity $\dot{\delta}$ (m/s) in the frictional response of the fault.

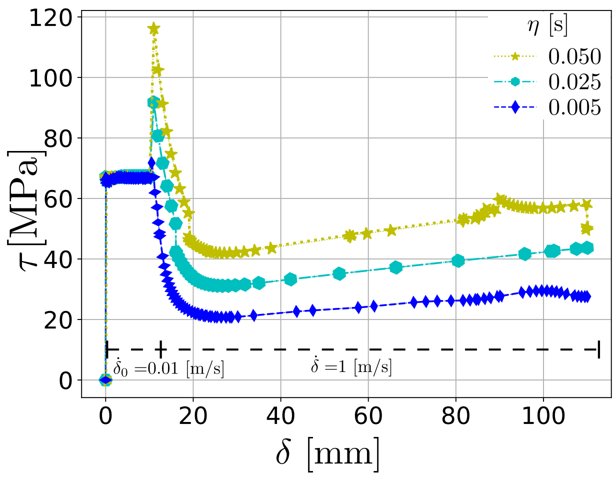

Figure 5.12 – Evolution of the fault's shear strength for a rapid change in shear rate $\dot{\delta}$ changes from 0.01 to 1.0 m/s, for different values of the viscosity parameter η (s). For large values of the viscosity parameter η (star curve), stress drops and kinks corresponding to stick slip events are presented.

In Figure 5.12 we present the effect of the viscosity parameter in the frictional response of the fault for a sudden increase of the seismic slip rate from $\dot{\delta}_0 = 0.01$ m/s to $\dot{\delta} = 1.0$ m/s. We observe that increasing the viscosity parameter η, the system becomes more sensitive to the sudden change of velocity reaching higher levels of peak frictional strength due to strain rate hardening. Three values are tested for the viscosity parameter $\eta = [0.005s, 0.025s, 0.05s]$ while the other material parameters are taken from Table 5.2. The lowest value corresponds to a meager increase in the fault's frictional strength due to the change in the shearing rate and is well in agreement with the results for the rate independent model. The frictional response initially reaches a minimum leading to velocity weakening. Afterwards, friction starts increasing due to pressure diffusion and strain-rate hardening. For the other values of the viscosity parameter the frictional strength increase is important. This change in the viscosity parameter also affects the minimum value of the frictional strength and its corresponding seismic slip displacement δ. For the higher viscosity parameter $\eta = 0.05$ (s) there are secondary frictional stress kinks that correspond to stick slip events during the shearing of the fault.

The viscosity parameter η introduced in the THM model accounts for the positive shear rate dependence coefficient (α) of the rate and state model. Typical values for the non-dimensional coefficient α for faults, lie in the range of $10^{-4} - 10^{-3}$, thus the lower values of η of our analyses leading to the estimation of $\alpha = \Delta\tau / \left[\ln(\frac{\dot{\delta}}{\dot{\delta}_0})(\sigma_n - p_f) f\right] = 2\ 10^{-4}$ correspond well to the stress rate increase predicted by the rate and state model (assuming scaling of η with $\dot{E} = \frac{\dot{\delta}}{h} = 1000\ \mathrm{s}^{-1}$).

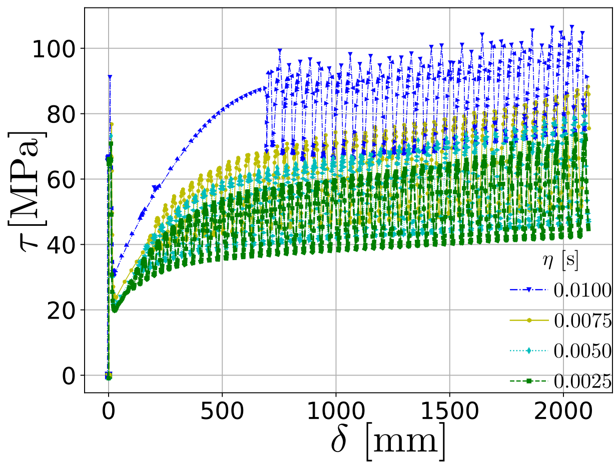

Figure 5.13 – Evolution of the fault's shear strength for viscous parameter η for common values of the rate and state parameter $\alpha = 10^{-4} - 10^{-3}$ large seismic slip displacements $\delta = 2$ m. The strain rate hardening leads to a constant increase of the center of the oscillations, that tend to reach the overstrength value.

Next, we apply a higher seismic slip displacement δ of 2 m during the stage of fast shear for the low values of the viscosity parameter in order to capture the response of our model for larger seismic slips. In the right part of Figure 5.13 we present the shear stress, seismic slip displacement (τ, δ) evolution for shearing of a fault gouge with viscosity parameters η in the range of [0.005 s to 0.075 s] for a seismic slip velocity, during the fast shear step, of $\dot{\delta} = 1$ m/s. We note the small strain rate increase of the stress due to η and the shear stress drop due to the apparent velocity weakening. The viscosity parameter enables the fault gouge to regain its overstrength in the latter analysis stages, since viscosity increases the localization width reducing the efficiency of thermal pressurization. We notice also that the oscillatory frictional response moves upward as seismic slip increases, while the oscillation maxima trace a curve of viscous evolution.

The oscillatory behavior of the frictional strength diagram could give rise to so called stick slip events in experiments. Thermal pressurization cannot completely halt strain rate hardening, mainly due to the increased localization width the model exhibits. We still can trace, however, a region of mild increases in the shear strength that can be used as an estimation of the characteristic weakening length, D_c, of the order of some centimeters. We note here that the estimation of the D_c in the context of thermal pressurization is different than in the case of rate and state in the sense that in the case of rate and state friction D_c is independent of the shearing velocity (see Ruina, 1983b, among others). In our case the characteristic distance depends on the shear velocity $\dot{\delta}$ the viscous parameter η and the internal length R and pressure- temperature diffusion lengths of the problem.

Next, we explore the influence of the internal length (Cosserat radius) R, in the evolution of the fault's frictional strength for a sudden change in the shearing rate from $\dot{\delta} = 0.01$ m/s to 1 m/s (see Figure 5.14). We notice that an increase in the value of R leads to higher shear overstrength due to the fast change in the shear rate. However, the post peak behavior changes little for values of R varying from $0.1R_{ref}$ to $10R_{ref}$ where R_{ref} is the Cosserat radius value in Table 5.2. For $R = 100R_{ref}$ the increase in overstrength is substantial and the results show a faster regain of the strength and a higher minimum for the frictional strength after the initial apparent softening response.

In Figure 5.14 on the right we present the influence of the mixture compressibility parameter β^* in the frictional response of the fault for a value of the viscosity parameter $\eta = 0.025$ s and a fast seismic slip velocity of $\dot{\delta} = 1$ m/s. The parameter β^* affects two terms in the equation (5.7), namely the hydraulic diffusivity parameter $c_{hy} = \frac{\kappa}{\beta^*}$, where κ

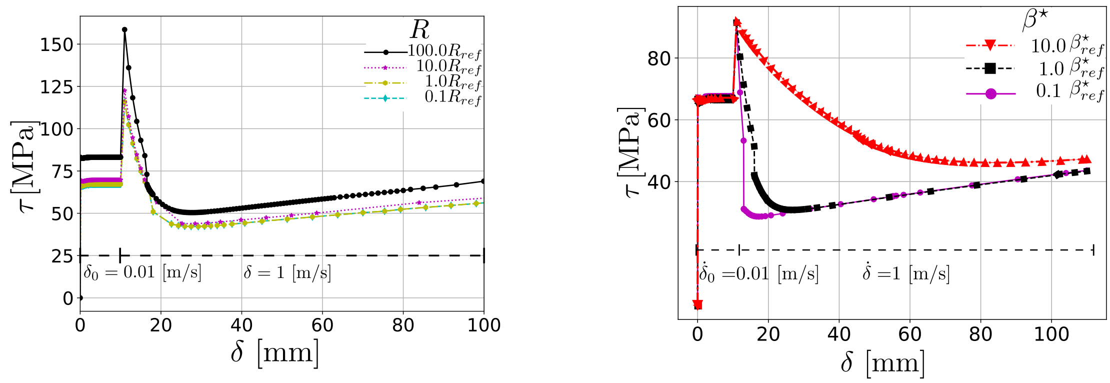

Figure 5.14 – Left: Evolution of the fault's shear strength for a rapid change in shear rate $\dot{\delta}$ from 0.01 to 1.0 m/s, for different values of the internal length (Cosserat radius) parameter R (mm). The response is largely unaffected by the increase of the internal length. Right: Evolution of the fault's shear strength for a rapid change in shear rate $\dot{\delta}$ changes from 0.01 to 1.0 m/s, for different values of the mixture's compressibility parameter $\beta^\star$ (MPa^{-1}). Increasing mixture's compressibility leads to milder stress drop.

is the permeability of the solid skeleton, and the term concerning the pressure decrease due to the porosity increase. Both these terms are affected the same by an increase (decrease) of β^*, however, the influence of the thermal pressurization term $\frac{\lambda^*}{\beta^*}$ decreases (increases) respectively. Taking the β^* value for which we run the rate independent analyses as a reference value β^*_{ref} (see Table 5.2), this corresponds to a smoother in the case of $\beta^* = 10\beta^*_{ref}$ or steeper (in the case of $\beta^* = 0.1\beta^*_{ref}$) decrease of the peak frictional strength during the initial stages of the slip. The parameter β^* also controls the minimum frictional strength of the fault and the seismic slip δ for which, the frictional strength increase due to diffusion will become prevalent. The results agree qualitatively well with the behavior observed in Badt et al., 2020 for higher compressibilities due to the formation of gouge material at the initial stages (see next section).

Finally, in Figure 5.15, we explore the influence of the shearing velocity in the frictional strength behavior of the fault for constant compressibility and viscosity parameters $\beta^s = \beta^s_{ref}$ and $\eta = 0.05$ respectively. After the initial slow shear $\dot{\delta} = 0.01$ m/s, we vary the fast shear velocity from $\dot{\delta}$=0.1 m/s to 1.0 m/s. The model exhibits two distinct behaviors, according to the prescribed seismic slip velocity values $\dot{\delta}$. For the low velocities $\dot{\delta} = 0.1 \sim 0.2$ m/s we observe periodic kinks in shear strength during the phase of shear strength increase. For higher velocities we observe a snap-back behavior during the apparent softening phase of the model. Furthermore a secondary stick slip event is observed

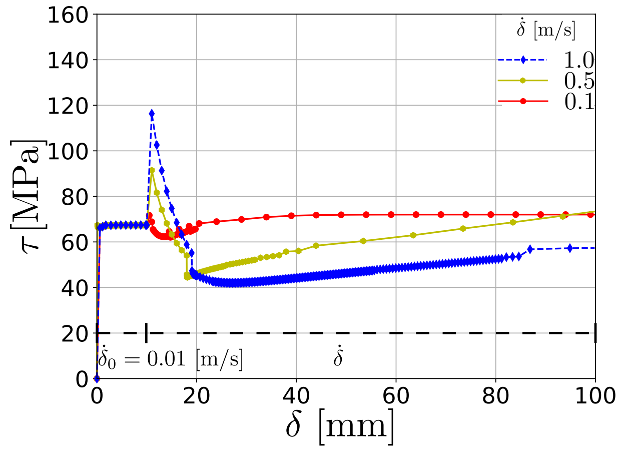

Figure 5.15 – Frictional strength evolution of a Perzyna viscoplastic layer ($\eta = 0.05$ s) under variable seismic slip velocities for a slip of $\delta = 100$ mm.

during the strength regaining phase of the simulation due to the diffusion.

The above results suggest that with the introduction of viscosity, our model can describe the rate and state phenomenology. For different values of the viscosity parameter η as well as the permeability β^*, stick slip behavior can be observed. This behavior suggests that our model of thermal pressurization together with a Perzyna viscoplastic law applied on a conceptually simple Drucker Prager yield criterion can capture a lot of the characteristics proposed by heuristic, phenomenological models like the rate and state friction lwa and its variations. Moreoverit can give further insights about the physical processes taking place during coseismic slip.

5.5 Comparison with existing analytical solutions

We compare the nonlinear numerical solutions under adiabatic, undrained conditions ($q_T = q_p = 0$) and isothermal, drained condtitions ($\Delta T = \Delta p = 0$) to the reference analytical solutions obtained in bibliography for uniform shear of the layer (Lachenbruch, 1980b), as well as the concentrated shear on the mathematical plane (Mase and Smith, 1987; Rice, 2006a). The results are presented in Figure 5.16.

For adiabatic undrained conditions, the Cosserat numerical solution with THM couplings tends to the Lachenbruch solution after sufficiently large slip δ. For isotropic drained conditions the numerical solution initially lies in between the reference analytical solu-

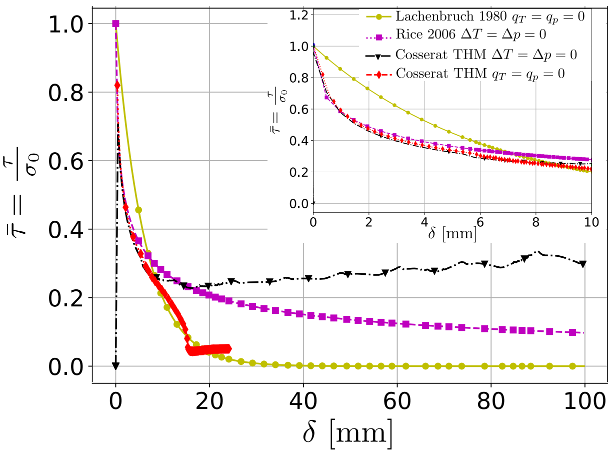

Figure 5.16 – Comparison between the available numerical and analytical solutions for adiabatic undrained and isotropic drained conditions. The response of the Cosserat-THM model with isothermal drained boundary conditions (black-triangle line) lies close to the response of the slip on a plane solution provided in Rice (2006b) (purple-square line). In the numerical model, localization is not constrained in a mathematical plane, leading to a steeper softening branch since more heat is produced in the yielding region enhancing thermal pressurization. Diffusion at the boundaries transfers heat and pressure away from the yielding region leading to partial strength regain causing a disagreement in the results. For the case of adiabatic undrained conditions, the Cosserat THM model (red-diamond line) eventually reaches the Lachenbruch solution (yellow-circle line).

tions, however the solution diverges as the seismic slip accumulates due to the existence of the limit cycle that restores part of the residual shear stress of the fault in later part of the analyses (traveling waves of strain localization). This tendency was also observed in the numerical analyses in Mase and Smith, 1987, where the authors applied seismic slip pulses of different shape and duration showing a tendency for frictional restrengthening. However, the analytical solution of the above problem in Rice (2006a) does not show this behavior. The reason is that the model in Rice, 2006b is solved in a linear manner assuming that the frictional strength $\tau(t)$ is fully described by an arbitrary function of time, while yielding is constrained on a fixed mathematical plane, thus neglecting the ventilation phenomena that take place due to the interaction between a moving heat source and temperature and pressure diffusion along the height of the layer. In the next chapter we will extend this solution to cover the aforementioned phenomenaand thus, to represent better the main underlying physics captured by the detailed numerical simulations presented in this chapter.

It is worth pointing out, that The traveling instability discussed here has been observed also in Platt et al., 2014b; Rice et al., 2014b. However, the authors of this study applied periodic boundary conditions at the edges of the fault gouge instead of the isothermal drained conditions employed here. Furthermore, no connection was made in their model about the origin of these instabilities. In this chapter we have identified the source of the traveling oscillations as an instability resulting from a Hopf bifurcation. While our analyses and the model proposed in Platt et al., 2014b; Rice, 2006a; Rice et al., 2014b agree well with the dynamic weakening role of thermal pressurization at the initial stages of the phenomenon, they diverge in later stages of the analyses in particular due to the role of the boundary conditions affecting thermal and hydraulic diffusion in the fault gouge.

5.6 Comparison with existing experimental studies

The results of the numerical analyses presented in section 5.3 are also observed in experiments (see Badt et al., 2020; Di Toro et al., 2011a; Rempe et al., 2020). A great challenge seen in experimental studies about the role of thermal pressurization is the isolation of all other slip weakening mechanisms in particular those of flash heating, silicate formation and thermal decomposition of minerals. Even bigger challenge is the replication of the exact temperature and pressure conditions of the seismogenic zone in the laboratory. Therefore, comparisons of analytical results to experimental findings are of a qualitative nature.

In Di Toro et al., 2011a the authors, have accumulated a large body of experiments performed at rates and displacement ranges comparable to those during seismic slip. The experiments were performed in a range of normal stresses of the order of 0.6 to 20 MPa. The authors advocate that for seismic slip velocities of the order of 1 m/s the frictional stress drop is around $0.2-0.4$ of the initial strength with higher drop as the normal stress increases. This tendency is also present in our analyses (see Figure 5.10). Furthermore, the obtained experimental frictional response presents oscillations, which could be attributed to Portevin Le Chatelier traveling instabilities during shearing of the specimen. The authors of this study also introduce the thermal weakening distance D_{th} that scales with the applied effective pressure on the specimen. From extrapolation of the available data to the pressure ranges found in the seismogenic zone they estimate the weakening distance D_{th} to the order of centimeters. This observation is consistent with our analyses. We note here that the boundary conditions (adiabatic, undrained) vs (isothermal,drained), the height of the specimen and the thermal and hydraulic diffusivities (c_{th}, c_{hy}), affect the calculation of D_{th}. In particular, fully saturated (wet) specimens of larger height under isothermal drained conditions will drop to lower values of friction before the effect of the boundaries becomes noticeable (see also section 5.3.4). The ratio between thermal and hydraulic diffusivities (Lewis number $Le = \frac{c_{th}}{c_{hy}}$), controls the effectiveness of thermal pressurization. We note here that the value of c_{hy} affects the characteristic time after which the effects of the boundaries will be felt in the frictional response. Therefore, the minimum value of the frictional response is controlled both by the ratio of the diffussivities c_{th}, c_{hy} as well as the height of the layer.

In the experiments performed in Badt et al., 2020, care was taken in order for the effect of thermal pressurization to be isolated from other weakening mechanisms. The authors of this study performed velocity stepping experiments in a rotary shear apparatus, with velocities of order $2.5 \sim 5$ mm/s, well below the seismic range, under normal stresses of $20 \sim 25$ MPa and confining pressure of $20 \sim 49$ MPa. The specimens height was 30 mm. Their results suggest that frictional strength drops during the initial stages of thermal pressurization while depending on the evolution of the microstructure inside the fault (formation of fault gouge particles) partial regaining of the frictional strength is possible. The authors specify that steeper stress drop and restrengthening are observed in younger specimens that have not yet been subjected to large shear displacements ($\delta < 1$ m) before the experiment. For specimens subjected to prior displacement the authors observe smoother stress drop and less tendency to regain frictional strength. They attribute this behavior to the formation of fault gouge inside the specimen that significantly affect the fault's compressibility coefficient β^* and therefore, the hydraulic diffusivity c_{th}.

Comparing with our numerical results and extrapolating to the in situ pressure range, we observe that our model agrees very well with the experimental findings for the younger specimens (see Figure 5.17). Since our model does not possess a memory mechanism to account for the damage of the microstructure and therefore for the change in permeability, it suffices to say that the older specimens could be modeled with higher values for the hydraulic diffusivity c_{hy}. An expansion to our model could be made by taking into account a microstructure evolution model as the one considered in Collins-Craft et al., 2020. We note here, that based on the scaled system (5.16), the experimental results obtained during shearing of a specimen with height H = 30 mm under a slip rate $\dot{\delta}$ = 5 mm, are comparable to our numerical experiments with fault gouge height H = 1 mm and coseismic slip velocities in the range of $\dot{\delta} = 100 \sim 300$ mm/s.

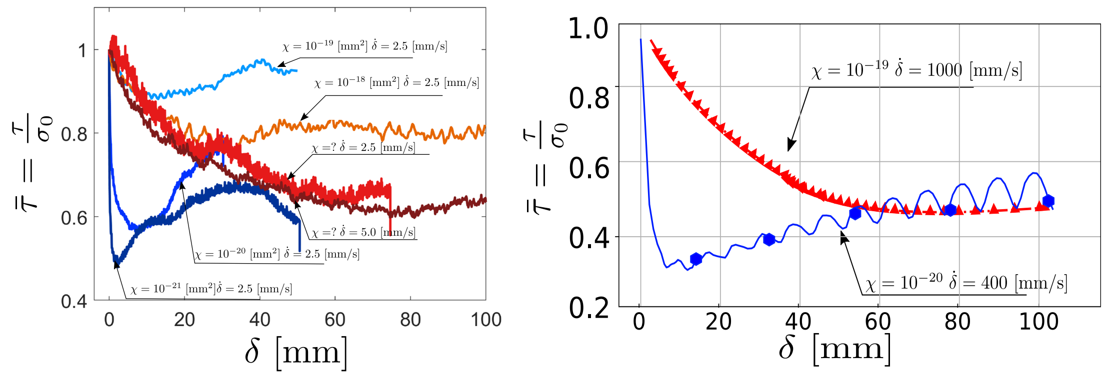

Figure 5.17 – Qualitative comparison between experimental (left part of Figure) and numerical results (right part of Figure) examining the role of thermal pressurization. The experimental results were taken from Badt et al., 2020. In both cases shear velocity $\dot{\delta}$ and permeability χ influence heavily the results. Both the experiment and the numerical analysis predict frictional strength regain after the stress drop due to shear. The oscillatory frictional strength behavior of the numerical analyses is also present in the experiments of Badt et al., 2020.

5.7 Key points

In this chapter the shearing of a fault gouge was studied under a variety of seismic slip velocities $\dot{\delta}$ and seismic slip displacements δ. First a linear stability analysis was performed, indicating the possibility of traveling instabilities present in the medium. This result is further validated by the numerical results presented in section 5.3.3. The effect of the seismic slip velocity $\dot{\delta}$ on the apparent softening of the layer was presented, as well as the influence of the different boundary conditions considering the energy (5.6) and mass balance (5.7) equations. It is shown that at the initial stages of the shearing (seismic slip δ=10 mm), after localization, the apparent softening follows the same decreasing behavior in all cases (see Figure 5.5). The response, however, changes as the slip δ accumulates as shown in Figure 5.16. Next, we investigate the influence of the seismic slip velocity $\dot{\delta}$ on the frictional behavior under isothermal drained conditions ($\Delta T = \Delta p = 0$) for a seismic slip of 100 mm, see Figure 5.6. It is shown that after the initial slip rate-dependent apparent softening, the layer tends to regain part of its strength τ, as slip δ accumulates due to the existence of a limit cycle.

The residual strength recovered is dependent on the seismic slip rate $\dot{\delta}$,the thermal and hydraulic diffusivity properties (c_{th}, c_{hy}) and the height h of the layer. Furthermore, we study the effects of the seismic slip rate on the evolution of the localization width l_{loc}. We notice the decrease of the localization width due to the increase in seismic slip velocity $\dot{\delta}$. This decrease indicates that localization width is no longer dependent only on the Cosserat radius R, rather it is also dependent on the apparent softening due to thermal pressurization. There is an oscillatory behavior present in localization width particularly for low velocities. As the seismic slip rate increases, this oscillatory interaction reduces substantially. This further highlights the interplay between the different characteristic lengths in our model in particular, between the Cosserat radius and the diffusion lengths.

Next, we study the evolution of the frictional resistance τ with seismic slip δ for a rate independent material applying even larger seismic slip. In particular, we impose a realistic seismic slip displacement of 1 m and seismic slip velocity of 1 m/s. The oscillatory behavior first described in Figure 5.6 for smaller slip is also present in Figure 5.8 for large coseismic slip. We notice that in Figure 5.8 oscillations stabilize in frequency and amplitude. This implies a partial recovery of the fault strength without it being explicitly implied by the mechanical behavior of the model as in the case of rate and state friction laws (see Dieterich, 1992; Rice et al., 2001; Ruina, 1983a). Therefore, the traveling instability mechanism might work also in the progressive healing of the fault during coseismic slip (see Platt et al., 2014a; Rice, 1973a; Rice et al., 2014a; Viesca & Garagash, 2015).

Considering the oscillatory behavior of the fault's frictional strength, which is observed during the isothermal drained analyses as well as the initial stages of the adiabatic undrained analyses, it is a result of the traveling instability inside the slip zone. The width and period of the oscillations are dependent on the geometrical properties of the band namely its height as they are the result of the high pressure and temperature diffusion gradients. A similar result was achieved under periodic boundary conditions in Rice et al., 2014b, however the authors did not comment on the nature of the traveling instability. A very important consequence of the traveling shear strain rate instability is the fact that field observations regarding the principal slip zone and its width may not be accurate as it is impossible to know the strain rate history of the band (see Figure

5.9). As a consequence the principal slip zone may be smaller than the one identified by current experimental methods. Traveling instabilities may also offer an explanation to the formation of parallel slip zones as the ones examined in Nicchio et al., 2018.

We conclude our analyses, assuming a rate dependent material through the implementation of an elasto-viscoplastic Perzyna material with THM couplings. We notice that our model exhibits a strain rate hardening behavior after the sudden change of the shear rate. We further note that the value of the viscosity parameter η controls important aspects of the simulation such as the overstrength achieved due to the shearing rate, the existence and the magnitude of traveling instabilities (oscillations) in the solution as well as the steady state the material reaches after sufficient shearing for varying shear rates. Overall, our Cosserat THM model with viscoplasticity is exhibiting a lot of the characteristics of a rate and state phenomenological model indicating that the procedure of thermal pressurization has still a lot of potential explaining the frictional strength drop during an earthquake together with the fault nucleation.

Finally, it can be shown that the results of the above numerical analyses agree qualitatively well with the experimental results obtained in Badt et al., 2020, where the thermal pressurization mechanism was studied in isolation to different frictional weakening mechanisms. Considering the evolution of the fault's frictional strength with accumulated seismic slip we observe that a single value for the characterization of the critical slip distance D_c is not possible. Namely according to Figure 5.8, the fault strength drops almost immediately after a slip of few centimeters to a minimum value close to 1/3 of the initial strength, this result agrees with extrapolations from experimental data to higher confining stresses Di Toro et al., 2011a. However, the final value around which the residual strength oscillates is reached for a slip distance of 0.4 m (see Figure 5.8). The latter result agrees with the estimation of Rempel and Rice, 2006; Rice, 2006a.

Our nonlinear analyses of a classical Drucker-Prager material with Cosseart microstructure and rate dependent Perzyna viscoplasticity together with the THM couplings, have shown that thermal pressurization can exhibit characteristics of a rate and state friction law namely, slip rate hardening as well as transition of friction to different steady states according to the shearing velocity $\dot{\delta}$ (velocity weakening), the viscosity parameter η and the mixture compressibility β^* without the need for the incorporation of the internal frictional state ψ variable and its evolution law.

Our results are in contrast to the classical models of THM proposed in Lachenbruch, 1980b; Rice, 2006b that assume only monotonic reduction of the shear frictional strength during the seismic event. In order to understand the extreme difference between the predictions of the model described in Lachenbruch (1980a), Rice (2006a) and our numerical results, we revisit in chapter 6 the main assumptions of the theory of Rice (2006a) considering a traveling mode of strain localization and the boundary conditions.We will examine how each one of these parameters affect the theoretical predictions and justify our numerical results.

Chapter 6

Expansion of the frictional slip model in cases of traveling strain localization modes and bounded fault gouges

Summary

In this chapter, we study the effect of the strain localization mode and boundary conditions in the evolution of the frictional shear strength of a fault under coseismic slip. We consider thermal pressurization as the main weakening mechanism. We make the assumption that the seismic slip is localized on a mathematical plane. We solve the linear Volterra integral equation of the second kind provided in Rice, 2006a, for different strain localization modes, temperature and pore fluid pressure boundary conditions, departing from the original assumptions of a stationary instability on an unbounded domain. We investigate the influence of a traveling instability inside the fault gouge considering isothermal, drained boundary conditions for the bounded and unbounded domain respectively. We compare our results to the ones available in Lachenbruch, 1980b; Lee and Delaney, 1987; Mase and Smith, 1987 and Rice (2006a). Our results establish that when a stationary strain localization profile is applied on a bounded domain, the boundary conditions lead to a steady state, where total strength regain is achieved. In the case of a traveling instability such a steady state is not possible and the fault only regains part of its frictional strength, depending on the seismic slip velocity and the traveling velocity of the shear band. In this case frictional oscillations increasing the frequency content of the earthquake are also developed. Our results indicate a reappraisal of the role of thermal pressurization as a frictional weakening mechanism and its role in earthquake nucleation (see Rice, 1973b; Viesca & Garagash, 2015) and control (see Stefanou & Tzortzopoulos, 2020; Stefanou, 2019; Tzortzopoulos, 2021)

6.1 Introduction

The results of the previous chapter concerning the influence of the weakening mechanism of thermal pressurization diverge -spectacularly- from the expected behavior based on the model of Rice (2006a). Furthermore, we note that the results of chapter 5, indicate the divergence to take place long before the completion of the seismic slip δ. This holds true for the range of commonly observed seismic slip velocities $\dot{\delta} \in \{0.1 \sim 1\}$ m/s and seismic slip displacements $\delta \in \{0.1 \sim 1\}$ m. In this chapter we investigate the reasons for this divergence between the theoretical results and their implications for the appreciation of thermal pressurization as one of the main weakening mechanism during coseismic slip.

The results of sections 5.3.2, 5.4 (see Figures 5.6,5.14) lead us to the assumption that it is the hydraulic and thermal parameters of the fault that affect mainly thermal pressurization and not the radius of the Cosserat medium, which is a parameter connected with the grain size and the material properties of the granular medium. We will use this observation to propose a conceptually simpler model accounting for thermal pressurization. The new model incorporates the geometrical characteristics of the model in chapter 5. We assume that the yield (dissipation) obeys a Coulomb friction law with Terzaghi effective stress and is confined in only one point in the layer. Outside the layer the medium behaves elastically. This allows to avoid solving a BVP for the mechanical part, which significantly simplifies the problem.

Previous researchers (see Lachenbruch, 1980b; Rempel & Rice, 2006; Rice, 2006a; Viesca & Garagash, 2015) have examined thermal pressurization as the main frictional weakening mechanism, in their effort to provide realistic estimates for the dissipation and fracture energy during the earthquake nucleation phase. In their analyses the response was assumed to be bounded by two regimes, the initial adiabatic undrained stage corresponding to uniform seismic slip across the fault gouge (see Lachenbruch, 1980b) and the final state where the seismic slip is sufficiently concentrated in a region, called the principal slip zone (PSZ), inside the fault gouge (see Rice et al., 2014b). Then as a first approximation the width of the principal slip zone was assumed to be zero (slip on a mathematical plane). The frictional response of the fault then transitions as the slip evolves from the uniform shear response to the localized response.

Mase and Smith, 1987 studied the effects of frictional heating on the thermal, hydraulic and mechanical response of the fault and provided numerical solutions, via a finite element procedure, for drained and undrained boundary conditions, assuming a fault gouge with a fixed localization width under homogeneous deformation. The fault layer boundaries are taken to infinity. Later, Lee and Delaney (1987), based in the work of Carslaw and Jaeger (1959) and Mase and Smith (1987), solved the coupled thermal pressurization equations for a variety of arbitrary thermal loading conditions and duration excluding, however, the material behavior form their considerations.

Naturally the question of the material dissipative behavior is of paramount importance for two reasons. Firstly it indicates the intensity of the thermal loading since for a geomaterial, yield strength and dissipation are mainly connected to the spherical part of the effective stress tensor. Secondly it directly influences the shape of the principal slip zone and therefore the profile of the thermal load. The coupled problem, where the increase of the pore fluid pressure affects the frictional strength of the fault was first studied analytically in Rice, 2006a. There, the author, by assuming a specific plastic strain rate profile, which corresponds to a stationary strain localization on a mathematical plane, couples pore fluid pressure and the fault's frictional response, providing for the first time analytical estimates for the energy of the fault system that is lost to dissipation and the advancement of slip.

From the procedure described above (see Rice, 2006a), we conclude that the obtained results are heavily dependent on the plastic strain rate profile selected. The authors in Rempel and Rice (2006), Rice (2006a) comment on this and they proceed in using profiles of different shape in their analyses, noting however that due to the nature of the Cauchy continuum and equilibrium considerations, such profiles are strictly not applicable under such a kind of analysis. In the above works the initial choice of the plastic strain rate profile to correspond on a mathematical plane was dictated by the localization mode valid for a Cauchy continuum that exhibits a softening behavior. However, we know that localization in nature is not happening on a mathematical plane, rather it is contained in a small region of finite width (see chapter 5 and Muhlhaus and Vardoulakis (1988), J. Sulem et al. (2011), the questions of equilibrium were also discussed in I. Vardoulakis (1996a, 1996b, 2000b), where a second gradient model was introduced to properly account for the changes in equllibrium due to the introduction of localized profile of finite width).

This of course immediately calls into question the results of the analyses in Rempel and Rice (2006), Rice (2006a). In order to answer this critique Platt et al. (2014b), Rice et al. (2014b) developed a model based on a material law assuming strain rate strengthening coupled with the thermal pressurization equations. Their model then localizes on a zone of finite width respecting equilibrium considerations.

Nevertheless, the previous analysis is constrained by two fundamental assumptions. First, it is assumed that the boundaries of the fault gouge lie far away and they don't affect the temperature and pressure diffusion evolution at least during the timescales required for the evolution of the earthquake phenomenon. Secondly, they do not account for all types of instabilities possibly present in a (Cauchy) continuum coupled with pressure and temperature diffusion equations. In particular it was shown in Benallal, 2005b; Benallal and Comi, 2003 that under stress states common in faults the preferred mode of instability might not be that of the divergence kind described in Rice, 1975, rather it can be a "flutter" type instability, herein shown to be a traveling instability. From a mathematical point of view this instability is manifested by the appearance of a Lyapunov exponent with imaginary parts. The transition form a stationary instability of divergence type to a flutter traveling instability is called a Hopf bifurcation. For more details we refer to sections 3.4,3.5.2 of chapter 3 and section 5.2.8 of chapter 5, where we have shown that traveling instabilities are present in the linear stability analysis for Cauchy and Cosserat continua under strain hardening and strain-rate softening or apparent softening due to multiphysical couplings.

In this chapter, we are primarily concerned with the fault gouge behavior when the effects of the boundary conditions cannot be ignored and when the principal slip zone is allowed to travel inside the fault gouge (see results of detailed simulations in section 5.3). We find that under these conditions the frictional response of the fault significantly differs compared to the one obtained in Rice, 2006a for values of the seismic slip δ and seismic slip velocity $\dot{\delta}$ that are representative of real seismic events. In section 6.2 we briefly present the basic equations of our model and the methodology obtained in Rempel and Rice, 2006; Rice, 2006a. Due to the added complexity of the moving principal slip zone and the boundary conditions that affect the kernel of the linear Volterra integral equation of the second kind, its solution by means of classical solution techniques such as Laplace transform, Adomian decomposition Method and Taylor series expansion face a lot of convergence difficulties (see Wazwaz, 2011). The main difficulties in the numerical solution of the derived integral equations stem from the fact that the kernel of the problem consists of the difference between exponentials that have vastly different decay rates, and the fact that for the unbounded case the convolution integral contains a weakly singular kernel.

To account for these numerical challenges we apply a novel procedure using the $\mathcal{Z}$-Transform and the Convolution Quadrature Method ($\mathcal{Z}$-CQM) (Mavaleix-Marchessoux et al., 2020). In section 6.3.1 we present the basic application of the $\mathcal{Z}$-CQM procedure in the case on non homogeneous linear integral equations, and we comment on the properties of the $\mathcal{Z}$-Transform, that allow us to calculate efficiently the solution to our numerical applications. The $\mathcal{Z}$-CQM procedure is used in the cases involving an unbounded domain, where numerical integration becomes challenging because of the existence of a weakly singular kernel in the convolution integrals.

For the case involving a periodic strain localization traveling on a bounded domain, we used a Spectral Collocation Method with Lagrange basis functions (SCML), for the solution of general Volterra integral equations of the second kind, based on the work of Tang et al. (2008). This method is more general and can handle the more challenging case of a periodic traveling thermal load on the bounded domain, which is intractable by use of the $\mathcal{Z}$-CQM method.

Having described our model and the solution procedure, we present in section 6.4 a series of applications showcasing the differences with the analyses in Rice, 2006a. The applications include the frictional responses of: (a) a stationary PSZ on a bounded isothermal drained domain, (b) a moving PSZ on an unbounded isothermal drained domain, and (c) a moving PSZ on a bounded isothermal drained domain. The original solution in Rice (2006a) is obtained as a special case of the more general solutions presented here and is taken as reference (see Figure 6.1).

Throughout section 6.4, we compare the numerical results obtained for the different cases of boundary conditions and strain localization modes by solving the basic integral equation (6.16) against the reference solution obtained in Rice, 2006a. We can expand our general numerical results, following the solution of equation (6.16), in the cases of micromorphic Cosserat continua. Thus, the results of the present chapter constitute a benchmark to explain the fault frictional behavior under the more realistic modeling hypotheses considered in the chapter 5. We show that the introduction of traveling instabilities inside the fault gouge naturally enhances the frictional response with oscillations, which in turn enhances the ground acceleration spectra with higher frequencies Aki, 1967; Brune, 1970 as observed in nature. Our results are important in the context of experiments for the description of the weakening behavior due to thermal pressurization, for controlling the transition from steady to unsteady slip and for the nucleation of the fault. They are also important in earthquake control, as they provide bounds for the apparent friction coefficient with slip and slip-velocity (see Stefanou & Tzortzopoulos, 2020; Stefanou, 2019; Tzortzopoulos, 2021).

6.2 Thermal pressurization model of slip on a plane

During shearing of a layer under constant seismic slip displacement $\dot{\delta}$ and constant normal stress σ_n the profile of the shear strain rate $\dot{\gamma}(x,t)$ will vary from the initially uniform solution to a slip completely confined on a mathematical plane within the fault zone. Considering that the region of the fault gouge is saturated with water at its pores, frictional heating will then lead to temperature increase $T(x,t)$ and subsequent pore fluid pressure increase $p(x,t)$. The description of the above frictional weakening mechanism requires the coupling of the mechanical equilibrium equation with those of mass and energy equilibria. In the case of simple shear of a 1D layer under constant total normal stress, the system of equations can then be written as:

$$\sigma_{12,2} = 0, \quad \sigma_{22,2} = 0 \tag{6.1}$$

$$\frac{\partial T}{\partial t} = c_{th} T_{,22} + \sigma_{12}\dot{\gamma}^p_{12} + \sigma_{22}\dot{\gamma}^p_{22}, \tag{6.2}$$

$$\frac{\partial p}{\partial t} = c_{hy} p_{,22} + \Lambda \frac{\partial T}{\partial t}, \tag{6.3}$$

where σ_{12} is the shear stress, σ_{22} is the normal stress,c_{th}, c_{hy} are the thermal and hydraulic diffusivities and $\Lambda = \frac{\lambda^\star}{\beta^\star}$ is the thermal pressurization coefficient dependent on the mixture's coefficient of thermal expansion $\lambda^\star$ and compressibility $\beta^\star$ (see also chapter 5). The material of the layer is elastic perfectly plastic with a linear dependence on the effective pressure $p' = \frac{\sigma'_{kk}}{3} = \frac{1}{3}(\sigma_{kk} - p)$ following the Mohr-Coulomb yield criterion. Following the notation in Rice (2006a), we will rename the shear and normal stress in order to enhance readability. Therefore, $\sigma_{12}(t) = \tau(t)$ and $\sigma_{22}(t) = \sigma_n(t)$. The Mohr-Coulomb yield criterion is given then by:

$$f(\tau, \sigma_n) = \tau(t) - f(\sigma_n - p(x,t)), \tag{6.4}$$

where, f is the friction coefficient, to be taken constant in our analyses. Furthermore, we take into account the shearing of a mature fault gouge. In this case we note that the fault gouge material has undergone fully the stages of cataclasis and bresciation, therefore, the dilation of the fault gouge during shear will be negligible. This means that the normal plastic strain rate $\dot{\gamma}^p_{22}$ is zero, which renders the component of the plastic work due to yielding in the normal direction zero (zero dilatancy). We can therefore write $\dot{\gamma}^p_{12} = \gamma^p$. The heat equation is then written:

$$\frac{\partial T}{\partial t} = c_{th}T_{,22} + \tau(t)\dot{\gamma}^p(x,t), \tag{6.5}$$

During yielding of the layer the shear strength capacity in the yielding region is given by $\tau_{cr}(x,t) = f(\sigma_n - p(x,t))$. The layer yields in the position where the pore fluid pressure is maximum, $p(x,t) = p_{max}(t)$, which in turn presents the minimum shear strength $\tau_{cr,min}(t)$. The equilibrium equation (6.1) dictates that $\frac{\partial \tau}{\partial x} = 0$ throughout the layer, meaning that shear stress is constant along the layer. Therefore, in order for equilibrium to be satisfied inside the layer, the shear stress of the layer, $\tau(t)$, must be equal to the shear strength at the point, where pore fluid pressure is maximum, $\tau(t) = \tau_{cr,min}$. In essence, the value of friction in the yielding region dictates the shear stress value along the height of the layer.

For the mathematical description of the phenomenon of thermal pressurization the distribution of the plastic strain rate $\dot{\gamma}^p_{ij}$ is of primary importance. Considering the case of a mature fault, temperature increase (6.5) and consequently, thermal pressurization depend on the plastic shear strain rate profile $\dot{\gamma}^p_{12} = \dot{\gamma}^p$.

Based on the discussion in Rempel and Rice (2006), Rice (2006a) we focus on two cases for the plastic strain rate distribution. The first case in which the shear rate remains uniform corresponds to a case of adiabatic undrained boundary, was first discussed in Lachenbruch, 1980b, where an analysis for the coupling terms and the second order advection terms was performed. However, we have shown in chapter 3 that in the case of classical Cauchy continuum, the profile of the homogeneous deformation is unstable and will localize on a mathematical plane. Furthermore, we cannot be sure about the conditions constraining the flow of heat and pore fluid to the surrounding foliated rockmass (boundaries of the fault gouge). It has been observed that in the case of mature faults, heat and pore fluid, flow away from the fault gouge are promoted (see Aydin, 2000). Therefore, the second case of the perturbed solution corresponding to a localization of strain on the mathematical plane presents more interest. Modeling this problem, we will provide a reasonable basis for calculating pressure and temperature maxima during an earthquake in cases where the temperature and pore pressure diffusion characteristic lengths are greater than the thickness of the principal slip zone (PSZ).

We investigate two distinct modes of strain localization on a mathematical plane. The first case corresponds to a stationary profile $\dot{\gamma}^p(x,t) = \dot{\delta}\ \delta_{Dirac}(x)$ indicating a divergent growth instability, where $\dot{\delta}$ is the rate of the coseismic slip. In the second case a traveling plastic strain rate profile is assumed indicating a flutter type instability (see Benallal, 2005b; Benallal and Comi, 2003; Rice, 1975). In the latter case, assuming the localization travels with a velocity v inside the fault gouge leads to the following description of the plastic strain rate profile:

$$\dot{\gamma}^p(x,t) = \dot{\delta}\ \delta_{Dirac}(x - vt). \tag{6.6}$$

$\delta_{\mathrm{Dirac}}(x)$ is the Dirac-delta distribution.

The process of thermal pressurization indicates that in the yielding region, which from now on is assumed to be a mathematical plane, the temperature is increasing due to the heat provided form the mechanical dissipation. The position of the yielding mathematical plane indicates the position of a point thermal source, which subsequently leads to an increase of pore fluid pressure in the layer. For the purposes of our analyses we prescribe the trajectory of the thermal load inside the layer to always travel with the plastic strain rate profile. The results of our analysis are valid as long as the position of the yielding plane (and thermal source) coincides with the position of the maximum pore fluid pressure in the layer. In the case of constant traveling velocity of the shear band [1], we have proven that this assumption holds true (see Appendix I).

1. We will continue to use the terms of shear band or PSZ, even though the thickness of the yielding region is zero.

Knowing the form of the profile of the shear plastic strain-rate in $\dot{\gamma}^p(x,t)$ (equation (6.6)), the two way coupled problem in the form of temperature and pressure diffusion equations is given by:

- Heat diffusion BVP:

$$
\begin{aligned}
&\frac{\partial T}{\partial t} = c_{th}\frac{\partial T}{\partial x^2} + \frac{1}{\rho C}\tau(t)\dot{\delta}\delta_{Dirac}(x-vt),\\
&T\Big\|_{x=0} = T\Big\|_{x=\mathrm{H}} = 0,\\
&T(x,0) = 0,
\end{aligned}
\tag{6.7}
$$

  where $T(x,t)$ is the unknown change in temperature in the fault gouge layer of height H. The fault gouge is considered to be in isothermal boundary conditions during shearing. The coupled pressure problem is given by:

- Pressure diffusion BVP, in its Homogeneous form:

$$
\begin{aligned}
&\frac{\partial \Delta p}{\partial t} = c_{hy}\frac{\partial \Delta p}{\partial x^2} + \Lambda\frac{\partial T}{\partial t},\\
&\Delta p\Big\|_{x=0} = \Delta p\Big\|_{x=H} = p(x,t) - p(x,0) = 0,\\
&p(x,0) = p_0,
\end{aligned}
\tag{6.8}
$$

  where $\Delta p(x,t)$ is the unknown pressure difference between the fault gouge layer and the boundaries, while p_0 is the initial pore fluid pressure, that is kept constant at the boundaries of the fault gouge (drained boundary conditions).

We note that the above formulations are also valid in the case of an unbounded doamin considering $\mathrm{H} \rightarrow \pm\infty$. The pressure problem affects also the temperature BVP through the value of shear stress (fault friction), $\tau(t)$, in the yielding region. According to the Mohr-Coulomb yield criterion, subtracting the initial pressure p_0 we get:

$$
\tau(t) = f(\sigma_n - p_0) - f\Delta p_{max}(t). \tag{6.9}
$$

We note here that once we know the form of the plastic strain-rate profile $\dot{\gamma}^p(x,t)$ as in equation (6.7) the only unknown is the fault friction $\tau(t)$. We can find the solution of the temperature equation $T(x,t)$ in terms of the unknown fault friction $\tau(t)$ and replace into the pressure equation, which can then also be described as an unknown function of friction. Finally, we can define the value of fault friction $\tau(t)$ by inserting the pressure solution $\Delta p(x,t)$ into the material equation (6.9) and solving for $\tau(t)$. The above equations have constant coefficients and since the loading is prescribed (based on the unknown $\tau(t)$), the system has been transformed to a one-way coupled set of linear differential 1D diffusion equations of the form:

$$\begin{aligned}
&\frac{\partial u(x,t)}{\partial t} = c\frac{\partial^2 u(x,t)}{\partial x^2} + \frac{1}{k}g(x,t),\\
&a_1\frac{\partial u}{\partial n_1}\Big\|_{x=0} + b_1 u\Big\|_{x=0}(t) = f_1(t),\ t>0,\\
&a_2\frac{\partial u}{\partial n_2}\Big\|_{x=H} + b_2 u\Big\|_{x=H}(t) = f_2(t),\ t>0,\\
&u(x,0) = I(x),
\end{aligned} \tag{6.10}$$

where $u(x,t)$ is the unknown function (e.g. the temperature $T(x,t)$), $f_i,\ i=1,2$ are the values of the general Robin boundary conditions with coefficients $(a_i,\ b_i,\ i=1,2)$, $I(x)$ is the initial condition and $g(x,t)$ is the loading function (here related to frictional dissipation). We denote by c the diffusivity and by k the conductivity of the material.

We can find the solution to the above BVP by application of the Green's theorem, which for the general diffusion case in 1D reads (see Cole et al., 2010):

$$\begin{aligned}
u(x,t) = &\int_0^{\mathrm{H}} G(x,x',t,c)I(x')dx' + \frac{c}{k}\int_0^t\int_0^{\mathrm{H}} g(x',t')G(x,x',(t-t'),c)dx'dt'\\
&+c\int_0^t\sum_{i=1}^{2}\left[\frac{f_i(t')}{a_i}G(x,x_i',(t-t'),c)\right]dt' - \alpha\int_0^t\sum_{i=1}^{2}\left[f_i(t')\frac{G(x_i,x',(t-t'),c)}{n_i'}\Big\|_{x'=x_i}\right]dt',
\end{aligned} \tag{6.11}$$

where $G(x,x',(t-t'),c)$ is the appropriate Green's function. The first two terms correspond to the initial condition $I(x,0)$ and the loading term $g(x,t)$ respectively. The terms α, k represent the diffusivity and the conductivity of the unknown quantity $u(x,t)$ respectively. The third term is important for non homogeneous Neumann and Robin boundary conditions while the fourth term refers to non homogeneous Dirichlet boundary conditions. In what follows the last two terms in equation (6.11) are omitted due to the existence of homogeneous Dirichlet boundary conditions in the problems of temperature and pressure difference diffusion at hand.

Applying the solution in terms of the Green's function (6.11) to problems (6.7),(6.8) we obtain the solution in terms of the Green's function specific to each diffusion problem.

$$T(x,t) = \frac{c_{th}}{k_T}\int_0^t \int_{-\infty}^{\infty} g_T(x',t')G(x,x',t-t',c_{th})dx'dt', \tag{6.12}$$

$$p(x,t) - p_0 = \frac{c_{hy}}{k_H}\int_0^t \int_{-\infty}^{\infty} g_H(x',t')G(x,x',t-t',c_{hy})dx'dt', \tag{6.13}$$

where c_{th}, k_T are the thermal diffusivity, conductivity pair and c_{hy}, k_H are their hydraulic counterparts. Similarly (g_T, g_H) are the loading functions, while $G(x,x',t-t',c)$ is the Green's function kernel for the thermal ($c = c_{th}$) and pressure ($c = c_{hy}$) diffusion problems respectively.

In the case of the coupled pressure problem (6.8) with the temperature as a loading function, we are interested in rewriting the system's response with the help of the dissipative loading ($\frac{1}{\rho C}\tau(t)\dot{\gamma^p}$) of the temperature equation (6.7). This way we can connect the pressure response $p(x,t)$ to the fault friction $\tau(t)$ which is the main unknown. We can do this by replacing in the expression of $T(x,t)$ in the pressure diffusion equation (6.8) the temperature impulse response of equation (6.7) due to a impulsive (Dirac) thermal load. This way the response obtained from the pressure diffusion equation is a Green's function kernel that contains the influence of an impulse thermal load (see Appendix E for detailed derivation in the cases of 1) a bounded domain for a stationary impulsive thermal load and 2) an unbounded domain ubjected to a moving impulsive thermal load). The pressure solution can then be written as:

$$p(x,t) - p_0 = C\int_0^t \int_{-\infty}^{\infty} g_T(x',t')G^{\star}(x,x',t-t',c_{hy},c_{th})dx'dt', \tag{6.14}$$

where $C = \frac{\Lambda\dot{\delta}}{\rho C(c_{hy}-c_{th})}$ and $G^{\star}(x,x',t-t',c_{hy},c_{th})$ is the Green's function kernel of the pressure equation (6.8) containing the influence of an impulse thermal load from the temperature equation (6.7).

Having found the pressure solution $p(x,t)$ as a function of g_T we can then replace (6.14) into the material description equation (6.9). For the case of 1D shear τ under constant normal load σ_n that we will consider throughout the chapter, the material law is transformed into the integral equation:

$$\tau(t) = f(\sigma_n - p_0) - C\int_0^t \int_{-\infty}^{\infty} g_T(x',t')G^\star(x,x',t-t',c_{hy},c_{th})dx'dt' \tag{6.15}$$

Due to the concentrated nature of the thermal load (Dirac distribution) the integral equation (6.15) can be brought to its final form:

$$\tau(t) = f(\sigma_n - p_0) - C\int_0^t \tau(t')G^\star(x,t-t',c_{hy},c_{th})\Big\|_{x=x'(t')}dt' \tag{6.16}$$

The above integral equation is a linear Volterra integral equation of the second kind. We note here that this equation is valid only at the position of the yielding plane which has to coincide with the position of the maximum pressure inside the layer ($x = x'(t')$), which we have proven to hold true for all cases studied here (see Appendix I).

6.2.1 Cases of Interest

Having derived the linear Volterra integral equation of the second kind (6.16), we turn our attention in the cases of interest concerning our analyses. We consider four cases for the loading and boundary conditions concerning the evaluation of the fault friction during coseismic slip. We first separate between stationary and traveling modes of strain localization and then we further discriminate between unbounded and bounded domains. The separation of the fault's frictional response into these categories leads to four different expressions for the Green's function kernel $G^\star(x,x',t-t',c_{hy},c_{th})$ in equation (6.15).

Here we will provide the analytical expressions, for the kernels to be substituted into equation (6.15). In naming the Green's function kernels we used the subscript naming conventions of Cole et al. (2010). Namely for diffusion in 1D line segment domains, the letter $X\alpha\beta$ is adopted, where α, β are the left ($x = 0$) and right $x =$ H boundaries of the domain respectively. They can take the values 0 or 1 indicating an unbounded or a bonded domain respectively, under homogeneous Dirichlet boundary conditions.

We begin by introducing the Green's function kernels of the unbounded $X00$ and the bounded $X11$ cases in the case of a 1D diffusion equation under homogeneous Dirichlet boundary conditions.

For the unbounded case we use:

$$G_{X00}(x, x', t-t', c) = \frac{1}{2\sqrt{\pi c(t-t')}} \exp\left[-\frac{(x-x')^2}{4c(t-t')}\right]. \tag{6.17}$$

Similarly for the bounded case we use:

$$G_{X11}(x, x', t-t', c) = \frac{2}{L}\sum_{m=1}^{\infty} \exp\left[-m^2\pi^2 c\frac{t-t'}{\mathrm{H}^2}\right] \sin\left(m\pi\frac{x}{\mathrm{H}}\right) \sin\left(m\pi\frac{x'}{\mathrm{H}}\right). \tag{6.18}$$

We note here that c can be either c_{th} or c_{hy} depending on the diffusion problem in question. The kernels $G^{\star}_{X\alpha\beta}(x, x', t-t', c_{hy}, c_{th})$ of the pressure diffusion problem based on the impulse of the frictional response for given boundary strain localization modes and boundary conditions are given by:

- Stationary mode of strain localization
  - Unbounded domain, $\alpha = 0,\ \beta = 0,\ x' = 0$, (see Rice, 2006a)

$$G^{\star}_{X00}(x, t-t', c_{hy}, c_{th}) = c_{hy}G_{X00}(x, 0, t-t', c_{hy}) - c_{th}G_{X00}(x, 0, t-t', c_{th}). \tag{6.19}$$

  - Bounded domain $\alpha = 1,\ \beta = 1,\ , x' = 0$

$$G^{\star}_{X11}(x, t-t', c_{hy}, c_{th}) = \ c_{hy}G_{X11}(x, 0, t-t', c_{hy}) - c_{th}G_{X11}(x, 0, t-t', c_{th}). \tag{6.20}$$

- Traveling mode of strain localization
  - Unbounded domain, $\alpha = 0,\ \beta = 0,\ x' = vt'$:

$$G^{\star}_{X00}(x, t-t', c_{hy}, c_{th}) = c_{hy}G_{X00}(x, vt', t-t', c_{hy}) - c_{th}G_{X00}(x, vt', t-t', c_{th}). \tag{6.21}$$

  - Bounded domain, periodic trajectory in time, $\alpha = 1,\ \beta = 1,\ x' = x(t')$:

$$G^{\star}_{X11}(x, t-t', c_{hy}, c_{th}) = \ c_{hy}G_{X11}(x, x(t'), t-t', c_{hy}) - c_{th}G_{X11}(x, x(t'), t-t', c_{th}). \tag{6.22}$$

In section 6.4 we present the frictional response obtained from the solution of equation (6.16) for the different Green's function kernels defined above.

6.3 Methods for the numerical solution of linear Volterra integral equations of the second kind

The solution of linear integral equations of the second kind can be sought with a variety of different analytical and numerical methods. From an analytical standpoint, these methods include methods from operational calculus namely, Laplace, Fourier or $\mathcal{Z}$-Transform (see Brown, Churchill, et al., 2009; Churchill, 1972), the use of Taylor expansions for the integrand inside the integral and the method of Adomian decomposition (see Wazwaz, 2011). The case of a stationary yielding mathematical plane described in Rice (2006a), has been solved making use of the Laplace transform. Those methods depend on the convolution property of the integral in the integral equation to transform it into a simpler algebraic equation. The challenge then lies in the inversion of the relation obtained in the auxillary (frequency) domain back to the time domain. However, as the complexity of the Green's function kernels and the loading function increases due to the introduction of boundary conditions and different assumptions concerning the trajectory of the shear band along the fault gouge, such an inversion is not always possible. We are then forced to use numerical methods for the solution of the above Volterra integral equation.

The above analytical methods have also their numerical counterparts, with the use of the Inverse Fast Fourier Transform (IFFT) being a central part in most numerical solution procedures. Still even with the use of $IFFT$, the inversion from the frequency domain remains a challenge. Here we will refer to another class of numerical methods called spectral collocation methods, which solve the integral differential equation directly in the time domain. These methods are conceptually easy to use, and since no inversion is required, they are able to handle very general cases of Green's function kernels and loading functions.

In what follows we will make use of the $\mathcal{Z}$-Transform and Convolution Quadrature Method ($\mathcal{Z}$-CQM) procedure (see Chaillat et al., 2009, and section 6.3.1) and the Spectral Collocation Method with Lagrange basis functions (SCML) (see Tang et al., 2008, and section 6.3.2) for the numerical solution of the integral equation (6.16).

More specifically in the cases of an unbounded domain, where the kernel of the pressure diffusion equation is weakly singular and the loading function is stationary or moving with a constant velocity v, we will make use of the $\mathcal{Z}$-CQM procedure, while in the cases of more complex loading conditions (periodic movement of the thermal load) inside bounded domains, where the kernel presents no analytical challenges, the SCLM collocation method will be used instead. The choice between the two methods is mainly made due to the difficulty in the generalization of the $\mathcal{Z}$-CQM procedure to more general loading and boundary conditions.

6.3.1 $\mathcal{Z}$-Transform convolution quadrature method ($\mathcal{Z}$-CQM) for integral differential equations

Before we continue with the applications to the shearing of a fault gouge, we present in brief the method used for calculating the convolutional integrals present in the integral equation (6.16). For more details see Mavaleix-Marchessoux et al., 2020.

First, we rewrite the Green's function kernel with the help of its inverse Laplace transform:

$$\tau(t) = f(\sigma_n - p_0) - C\int_0^t \tau(t')\frac{1}{2\pi i}\int_{\gamma-i\infty}^{\gamma+i\infty} G^{-1}(s, c_{hy}, c_{th}) \exp s(t-t')dsdt', \tag{6.23}$$

where $G^{-1}(s, c_{hy}, c_{th})$ is the inverse Laplace transform of the Green's function. We note here that γ is a real number who is bigger than the pole with the largest real part in the s complex plane. Since we know that the original problem has a solution that is bounded and, therefore, the integral expression on the right of equation (6.23) remains bounded, we can exchange the integration order, namely:

$$\tau(t) = f(\sigma_n - p_0) - C\frac{1}{2\pi i}\int_{\gamma-i\infty}^{\gamma+i\infty} G^{-1}(s, c_{hy}, c_{th})\int_0^t \tau(t') \exp s(t-t')dt'ds. \tag{6.24}$$

We note next that the integral inside the integrand of equation (6.24) can be written as the solution $h(t,s)$ to the ordinary differential equation problem:

$$\frac{\partial h}{\partial t} = sh(t) + \tau(t),\ h(0) = 0, t \geq 0. \tag{6.25}$$

To continue with our calculation, we sample the equation into n times with $\frac{1}{\Delta t}$ being the sampling frequency. The integral equation is then transformed:

$$\tau[n] = f(\sigma_n - p_0)u[n] - C\frac{1}{2\pi i}\int_{\gamma-i\infty}^{\gamma+i\infty} G^{-1}(s, c_{hy}, c_{th})h[n, s]ds, \tag{6.26}$$

where $\tau[n]$ is the sampled unknown friction and $u[n]$ is the sampled Heaviside step function. Applying next the $\mathcal{Z}$-Transform on both sides of equation (6.26), we obtain:

$$T(z) = f(\sigma_n - p_0)\frac{z}{z-1} - C\frac{1}{2\pi i}\int_{\gamma-i\infty}^{\gamma+i\infty} G^{-1}(s, c_{hy}, c_{th})H(z, s)ds. \tag{6.27}$$

Next we proceed by deriving an expression for $H(z)$. Sampling the differential equation that relates $h(t), \tau(t)$ by applying the Backward Euler difference scheme we arrive at:

$$\frac{h[n] - h[n-1]}{\Delta t} = sh[n] + \tau[n],\ h[0] = 0. \tag{6.28}$$

Applying the $\mathcal{Z}$-Transform on the auxiliary problem (6.28), we obtain $H(z)$ with respect to $T(z)$, namely:

$$H(z, s) = T(z)\frac{1}{\frac{z-1}{z\Delta t} - s}. \tag{6.29}$$

Replacing back into equation (6.27) and noting that we can replace the integral along the line with a contour integration, we finally obtain:

$$T(z) = f(\sigma_n - p_0)\frac{z}{z-1} - CG^{-1}\left(\frac{z-1}{z\Delta t}, c_{hy}, c_{th}\right)T(z), \tag{6.30}$$

which we can solve for $T(z)$ provided $(1 + CG^{-1}\left(\frac{z-1}{z\Delta t}, c_{hy}, c_{th}\right))$ is not singular. Reversing the transform, we can calculate the values of $\tau[n]$ at the sampling points $t_n = n\Delta t$.

By making use of the $\mathcal{Z}$-Transform we have transformed the original problem of the linear Volterra equation of the second kind into an algebraic equation, which we can solve directly for $T(z)$. Applying the inverse of the $\mathcal{Z}$-Transfrom (see Appendix G) we arrive finally at the frictional evolution of the fault w.r.t. time, $\tau(t)$.

6.3.2 Collocation method

As we will see in section 6.4, although the $\mathcal{Z}$-Transform method allows for calculation of the fault's frictional response for the cases of traveling strain localization on the unbounded domain and stationary strain localization on the bounded domain, its generalization in the case of a traveling instability on the bounded domain is not straightforward. This is due to the complexity of the traveling loading function. In particular, following the procedure described above and in Appendix F we arrive at a system of functional equations for the determination of the frictional response, which is a rather complicated procedure for the solution of a conceptually simple problem. The situation complicates even further if we want to study a periodic traveling strain localization as the one of chapter 5; there the procedure described in Appendic F reaches its limits.

We, therefore, turn towards a different, more efficient approach for the numerical solution of the integral equation in the case of a bounded domain subjected to a periodically traveling thermal load. Based on the work of Tang et al. (2008), we apply a spectral collocation method for the calculation of the frictional response. Spectral methods allow for evaluation of the solution in the whole domain of the problem yielding exponential degree of convergence. The principle of the method is the substitution of the unknown quantity inside the integral equation by a series of polynomials that constitute a polynomial basis. We then opt for the minimization of the residual between the exact and the approximate solution at specific points inside the problem's domain. We choose to approximate the frictional response in the space of the Lagrange polynomials. In order to make use of the exponential degree of convergence of the spectral method we transform and calculate both the integral equation and its convolution integral in the interval $[-1, 1]$ (see Appendix H).

We solve for the values of the frictional response at the Gauss-Legendre integration points that allow for an efficient computation of the integral in the modified integral equation. Different quadrature or integration rules can be used for the calculation of the integral and the solution of the integral equation. The choice of the quadrature or integration rule depends on the expected properties of the solution. Calculation on the same Gauss-Legendre integration points for the equation and the convolution integral allows for optimal interpolation of the solution in the space of Lagrange polynomials and exponential convergence of the results (see Tang et al., 2008; Wazwaz, 2011). Another popular choice is the calculation of the residual at the Gauss-Lobatto integration points. The last option allows us to evaluate exactly the values of the unknown function at the beginning and the end of the interval of interest, however, the efficiency of the interpolation decreases (see Tang et al., 2008).

More specifically, we write the solution of the linear Volterra integral equation of the second kind (6.16) in the form of a series $\tau(t) = \sum_{k=0}^{\infty} \tau_k F_k(t)$, where $F_k(t)$ are the basis functions and k indicates the k^{th} Lagrange polynomial used in the solution summation:

$$\sum_{k=0}^{\infty} \tau_k F_k(t_l) = f(\sigma_n - p_0) - C \int_0^t \sum_{k=0}^{\infty} \tau_k F_k(t') G_{(H,T)}(\tau_l - t', c_{hy}, c_{th}) dt'. \tag{6.31}$$

By performing a series of change of variables (see appendix H) we are able to write the equivalent algebraic equation as:

$$u_l + C\frac{1+x_l}{2} \sum_{k=0}^{N} u_k \left(\sum_{p=0}^{N} K(x_l, s(x_l, \theta_p)) F_k(s(x_l, \theta_p)) w_p \right) = f(\sigma_n - p_0),\ 0 \leq l \leq N. \tag{6.32}$$

By adopting the indicial notation with summation over repeated indices our system is written as:

$$(\delta_{m,n} + A_{m,n}) u_n(t_m) = g, \tag{6.33}$$

or in matrix form:

$$(I + A)\, u = g, \tag{6.34}$$

where $A_{m,n} = C\frac{1+x_m}{2} \sum_{n=0}^{N} \left(\sum_{p=0}^{N} K(x_m, s(x_m, \theta_p)) F_n(s(x_m, \theta_p)) w_p \right)$ and $g = \sigma_n - p_0$. We can then solve the algebraic system to find the interpolation coefficients u_j of the numerical solution. Due to the properties of the Lagrange polynomials the coefficients u_k are also the values of the numerical solution at the specific times t_k.

6.4 Applications

In this section we will present the evolution of the frictional strength $\tau(t)$ for the different cases of loading and boundary conditions described in section 6.2.1. The available values for the fault gouge properties considered homogeneous along its height are given in Table 6.1.

Parameters	Values	Properties	Parameters	Values	Properties
G	10.	GPa	β	0	-
σ_n	200	MPa	α_s	10^{-5}	$/^o$C
p_0	66.67	MPa	χ	1210^{-15}	m^2

Table 6.1 – Material parameters of a mature fault at the seismogenic depth (see Rattez, Stefanou, & Sulem, 2018; Rice, 2006b).

6.4.1 Stationary strain localization mode

6.4.1.1 Stationary strain localization on an unbounded domain

The solutions for the temperature field on an infinite layer under a stationary point source thermal load were first derived in Carslaw and Jaeger (1959). Mase and Smith (1987) and Andrews (2005), present temperature field solutions for stationary distributed thermal loads. Later in Lee and Delaney (1987) the authors used the above temperature solutions to derive the pressure solution fields $p(x,t)$ of the coupled pore fluid pressure equation.

In the work of Rempel and Rice, 2006; Rice, 2006a the authors introduce a methodology for the determination of the coupled frictional response of a Cauchy layer under constant shear rate. The results for the stationary instability on an infinite domain have already been derived in Rice (2006b) for yielding on a mathematical plane, and further expanded in the case of distributed yield in Rempel and Rice (2006). In this case a closed form analytical solution is possible: $\tau(\delta) = f(\sigma_n - p_0)\exp(\frac{\delta}{L^\star})\operatorname{erfc}(\sqrt{\frac{\delta}{L^\star}})$, $L^\star = \frac{4}{f^2}\left(\frac{\rho C}{\Lambda}\right)^2 \frac{\left(\sqrt{c_{hy}}+\sqrt{c_{th}}\right)^2}{\dot{\delta}}$. In Figure 6.1 we present the results of slip on a stationary mathematical plane based on the above mentioned analytical solution.

We note that this solution is dependent on the seismic slip rate $\dot{\delta}$. The dependence of the fault friction on the seismic slip rate $\dot{\delta}$ (velocity weakening) has been shown in experiments (see Badt et al., 2020; Harbord, Brantut, Spagnuolo, & Toro, 2021; Rempe et al., 2020, among many others).

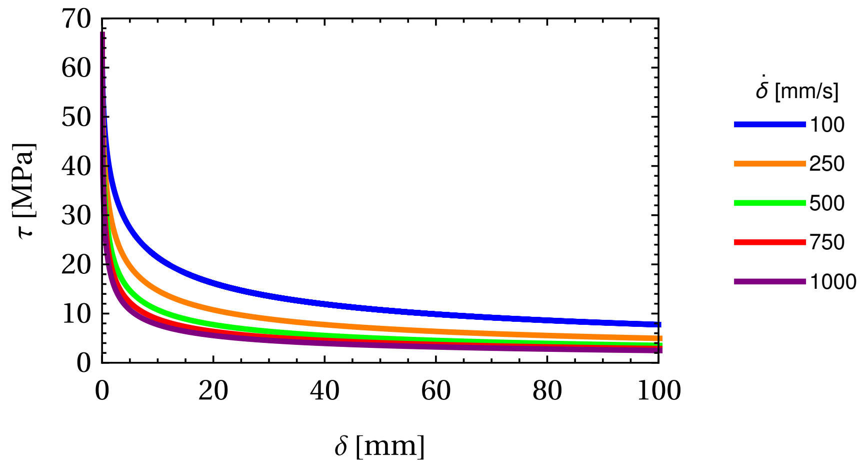

Figure 6.1 – Left: $\tau - \delta$ response of the layer for different slip velocities $\dot{\delta}$ applied. Due to the constant isothermal drained conditions at the boundary near infinity the solution tends asymptotically to the zero steady state solution.

6.4.1.2 Stationary strain localization on a bounded domain

When the yielding region (PSZ) is wholly contained on a mathematical plane one might assume that the true boundaries of the fault gouge play little role in the evolution of the phenomenon, simulating the fault gouge region as an infinite layer. However, the validity of this model depends heavily on the pressure and temperature diffusion characteristic times in comparison to the total evolution time of the seismic slip. In essence, the question is: Does the phenomenon evolve so fast that the boundaries do not play a role in the overall frictional response?

This is a valid question, considering that in experiments and in the majority of the numerical simulations, we need to assign some kind of boundary conditions to the problem in question. We address this question by investigating the case of a stationary instability (point thermal source) in the middle of a bounded domain representing the fault gouge, with the linear Volterra integral equation of the second kind (6.16). We do so by applying the new form of the kernel $G^{\star}_{X11}(x, x', t-t', c_{hy}, c_{th})$, which takes into account the boundary conditions of coseismic slip, pressure and temperature discussed in the previous chapter 5. Namely, the domain of the fault gouge was assumed to have a width of H = 1 mm. We remind also that the boundary conditions correspond to an isothermal $(T(0,t) = T(L,t) = 0)$ drained $(p(0,t) = p(L,t) = p_0)$ case.

In order to solve equation (6.16) for the new kind of boundary conditions, we need to derive the new expressions for the Green's function kernel for the thermal diffusion and coupled pore fluid pressure diffusion equations on the bounded domain. The expression for the bounded Green's function kernel under Dirichlet boundary of the heat diffusion equation (6.18), can be found by applying the method of separation of variables according to Cole et al., 2010.

Equation (6.18) is termed the long co-time Green's function kernel. A mathematically equivalent short co-time solution can be constructed making use of the Green's kernel defined for the infinite domain case via the method of images, however, its form is significantly more complicated than (6.18) and is not convenient for the numerical procedures used in this chapter. Namely the short co-time solution is best suited when studying transient diffusion at the very start of the phenomenon. For fast timescales we don't need a lot of terms for the short co-time series to converge to the expected degree of accuracy. However, for large timescales after the initiation of the phenomenon the large co-time solution converges faster. Furthermore, the form of the large co-time solution is simpler and can be integrated numerically faster than that of the short co-time.

Next, we need to obtain the Green's function for the coupled pore fluid pressure diffusion equation. This is done by solving the coupled pressure differential equation on the bounded domain, using the method of separation of variables. We note that the two diffusion problems (thermal and coupled pore fluid pressure) are bounded by Dirichlet boundary conditions on the same domain and therefore, their Fourier expansions belong to the same Sturm-Liouville problem. This allows us to express, for the first time in the literature, the Green's function kernel of the coupled temperature diffusion system on a bounded domain due to an impulsive thermal load. Full derivation details are shown in Appendix E, where we prove that the kernel in question can be given in a manner similar to the original expression for the infinite domain case found in Lee and Delaney, 1987.

Next, we apply the kernel of equation (6.18) in the equation (6.16). Using the $\mathcal{Z}$-CQM procedure as described in Mavaleix-Marchessoux et al., 2020, the values of friction at specific values of time (t) and seismic slip displacement (δ) can be derived for different seismic slip velocities ($\dot{\delta}$). The results of such an analysis are presented in Figure 6.2.

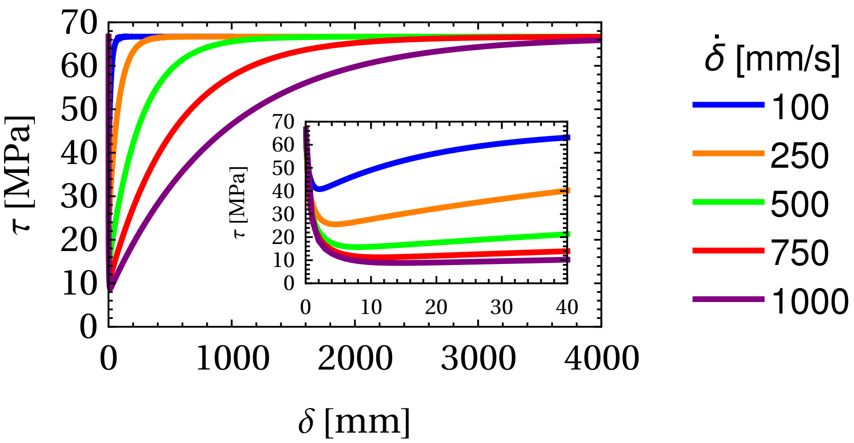

Figure 6.2 – $\tau - \delta$ response of the layer for different slip velocities $\dot{\delta}$ applied. We observe that as the shearing rate increases, the softening behavior becomes more pronounced. For typical values of the seismic slip displacement we note that the effect of the boundaries becomes important. Due to the existence of a steady state the fault recovers all of its strength lost to thermal pressurization at the beginning of the phenomenon.

We note here that contrary to the results obtained in the case of the infinite layer in Rempel and Rice, 2006; Rice, 2006a, where the frictional response is decreasing monotonously (see also Figures 6.2,6.3), in the case of the stationary thermal load on a bounded layer the frictional response is eventually influenced by the boundaries of the domain (see Figure 6.3). Since the conditions on the boundaries are constant in time and the frictional source provides heat to the layer at a rate that is bounded by a constant ($\frac{1}{\rho C}\tau(t)\dot{\delta} \leq \frac{1}{\rho C}\tau_0\dot{\delta} = M$), the temperature field will eventually reach a steady state. This in turn means that at the later stages of the phenomenon the temperature profile will remain constant in time, therefore its rate of change $\frac{\partial T}{\partial t}$ will become zero. Consequently, the phenomenon of thermal pressurization will cease, leading to rapid pore fluid pressure decrease due to the diffusion at the boundaries. As a result pore fluid pressure will return to its ambient value, and therefore, friction will regain its initial value too.

It is important to note here that as we show in Figure 6.3, frictional regain happens well inside the time and coseismic slip margins observed in nature during evolution of the earthquake phenomenon. Of course frictional regain depends on the height of the layer. Namely as the height of the layer increases, the stress drop due to thermal pressurization at the initial stages becomes larger and the fault gouge recovers its frictional strength slower and in later stages of slip. However, the height of the fault gouge H=1 mm cor-

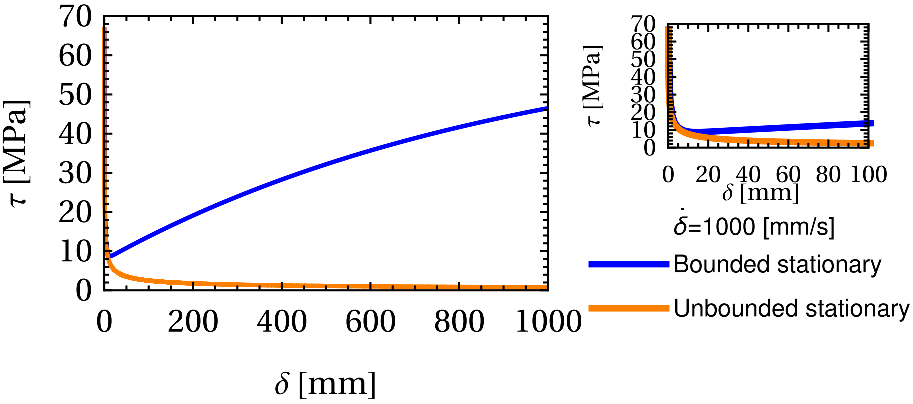

Figure 6.3 – Comparison of the $\tau - \delta$ response of the layer for an applied slip velocity $\dot{\delta} = 1000$ mm/s. We see that the influence of the boundaries becomes important from the early stages of coseismic slip. In the bounded case, due to the existence of a steady state the fault tends to recover all of its strength lost to thermal pressurization at the beginning of the phenomenon. namely for a typical value of coseismic slip $\delta = 1000$ mm, the fault has recovered more than half of its initial frictional strength.

responds to typical values from fault observations around the globe (see Myers & Aydin, 2004; Rice, 2006a; Sibson, 2003a; J. Sulem et al., 2004, among others). Furthermore, based on the significantly higher hydraulic, and to a lesser extent thermal, diffussivities of the surrounding damaged zone (see Aydin, 2000, and chapter 5), we conclude that the assumption of isothermal drained conditions at the boundaries of the fault gouge as a first approximation, is also justified [2]. Therefore, the a priori assumption that an infinite layer describes adequately well the fault gouge during seismic slip should, in our opinion, be revised.

6.4.2 Traveling mode of strain localization

In the available literature Rice, 2006a, 2006b and the subsequent works Platt et al., 2014b; Rempel and Rice, 2006; Rice et al., 2014b one of the main assumptions is that the principal slip zone (PSZ), which is described by the profile of the plastic strain rate (localized on a mathematical plane or distributed over a wider zone) remains stationed during shearing of the infinite layer. In this work we depart from this assumption, by assuming that the principal slip zone is traveling inside the fault gouge.

2. For a nature fault gouge the ratio of the hydraulic permeability of the fault gouge to the surrounding damaged zone lies between $r_{hy} = \frac{k^f_{hy}}{k^d_{hy}} = 10^2 \sim 10^6$

Two cases will be discussed, the first one discusses the implications of a traveling shear band inside the infinite layer, while the other case focuses on a moving shear band inside the bounded layer. The difference between a stationary and a moving shear band is that in the second case a steady state [3] for temperature and consequently pressure is not possible, since the profile of temperature constantly changes due to the thermal load constantly moving around the domain. This ensures that thermal pressurization never ceases. Thus, the value of the residual friction τ_{res} depends on the fault gouge's thermal and hydraulic properties (c_{th}, c_{hy}), the coseismic slip velocity $\dot{\delta}$, and the traveling velocity of the strain localization mode (v). This has serious implications for the frictional response of the layer during shearing. More specifically, as the load does not stay stationary, thermal pressurization does not have enough time to act by increasing the pore fluid pressure. Therefore, according to the Mohr-Coulomb yield criterion, friction does not vanish as in the case of Rice (2006a). Instead friction reaches a residual value τ_{res} different than zero. This is central for the dissipated energy (see Andrews, 2005; Kanamori & Brodsky, 2004b; Kanamori & Rivera, 2006, among others) and the control of the fault transition from steady to unsteady seismic slip (see Stefanou & Tzortzopoulos, 2020; Stefanou, 2019; Tzortzopoulos, 2021).

6.4.2.1 Traveling mode of strain localization on the unbounded domain.

Here we consider the shearing of a fault gouge, whose boundaries are taken at infinity. In what follows, we distinguish between the seismic slip velocity $\dot{\delta}$ and the velocity of the traveling shear band v. In Figure 6.4, we consider the PSZ (moving point heat source) to travel inside the fault gouge with a velocity v=50 mm/s, while different values for the rate of coseismic slip parameter $\dot{\delta}$ are taken into account. The shear band velocity v taken here is in agreement with observations from the numerical results of chapter 5. Contrary to the results obtained in the case of a stationary strain localization studied in Rice (2006a), our results indicate the existence of a lower bound in the frictional strength τ_{res}, dependent on the rate of seismic slip $\dot{\delta}$ (see Figure 6.5).

In Figure 6.4, we observe that an increase in seismic slip velocity $\dot{\delta}$ leads to a decrease of the frictional plateau. Since the plateau reached in these cases is other that the initial friction value corresponding to the ambient pore fluid pressure, we conclude that ther-

3. A steady state for the temperature $T(x,t)$ and pressure $p(x,t)$ fields is reached when their rates of change become zero, $\frac{\partial T}{\partial t} = 0$, $\frac{\partial p}{\partial t} = 0$

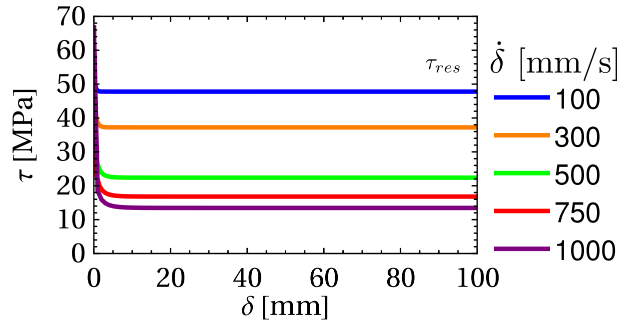

Figure 6.4 – $\tau - \delta$ response of the layer for different slip velocities $\dot{\delta}$ applied. We observe that as the shearing rate increases, the softening behavior becomes more pronounced. Higher seismic slip rates correspond to lower residual values for friction.

mal pressurization is still present in the model's response. This is true since the profile of temperature changes continuously, the maximum temperature, T_{max}, moves around in the same way as the yielding plane, therefore, the rate of change of the temperature field $\frac{\partial T}{\partial t}$, which is the cause of thermal pressurization does not vanish, rather it becomes constant.

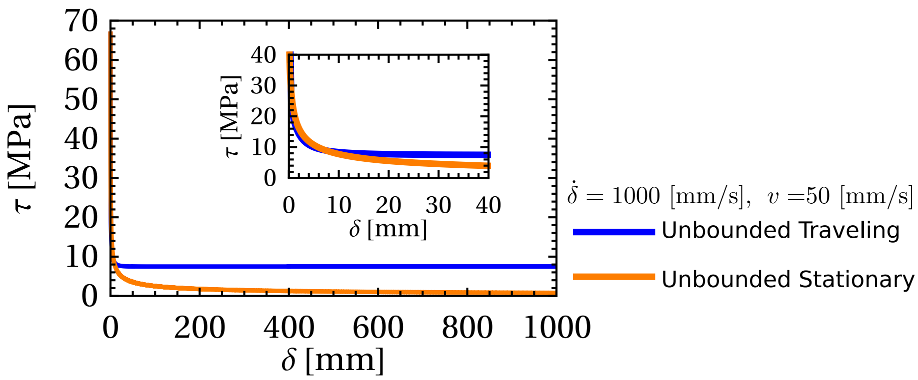

Figure 6.5 – Comparison of the $\tau - \delta$ frictional response between a moving and astationary strain localization (PSZ) on an unbounded domain. The assumption of a traveling strain localization leads to a plateau of non zero residual friction τ_{res}.

In Figure 6.6, we plot the frictional response of the fault for a given seismic slip velocity $\dot{\delta} = 1000$ mm/s treating the shear band velocity v as a parameter. We notice that the slower moving shear bands force the fault to faster and larger frictional strength drops, before they eventually reach a plateau. This is consistent with the observations made in Rice (2006a), where the stationary shear band that presents an infinite negative slope at the start of the slip δ and tends asymptotically to zero as δ increases, can be treated as a special case of the model of traveling localization mode as the shear band velocity tends to zero ($v = 0$). Again we emphasize that for this frictional behavior to hold true, we need to secure that the position of the yielding plane (PSZ) coincides with that of the maximum pore fluid pressure p_{max}. This is proven in Appendix I.

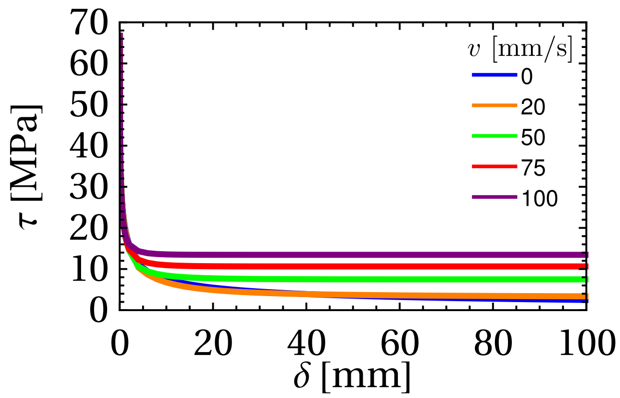

Figure 6.6 – Frictional response τ of the layer for different slip velocities $\dot{\delta}$ applied. For low traveling velocities the response tends to the behavior of stationary slip on a mathematical plane. As the traveling velocity increases the drop in friction becomes smaller.

6.4.2.2 Traveling mode of strain localization on the bounded domain.

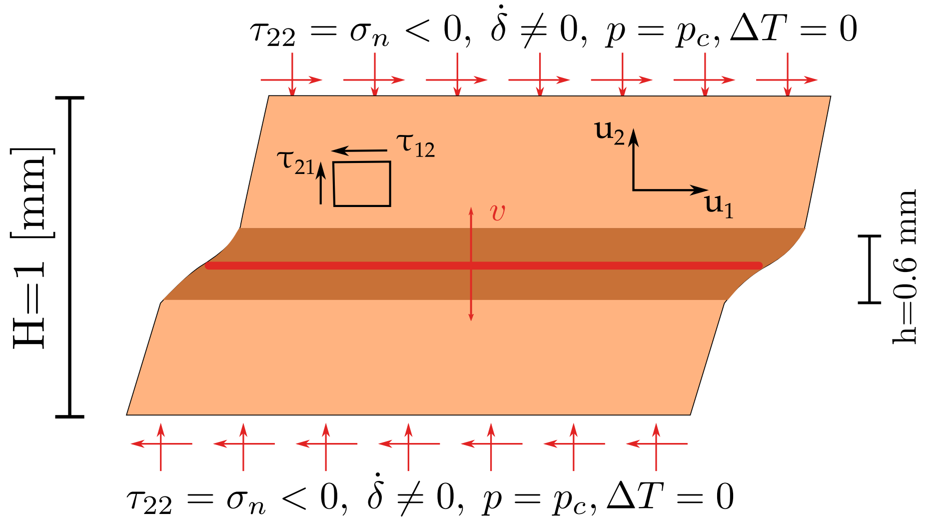

Figure 6.7 – Schematic representation of a fault gouge of height $H = 1$ mm, under seismic slip δ. The plastified region (brown color) is denoted with a thickness of $h = 0.6$ mm. The traveling strain localization on a mathematical plane (red color) is moving periodically inside the region h with velocity v.

In this section we investigate the frictional response of the layer of height H = 1 mm, when the plastic strain localization travels inside a predefined plastified region with a width h = 0.6 mm as shown in Figure 6.7. This is the same plastified region thickness as the one predicted by our numerical model in chapter 5 (see Figures 5.9). Based on the numerical results of chapter 5, we apply a periodic mode of traveling strain localization, with a constant velocity $v = 30$ mm/s. We prescribe the trajectory of the yielding plane by the following equation:

$$x(t) = \frac{\mathrm{H}}{2} + \frac{\mathrm{h}}{2\mathrm{H}} Tr(vt), \tag{6.35}$$

where H is the height of the layer, h is the width of the plastified region, v is the velocity of the strain localization and $Tr(\cdot)$ is the triangle wave periodic function. The period is given by $T = \frac{2\mathrm{h}}{v}$. Because of the complexity of the loading function, the application of the $\mathcal{Z}$-CQM procedure is presented separately in Appendix F. Moreover, the application of this numerical approach becomes cumbersome if not impossible for this case as explained in more details in Appendix F.
Instead, the resulting linear Volterra integral equations of the second kind will be solved numerically by making use of the spectral collocation method, that solves the corresponding algebraic system described in equations (6.32) and (6.33).

We observe that as the shearing rate increases, the softening behavior becomes more pronounced. For typical values of the seismic slip displacement we note that the effect of the boundaries becomes important. The frictional response presents oscillations due to the periodic movement of the strain localization. Since the strain localization is constantly moving, a steady state is not possible for the fields of temperature and pressure ($\frac{\partial T}{\partial t} \neq 0 \rightarrow \frac{\partial p}{\partial t} \neq 0$). This means that the friction presents a residual value, τ_{res}, which is lower than the fully recovered value of the stationary bounded case. Assuming the material parameters c_{th}, c_{hy} and the height of the layer H constant, characteristics such us the oscillations amplitude A, circular frequency ω and the residual value of friction τ_{res} are controlled by three parameters, the height of the plastified region inside the layer, h, the velocity of the strain localization mode, v, and the seismic slip rate applied at the fault gouge, $\dot{\delta}$.

We note here that for given fault gouge properties (c_{th}, c_{hy}, H) and seismic slip veloc-

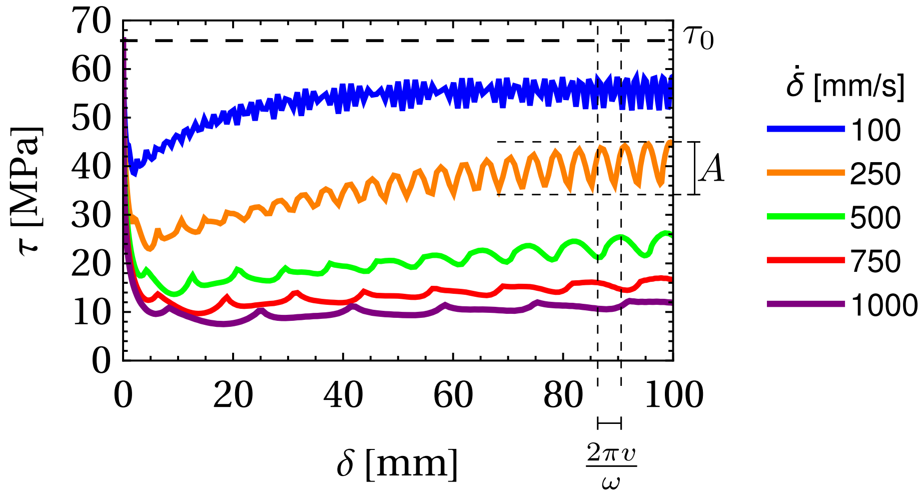

Figure 6.8 – $\tau - \delta$ response of the bounded layer for different slip velocities $\dot{\delta}$ applied. A periodic traveling localization mode is applied. We observe that as the shearing rate increases, the softening behavior becomes more pronounced. For typical values of the seismic slip displacement we note that the effect of the boundaries becomes important. Because the periodic traveling localization mode is constantly moving, a steady state is not possible. This means that the friction presents a residual value lower than the fully recovered value of the stationary bounded case.

ity $\dot{\delta}$ the residual frictional response presents a minimum for adequate selection of the plastified region and the velocity of the traveling strain localization mode (h, v). Considering that the fault gouge during elastic unloading will reach the smallest possible value of the residual friction dictated by the problem setting at hand, we expect that the values for the width of the plastified region h and the velocity of the strain localization mode v can be determined by minimizing the elastic energy i.e residual friction τ_{res} near the end of the seismic slip.

In Figure 6.9, we present a comparison between the friction developed during shearing of a bounded fault gouge with a seismic slip velocity $\dot{\delta} = 1000$ mm/s when the shear band is considered to travel with a velocity $v = 20$ mm/s inside a plastified region of height $\mathrm{h} = 0.4$ mm, and the model of slip on a stationary mathematical plane presented in section 6.4.1.1 and in Rice (2006a). The two responses differ. We note that the traveling strain localization presents a milder slope at the beginning of thermal pressurization w.r.t. the solution of Rice (2006a). This happens because the yielding plane moves towards the isothermal drained boundaries that function as heat and pressure sinks. The periodic movement of the yielding plane (thermal load) inside the layer leads to frictional oscillations. The crests of the oscillation correspond to the time the load approaches the fault gouge boundaries, while troughs correspond to the time the PSZ is closer to the middle of the layer. We note here that the average friction inside the layer, τ_{ave}, is increasing due to the diffusion of pressure and temperature at the boundaries of the fault gouge. We note also that the oscillatory movement of the fault gouge moves excess heat and pressure towards the boundaries of the fault gouge leading to a ventilation phenomenon that further enhances the recovery of frictional strength. It is likely that removing the invariance along the slip direction would lead to vortices and other convective phenomena inside the layer (see Griffani et al., 2013; Miller et al., 2013; Rognon et al., 2015). However, 2D and 3D phenomena inside the fault gouge are not explored here.

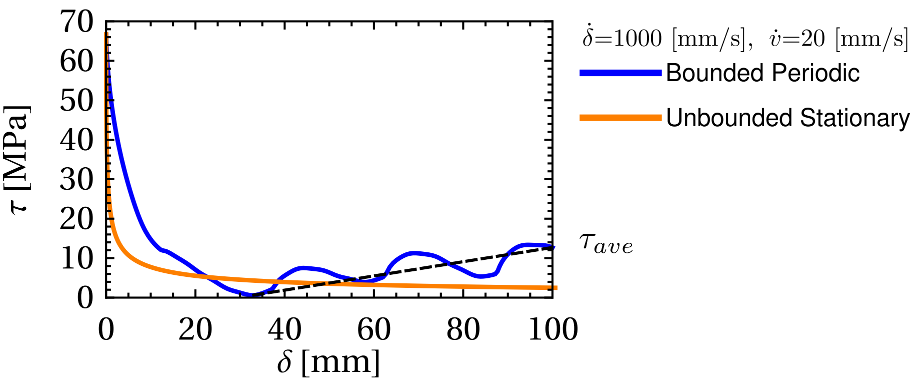

Figure 6.9 – Comparison of the $\tau - \delta$ frictional response between a moving periodic strain localization on a bounded domain and a stationary strain localization (PSZ) on an unbounded domain. The influence of the boundary conditions becomes clear from the initial stages of the coseismic slip δ. The average frictional response, τ_{ave}, in the case of the periodic strain localization exhibits frictional regain due to diffusion at the boundaries and ventilation phenomena from traveling inside the plastified region h.

The results obtained here (see Figure 6.8, 6.9), present a qualitative agreement with those of chapter 5. The difference in the values is due to the assumption of Dirac load in this chapter in order to preserve the equilibrium inside the band. Assuming a distribution of the yielding rate $\dot{\gamma}^p$ that is not singular while respecting the equilibrium conditions along the layer -as it is the case for the Cosserat continuum- would allow for higher minima in the frictional response, because the thermal load due to yield in this case will be distributed, leading to more efficient diffusion at the initial stages of thermal pressurization.

6.5 Key points

In this chapter a series of analytical results have been obtained for the coupled thermal and pore fluid pressure diffusion equations. We follow the methodology developed in Rempel and Rice, 2006; Rice, 2006a, and we expand it to the cases of bounded domains and moving thermal loads resulting from traveling (flutter) instabilities on a Cauchy continuum (see Benallal, 2005b; Benallal & Comi, 2003; Platt et al., 2014a; Rice, 2006a; Rice et al., 2014a).

To handle the integral differential equations a new method named the $\mathcal{Z}$-CQM procedure, was used based on the work of Mavaleix-Marchessoux et al., 2020. This is the first time this procedure is used for the solution of linear Volterra integral equations of the second kind. The method can handle the weakly singular kernels that appear in the unbounded case and the stationry thermal load on the bounded case. However, its generalization in the case of a periodic traveling strain localization inside the bounded domain, which is in accordance with the numerical results of chapter 5, is not straightforward (see Appendix F). Therefore, we apply a more general methodology, the spectral collocation method for the numerical solution of the more complicated case.

It is found that contrary to the case of a stationary thermal load on an unbounded domain described in Rice, 2006a, taking into account the existence of the boundary conditions at the ends of the fault gouge plays an important role at the frictional evolution of the fault for a range of values of the seismic slip velocities commonly observed during earthquake events. Namely, for a seismic slip δ of 1 m under a seismic slip velocity $\dot{\delta}$=1 m/s, the influence of the boundaries becomes important after the first 0.4 m of slip. It is shown that under the influence of homogeneous Dirichlet conditions on the bounded domain, a steady state is reached for the temperature field, which in turn implies that the effects of thermal pressurization progressively attenuate until it completely ceases. In this case the temperature rise inside the fault gouge is well above the limit of chemical decomposition and melting of quartzites (see Brantut et al., 2008; Kanamori & Brodsky, 2004a; Rice, 2006a; J. Sulem & Famin, 2009). Absence of widespread melting observations in faults, however, indicates that other possible frictional weakening mechanisms will become prevalent.

Furthermore, the effects of a moving thermal load corresponding to a traveling strain localization (flutter instability) inside the fault gouge, were examined under both unbounded and bounded boundary conditions. In both cases, traveling instabilities showed the existence of a plateau in the frictional strength of the fault, τ_{res} (see Figures 6.4, 6.8).

In the case of the traveling load on the unbounded domain, the fact that the load changes its position constantly leads to a non zero change of the temperature field ($\frac{\partial T(x,t)}{\partial t} \neq 0$) and constant influence of the pore fluid pressure profile by the thermal pressurization term. Moreover, because the thermal load changes its position, temperature does not have time to accumulate in one point and provoke a pressure increase that eliminates fault friction. Instead fault friction reaches a plateau (see Figure 6.4). This is an important result since it directly influences the dissipation energy produced during seismic slip.

Moreover, we examined the influence of the velocity of the strain localization (moving thermal load) in the frictional evolution. We established based on our analyses that the faster traveling shear bands have a smoother stress drop at the first stages of the analysis and they reach a higher plateau of frictional strength, see Figure 6.6. When the velocity of the shear band tends to zero we retrieve the solution described in Rice (2006a) as expected.

Next, a traveling instability was applied into a bounded domain with homogeneous Dirichlet boundary conditions. Again the results show that the frictional strength of the fault reaches a plateau and is not fully recovered as in the case of a stationary instability (see Figure 6.8). The reason is the change of the thermal load position during the analysis and the subsequent change of the temperature profile leading to a non attenuating thermal pressurization phenomenon. Again the plateau reached, differs based on the traveling velocity of the shear band v, which ranges in the order of $20 \sim 50$ mm/s according to the numerical analyses of chapter 5. In this case it is shown that in contrast to the case of a stationary thermal load on the bounded domain the fault never recovers entirely its frictional strength since the effects of thermal pressurization never cease.

The results presented above clearly show a strong dependence of the fault's frictional behavior in both the fault gouge boundary conditions and the type of instability permitted into the medium. These results can be used as a preliminary model in order to evaluate qualitatively the results obtained by numerical analyses taking into account the microstructure of the fault gouge material, where discerning between the effects of the different mechanisms affecting the frictional response of a fault undergoing thermal pressurization is more involved. The results of the fully non-linear numerical analyses with the Cosserat micromorphic continuum of chapter 5 agree qualitatively with the results from the linear model of this chapter. This indicates that the driving cause behind the obtained results is the diffusion from the thermal and hydraulic couplings to the mechanical description. The microstructure follows to a lesser extend. Its use in the solution of the BVP presented in chapter 5 is required in order for the dissipation and the meta-stable frictional response of the fault gouge to be calculated correctly excluding mesh dependency from the numerical results.

In conclusion, our results show that for typical values of seismic slip δ and seismic slip velocity $\dot{\delta}$, the effects of the boundaries of the fault gouge cannot be ignored. This means that those effects need to be accounted in both numerical analyses and laboratory experiments. The influence of different kind of boundary conditions needs to be studied. The introduction of a traveling (flutter-type) strain localization mode is an important aspect of our model. Its presence increases the frequency content of the earthquake and it prevents the bounded fault gouge from fully recovering its frictional shear strength due to the diffusion at the boundaries. The existence of oscillations and the reduction of the peak residual frictional strength are also important in understanding the transition form a stable to unstable seismic slip and subsequent fault nucleation (see Rempel & Rice, 2006; Rice, 1973b, 2006a; Viesca & Garagash, 2015). Furthermore, the existence of non zero upper and lower bounds in the fault's frictional behavior (τ_{min}, τ_{res}), has serious implications for any attempt in controling the transition form stable (aseismic) to unstable (coseismic) slip (see Stefanou & Tzortzopoulos, 2020; Stefanou, 2019; Tzortzopoulos, 2021).

Chapter 7

Conclusions and future perspectives

7.1 Conclusions

In this work we focused on describing the behavior of a fault gouge under the influence of multiphysical couplings during large coseismic slip. The role of thermal pressurization as a frictional weakening mechanism during coseismic slip was taken into consideration. We studied different approaches of strain regularization in an effort to correctly regularize strain localization on a mathematical plane in the presence of nominal or apparent strain softening. Out of detailed comparison of the numerical results in chapters 3 and 4 and mathematical arguments, we concluded that the first order micromorphic Cosserat continuum is the best choice for regularizing strain localization on a mathematical plane in our analyses. Furthermore, application of the Cosserat continuum allows us to consider the role of the microstructure during shearing of the fault. In chapter 5, we studied the influence of the seismic slip velocity $\dot{\delta}$ and the boundary conditions in the frictional behavior of a fault gouge. The effect of rate dependency within the framework of rate and state frictional modeling was also examined. We note that our numerical analyses are in qualitative agreement with the experimental results of other researchers (see Badt et al., 2020; Rempe et al., 2020), whose experiments lie in the same range of normalized parameters. Finally, in chapter 6, we verify the numerical results of chapter 5 by studying the basic model of seismic slip on a mathematical plane under the weakening mechanism of thermal pressurization available in Rice (2006a). We expand the theoretical model of thermal pressurization by expanding on its assumptions namely applying more realistic boundary conditions and a traveling strain localization mode.

Getting into the details, in chapter 3 we investigated by means of numerical analyses, the ability of different material laws in the frame of a Cauchy continuum to regularize strain localization as the solution bifurcates from the homogeneous deformation. Our analyses took place under quasistatic conditions, which is an acceptable idealization of the problem at hand. We investigated 1) viscosity regularization, 2) regularization through the use of multiphysical couplings in the case of a classical Cauchy continuum, and 3) regularization through the use of a first order micromorphic Cosserat continuum. In particular, we investigated the ability of viscosity to regularize strain localization on a mathematical plane. In the context of quasistatic analysis such a regularization is possible, however, it requires that the exact dimensions of the localization are known a priori. In addition, such an approach relies heavily on the accuracy of the numerical solver. We show that by reducing the solver accuracy, the numerical results indicate localization on a mathematical plane. Next, we examined the classical Cauchy continuum coupled with multiphysics equations, describing the generation of heat due to yielding and the subsequent pore fluid pressure increase due to thermal pressurization. This formulation introduces to the classical continuum the internal lengths due to the diffusion terms in the heat and mass transfer equations. Nevertheless, through the use of numerical analyses and bifurcation analyses, in chapter 3 we have shown that the introduction of multiphysical couplings in the case of a classical Cauchy continuum, does not regularize strain localization on a mathematical plane. The lack of an inherent length scale in the material description of the classical Cauchy continuum is the reason for the localization on a mathematical plane and mesh dependency of the numerical results.

The case of elasto-viscoplasticity of Perzyna or concistency type in the presence of inertia has been studied in particular in chapter 4. While the available literature in this subject is affluent, no conclusive results have been reached on the subject of viscous regularization in the framework of a classical Cauchy continuum. Following on the work of de Borst and Duretz, 2020; Loret and Prevost, 1990; Needleman, 1988; Sluys and de Borst, 1992; W. Wang et al., 1997, we apply the method of linear stability analysis for investigating the stability and post bifurcation regime of a classical elasto-viscoplastic Cauchy continuum under homogeneous deformation. We expand previous attempts of studying the regularization properties of viscoplasticity (see de Borst & Duretz, 2020, among others), by assuming that both the circular frequency ω and the wavenumber k of the perturbation are complex numbers. A new dispersion relation is derived, which involves a pole on the complex plane, whose existence was ignored in previous attempts in studying viscous regularization. This pole is responsible for strain localization on a mathematical plane.

The theoretical results were also tested numerically with the use of commercial software Abaqus, (Smith, 2009) and application of a user material of Perzyna type. We examined the dynamic behavior of the elasto-viscoplastic momentum equation under different kinds of initial conditions and we have established that viscous regularization does not prevent strain localization and mesh dependency. Our dynamical numerical analyses in the context of elasto-viscoplasticity were fully nonlinear taking into account elastic unloading of the region outside the strain localization. We have shown that linear strain softening and linear strain-rate hardening (Perzyna viscoplasticity) do not regularize strain localization on a mathematical plane and mesh dependency. Theoretical and numerical analyses have led us to the formulation of a criterion which indicates conditions for the perturbation of infinitesimal wavelength to grow and be noticeable in numerical analyses.

Through the theoretical and numerical analyses in the above chapters, we have shown that only the Cosserat continuum among the ones explored, being also the simplest micromorphic continuum, is able to regularize strain localization by means of a material parameter (internal length), which constitutes a characteristic of the material. In chapter 5 going beyond the works of Rattez, Stefanou, and Sulem, 2018; Rattez, Stefanou, Sulem, Veveakis, et al., 2018b, we perform numerical analyses of a fault gouge under large coseisimic slip using a Cosserat linear elastic perfectly plastic material, coupled with the energy and pore fluid pressure diffusion equations. To this end, the in house developed code Numerical Geolab (Stefanou, 2021) software was used, which is based on the open source FeniCs finite element library (see Alnæs et al., 2015). We expand the previous numerical results, which achieved a coseismic slip of 0.5 mm, presented in Rattez, Stefanou, and Sulem (2018), Rattez, Stefanou, Sulem, Veveakis, et al. (2018a, 2018b), by considering large coseismic slip of $\delta = 1000$ mm in relation to the small fault gouge thickness of H = 1 mm. To this end, we make use of the updated Lagrangian, Eulerian method (ALE), in order to study the fault gouge frictional evolution over large seismic slip and different seismic slip velocities.

Moreover, we investigate the effect of the boundary conditions at the beginning of the slip incorporating Dirichlet or Neumann boundary conditions for the temperature and pore fluid pressure diffusion equations as well as their combinations. As expected, the results form an envelope defined by the isothermal drained response and the adiabatic undrained response as upper and lower bound respectively. Next, we examine the influence of different seismic slip shearing velocities in the localization width inside the fault gouge. We note that smaller shear velocities $\dot{\delta}$ correspond to larger localization widths, and that the localization width for larger velocities ($\dot{\delta} > 0.7$ m/s) stays constant after the initial localization at the start of the analysis. We note furthermore, the existence of frictional regain due to the effect of the isothermal drained boundary conditions and the emergence of a traveling instability, moving inside the fault gouge.

The traveling instability affects the frictional response of the fault during shearing. In particular, the traveling instability is responsible for the faster diffusion of heat inside the fault gouge ("ventilation"), thus mitigating the effect of thermal pressurization. We note also that the effect of thermal pressurization is constrained due to isothermal drained conditions used in the numerical simulations. The interaction between the boundaries of the fault gouge and the traveling instability leads to the instability performing a periodic motion inside the yielding region. The existence of a traveling instability may explain observations, where adjacent fault gouges are found (see Nicchio et al., 2018), or the fault gouge is found to be unusually large, (see Platt et al., 2014b; Rice, 2006a; Rice et al., 2014b).

We propose a mathematical explanation for the emergence of the traveling instability in terms of the imaginary part of the Lyapunov exponent. We find that by increasing the softening parameter, the solution bifurcates from the initial fixed point, as a limit cycle makes its appearance in the phase space. Thus, due to the Hopf bifurcation present in the phase space of the numerical analysis, traveling instabilities become possible. We investigate the effect of the height of the fault gouge in the period of the oscillations of the traveling shear band. Based on the appropriate scaling performed in chapter 5, we find that indeed the shearing velocity $\dot{\delta}$ and the height of the layer directly influence the non dimensionalized diffusion coefficient $\bar{c_{hy}}$ of the normalized coupled partial differential equations. For instance, when a layer that is two times thicker than the reference, while we shear both of them equally fast the non dimensionalized diffusion coefficient $\bar{c_{hy}}$ of the thicker layer is halved. This leads to lower minima of fault friction and to an increase in the period of the frictional oscillations. In general, this oscillations behavior may indicate an increase in the frequency spectrum of the earthquake that may explain better the surface observations concerning the higher frequencies in the spectral content of the earthquake (see Aki, 1967; Brune, 1970; Haskell, 1964; Tsai and Hirth, 2020).

Finally, we enhance our numerical model by adding viscosity. It is found that the introduction of strain-rate hardening of Perzyna type, leads our model to exhibit characteristics that are close to those of the rate and state phenomenological friction law proposed in the literature (see Dieterich, 1992; Ruina, 1983a). The combination of multiphysical couplings and viscosity allows our model to describe both frictional jumps due to the sudden change in the seismic slip rate and the apparent softening due to the seismic slip rate as in the rate independent case. Furthermore, we emphasize that depending on the value of the viscosity parameter, our model can lead to stick slip events similar to those described in Kanamori and Rivera, 2006; Scholz, 2019 at the latter stages of the analyses.

Our results and the theoretical predictions of the model described in Rice (2006a) diverge significantly. The difference in the calculated responses motivates us to make an inquiry on the original assumptions of the frictional slip model proposed in Rice (2006a), Rice et al. (2014b). This model investigates the frictional response of the principal slip zone of the fault under coseismic slip, taking into account the frictional weakening mechanism of thermal pressurization. The approach followed in Rice (2006a), assumes that the principal slip zone (PSZ) is contained in a mathematical plane, and that the boundaries of the fault gouge are considered to be at infinity. This leads inevitably to a stationary shear band, with isothermal, drained boundary conditions at infinity. Moreover, in Rice (2006a), the yielding region is contained on a mathematical plane. Furthermore, its frictional value during plastic loading is given by a Mohr-Coulomb yield criterion dependent on the Terzaghi stress, while the domain outside the shear band is considered to be rigid, assuring the equilibrium of the shear stress. This approach leads finally to the solution of a linear Volterra integral equation of the second kind for the determination of the frictional response of slip on a mathematical plane. However, we find the assumptions about 1) the unbounded domain and 2) the localization mode of the infinite layer to be restrictive.

Departing from the previous approach, we assume that the boundaries of the fault gouge are not at infinity, but that the fault gouge is well formed with a specific height as also shown in Rattez, Stefanou, and Sulem (2018), Rattez, Stefanou, Sulem, Veveakis, et al. (2018a, 2018b). Due to the in situ thermo- hydraulic properties of the rock mass outside the fault gouge, it is considered to act more as a thermostat and a pressostat leading to isothermal, drained boundary conditions at the boundaries (see chapter 5, section 5.3.4 for more details). We evaluate the frictional response based on this assumption, and we find that the effects of drainage become apparent before the seismic slip reaches its final value. This by itself indicates the positive influence of the boundary conditions in mitigating the weakening of the frictional strength of the fault. We applied different values of seismic slip velocity $\dot{\delta}$ and we have established that in the case of a stationary principal slip zone (PSZ) due to the drainage at the boundaries the fault tends to regain all of it strength. A new steady state different than the one predicted in Rempel and Rice, 2006; Rice, 2006a; Rice et al., 2014b is found. Frictional regain is faster for the slowest seismic slip velocities since the initial frictional weakening due to thermal pressurization is less pronounced. This is in contrast to the case highlighted in the literature described in Lee and Delaney, 1987; Mase and Smith, 1987; Rice, 2006a, where due to the boundary conditions set to infinity, the frictional shear strength is monotonously decreasing. We note that in all cases the majority of the frictional regain ($\sim 60\%$) happens during shearing of 1 m of seismic slip displacement, therefore, the frictional regain during important earthquakes can become substantial (see Sibson, 2003a).

Next, we investigate the role of the localization mode in the frictional evolution of the fault friction. In chapter 5, making use of a Cosserat micromorphic continuum under the weakening mechanism of thermal pressurization, we have noticed traveling instabilities taking place inside the fault gouge. Furthermore, according to Benallal and Comi, 2003, in a saturated Cauchy continuum exhibiting apparent softening due to the pore fluid pressure, an initial divergence instability might give rise to a flutter (traveling) instability. Similar behavior has been noticed in numerical analyses by Collins-Craft et al., 2020, where the damage and evolution of the microstructure of a Cosserat micromorphic continuum is taken into account. Indications of a traveling shear band in situ observations have been given in Badt et al., 2020; Nicchio et al., 2018 (according to our interpretation of their experimental results). Therefore, we first consider the case, where such a traveling instability develops in an infinite domain. Contrary to the stationary case, where a steady state is reached and the frictional response of the fault tends to zero, in this case friction reaches a constant non zero value. The residual value of friction depends on the seismic slip velocity $\dot{\delta}$ and the velocity of the traveling shear band v. We have established that higher values of seismic slip velocity, $\dot{\delta}$, indicate lower values for the remaining frictional strength due to the increase of thermal pressurization. By varying the velocity of the shear band v, we change the time the thermal load acts along the layer's height. As the thermal load moves faster along the the layer's height thermal pressurization becomes less efficient due to "ventilation" phenomena. This leads to higher residual shear strength of the layer. Non zero residual shear strength at the later stages of the seismic slip indicates major changes to the estimations for the dissipation of energy inside the fault, and the earthquake nucleation criteria and rupture propagation (see Andrews, 2005; Kanamori and Rivera, 2006; Lykotrafitis et al., 2006; Rice, 1973b; Rosakis et al., 1999). The existence of lower and upper bounds of friction during coseismic slip under thermal pressurization are of major importance for applications concerning the control of the transition from stable (aseismic) to unstable (coseismic) slip (see Stefanou & Tzortzopoulos, 2020; Stefanou, 2019; Tzortzopoulos, 2021).

Summarizing, the main findings of this thesis are:

- We investigated under the general assumption of quasistatic conditions, the regularization properties of different material models under plastic strain softening, involving a) a Cauchy continuum with: 1)viscosity of Perzyna and concistency type, 2) THM couplings, and b) a first order micromorphic Cosserat continuum. We show with the help of Lyapunov stability analysis and numerical analyses that the simplest model capable of regularizing strain form localizing on a mathematical plane is the Cosserat first order micromorphic continuum. This happens due to the introduction of internal lengths in the material behavior.
- We have also studied with the help of Lyapunov stability analysis the regularization properties of the Cauchy strain softening, strain-rate hardening Perzyna or consistency elastoviscoplastic model in the presence of inertia. To do so we have made extensive use of complex analysis to show the existence of a pole in the positive imaginary axis, neglected by former attempts that studied this problem. We have proven both theoretically and numerically with the use of fully non linear dynamic analyses, that viscoplasticity in the presence of inertia leads to strain localization on a mathematical plane. Our analyses and results were published in the CMAME journal Stathas and Stefanou (2022c).
- We apply the above conclusion in the modeling of a fault gouge under large coseismic slip. We introduce the influence of THM couplings in our model that lead to apparent strain softening due to the frictional weakening mechanism of thermal

pressurization. We advance further than the analyses presented in Rattez, Stefanou, and Sulem (2018), Rattez, Stefanou, Sulem, Veveakis, et al. (2018a, 2018b) by applying realistic seismic slip values that are orders of magnitude larger (m) than the height of the fault gouge (mm). We consider the influence of large displacements in the numerical results of our analyses by implementing an Adaptive Lagrangian Eulerian (ALE) procedure.

- We explored different combinations of boundary conditions, ranging from isothermal drained to adiabatic undrained. Their influence in the fault's frictional response at the early stages of the coseismic slip was taken into account.
- The numerical results of the above described analyses indicate that our model during the later stages of coseismic slip recovers a large part of its frictional strength initially lost to thermal pressurization. This is true due to diffusion at the boundaries of the model.
- Furthermore, the above numerical results present frictional oscillations during the later stages of coseismic slip. This is due to the existence of a traveling strain localization inside the fault gouge.
- We investigated the influence of the height of the layer in the layer's residual friction and the period of the frictional oscillations. We find that applying the same seismic slip velocity, while doubling the height of the layer leads to lower minima in the frictional response with meager and slower frictional recovery in comparison to the reference case. Furthermore, the period of the oscillations inside the thicker layer increases as does also the width of the plastified region. These observations are in agreement with the conclusions derived from the normalized form of the coupled THM system of PDEs.
- We further extend our model by taking into account strain rate hardening of Perzyna type (viscosity effects). We find that intrduction of viscosity in the THM coupled system leads to our model exhibiting rate and state phenomenology, without us making any assumption for the existence of internal memory state variables as in the, phenomenological, rate and state friction laws (see Dieterich, 1992; Ruina, 1983a).
- We observe that the numerical analyses performed concerning the influence of the THM couplings in the fault's frictional response are in close agreement with experiments performed on wet rocks, where care was taken to isolate Thermal pressurization as the only frictional weakening mechanism present during shear (see

Badt et al., 2020). We note here that numerical analyses and experimental results were done on the same parameter range for the non dimensionalized diffusion equations, therefore the numerical and experimental results are comparable.

- Our numerical results diverge spectacularly from the predictions of the thermal pressurization model during slip on a mathematical plane described in Rice (2006a). We explain this difference by investigating the assumptions presented in Rice (2006a). In particular, the model in Rice (2006a) assumes that seismic slip takes place on a stationary mathematical plane lying inside an infinite (unbounded domain) under isothermal drained boundary conditions. In our opinion, these assumptions are very restrictive. Considering the Volterra integral equation of the second kind described in Rice (2006a), we study the frictional evolution when the boundaries are taken into account in a bounded domain. Furthermore, based on the numerical results of chapter 5 we apply a traveling strain localization instead of a stationary one. The response obtained by solving the linear Volterra integral equation of the second kind is in qualitative agreement with the numerical results of the THM analyses, indicating a reappraisal of the frictional weakening mechanism of thermal pressurization.
- In preforming the analyses of chapter 6 different numerical methods were used. To tackle the numerical challenges posed by the Green's function kernels inside the linear Volterra integral equation of the second kind, we used two different methods availlable in the literature. For the singular kernels resulting from diffusion on an unbounded domain, the $\mathcal{Z}$-Transform with Convolution Quadrature Method ($\mathcal{Z}$-CQM) procedure was used. This is the first time this method is used for the solution of linear Volterra integral equations of the second kind. While for the bounded domain, with periodic traveling yielding plane (thermal load due to dissipation) a more general Spectral Collocation Method with Lagrange basis functions (SCML) was used.
- In order to investigate the response of the coupled thermal, pressure diffusion problem in chapter 6 for a isothermal drained bounded domain, the Green's function kernel describing the pressure response for an impulsive thermal load was derived for the first time in the literature.
- Finally, our results provide new boundaries for the minimum and residual friction during coseismic slip. This has important implications for the energy dissipated during coseismic slip, therefore affecting the energy equilibrium during coseismic

slip (see Andrews, 2005; Kanamori & Brodsky, 2004b), the criteria that are currently in use for fault nucleation (see Rempel & Rice, 2006; Rice, 1973a, 2006a; Viesca & Garagash, 2015), as well as any attempt in controlling the transition from aseismic to coseismic slip (see Stefanou & Tzortzopoulos, 2020; Stefanou, 2019; Tzortzopoulos, 2021).

Perspectives

In this thesis we studied theoretically and numericaly, the frictional response of the fault gouge when thermal pressurization is considered as the main weakening mechanism during coseismic slip and large deformations. The role of the microstructure, the shear velocity and the introduction of viscosity was studied in particular. This work can be expanded to incorporate some crucial characteristics emerging from the interactions of the grains at the microscale and other THM couplings. Namely:

- A new yield condition might be added based on the grain interactions at the microscale and incorporating damage of the material particles (see Alaei et al., 2021; Collins-Craft et al., 2020).
- The effect of other weakening mechanisms such as thermal decomposition of minerals should be also considered (see J. Sulem and Famin, 2009; E. Veveakis et al., 2007).
- The mechanism of flash heating Rice, 2006a should be also implemented as a precursor to thermal pressurization in combination with other thermal weakening mechanisms (I. Vardoulakis, 2000b).
- The model we use in this thesis for the determination of the fault gouge frictional behavior during coseismic slip is a model at the mesoscale, where we incorporate the behavior of the microscale through the use of the Cosserat continuum. We should incorporate in our analyses a more detailed description of the microstructure, which can be used at the level of the auxillary problem in upscaling techniques such as asymptotic homogenisation (see Bakhvalov & Panasenko, 1989; Forest, Pradel, et al., 2001; Froiio et al., 2006; Rezakhani & Cusatis, 2016; Sanchez-Palencia, 1986)
- Taking into account a more detailed description of the microstructure requires finer discretization in the spatial and time domains. This in turn increases the computational cost of any numerical procedure, especially in what concerns the material algorithm. We intend on solving this problem by incorporating a Thermodynamics-

based Artificial Neural Network both for the material behavior and upscaling to the macrostructure (TANN, see Masi & Stefanou, 2021; Masi et al., 2021).

We note here that the specific boundary conditions used (isothermal, drained), together with the traveling instability, lead to increased temperatures inside the fault gouge. However, the absence of pseudodactylites inside the fault gouge (see Brantut et al., 2008; Kanamori and Rivera, 2006; Sibson and Toy, 2006), indicates that such increased temperatures are not possible. This indicates that the influence of boundary heterogeneities, the role of the microstructure in the formation of an adequate yield criterion taking into account the comminution of the grains (see Collins-Craft et al., 2020), and the coexistence of other weakening mechanisms such as thermal decomposition of minerals (see J. Sulem and Famin, 2009) should be also taken into account.

Following the findings of our research, we propose that the role of the boundary conditions should be investigated in depth experimentally. In particular, the interaction of the traveling shear band with the regions adjacent to the fault gouge will give us insights about the formation of the fault gouge. This way we can also investigate the heterogeneity in the material parameters inside the fault gouge and the adjacent region. By incorporating earth blocks in vertical direction, adjacent to the fault, into the analysis, we expect to increase more the frequency content of the produced earthquake. This is due to the relative movement of the blocks along the height of the rockmass.

The above point can be comnbined with the frictional oscillations present in the model's frictional response. Through the use of a Fast Fourier Transform (FFT) procedure we can calculate the acceleration spectra obtained in the rock and compare with existing observations leading to additional answers in the problem of absence of higher frequencies from the calculated seismic spectra based on the current models (Aki, 1967; Brune, 1970; Tsai & Hirth, 2020). Furthermore, we propose that there is a relationship between the thickness of the fault gouge and the oscillatory frequency of the frictional oscillations. Thus, by identifying the high frequencies of the seismic response spectrum observed at the earth's surface, correlations could be made for identifying the thickness of the fault gouge and the amplitude of the frictional oscillations.

Our analyses have indicated a relationship between the layer's height, the rate of coseismic slip, the velocity of the PSZ inside the fault gouge and the period of the frictional oscillations. We intend on examining further the theoretical results in order to define the velocity of the traveling strain localization, PSZ based on our coupled simplified THM model.

In our analyses, we have always assumed that the slip distribution during the seismic event is uniform, by shearing with a constant average seismic slip velocity. However, this is not true and it is expected that the majority of the slip happens in the middle of the fault and not near the propagating fracture tips. This leaves us with different seismic slip and seismic slip velocity distributions, that will affect thermal pressurization and the effect of drainage and the localization mode in the final results (see Harbord, Brantut, Spagnuolo, and Di Toro, 2021; Lee and Delaney, 1987; Mase and Smith, 1987; Platt et al., 2014b). We can obtain a preliminary estimate of such a change by modifying the shearing velocity of the thermal load in the simplified linear model of chapter 6, based on the slip-rate evolution determined by elasto-dynamic analyses of specific faults.

The frictional response obtained by our analyses, can be used as an interface law for the sliding between earth blocks during coseismic slip. Implementing the proposed frictional law, with strain-rate dependence due to the viscous parameter and weakening due to thermal pressurization will give us realistic results concerning the energy partition during coseismic slip.

Finally, this thesis is mainly concerned with the determination of the frictional response under coseismic slip. This constitutes one branch of interest for the CoQuake project, which provided support for the completion of this thesis. The derived results allow us to present new bounds for the minimum and residual values of friction during coseismic slip, when the mechanism of thermal pressurization is the only frictional weakening mechanism taken into account. In addition, the existence of frictional oscillations is also an important aspect of our model, because during evolution of the coseismic slip the frictional slope of the weakening part of the oscillation can be lower than that of the main softening branch at the initial phase of the slip. These observations are central for control applications considering the transition from unstable (coseismic) to stable (aseismic) slip, which constitute the other branch of the CoQuake project (see Stefanou & Tzortzopoulos, 2020; Stefanou, 2019; Tzortzopoulos, 2021).

PUBLICATIONS

Stathas, A., & Stefanou, I. (2022a). Fault friction under thermal pressurization during large coseismic-slip Part I: Numerical analyses. *under review*, -, -.

Stathas, A., & Stefanou, I. (2022b). Fault friction under thermal pressurization during large coseismic-slip Part II: Expansion to the model of frictional slip. *under review*, -, -.

Stathas, A., & Stefanou, I. (2022d). The role of viscous regularization in dynamical problems, strain localization and mesh dependency. *Computer Methods in Applied Mechanics and Engineering*, *388*, 114185.

Stefanou, I., Gerolymatou, E., & Stathas, A. (2022). Strain localization in geomaterials and regularization:rate-dependency, higher order continuum theories andmultiphysics. *in preparation.*

Conferences

Stathas, A., & Stefanou, I. (2021a). Numerical investigation of the role of thermal pressurization in the fault's frictional response under large coseismic slip. *32th ALERT Workshop, Aussois, France, 27 – 03 October 2021.*

Stathas, A., & Stefanou, I. (2021b). Numerical investigation of the role of Thermal pressurization in the fault's frictional response under large coseismic slip. *AGU Fall meeting, New Orleans,13-17 December 2021.*

Stathas, A., & Stefanou, I. (2021c). Thermal pressurization of earthquake faults under large co-seismic slip using Cosserat continuum. *IUTAM Symposium - Generalized continua emerging from microstructures, Paris, France, 22 – 27 July 2021.*

Stathas, A., & Stefanou, I. (2021d). Viscous regularization does not regularize strain localization on a mathematical plane and mesh dependence! *32th ALERT Workshop, Aussois, France, 27 – 03 October 2021.*

REFERENCES

Abellan, M. A., & de Borst, R. (2006). Wave propagation and localisation in a softening two-phase medium. *Computer Methods in Applied Mechanics and Engineering*, *195*(37-40), 5011–5019. https://doi.org/10.1016/j.cma.2005.05.056

Aifantis, K., Konstantinidis, A., & Forest, S. (2010). Modeling strain localization bands in metal foams. *Journal of computational and theoretical nanoscience*, *7*(2), 360–366.

Aki, K. (1967). Scaling law of seismic spectrum. *Journal of Geophysical Research*, *72*(4), 1217–1231. https://doi.org/10.1029/jz072i004p01217

Alaei, E., Marks, B., & Einav, I. (2021). A hydrodynamic-plastic formulation for modelling sand using a minimal set of parameters. *Journal of the Mechanics and Physics of Solids*, *151*(September 2020), 104388. https://doi.org/10.1016/j.jmps.2021.104388

Alevizos, S., Poulet, T., & Veveakis, E. (2014). Thermo-poro-mechanics of chemically active creeping faults. 1: Theory and steady state considerations. *Journal of Geophysical Research: Solid Earth*, *119*(6), 4558–4582. https://doi.org/10.1002/2013JB010070

Alnæs, M. S., Blechta, J., Hake, J., Johansson, A., Kehlet, B., Logg, A., Richardson, C., Ring, J., Rognes, M. E., & Wells, G. N. (2015). The FEniCS Project Version 1.5. *Archive of Numerical Software*, *3*(100). https://doi.org/https://doi.org/10.11588/ans.2015.100.20553

Andrews, D. J. (2002). A fault constitutive relation accounting for thermal pressurization of pore fluid. *Journal of Geophysical Research: Solid Earth*, *107*(B12), ESE 15–1–ESE 15–8. https://doi.org/10.1029/2002jb001942

Andrews, D. J. (2005). Rupture dynamics with energy loss outside the slip zone. *Journal of Geophysical Research: Solid Earth*, *110*(1), 1–14. https://doi.org/10.1029/2004JB003191

Arfken, G. B., & Weber, H. J. (1999). Mathematical methods for physicists. American Association of Physics Teachers.

Arnol'd, V. I. (2013). *Mathematical methods of classical mechanics* (Vol. 60). Springer Science & Business Media.

Aydin, A. (2000). Fractures, faults, and hydrocarbon entrapment, migration and flow. *Marine and petroleum geology*, *17*(7), 797–814.

Badt, N. Z., Tullis, T. E., Hirth, G., & Goldsby, D. L. (2020). Thermal Pressurization Weakening in Laboratory Experiments. *Journal of Geophysical Research: Solid Earth*, *125*(5), 1–21. https://doi.org/10.1029/2019JB018872

Bakhvalov, N. S., & Panasenko, G. P. (1989). *Homogenisation : averaging processes in periodic media : mathematical problems in the mechanics of composite materials*. https://doi.org/10.1007/978-94-009-2247-1

Beltzer, A. I. (1988). *Acoustics of solids*. Springer-Verlag Berlin Heidelberg. https://doi.org/10.1007/978-3-642-83370-0

Benallal, A., Berstad, T., Børvik, T., Clausen, A., & Hopperstad, O. (2006). Dynamic strain aging and related instabilities: experimental, theoretical and numerical aspects. *European Journal of Mechanics - A/Solids*, *25*(3), 397–424. https://doi.org/https://doi.org/10.1016/j.euromechsol.2005.10.007

Benallal, A., Berstad, T., Børvik, T., Hopperstad, O., Koutiri, I., & de Codes, R. N. (2008). An experimental and numerical investigation of the behaviour of AA5083 aluminium alloy in presence of the Portevin–Le Chatelier effect [Special Issue in Honor of Jean-Louis Chaboche]. *International Journal of Plasticity*, *24*(10), 1916–1945. https://doi.org/https://doi.org/10.1016/j.ijplas.2008.03.008

Benallal, A. (2005a). On localization modes in coupled thermo-hydro-mechanical problems. *Comptes Rendus Mécanique*, *333*(7), 557–564. https://doi.org/https://doi.org/10.1016/j.crme.2005.05.005

Benallal, A. (2005b). On localization modes in coupled thermo-hydro-mechanical problems. *Comptes Rendus Mécanique*, *333*(7), 557–564. https://doi.org/https://doi.org/10.1016/j.crme.2005.05.005

Benallal, A., & Comi, C. (2003). Perturbation growth and localization in fluid-saturated inelastic porous media under quasi-static loadings. *Journal of the Mechanics and Physics of Solids*, *51*(5), 851–899. https://doi.org/10.1016/S0022-5096(02)00143-6

Bernard, A., Lowe, M. J. S., & Deschamps, M. (2001). Guided waves energy velocity in absorbing and non-absorbing plates. *The Journal of the Acoustical Society of America*, *110*(1), 186–196. https://doi.org/10.1121/1.1375845

Bernard, P.-E., Moës, N., & Chevaugeon, N. (2012). Damage growth modeling using the Thick Level Set (TLS) approach: Efficient discretization for quasi-static loadings. *Computer Methods in Applied Mechanics and Engineering*, *233*, 11–27.

Bigoni, D. (2012). *Nonlinear solid mechanics: bifurcation theory and material instability*. Cambridge University Press.

Bizzarri, A., & Bhat, H. (2012). *The Mechanics of Faulting: From Laboratory to Real Earthquakes*. Research Signpost. https://books.google.fr/books?id=tlr6lgEACAAJ

Blanpied, M. L., Lockner, D. A., & Byerlee, J. D. (1995). Frictional slip of granite at hydrothermal conditions. *Journal of Geophysical Research*, *100*(B7). https://doi.org/10.1029/95jb00862

Bonelli, S., Dascalu, C., & Nicot, F. (2011). *Advances in Bifurcation and Degradation in Geomaterials: Proceedings of the 9th International Workshop on Bifurcation and Degradation in Geomaterials*. Springer Science & Business Media.

Borcherdt, R. D. (1973). Energy and plane waves in linear viscoelastic media. *Journal of Geophysical Research*, *78*(14), 2442–2453. https://doi.org/10.1029/jb078i014p02442

Boullier, A. M., Yeh, E. C., Boutareaud, S., Song, S. R., & Tsai, C. H. (2009). Microscale anatomy of the 1999 Chi-Chi earthquake fault zone. *Geochemistry, Geophysics, Geosystems*, *10*(3). https://doi.org/10.1029/2008GC002252

Brantut, N., Schubnel, A., Rouzaud, J. N., Brunet, F., & Shimamoto, T. (2008). High-velocity frictional properties of a clay-bearing fault gouge and implications for earthquake mechanics. *Journal of Geophysical Research: Solid Earth*, *113*(10), 1–18. https://doi.org/10.1029/2007JB005551

Brauer, F., & Nohel, J. (1969). *The Qualitative Theory of Ordinary Differential Equations: An Introduction*. New York, Dover Publications.

Brown, J. W., Churchill, R. V. Et al. (2009). *Complex variables and applications*. Boston: McGraw-Hill Higher Education.

Brune, J. N. (1970). Tectonic stress and the spectra of seismic shear waves from earthquakes. *J Geophys Res*, *75*(26), 4997–5009. https://doi.org/10.1029/jb075i026p04997

Burns, T. J. (1985). Approximate linear stability analysis of a model of adiabatic shear band formation. *Quarterly of Applied Mathematics*, *43*(1), 65–84.

Burns, T. (1985). *Influence of effective rate sensitivity on adiabatic shear instability* (tech. rep.). Sandia National Labs., Albuquerque, NM (USA).

Cappa, F., Scuderi, M. M., Collettini, C., Guglielmi, Y., & Avouac, J.-P. (2019). Stabilization of fault slip by fluid injection in the laboratory and in situ. *Science advances*, *5*(3), eaau4065.

Carcione, J. M. (Ed.). (2015). *Wave Fields in Real Media (Third Edition)* (Third Edition). Oxford, Elsevier. https://doi.org/https://doi.org/10.1016/B978-0-08-099999-9.00002-9

Carpenter, B. M., Marone, C., & Saffer, D. M. (2011). Weakness of the San Andreas Fault revealed by samples from the active fault zone. *Nature Geoscience*, *4*(4), 251–254. https://doi.org/10.1038/ngeo1089

Carslaw, H. S., & Jaeger, J. C. (1959). *Conduction of heat in solids* (tech. rep.). Clarendon Press.

Chaillat, S., Bonnet, M., & Semblat, J.-F. (2009). A new fast multi-domain BEM to model seismic wave propagation and amplification in 3-D geological structures. *Geophysical Journal International*, *177*(2), 509–531.

Chambon, R., Caillerie, D., & Matsuchima, T. (2001). Plastic continuum with microstructure, local second gradient theories for geomaterials: localization studies. *International Journal of Solids and Structures*, *38*(46-47), 8503–8527. https://doi.org/https://doi.org/10.1016/S0020-7683(01)00057-9

Chambon, R., Caillerie, D., & Viggiani, G. (2004). Loss of uniqueness and bifurcation vs instability: some remarks. *Revue française de génie civil*, *8*(5-6), 517–535.

Chester, F. M., & Chester, J. S. (1998a). Ultracataclasite structure and friction processes of the Punchbowl fault, San Andreas system, California. *Tectonophysics*, *295*(1-2), 199–221. https://doi.org/10.1016/S0040-1951(98)00121-8

Chester, F. M., & Chester, J. S. (1998b). Ultracataclasite structure and friction processes of the Punchbowl fault, San Andreas system, California. *Tectonophysics*, *295*(1), 199–221. https://doi.org/https://doi.org/10.1016/S0040-1951(98)00121-8

Chester, J. S., Chester, F. M., & Kronenberg, A. K. (2005). Fracture surface energy of the Punchbowl fault, San Andreas system. *Nature*, *437*(7055), 133–136. https://doi.org/10.1038/nature03942

Churchill, R. V. (1972). Operational mathematics.

Ciardo, F., Lecampion, B., Fayard, F., & Chaillat, S. (2020). A fast boundary element based solver for localized inelastic deformations. *International Journal for Numerical Methods in Engineering*, *121*(24), 5696–5718.

Cole, K., Beck, J., Haji-Sheikh, A., & Litkouhi, B. (2010). *Heat conduction using Greens functions*. CRC Press.

Collins-Craft, N. A., Stefanou, I., Sulem, J., & Einav, I. (2020). A Cosserat Breakage Mechanics model for brittle granular media. *Journal of the Mechanics and Physics of Solids*, 103975.

Collins-craft, N. A., Stefanou, I., Sulem, J., Einav, I., Navier, L., Paristech, P., & Eiffel, G. (2019). A Cosserat Breakage Mechanics model for brittle granular media, 1–29.

Cook, F. A., White, D. J., Jones, A. G., Eaton, D. W., Hall, J., & Clowes, R. M. (2010). How the crust meets the mantle: Lithoprobe perspectives on the Mohorovičić discontinuity and crust–mantle transition. *Canadian Journal of Earth Sciences*, *47*(4), 315–351.

Coussy, O. (2004). *Poromechanics*. John Wiley & Sons. https://doi.org/https://doi.org/10.1002/9780470710388

Da Cruz, F., Emam, S., Prochnow, M., Roux, J.-N., & Chevoir, F. (2005). Rheophysics of dense granular materials: Discrete simulation of plane shear flows. *Physical Review E*, *72*(2), 021309.

Dafermos, C. M., Joseph, D. D., & Leslie, F. M. (1986). *The Breadth and Depth of Continuum Mechanics*. https://doi.org/10.1007/978-3-642-61634-1

Datta, S. K. (1986). *The Excitation and Propagation of Elastic Waves (J. A. Hudson)* (Vol. 28). https://doi.org/10.1137/1028127

De Borst, R. (1991). Simulation of strain localization: A reappraisal of the cosserat continuum. *Engineering Computations*, *8*(4), 317–332. https://doi.org/10.1108/eb023842

de Borst, R., & Sluys, L. J. (1991). Localisation in a Cosserat continuum under static and dynamic loading conditions. *Computer Methods in Applied Mechanics and Engineering*, *90*(1-3), 805–827. https://doi.org/10.1016/0045-7825(91)90185-9

de Borst, R., & Duretz, T. (2020). On viscoplastic regularisation of strain-softening rocks and soils. *International Journal for Numerical and Analytical Methods in Geomechanics*, (January). https://doi.org/10.1002/nag.3046

Deschamps, M., Poirée, B., & Poncelet, O. (1997). Energy velocity of complex harmonic plane waves in viscous fluids. *Wave Motion*, *25*(1), 51–60. https://doi.org/10.1016/s0165-2125(96)00032-7

Di Toro, G., Han, R., Hirose, T., De Paola, N., Nielsen, S., Mizoguchi, K., Ferri, F., Cocco, M., & Shimamoto, T. (2011a). Fault lubrication during earthquakes. *Nature*, *471*(7339), 494–499. https://doi.org/10.1038/nature09838

Di Toro, G., Han, R., Hirose, T., De Paola, N., Nielsen, S., Mizoguchi, K., Ferri, F., Cocco, M., & Shimamoto, T. (2011b). Fault lubrication during earthquakes. *Nature*, *471*(7339), 494–498. https://doi.org/https://doi.org/10.1038/nature09838

Dieterich, J. H. (1992). Earthquake nucleation on faults with rate-and state-dependent strength. *Tectonophysics*, *211*(1-4), 115–134. https://doi.org/https://doi.org/10.1016/0040-1951(92)90055-B

Donea, J., Huerta, A., & Ponthot, J. (2004). Chapter 14: Arbitrary Lagrangian–Eulerian Methods. *Encyclopedia of Computational*, 1–25. http://scholar.google.com/scholar?hl=en%7B%5C&%7DbtnG=Search%7B%5C&%7Dq=intitle:Chapter+14+Arbitrary+Lagrangian?Eulerian+Methods%7B%5C#%7D2

Elsworth, D., Spiers, C. J., & Niemeijer, A. R. (2016). Understanding induced seismicity. *Science*, *354*(6318), https://www.science.org/doi/pdf/10.1126/science.aal2584, 1380–1381. https://doi.org/10.1126/science.aal2584

Eremeyev, V. A. (2018). On the material symmetry group for micromorphic media with applications to granular materials. *Mechanics Research Communications*, *94*, 8–12.

Eringen, A. C. (1968). Mechanics of micromorphic continua. In *Mechanics of generalized continua* (pp. 18–35). Springer.

Erlich, D., Curran, D., & Seaman, L. (1980). *Further Development of a Computational Shear Band Model.* (tech. rep.). SRI INTERNATIONAL MENLO PARK CA.

Etse, G., & Carosio, a. (1999). Constitutive equations and numerical approaches in rate dependent material formulations. *Mecom99*, (1), 289–296.

Farina, J. E. G., & Main, I. G. (1985). Vibrations and Waves in Physics. *The Mathematical Gazette*, *69*(449), 242. https://doi.org/10.2307/3617557

OECD. (2018). Financial Management of Earthquake Risk. www.oecd.org/finance/Financial-Management-of-Earthquake-Risk.htm.

Forest, S. (2019). Micromorphic approach to gradient plasticity and damage. *Handbook of Nonlocal Continuum Mechanics for Materials and Structures*, 499–546.

Forest, S. (2020a). Continuum thermomechanics of nonlinear micromorphic, strain and stress gradient media. *Philosophical Transactions of the Royal Society A*, *378*(2170), 20190169.

Forest, S. (2020b). Micromorphic approach to materials with internal length. *Encyclopedia of Continuum Mechanics*, 1643–1652.

Forest, S., Boubidi, P., & Sievert, R. (2001). Strain localization patterns at a crack tip in generalized single crystal plasticity. *Scripta Materialia*, *44*(6), 953–958.

Forest, S., Pradel, F., & Sab, K. (2001). Asymptotic analysis of heterogeneous Cosserat media. *International Journal of Solids and Structures*, *38*(26-27), 4585–4608. https://doi.org/10.1016/S0020-7683(00)00295-X

Froiio, F., Tomassetti, G., & Vardoulakis, I. (2006). Mechanics of granular materials: The discrete and the continuum descriptions juxtaposed. *International journal of solids and structures*, *43*(25-26), 7684–7720.

Gerasik, V., & Stastna, M. (2010). Complex group velocity and energy transport in absorbing media. *Physical Review E - Statistical, Nonlinear, and Soft Matter Physics*, *81*(5). https://doi.org/10.1103/PhysRevE.81.056602

Germain, P. (2014). The Method of Virtual Power in Continuum Mechanics . Part 2 : Microstructure. *SIAM Journal on Applied Mathematics*, *25*(3), 556–575.

Germain, P. (1973). The method of virtual power in continuum mechanics. Part 2: Microstructure. *SIAM Journal on Applied Mathematics*, *25*(3), 556–575.

Godio, M., Stefanou, I., Sab, K., & Sulem, J. (2016). Multisurface plasticity for Cosserat materials: plate element implementation and validation. *International Journal for Numerical Methods in Engineering*, *108*(5), 456–484. https://doi.org/https://doi.org/10.1002/nme.5219

Griffani, D., Rognon, P., Metzger, B., & Einav, I. (2013). How rotational vortices enhance transfers. *Physics of Fluids*, *25*(9), 093301.

Guglielmi, Y., Cappa, F., Avouac, J.-P., Henry, P., & Elsworth, D. (2015). Seismicity triggered by fluid injection–induced aseismic slip. *Science*, *348*(6240), 1224–1226.

Hadamard, J. (1903). *Leçons sur la propagation des ondes et les équations de l'hydrodynamique*. A. Hermann. https://doi.org/https://doi.org/10.1007/BF01693861

Hähner, P., Ziegenbein, A., Rizzi, E., & Neuhäuser, H. (2002). Spatiotemporal analysis of Portevin-Le Châtelier deformation bands: Theory, simulation, and experiment. *Physical Review B - Condensed Matter and Materials Physics*, *65*(13), 1–20. https://doi.org/10.1103/PhysRevB.65.134109

Harbord, C., Brantut, N., Spagnuolo, E., & Di Toro, G. (2021). Fault friction during simulated seismic slip pulses. *Earth and Space Science Open Archive ESSOAr*.

Harbord, C., Brantut, N., Spagnuolo, E., & Toro, G. D. (2021). Fault friction during simulated seismic slip pulses.

Haskell, N. A. (1964). Energy Wave and Energy From By Density of Elastic Radiation Propagating Faults. *Bulletin of the Seismological Society of America*, *54*(6), 1811–1841.

Hayes, W. D. (1970). Kinematic wave theory. *Proceedings of the Royal Society of London. A. Mathematical and Physical Sciences*, *320*(1541), 209–226.

Heeres, O. M., Suiker, A. S., & De Borst, R. (2002). A comparison between the Perzyna viscoplastic model and the consistency viscoplastic model. *European Journal of Mechanics, A/Solids*, *21*(1), 1–12. https://doi.org/10.1016/S0997-7538(01)01188-3

Hincks, T., Aspinall, W., Cooke, R., & Gernon, T. (2018). Injection Depth. *Science*, *1255*(March), 1251–1255.

Ikari, M. J., Kameda, J., Saffer, D. M., & Kopf, A. J. (2015). Strength characteristics of Japan Trench borehole samples in the high-slip region of the 2011 Tohoku-Oki earthquake. *Earth and Planetary Science Letters*, *412*, 35–41. https://doi.org/10.1016/j.epsl.2014.12.014

Ingebritsen, S., & Manga, M. (2019). Earthquake hydrogeology. *Water Resources Research*, *55*(7), 5212–5216.

Jacquey, A. B., Rattez, H., & Veveakis, M. (2021). Strain localization regularization and patterns formation in rate-dependent plastic materials with multiphysics coupling. *Journal of the Mechanics and Physics of Solids*, *152*, 104422.

Kamasamudram, V., Coret, M., & Moës, N. (2021). The role played by viscoelasticity in the bulk material during the propagation of a dynamic crack in elastomers. *International Journal of Fracture*, *231*(1), 43–58.

Kanamori, H., & Brodsky, E. E. (2004a). The physics of earthquakes. *Reports on Progress in Physics*, *67*(8), 1429–1496. https://doi.org/https://doi.org/10.1088/0034-4885/67/8/r03

Kanamori, H., & Brodsky, E. E. (2004b). The physics of earthquakes. *Reports on Progress in Physics*, *67*(8), 1429–1496. https://doi.org/10.1088/0034-4885/67/8/R03

Kanamori, H., & Rivera, L. (2006). Energy partitioning during an earthquake. *Geophysical Monograph Series*, *170*, 3–13. https://doi.org/10.1029/170GM03

Kounadis. (1995). *Nonlinear Stability of Structures* (Vol. 1). https://doi.org/10.1017/CBO9781107415324.004

Lachenbruch, A. H. (1980a). Frictional heating, fluid pressure, and the resistance to fault motion. *Journal of Geophysical Research*, *85*(B11), 6097–6112. https://doi.org/10.1029/JB085iB11p06097

Lachenbruch, A. H. (1980b). Frictional heating, fluid pressure, and the resistance to fault motion. *Journal of Geophysical Research: Solid Earth*, *85*(B11), 6097–6112. https://doi.org/https://doi.org/10.1029/JB085iB11p06097

Langtangen, H. P. (2016). Solving nonlinear ODE and PDE problems. *Center for Biomedical Computing, Simula Research Laboratory and Department of Informatics, University of Oslo*.

Lee, T. C., & Delaney, P. T. (1987). Frictional heating and pore pressure rise due to a fault slip. *Geophysical Journal of the Royal Astronomical Society*, *88*(3), 569–591. https://doi.org/10.1111/j.1365-246X.1987.tb01647.x

Lemaitre, J., Chaboche, J.-L., Benallal, A., & Desmorat, R. (2020). *Mécanique des matériaux solides-3e éd.* Dunod.

Liao, S. (2003). *Beyond perturbation: introduction to the homotopy analysis method*. CRC press.

Lorefice, R., Etse, G., & Carol, I. (2008). Viscoplastic approach for rate-dependent failure analysis of concrete joints and interfaces. *International Journal of Solids and Structures*, *45*(9), 2686–2705. https://doi.org/10.1016/j.ijsolstr.2007.12.016

Loret, B., & Prevost, J. (1990). Dynamic strain localization in elasto-(visco-)plastic solids, Part 1. General formulation and one-dimensional examples. *Computer Methods in Applied Mechanics and Engineering*, *83*(3), 247–273.

Lucarini, V. (2009). Evidence of dispersion relations for the nonlinear response of the lorenz 63 system. *Journal of Statistical Physics*, *134*(2)arXiv 0809.0101, 381–400. https://doi.org/10.1007/s10955-008-9675-z

Lyapunov, A. M. (1992). The general problem of the stability of motion. *International journal of control*, *55*(3), 531–534.

Lykotrafitis, G., Rosakis, A. J., & Ravichandran, G. (2006). Self-healing pulse-like shear ruptures in the laboratory. *Science*, *313*(5794), 1765–1768.

Ma, K. F., Tanaka, H., Song, S. R., Wang, C. Y., Hung, J. H., Tsai, Y. B., Mori, J., Song, Y. F., Yeh, E. C., Soh, W., Sone, H., Kuo, L. W., & Wu, H. Y. (2006). Slip zone and energetics of a large earthquake from the Taiwan Chelungpu-fault Drilling Project. *Nature*, *444*(7118), 473–476. https://doi.org/10.1038/nature05253

Madariaga, R. (2015). *Seismic Source Theory* (Vol. 4). Elsevier B.V. https://doi.org/10.1016/B978-0-444-53802-4.00070-1

Madariaga, R., Olsen, K., & Archuleta, R. (1998). Modeling dynamic rupture in a 3D earthquake fault model. *Bulletin of the Seismological Society of America*, *88*(5), 1182–1197.

Mainardi, F. (1984). On linear dispersive waves with dissipation. In *North-Holland Mathematics Studies* (pp. 307–317). Elsevier.

Mainardi, F. (1987). Energy velocity for hyperbolic dispersive waves. *Wave motion*, *9*(3), 201–208.

Marion, J. B. (2013). *Classical dynamics of particles and systems*. Academic Press.

Mase, C. W., & Smith, L. (1987). Effects of frictional heating on the thermal, hydrologic, and mechanical response of a fault. *Journal of Geophysical Research*, *92*(B7), 6249–6272. https://doi.org/10.1029/JB092iB07p06249

Maugin, G. A. (2007). Nonlinear kinematic wave mechanics of elastic solids. *Wave Motion*, *44*(6), 472–481. https://doi.org/10.1016/j.wavemoti.2007.02.005

Maugin, G. A. (1992). *The Thermomechanics of Plasticity and Fracture*. Cambridge University Press. https://doi.org/10.1017/CBO9781139172400

Mavaleix-Marchessoux, D., Bonnet, M., Chaillat, S., & Leblé, B. (2020). A fast BEM procedure using the Z-transform and high-frequency approximations for large-scale 3D transient wave problems. *International Journal for Numerical Methods in Engineering*.

Mawhin, J. (2005). Alexandr Mikhailovich Lyapunov, thesis on the stability of motion (1892). In *Landmark Writings in Western Mathematics 1640-1940* (pp. 664–676). Elsevier.

Mazière, M., Besson, J., Forest, S., Tanguy, B., Chalons, H., & Vogel, F. (2010). Numerical aspects in the finite element simulation of the Portevin-Le Chatelier effect. *Computer Methods in Applied Mechanics and Engineering*. https://doi.org/10.1016/j.cma.2009.11.004

Meza-Fajardo, K. C., Papageorgiou, A. S., & Semblat, J.-F. (2015). Identification and extraction of surface waves from three-component seismograms based on the normalized inner product. *Bulletin of the Seismological Society of America*, *105*(1), 210–229.

Miller, T., Rognon, P., Metzger, B., & Einav, I. (2013). Eddy viscosity in dense granular flows. *Physical review letters*, *111*(5), 058002.

Mindlin, R. D. (1963). *Microstructure in linear elasticity* (tech. rep.). Columbia Univ New York Dept of Civil Engineering and Engineering Mechanics.

Moes, N., & Chevaugeon, N. (2021). Lipschitz regularization for softening material models: the Lip-field approach. *arXiv preprint arXiv:2103.16345*.

Moës, N., Cloirec, M., Cartraud, P., & Remacle, J.-F. (2003). A computational approach to handle complex microstructure geometries. *Computer methods in applied mechanics and engineering*, *192*(28-30), 3163–3177.

Moës, N., Dolbow, J., & Belytschko, T. (1999). A finite element method for crack growth without remeshing. *International journal for numerical methods in engineering*, *46*(1), 131–150.

Moës, N., Stolz, C., Bernard, P.-E., & Chevaugeon, N. (2011). A level set based model for damage growth: the thick level set approach. *International Journal for Numerical Methods in Engineering*, *86*(3), 358–380.

Moreau, K., Moës, N., Picart, D., & Stainier, L. (2015). Explicit dynamics with a non-local damage model using the thick level set approach. *International Journal for Numerical Methods in Engineering*, *102*(3-4), 808–838.

Muhlhaus, H.-B., & Vardoulakis, I. (1988). The thickness of shear hands in granular materials. *Géotechnique*, *38*(2), 331–331. https://doi.org/10.1680/geot.1988.38.2.331b

Muschietti, L., & Dum, C. T. (1993). Real group velocity in a medium with dissipation. *Physics of Fluids B*, *5*(5), 1383–1397. https://doi.org/10.1063/1.860877

Myers, R., & Aydin, A. (2004). The evolution of faults formed by shearing across joint zones in sandstone. *Journal of Structural Geology*, *26*(5), 947–966.

Needleman, A. (1988). Material rate dependence and mesh sensitivity in localization problems. *Computer methods in applied mechanics and engineering*, *67*(1), 69–85. https://doi.org/https://doi.org/10.1016/0045-7825(88)90069-2

Needleman, A., & Tvergaard, V. (1992). Analyses of plastic flow localization in metals.

Neff, P., Ghiba, I.-D., Madeo, A., Placidi, L., & Rosi, G. (2014). A unifying perspective: the relaxed linear micromorphic continuum. *Continuum Mechanics and Thermodynamics*, *26*(5), 639–681.

Nicchio, M. A., Nogueira, F. C., Balsamo, F., Souza, J. A., Carvalho, B. R., & Bezerra, F. H. (2018). Development of cataclastic foliation in deformation bands in feldspar-rich conglomerates of the Rio do Peixe Basin, NE Brazil. *Journal of Structural Geology*, *107*, 132–141. https://doi.org/https://doi.org/10.1016/j.jsg.2017.12.013

Niemeijer, A. R., Boulton, C., Toy, V. G., Townend, J., & Sutherland, R. (2016). Large-displacement, hydrothermal frictional properties of DFDP-1 fault rocks, Alpine

Fault, New Zealand: Implications for deep rupture propagation. *Journal of Geophysical Research: Solid Earth*, 3782–3803. https://doi.org/10.1002/2015JB012608. Received

Okubo, K., Bhat, H. S., Rougier, E., Marty, S., Schubnel, A., Lei, Z., Knight, E. E., & Klinger, Y. (2019). Dynamics, radiation, and overall energy budget of earthquake rupture with coseismic off-fault damage. *Journal of Geophysical Research: Solid Earth*, *124*(11), 11771–11801.

Pain, H. J., & Beyer, R. T. (1993). The Physics of Vibrations and Waves, Fourth Edition. *The Journal of the Acoustical Society of America*, *94*(6), 3529–3529. https://doi.org/10.1121/1.407174

Papamichos, E., Papanastasiou, P., Pasternak, E., & Dyskin, A. (2017). *Bifurcation and Degradation of Geomaterials with Engineering Applications: Proceedings of the 11th International Workshop on Bifurcation and Degradation in Geomaterials Dedicated to Hans Muhlhaus, Limassol, Cyprus, 21-25 May 2017*. Springer.

Papanastasiou, P. C., & Vardoulakis, I. (1989). Bifurcation analysis of deep boreholes: II. Scale effect. *International Journal for Numerical and Analytical Methods in Geomechanics*, *13*(2), 183–198.

Papanastasiou, P. C., & Vardoulakis, I. G. (1992). Numerical treatment of progressive localization in relation to borehole stability. *International Journal for Numerical and Analytical Methods in Geomechanics*, *16*(6), 389–424.

Parker, M. (2009). Group Velocity. *Solid State and Quantum Theory for Optoelectronics*, 789–795. https://doi.org/10.1201/9781420019452-a6

Peirce, D., Shih, C. F., & Needleman, A. (1984). A tangent modulus method for rate dependent solids. *Computers and Structures*, *18*(5), 875–887. https://doi.org/10.1016/0045-7949(84)90033-6

Platt, J. D., Rudnicki, J. W., & Rice, J. R. (2014a). Stability and localization of rapid shear in fluid-saturated fault gouge: 2. Localized zone width and strength evolution. *Journal of Geophysical Research: Solid Earth*, *119*(5), 4334–4359. https://doi.org/10.1002/2013JB010711

Platt, J. D., Rudnicki, J. W., & Rice, J. R. (2014b). Stability and localization of rapid shear in fluid-saturated fault gouge: 2. Localized zone width and strength evolution. *Journal of Geophysical Research: Solid Earth*, *119*(5), 4334–4359. https://doi.org/https://doi.org/10.1002/2013JB010711

Poeverlein, H. (1962). Sommerfeld-Runge law in three and four dimensions. *Physical Review*, *128*(2), 956.

Ponthot, J. P. (2002). Unified stress update algorithms for the numerical simulation of large deformation elasto-plastic and elasto-viscoplastic processes. *International Journal of Plasticity*, *18*(1), 91–126. https://doi.org/10.1016/S0749-6419(00)00097-8

Ponthot, J.-P. (1995). Radial return extensions for visco-plasticity and lubricated friction.

Puzrin, A., & Houlsby, G. (2001). On the thermodynamics of porous continua. *Report No OUEL*, *2235*(01). https://doi.org/https://doi.org/10.1007/978-3-540-35724-7_3

Raleigh, C., Healy, J., & Bredehoeft, J. (1976). An experiment in earthquake control at Rangely, Colorado. *Science*, *191*(4233), 1230–1237.

Rattez, H., Stefanou, I., & Sulem, J. (2018). The importance of Thermo-Hydro-Mechanical couplings and microstructure to strain localization in 3D continua with application to seismic faults. Part I: Theory and linear stability analysis. *Journal of the Mechanics and Physics of Solids*, *115*, 54–76. https://doi.org/10.1016/j.jmps.2018.03.004

Rattez, H., Stefanou, I., Sulem, J., Veveakis, M., & Poulet, T. (2018a). Numerical analysis of strain localization in rocks with thermo-hydro-mechanical couplings using Cosserat continuum. *Rock Mechanics and Rock Engineering*, *51*(10), 3295–3311.

Rattez, H., Stefanou, I., Sulem, J., Veveakis, M., & Poulet, T. (2018b). The importance of Thermo-Hydro-Mechanical couplings and microstructure to strain localization in 3D continua with application to seismic faults. Part II: Numerical implementation and post-bifurcation analysis. *Journal of the Mechanics and Physics of Solids*. https://doi.org/10.1016/j.jmps.2018.03.003

Rattez, H., Stefanou, I., Sulem, J., Veveakis, M., & Poulet, T. (2018c). The importance of Thermo-Hydro-Mechanical couplings and microstructure to strain localization in 3D continua with application to seismic faults. Part II: Numerical implementation and post-bifurcation analysis. *Journal of the Mechanics and Physics of Solids*, *115*, 1–29. https://doi.org/10.1016/j.jmps.2018.03.003

Rempe, M., Di Toro, G., Mitchell, T. M., Smith, S. A., Hirose, T., & Renner, J. (2020). Influence of Effective Stress and Pore Fluid Pressure on Fault Strength and Slip Localization in Carbonate Slip Zones. *Journal of Geophysical Research: Solid Earth*, *125*(11). https://doi.org/10.1029/2020JB019805

Rempel, A. W., & Rice, J. R. (2006). Thermal pressurization and onset of melting in fault zones. *Journal of Geophysical Research: Solid Earth*, *111*(9). https://doi.org/10.1029/2006JB004314

Ren, S., Morgeneyer, T., Mazière, M., Forest, S., & Rousselier, G. (2021). Effect of Lüders and Portevin–Le Chatelier localization bands on plasticity and fracture of notched steel specimens studied by DIC and FE simulations. *International Journal of Plasticity*, *136*, 102880.

Reyne, B., Manach, P.-Y., & Moes, N. (2019). Macroscopic consequences of Piobert–Lüders and Portevin–Le Chatelier bands during tensile deformation in Al-Mg alloys. *Materials Science and Engineering: A*, *746*, 187–196.

Rezakhani, R., & Cusatis, G. (2016). Asymptotic expansion homogenization of discrete fine-scale models with rotational degrees of freedom for the simulation of quasi-brittle materials. *Journal of the Mechanics and Physics of Solids*, *88*, 320–345.

Rice, J. R. (1973a). The growth of slip surfaces in the progressive failure of over-consolidated clay. *Proceedings of the Royal Society of London. A. Mathematical and Physical Sciences*, *332*(1591), 527–548. https://doi.org/10.1098/rspa.1973.0040

Rice, J. R. (1973b). The growth of slip surfaces in the progressive failure of over-consolidated clay. *Proceedings of the Royal Society of London. A. Mathematical and Physical Sciences*, *332*(1591), 527–548. https://doi.org/10.1098/rspa.1973.0040

Rice, J. R. (1973c). The growth of slip surfaces in the progressive failure of over-consolidated clay. *Proceedings of the Royal Society of London. A. Mathematical and Physical Sciences*, *332*(1591), 527–548. https://doi.org/10.1098/rspa.1973.0040

Rice, J. R. (1975). On the stability of dilatant hardening for saturated rock masses. *Journal of Geophysical Research*, *80*(11), 1531–1536. https://doi.org/10.1029/jb080i011p01531

Rice, J. R. (1976). Localization of Plastic Deformation. *Theoretical and Applied Mechanics*, *1*(January 1976), 207–220. https://doi.org/10.4028/www.scientific.net/ssp.3-4.347

Rice, J. R. (2006a). Heating and weakening of faults during earthquake slip. *Journal of Geophysical Research: Solid Earth*, *111*(5), 1–29. https://doi.org/10.1029/2005JB004006

Rice, J. R. (2006b). Heating and weakening of faults during earthquake slip. *Journal of Geophysical Research: Solid Earth*, *111*(B5). https://doi.org/https://doi.org/10.1029/2005JB004006

Rice, J. R., Lapusta, N., & Ranjith, K. (2001). Rate and state dependent friction and the stability of sliding between elastically deformable solids. *Journal of the Mechanics and Physics of Solids*, *49*(9), 1865–1898. https://doi.org/10.1016/S0022-5096(01)00042-4

Rice, J. R., Rudnicki, J. W., & Platt, J. D. (2014a). Stability and localization of rapid shear in fluid-saturated fault gouge: 1. Linearized stability analysis. *Journal of Geophysical Research: Solid Earth*, *119*(5), 4311–4333. https://doi.org/10.1002/2013JB010710

Rice, J. R., Rudnicki, J. W., & Platt, J. D. (2014b). Stability and localization of rapid shear in fluid-saturated fault gouge: 1. Linearized stability analysis. *Journal of Geophysical Research: Solid Earth*, *119*(5), 4311–4333. https://doi.org/https://doi.org/10.1002/2013JB010710

Rognon, P., Miller, T., & Einav, I. (2015). A circulation-based method for detecting vortices in granular materials. *Granular Matter*, *17*(2), 177–188.

Rosakis, A., Samudrala, O., & Coker, D. (1999). Cracks faster than the shear wave speed. *Science*, *284*(5418), 1337–1340.

Rubinstein, J. L., & Mahani, A. B. (2015). Myths and facts on wastewater injection, hydraulic fracturing, enhanced oil recovery, and induced seismicity. *Seismological Research Letters*, *86*(4), 1060–1067.

Rudnicki, J. W., & Rice, J. R. (1975). Conditions for the localization of deformation in pressure-sensitive dilatant materials. *Journal of the Mechanics and Physics of Solids*, *23*(6), 371–394. https://doi.org/10.1016/0022-5096(75)90001-0

Ruina, A. (1983a). Slip instability and state variable friction laws. *Journal of Geophysical Research*, *88*(B12), 10359–10370. https://doi.org/10.1029/JB088iB12p10359

Ruina, A. (1983b). Slip instability and state variable friction laws. *Journal of Geophysical Research: Solid Earth*, *88*(B12), 10359–10370. https://doi.org/https://doi.org/10.1029/JB088iB12p10359

Sanchez-Palencia, E. (1986). Homogenization in Mechanics, a Survey of Solved and Open Problems. *Rend. Sem. Mat. Univ. Politec. ...*, *44*, 1–46. http://www.seminariomatematico.unito.it/rendiconti/cartaceo/44-1/1.pdf

Schneider, G., & Uecker, H. (n.d.). *Nonlinear PDEs A Dynamical Systems Approach*.

Scholz, C. H. (2019). *The mechanics of earthquakes and faulting*. Cambridge university press.

Shawki, T. G., & Clifton, R. J. (1989). Shear band formation in thermal viscoplastic materials. *Mechanics of Materials*, *8*(1), 13–43. https://doi.org/10.1016/0167-6636(89)90003-3

Shiferaw, B., Chupin, O., Piau, J.-M., & Moës, N. (2021). Development of a damage viscoelastic model using the thick level set approach to fracture: 1D modeling and comparison to uniaxial tension stress tests on bituminous specimens. *Engineering Fracture Mechanics*, 108026.

Sibson, R. H. (2003a). Thickness of the Seismic Slip Zone. *Bulletin of the Seismological Society of America*, *93*(3), 1169–1178. https://doi.org/10.1785/0120020061

Sibson, R. H. (2003b). Thickness of the Seismic Slip Zone. *Bulletin of the Seismological Society of America*, *93*(3), 1169–1178. https://doi.org/10.1785/0120020061

Sibson, R. H., & Toy, V. G. (2006). The habitat of fault-generated pseudotachylyte: Presence vs. absence of friction-melt. *Geophysical Monograph Series*, *170*(January), 153–166. https://doi.org/10.1029/170GM16

Sluys, L. J., & de Borst, R. (1992). Wave propagation and localization in a rate-dependent cracked medium-model formulation and one-dimensional examples. *International Journal of Solids and Structures*, *29*(23), 2945–2958. https://doi.org/10.1016/0020-7683(92)90151-I

Sluys, L. J., de Borst, R., & Mühlhaus, H. B. (1993). Wave propagation, localization and dispersion in a gradient-dependent medium. *International Journal of Solids and Structures*, *30*(9), 1153–1171. https://doi.org/10.1016/0020-7683(93)90010-5

Smith, M. (2009). *ABAQUS/Standard User's Manual, Version 6.9.* United States, Dassault Systèmes Simulia Corp.

Stathas, A., & Stefanou, I. (2019a). Elastoplastic response of a cosserat continuum layer for application in fault mechanics. *12th HSTAM International Congress on Mechanics Thessaloniki, Greece, 22 – 25 September 2019.*

Stathas, A., & Stefanou, I. (2022c). The role of viscous regularization in dynamical problems, strain localization and mesh dependency. *Computer Methods in Applied Mechanics and Engineering*, *388*, 114185.

Stathas, A., & Stefanou, I. (postponed to 2021). The role of seismic slip velocity in the evolution of shear band thickness. *12th International Workshop on Bifurcation and Degradation of Geomaterials (in preparation).*

Stefanou, I., & Tzortzopoulos, G. (2020). Control instabilities and incite slow-slip in generalized Burridge-Knopoff models. *arXiv:2008.03755*arXiv 2008.03755. https://arxiv.org/abs/2008.03755

Stefanou, I. (2018). *CoQuake*. https://coquake.eu

Stefanou, I. (2019). Controlling Anthropogenic and Natural Seismicity: Insights From Active Stabilization of the Spring-Slider Model. *Journal of Geophysical Research: Solid Earth*, *124*(8), 8786–8802. https://doi.org/10.1029/2019JB017847

Stefanou, I. (2020). Numerical Geolab. *coquake.eu*.

Stefanou, I. (2021). Numerical Geolab [Nantes, FR, 2021]. https://www.coquake.eu/

Stefanou, I., & Alevizos, S. (2016). Fundamentals of bifurcation theory and stability analysis. *Modelling of instabilities and bifurcation in Geomechanics, 26th ALERT Doctoral School*, *725*.

Stefanou, I., & Gerolymatou, E. (2019). Strain localization in geomaterials and regularization: rate-dependency, higher order continuum theories and multi-physics. *ALERT Doctoral School*, 47–85.

Stefanou, I., Gerolymatou, E., & Stathas, A. (2020). Strain localization in geomaterials and regularization:rate-dependency, higher order continuum theories andmulti-physics. *In preparation*.

Stefanou, I., Gerolymatou, E., & Stathas, A. (2021). Paper on regularization. *In preparation*, -(-), -. https://doi.org/-

Stefanou, I., Sulem, J., & Rattez, H. (2016). Cosserat approach to localization in geomaterials. https://doi.org/https://doi.org/10.1007/978-3-319-22977-5_10-1

Stefanou, I., Sulem, J., & Vardoulakis, I. (2010). Homogenization of interlocking masonry structures using a generalized differential expansion technique. *International Journal of Solids and Structures*, *47*(11-12), 1522–1536. https://doi.org/https://doi.org/10.1016/j.ijsolstr.2010.02.011

Strogatz, S. H. (2000). *Nonlinear Dynamics and Chaos: With Applications to Physics, Biology, Chemistry and Engineering*. Westview Press.

Strogatz, S. H. (2018). *Nonlinear dynamics and chaos with student solutions manual: With applications to physics, biology, chemistry, and engineering*. CRC press.

Sulem, J., & Famin, V. (2009). Thermal decomposition of carbonates in fault zones: Slip-weakening and temperature-limiting effects. *Journal of Geophysical Research: Solid Earth*, *114*(3), 1–14. https://doi.org/10.1029/2008jb006004

Sulem, J., & Stefanou, I. (2016a). Thermal and chemical effects in shear and compaction bands. *Geomechanics for Energy and the Environment*, *6*, 4–21. https://doi.org/10.1016/j.gete.2015.12.004

Sulem, J., & Stefanou, I. (2016b). Thermal and chemical effects in shear and compaction bands. *Geomechanics for Energy and the Environment*, *6*, 4–21. https://doi.org/https://doi.org/10.1016/j.gete.2015.12.004

Sulem, J., Stefanou, I., & Veveakis, E. (2011). Stability analysis of undrained adiabatic shearing of a rock layer with Cosserat microstructure. *Granular Matter*, *13*(3), 261–268. https://doi.org/https://doi.org/10.1007/s10035-010-0244-1

Sulem, J., & Vardoulakis, I. (1995). *Bifurcation analysis in geomechanics*. CRC Press. https://doi.org/https://doi.org/10.1201/9781482269383

Sulem, J., Vardoulakis, I., Ouffroukh, H., Boulon, M., & Hans, J. (2004). Experimental characterization of the thermo-poro-mechanical properties of the Aegion fault gouge. *Comptes Rendus Geoscience*, *336*(4-5), 455–466.

Takahashi, M., Van den Ende, M., Niemeijer, A., & Spiers, C. (2017). Shear localization in a mature mylonitic rock analog during fast slip. *Geochemistry, Geophysics, Geosystems*, *18*(2), 513–530.

Tanaka, H., Chen, W., Kawabata, K., & Urata, N. (2007). Thermal properties across the Chelungpu fault zone and evaluations of positive thermal anomaly on the slip zones: Are these residuals of heat from faulting? *Geophysical Research Letters*, *34*(1).

Tang, T., Xu, X., & Cheng, J. (2008). On spectral methods for Volterra integral equations and the convergence analysis. *Journal of Computational Mathematics*, 825–837.

Tanikawa, W., & Shimamoto, T. (2009). Frictional and transport properties of the Chelungpu fault from shallow borehole data and their correlation with seismic behavior during the 1999 Chi-Chi earthquake. *Journal of Geophysical Research: Solid Earth*, *114*(1), 1–15. https://doi.org/10.1029/2008JB005750

Trefethen, L. N., Birkisson, A., & Driscoll, T. A. (2017). *Exploring ODEs* (Vol. 157). SIAM.

Tsai, V. C., & Hirth, G. (2020). Elastic Impact Consequences for High-Frequency Earthquake Ground Motion. *Geophysical Research Letters*, *47*(5), 1–8. https://doi.org/10.1029/2019GL086302

Turing, A. M. (1990). The chemical basis of morphogenesis. *Bulletin of mathematical biology*, *52*(1), 153–197.

Tzortzopoulos, G., Braun, P., & Stefanou, I. (2021). Absorbent porous paper reveals how earthquakes could be mitigated. *Geophysical Research Letters*, *48*(3), e2020GL090792.

Tzortzopoulos, G. (2021). *Controlling earthQuakes in the laboratory using pertinent fault stimulating techniques*.

Vardoulakis, I. (1986). Dynamic stability analysis of undrained simple shear on water-saturated granular soils. *International journal for numerical and analytical methods in geomechanics*, *10*(2), 177–190. https://doi.org/https://doi.org/10.1002/nag.1610100206

Vardoulakis, I. (2000a). REGULARIZATION OF STRAIN SOFTENING MODELS FOR GEOMATERIALS. *Journal of the Mechanical Behavior of Materials*, *11*(1-3), 227–236. https://doi.org/doi:10.1515/JMBM.2000.11.1-3.227

Vardoulakis, I., & Papanastasiou, P. C. (1988). Bifurcation analysis of deep boreholes: I. Surface instabilities. *International Journal for Numerical and Analytical Methods in Geomechanics*, *12*(4), 379–399.

Vardoulakis, I., & Sulem, J. ((1995). *Bifurcation Analysis in Geomechanics (1st ed.)* CRC Press. https://doi.org/10.1201/9781482269383

Vardoulakis, I. (1996a). Deformation of water-saturated sand: I. uniform undrained deformation and shear banding. *Géotechnique*, *46*(3), 441–456.

Vardoulakis, I. (1996b). Deformation of water-saturated sand: II. Effect of pore water flow and shear banding. *Géotechnique*, *46*(3), 457–472.

Vardoulakis, I. (2000b). Catastrophic landslides due to frictional heating of the failure plane. *Mechanics of Cohesive-frictional Materials: An International Journal on Experiments, Modelling and Computation of Materials and Structures*, *5*(6), 443–467.

Vardoulakis, I. (2009). Lecture notes on Cosserat continuum mechanics with application to the mechanics of granular media, In *3rd National Meeting on Generalized Continuum Theories and Applications, Thessaloniki, Greece.*

Vardoulakis, I. (2018). *Cosserat Continuum Mechanics: With Applications to Granular Media* (Vol. 87). Springer. https://doi.org/https://doi.org/10.1007/978-3-319-95156-0

Vardoulakis, I. (2019). Cosserat Continuum Energetics. In *Cosserat Continuum Mechanics* (pp. 89–97). Springer.

Verberne, B. A., Niemeijer, A. R., De Bresser, J. H., & Spiers, C. J. (2015). Mechanical behavior and microstructure of simulated calcite fault gouge sheared at 20-600°C:

Implications for natural faults in limestones. *Journal of Geophysical Research: Solid Earth*, *120*(12), 8169–8196. https://doi.org/10.1002/2015JB012292

Verberne, B. A., Van Den Ende, M. P., Chen, J., Niemeijer, A. R., & Spiers, C. J. (2020). The physics of fault friction: Insights from experiments on simulated gouges at low shearing velocities. *Solid Earth*, *11*(6), 2075–2095. https://doi.org/10.5194/se-11-2075-2020

Veveakis, E., Poulet, T., & Alevizos, S. (2014). Thermo-poro-mechanics of chemically active creeping faults: 2. Transient considerations. *Journal of Geophysical Research: Solid Earth*, *119*(6), 4583–4605. https://doi.org/10.1002/2013JB010071

Veveakis, E., Vardoulakis, I., & Di Toro, G. (2007). Thermoporomechanics of creeping landslides: The 1963 Vaiont slide, northern Italy. *Journal of Geophysical Research: Earth Surface*, *112*(F3).

Viesca, R. C., & Garagash, D. I. (2015). Ubiquitous weakening of faults due to thermal pressurization. *Nature Geoscience*, *8*(11), 875–879. https://doi.org/https://doi.org/10.1038/ngeo2554

Wang, W. M., Sluys, L. J., & De Borst, R. (1996). Interaction between material length scale and imperfection size for localization phenomena in viscoplastic media. *European Journal of Mechanics, A/Solids*, *15*(3), 447–464.

Wang, W., Sluys, L. J., & De Borst, R. (1996). Interaction between material length scale and imperfection size for localisation phenomena in viscoplastic media. *European journal of mechanics. A. Solids*, *15*(3), 447–464.

Wang, W., Sluys, L., & De Borst, R. (1997). Viscoplasticity for instabilities due to strain softening and strain-rate softening. *International Journal for Numerical Methods in Engineering*, *40*(20), 3839–3864. https://doi.org/https://doi.org/10.1002/(SICI)1097-0207(19971030)40:20<3839::AID-NME245>3.0.CO;2-6

Wazwaz, A.-M. (1999). A reliable modification of Adomian decomposition method. *Applied mathematics and computation*, *102*(1), 77–86.

Wazwaz, A.-M. (2011). *Linear and nonlinear integral equations* (Vol. 639). Springer.

Wiggins, S., Wiggins, S., & Golubitsky, M. (1990). *Introduction to applied nonlinear dynamical systems and chaos* (Vol. 2). Springer.

Wolfram Research, I. (2020). Mathematica, Version 12.1 [Champaign, IL, 2020]. https://www.wolfram.com/mathematica

Wu, F. H., & Freund, L. B. (1984). Deformation trapping due to thermoplastic instability in one-dimensional wave propagation. *Journal of the Mechanics and Physics of Solids*, *32*(2), 119–132. https://doi.org/10.1016/0022-5096(84)90014-0

Zbib, H., & Aifantis, E. (1989). ‘On the Localization and Post Localization of Plastic Deformation—Part I: On the Initiation of Shear Bands. *Res. Mech*, 261–277. https://doi.org/https://doi.org/10.1115/1.3152403

Zbib, H. M., & Aifantis, E. C. (1992). On the gradient-dependent theory of plasticity and shear banding. *Acta Mechanica*, *92*(1-4), 209–225. https://doi.org/10.1007/BF01174177

Zervos, A., Papanastasiou, P., & Vardoulakis, I. (2001a). A finite element displacement formulation for gradient elastoplasticity. *International Journal for Numerical Methods in Engineering*, *50*(6), 1369–1388.

Zervos, A., Papanastasiou, P., & Vardoulakis, I. (2001b). Modelling of localisation and scale effect in thick-walled cylinders with gradient elastoplasticity. *International Journal of Solids and Structures*, *38*(30-31), 5081–5095.

Appendices

Appendix A

A.1 Derivation of the Elasto-viscoplastic wave equation.

In this Appendix the results presented in section 4.2 are obtained in detail.

A.1.1 Elasto-viscoplastic constitutive relations

A.1.1.1 Perzyna model.

In a Perzyna elasto-viscoplastic formulation the following relations hold:

$$F(\sigma_{ij}, \bar{\epsilon}^{vp}) = 0, \tag{A.1.1}$$

$$\dot{\varepsilon}_{ij} = \dot{\varepsilon}_{ij}^{e} + \dot{\varepsilon}_{ij}^{vp}, \tag{A.1.2}$$

$$\dot{\sigma}_{ij} = M_{ijkl}^{e} \left(\dot{\varepsilon}_{kl} - \dot{\varepsilon}_{kl}^{vp}\right), \tag{A.1.3}$$

$$\dot{\varepsilon}_{ij}^{vp} = \dot{\lambda} \frac{\partial F}{\partial \sigma_{ij}} = \left(\frac{F}{\eta F_0}\right)^{n} \frac{\partial F}{\partial \sigma_{ij}} \; n = 1, \tag{A.1.4}$$

$$\bar{\epsilon}^{vp} = \int_0^t \dot{\bar{\epsilon}}^{vp} dt. \tag{A.1.5}$$

where $F(\sigma_{ij}, \bar{\epsilon}^{vp})$ is the yield function incorporating the effects of strain hardening through the use of the accumulated viscoplastic strain $\bar{\epsilon}^{vp}$. We note that in this formulation the consistency condition is not respected. During plastic loading we we can find states where $F > 0$, while during unloading of the material, we see that viscoplastic stresses are still present even though $F < 0$.

We follow the approach described in Lorefice et al., 2008; J. P. Ponthot, 2002; J.-P. Ponthot, 1995 in order to derive the elasto-viscoplastic stress, strain, strain rate, material behavior. We start by considering the von Mises yield criterion:

$$F(\sigma_{ij}, \bar{\varepsilon}^{vp}) = \sqrt{3J_2(\sigma_{ij})} - F_0 - h\bar{\epsilon}^{vp}, \tag{A.1.6}$$

assuming dependence of yield on the deviatoric invariant of the stress tensor $J_2(s_{ij}) = \sqrt{\frac{1}{2}s_{ij}s_{ij}}$, and $\bar{\epsilon}^{vp} = \sqrt{\frac{2}{3}\varepsilon^{vp}_{ij}\varepsilon^{vp}_{ij}}$ where $s_{ij} = \sigma_{ij} - \frac{\sigma_{ii}}{3}$. From the above definitions we conclude that $\bar{\varepsilon}^{vp} = \lambda, \dot{\bar{\varepsilon}}^{vp} = \dot{\lambda}$. We define the viscoplastic potential $\Omega(\sigma_{ij}, \lambda, \dot{\lambda})$ as:

$$\Omega(\sigma_{ij}, \lambda, \dot{\lambda}) = F(\sigma_{ij}, \lambda) - F_0 F^{-1}(\dot{\lambda}\eta) = 0. \tag{A.1.7}$$

Now the consistency condition is valid for the visocplastic potential: $\dot{\lambda}\Omega = 0 \ \dot{\lambda} \geq 0, \ \Omega \leq 0$. During plastic loading $\dot{\Omega} = 0$ leading to:

$$\dot{\Omega} = \frac{\partial \Omega}{\partial \sigma_{ij}}\dot{\sigma}_{ij} + \frac{\partial \Omega}{\partial \bar{\lambda}}\dot{\lambda} + \frac{\partial \Omega}{\partial \dot{\lambda}}\ddot{\lambda} = 0, \tag{A.1.8}$$

multiplying (A.1.3) by $\frac{\partial \Omega}{\partial \sigma_{ij}}$. replacing $\dot{\varepsilon}^{vp}_{ij}$ with help from (A.1.4) and replacing the term in the lefthandside with equation (A.1.8) we finally get:

$$-\frac{\partial \Omega}{\partial \lambda}\dot{\lambda} - \frac{\partial \Omega}{\partial \dot{\lambda}}\ddot{\lambda} = \frac{\partial \Omega}{\partial \sigma_{ij}} M^e_{ijkl}\left(\dot{\varepsilon}_{kl} - \dot{\lambda}\frac{\partial \Omega}{\partial \sigma_{kl}}\right). \tag{A.1.9}$$

Grouping together the terms of $\dot{\lambda}$ and solving for $\dot{\lambda}$ we get:

$$\dot{\lambda} = \frac{\frac{\partial \Omega}{\partial \sigma_{ij}} M^e_{ijkl}}{-\frac{\partial \Omega}{\partial \lambda} + \frac{\partial \Omega}{\partial \sigma_{ij}} M^e_{ijkl}\frac{\partial \Omega}{\partial \sigma_{kl}}}\dot{\varepsilon}_{kl} + \frac{\frac{\partial \Omega}{\partial \dot{\lambda}}}{-\frac{\partial \Omega}{\partial \lambda} + \frac{\partial \Omega}{\partial \sigma_{ij}} M^e_{ijkl}\frac{\partial \Omega}{\partial \sigma_{kl}}}\ddot{\lambda}. \tag{A.1.10}$$

Inserting (A.1.24) into (A.1.15) we obtain:

$$\dot{\sigma}_{ij} = M^e_{ijkl}\left(\dot{\varepsilon}_{kl} - \frac{\frac{\partial \Omega}{\partial \sigma_{ij}} M^e_{ijkl}\frac{\partial \Omega}{\partial \sigma_{kl}}}{-\frac{\partial \Omega}{\partial \lambda} + \frac{\partial \Omega}{\partial \sigma_{ij}} M^e_{ijkl}\frac{\partial \Omega}{\partial \sigma_{kl}}}\dot{\varepsilon}_{kl} + \frac{\frac{\partial \Omega}{\partial \dot{\lambda}}\frac{\partial \Omega}{\partial \sigma_{kl}}}{-\frac{\partial \Omega}{\partial \lambda} + \frac{\partial \Omega}{\partial \sigma_{ij}} M^e_{ijkl}\frac{\partial \Omega}{\partial \sigma_{kl}}}\ddot{\lambda}\right), \tag{A.1.11}$$

replacing the time derivative with a variation taking advantage of the definition of variation we arrive at the constitutive equation describing the perturbed field of stress $\tilde{\sigma}_{ij}$.

$$\tilde{\sigma}_{ij} = M^e_{ijkl}\left(\tilde{\varepsilon}_{kl} - \frac{\frac{\partial \Omega}{\partial \sigma_{ij}} M^e_{ijkl}\frac{\partial \Omega}{\partial \sigma_{kl}}}{-\frac{\partial \Omega}{\partial \lambda} + \frac{\partial \Omega}{\partial \sigma_{ij}} M^e_{ijkl}\frac{\partial \Omega}{\partial \sigma_{kl}}}\tilde{\varepsilon}_{kl} + \frac{\frac{\partial \Omega}{\partial \dot{\lambda}}\frac{\partial \Omega}{\partial \sigma_{kl}}}{-\frac{\partial \Omega}{\partial \lambda} + \frac{\partial \Omega}{\partial \sigma_{ij}} M^e_{ijkl}\frac{\partial \Omega}{\partial \sigma_{kl}}}\dot{\tilde{\lambda}}\right). \tag{A.1.12}$$

A.1.1.2 Consistency model.

In a concistency elasto-viscoplastic formulation the following relations hold:

$$F(\sigma_{ij},\bar{\epsilon}^{vp},\dot{\bar{\epsilon}}^{vp})=0, \tag{A.1.13}$$

$$\dot{\varepsilon}_{ij}=\dot{\varepsilon}^{e}_{ij}+\dot{\varepsilon}^{vp}_{ij}, \tag{A.1.14}$$

$$\dot{\sigma}_{ij}=M^{e}_{ijkl}\left(\dot{\varepsilon}_{kl}-\dot{\varepsilon}^{vp}_{kl}\right), \tag{A.1.15}$$

$$\dot{\varepsilon}^{vp}_{ij}=\dot{\lambda}\frac{\partial F}{\partial\sigma_{ij}}, \tag{A.1.16}$$

$$\bar{\epsilon}^{vp}=\int_0^t\dot{\bar{\epsilon}}^{vp}dt. \tag{A.1.17}$$

The viscoplastic multiplier $\dot{\lambda}$ is given by the consistency condition

$$\dot{F}=0,\ \dot{\lambda}F=0, \tag{A.1.18}$$

where $F(\sigma_{ij},\bar{\epsilon}^{vp},\dot{\bar{\epsilon}}^{vp})$ is the yield function incorporating the effects of strain and strain-rate hardening through the use of the accumulated viscoplastic strain $\bar{\epsilon}^{vp}$ and its rate $\dot{\bar{\epsilon}}^{vp}$ respectively. The time derivative of the yield condition in this case is given as:

$$\dot{F}=\frac{\partial F}{\partial\sigma_{ij}}\dot{\sigma}_{ij}+\frac{\partial F}{\partial\bar{\epsilon}^{vp}}\dot{\bar{\epsilon}}^{vp}+\frac{\partial F}{\partial\dot{\bar{\epsilon}}^{vp}}\ddot{\bar{\epsilon}}^{vp}=0, \tag{A.1.19}$$

starting from the von Mises yield criterion:

$$F(\sigma_{ij},\bar{\varepsilon}^{vp},\dot{\bar{\varepsilon}}^{vp})=\sqrt{3J_2(\sigma_{ij})}-F_0-h\bar{\epsilon}^{vp}-g\dot{\bar{\epsilon}}^{vp}, \tag{A.1.20}$$

assuming dependence of yield on the deviatoric invariant of the stress tensor $J_2(s_{ij})=\sqrt{\frac{1}{2}s_{ij}s_{ij}}$, and $\dot{\bar{\epsilon}}^{vp}=\sqrt{\frac{2}{3}\dot{\varepsilon}^{vp}_{ij}\dot{\varepsilon}^{vp}_{ij}}$ where $s_{ij}=\sigma_{ij}-\frac{\sigma_{ii}}{3}$, we obtain that $\dot{\lambda}=\dot{\bar{\epsilon}}^{vp}_{ij}$ therefore the yield criterion as well as the consistency condition can be written as:

$$F(\sigma_{ij},\lambda,\dot{\lambda})=0, \tag{A.1.21}$$

$$\dot{F}=\frac{\partial F}{\partial\sigma_{ij}}\dot{\sigma}_{ij}+\frac{\partial F}{\partial\lambda}\dot{\lambda}+\frac{\partial F}{\partial\dot{\lambda}}\ddot{\lambda}=0, \tag{A.1.22}$$

multiplying (A.1.15) by $\frac{\partial F}{\partial \sigma_{ij}}$. replacing $\dot{\varepsilon}_{ij}^{vp}$ with help from (A.1.16) and replacing the term in the lefthandside with equation (A.1.22) we finally get:

$$-\frac{\partial F}{\partial \lambda}\dot{\lambda} - \frac{\partial F}{\partial \dot{\lambda}}\ddot{\lambda} = \frac{\partial F}{\partial \sigma_{ij}} M_{ijkl}^{e} \left(\dot{\varepsilon}_{kl} - \dot{\lambda}\frac{\partial F}{\partial \sigma_{kl}} \right). \tag{A.1.23}$$

Grouping together the terms of $\dot{\lambda}$ and solving for $\dot{\lambda}$ we get:

$$\dot{\lambda} = \frac{\frac{\partial F}{\partial \sigma_{ij}} M_{ijkl}^{e}}{-\frac{\partial F}{\partial \lambda} + \frac{\partial F}{\partial \sigma_{ij}} M_{ijkl}^{e} \frac{\partial F}{\partial \sigma_{kl}}} \dot{\varepsilon}_{kl} + \frac{\frac{\partial F}{\partial \dot{\lambda}}}{-\frac{\partial F}{\partial \lambda} + \frac{\partial F}{\partial \sigma_{ij}} M_{ijkl}^{e} \frac{\partial F}{\partial \sigma_{kl}}} \ddot{\lambda}, \tag{A.1.24}$$

Inserting (A.1.24) into (A.1.15) we obtain:

$$\dot{\sigma}_{ij} = M_{ijkl}^{e} \left(\dot{\varepsilon}_{kl} - \frac{\frac{\partial F}{\partial \sigma_{ij}} M_{ijkl}^{e} \frac{\partial F}{\partial \sigma_{kl}}}{-\frac{\partial F}{\partial \lambda} + \frac{\partial F}{\partial \sigma_{ij}} M_{ijkl}^{e} \frac{\partial F}{\partial \sigma_{kl}}} \dot{\varepsilon}_{kl} + \frac{\frac{\partial F}{\partial \dot{\lambda}} \frac{\partial F}{\partial \sigma_{kl}}}{-\frac{\partial F}{\partial \lambda} + \frac{\partial F}{\partial \sigma_{ij}} M_{ijkl}^{e} \frac{\partial F}{\partial \sigma_{kl}}} \ddot{\lambda} \right), \tag{A.1.25}$$

Replacing the time derivative with a variation taking advantage of the definition of variation we arrive at the constitutive equation describing the perturbed field of stress $\tilde{\sigma}_{ij}$.

$$\tilde{\sigma}_{ij} = M_{ijkl}^{e} \left(\tilde{\varepsilon}_{kl} - \frac{\frac{\partial F}{\partial \sigma_{ij}} M_{ijkl}^{e} \frac{\partial F}{\partial \sigma_{kl}}}{-\frac{\partial F}{\partial \lambda} + \frac{\partial F}{\partial \sigma_{ij}} M_{ijkl}^{e} \frac{\partial F}{\partial \sigma_{kl}}} \tilde{\varepsilon}_{kl} + \frac{\frac{\partial F}{\partial \dot{\lambda}} \frac{\partial F}{\partial \sigma_{kl}}}{-\frac{\partial F}{\partial \lambda} + \frac{\partial F}{\partial \sigma_{ij}} M_{ijkl}^{e} \frac{\partial F}{\partial \sigma_{kl}}} \dot{\tilde{\lambda}} \right). \tag{A.1.26}$$

A.1.2 Derivation of the perturbed equation

Inserting (A.1.26) into (4.3) we arrive at:

$$M_{ijkl}^{e} \left(\tilde{\varepsilon}_{kl,j} - \frac{\frac{\partial F}{\partial \sigma_{ij}} M_{ijkl}^{e} \frac{\partial F}{\partial \sigma_{kl}}}{-\frac{\partial F}{\partial \lambda} + \frac{\partial F}{\partial \sigma_{ij}} M_{ijkl}^{e} \frac{\partial F}{\partial \sigma_{kl}}} \tilde{\varepsilon}_{kl,j} + \frac{\frac{\partial F}{\partial \dot{\lambda}} \frac{\partial F}{\partial \sigma_{kl}}}{-\frac{\partial F}{\partial \lambda} + \frac{\partial F}{\partial \sigma_{ij}} M_{ijkl}^{e} \frac{\partial F}{\partial \sigma_{kl}}} \dot{\tilde{\lambda}}_{,j} \right) = \rho \ddot{\tilde{u}}_{i}. \tag{A.1.27}$$

Substituting (A.1.16) into the last term of the right hand side of eq. (A.1.27) such that $\dot{\varepsilon}_{kl}^{vp} = \frac{\partial F}{\partial \sigma_{kl}}\dot{\lambda}$ we arrive at:

$$M_{ijkl}^{e} \left(\tilde{\varepsilon}_{kl,j} - \frac{\frac{\partial F}{\partial \sigma_{ij}} M_{ijkl}^{e} \frac{\partial F}{\partial \sigma_{kl}}}{-\frac{\partial F}{\partial \lambda} + \frac{\partial F}{\partial \sigma_{ij}} M_{ijkl}^{e} \frac{\partial F}{\partial \sigma_{kl}}} \tilde{\varepsilon}_{kl,j} + \frac{\frac{\partial F}{\partial \dot{\lambda}}}{-\frac{\partial F}{\partial \lambda} + \frac{\partial F}{\partial \sigma_{ij}} M_{ijkl}^{e} \frac{\partial F}{\partial \sigma_{kl}}} \dot{\tilde{\varepsilon}}_{kl,j}^{vp} \right) = \rho \ddot{\tilde{u}}_{i}, \tag{A.1.28}$$

rewriting $\dot{\tilde{\varepsilon}}^{vp}_{kl} = \dot{\tilde{\varepsilon}}_{kl} - M^{e^{-1}}_{ijkl}\dot{\tilde{\sigma}}_{ij}$:

$$M^e_{ijkl}\left(\tilde{\varepsilon}_{kl,j} - \frac{\frac{\partial F}{\partial \sigma_{ij}} M^e_{ijkl} \frac{\partial F}{\partial \sigma_{kl}}}{-\frac{\partial F}{\partial \lambda} + \frac{\partial F}{\partial \sigma_{ij}} M^e_{ijkl} \frac{\partial F}{\partial \sigma_{kl}}}\tilde{\varepsilon}_{kl,j} + \frac{\frac{\partial F}{\partial \dot{\lambda}}}{-\frac{\partial F}{\partial \lambda} + \frac{\partial F}{\partial \sigma_{ij}} M^e_{ijkl} \frac{\partial F}{\partial \sigma_{kl}}}\dot{\tilde{\varepsilon}}_{kl,j} - \frac{\frac{\partial F}{\partial \dot{\lambda}} M^{e^{-1}}_{ijkl}}{-\frac{\partial F}{\partial \lambda} + \frac{\partial F}{\partial \sigma_{ij}} M^e_{ijkl} \frac{\partial F}{\partial \sigma_{kl}}}\dot{\tilde{\sigma}}_{ij,j}\right) \tag{A.1.29}$$

inserting finally (4.3) we obtain:

$$M^e_{ijkl}\left(\tilde{\varepsilon}_{kl,j} - \frac{\frac{\partial F}{\partial \sigma_{ij}} M^e_{ijkl} \frac{\partial F}{\partial \sigma_{kl}}}{-\frac{\partial F}{\partial \lambda} + \frac{\partial F}{\partial \sigma_{ij}} M^e_{ijkl} \frac{\partial F}{\partial \sigma_{kl}}}\tilde{\varepsilon}_{kl,j} + \frac{\frac{\partial F}{\partial \dot{\lambda}}}{-\frac{\partial F}{\partial \lambda} + \frac{\partial F}{\partial \sigma_{ij}} M^e_{ijkl} \frac{\partial F}{\partial \sigma_{kl}}}\dot{\tilde{\varepsilon}}_{kl,j} - \frac{\frac{\partial F}{\partial \dot{\lambda}} M^{e^{-1}}_{ijkl}}{-\frac{\partial F}{\partial \lambda} + \frac{\partial F}{\partial \sigma_{ij}} M^e_{ijkl} \frac{\partial F}{\partial \sigma_{kl}}}\rho\dddot{\tilde{u}}_i\right) \tag{A.1.30}$$

A.1.2.1 1D Example: shearing of a viscous Cauchy layer

We proceed in deriving the perturbed linear momentum equation for the shearing of a 1D elasto-visoplastic Cauchy layer. The basic kinematic equations and the constitutive relations with the von Mises yield criterion with linear strain and strain-rate hardening/softening, are given as follows:

$$F(\tau, \lambda, \dot{\lambda}) = \sqrt{3}\tau - \bar{\tau}(\lambda) - \eta F_0 \dot{\lambda}, \tag{A.1.31}$$

$$\dot{\gamma} = \dot{\gamma}^{el} + \dot{\gamma}^{vp}, \tag{A.1.32}$$

$$\dot{\gamma}^{vp} = \dot{\lambda}\frac{\partial F}{\partial \tau} = \frac{F}{\eta F_0}\frac{\partial F}{\partial \tau}, \tag{A.1.33}$$

$$\bar{\tau}(\lambda) = F_0 + H\lambda = F_0 + \frac{H}{\sqrt{3}}\gamma^{vp}, \tag{A.1.34}$$

where τ is the shear stress, $\gamma = 2\varepsilon_{12} = 2\varepsilon_{21} = u_{2,1}$ is the engineering shear strain, F_0 is the initial yield strength. H is a hardening/softening material parameters with units of pressure (MPa), while η is the viscosity parameter with units of time s.

Applying the procedure described above and taking advantage of the viscosity potential $F(\tau, \lambda, \dot{\lambda})$ assuming the consistency condition $\dot{F} = 0$, we obtain the following:

$$\dot{F} = \frac{\partial F}{\partial \tau}\dot{\tau} + \frac{\partial F}{\partial \lambda}\dot{\lambda} + \frac{\partial F}{\partial \dot{\lambda}}\ddot{\lambda} = \frac{\partial F}{\partial \tau}\dot{\tau} - \frac{\partial \bar{\tau}}{\partial \lambda}\dot{\lambda} - \eta F_0 \ddot{\lambda}, \tag{A.1.35}$$

$$\dot{\tau} = G\left(\dot{\gamma} - \dot{\gamma}^{vp}\right). \tag{A.1.36}$$

Multiplying the above equation (A.1.36) with $\frac{\partial F}{\partial \tau}$ and replacing $\frac{\partial F}{\partial \tau}\dot{\tau}$ we get:

$$\dot{\tau}\sqrt{3} = G\left(\dot{\gamma} - \dot{\gamma}^{vp}\right)\sqrt{3}, \tag{A.1.37}$$

$$\eta F_0 \ddot{\lambda} + \frac{\partial \bar{\tau}}{\partial \lambda}\dot{\lambda} = G\left(\dot{\gamma} - \dot{\gamma}^{vp}\right)\sqrt{3}, \tag{A.1.38}$$

separating $\dot{\lambda}$ we obtain:

$$\dot{\lambda} = \frac{G\dot{\gamma}\sqrt{3}}{-\frac{\partial \bar{\tau}}{\partial \lambda} + 3G} - \frac{\eta F_0 \ddot{\lambda}}{-\frac{\partial \bar{\tau}}{\partial \lambda} + 3G}, \tag{A.1.39}$$

substituting $\dot{\lambda}$ to the original equation for the calculation of $\dot{\tau}$:

$$\dot{\tau} = G\left(\dot{\gamma} - \frac{3G}{\frac{\partial \bar{\tau}}{\partial \lambda} + 3G}\right) + \frac{G\eta F_0\sqrt{3}\ddot{\lambda}}{\frac{\partial \bar{\tau}}{\partial \lambda} + 3}, \tag{A.1.40}$$

substituting $\frac{1}{G}\frac{\partial \bar{\tau}}{\partial \lambda} = \frac{H}{G} = \bar{h}$ (linear mechanical softening) we arrive finally at:

$$\dot{\tau} = G\left(\frac{\bar{h}}{\bar{h}+3}\right)\dot{\gamma} + \frac{\eta F_0}{\bar{h}+3}\ddot{\gamma}^{vp}. \tag{A.1.41}$$

It should be noted that the results derived until now can be also obtained using the Perzyna model instead of the consistency approach in the case of monotonic loading (no stress reversal, so that the rate dependent unloading overstress of the Perzyna model is not taken into account). Using the Perzyna material we assume the existence of the viscoplastic potential $\Omega(\tau, \lambda, \dot{\lambda})$ which constitutes a region outside the yield function that the stress vector τ is indeed applicable. The time derivative of the yield function $F(\tau, \lambda)$ is then given as:

$$\dot{F} = \eta F_0 \ddot{\lambda} = \frac{\partial F}{\partial \tau}\dot{\tau} + \frac{\partial F}{\partial \lambda}\dot{\lambda} = \frac{\partial F}{\partial \tau}\dot{\tau} - \frac{\partial \bar{\tau}}{\partial \lambda}\dot{\lambda}. \tag{A.1.42}$$

Using the same arguments as before, (multiplying (A.1.36) by $\frac{\partial F}{\partial \tau}$ and substituting (A.1.42)) we arrive at the same expression for $\dot{\lambda}$ and $\dot{\tau}$. Perturbing and replacing (A.1.41) in equation (4.3) we obtain:

$$G\frac{\bar{h}}{3+\bar{h}}\frac{\partial \tilde{\gamma}}{\partial x} + \frac{\eta F_0}{3+\bar{h}}\frac{\partial \dot{\tilde{\gamma}}^{vp}}{\partial x} = \rho \ddot{\tilde{u}}, \tag{A.1.43}$$

$$G\frac{\bar{h}}{3+\bar{h}}\frac{\partial \tilde{\gamma}}{\partial x} + \frac{\eta F_0}{3+\bar{h}}\left(\frac{\partial \dot{\tilde{\gamma}}}{\partial x} - \frac{1}{G}\frac{\partial \dot{\tilde{\tau}}}{\partial x}\right) = \rho \ddot{\tilde{u}}, \tag{A.1.44}$$

$$G\frac{\bar{h}}{3+\bar{h}}\frac{\partial^2 \tilde{u}}{\partial x^2} - \rho\frac{\partial^2 \tilde{u}}{\partial t^2} + \frac{\eta F_0}{(3+\bar{h})}\left(\frac{\partial^3 \tilde{u}}{\partial t \partial x^2} - \frac{1}{v_s^2}\frac{\partial^3 \tilde{u}}{\partial t^3}\right) = 0, \tag{A.1.45}$$

$$G\bar{h}\frac{\partial^2 \tilde{u}}{\partial x^2} - \frac{\partial^2 \tilde{u}}{\partial t^2}\frac{(3+\bar{h})G}{v_s^2} + \bar{\eta}^{vp}G\left(\frac{\partial^3 \tilde{u}}{\partial t \partial x^2} - \frac{1}{v_s^2}\frac{\partial^3 \tilde{u}}{\partial t^3}\right) = 0, \tag{A.1.46}$$

where $v_s = \sqrt{\frac{G}{\rho}}$, $\bar{\eta}^{vp}G = \eta F_0$.

A.1.2.2 Normalizing the 1D elasto-viscoplastic wave equation.

We consider $\bar{u} = \frac{u}{u_c}, \bar{t} = \frac{t}{t_c}, \bar{x} = \frac{x}{x_c}$. Applying and differentiating into (A.1.46) we arrive at:

$$\left(\frac{x_c^2}{v_s^2 t_c^2}\frac{\partial^3 \bar{u}}{\partial \bar{t}^3} - \frac{\partial^3 \bar{u}}{\partial \bar{x}^2 \partial \bar{t}}\right)\frac{\bar{\eta}^{vp}}{t_c \bar{h}} + \frac{x_c^2}{v_s^2 t_c^2}\frac{3+\bar{h}}{\bar{h}}\frac{\partial^2 \bar{u}}{\partial \bar{t}^2} - \frac{\partial^2 \bar{u}}{\partial \bar{x}^2} = 0. \tag{A.1.47}$$

Introducing the characteristic velocity $v_c = \frac{x_c}{t_c}$, the result is written as:

$$\left(\frac{v_c^2}{v_s^2}\frac{\partial^3 \bar{u}}{\partial \bar{t}^3} - \frac{\partial^3 \bar{u}}{\partial \bar{x}^2 \partial \bar{t}}\right)\frac{\bar{\eta}^{vp}}{t_c \bar{h}} + \frac{v_c^2}{v_s^2}\frac{3+\bar{h}}{\bar{h}}\frac{\partial^2 \bar{u}}{\partial \bar{t}^2} - \frac{\partial^2 \bar{u}}{\partial \bar{x}^2} = 0. \tag{A.1.48}$$

A.1.2.3 Dispersion relationship

Inserting into the normalized equation (A.1.48) the nondimensional solution assuming both $\bar{k}, \bar{\omega} \in \mathbb{C}$:

$$\bar{u}(\bar{x}, \bar{t}) = \exp i(\bar{k}\bar{x} - \bar{\omega}\bar{t}), \tag{A.1.49}$$

we arrive at:

$$\bar{h}\bar{k}^2 t_c v_s^2 - i\bar{k}^2 v_s^2 \bar{\eta}^{vp}\bar{\omega} - (3+\bar{h})\bar{t}_c v_c^2 \bar{\omega}^2 + i v_c^2 \bar{\eta}^{vp}\bar{\omega}^3 = 0. \tag{A.1.50}$$

Appendix B

B.1 Behavior of the dispersion relation near infinity.

B.1.1 Properties of the inverse transform $\bar{\omega} = \frac{1}{z}$

We present here in more detail the inverse transform $\bar{\omega} = \frac{1}{z}$ based on Brown, Churchill, et al., 2009. The inverse transform allows the analysis of the behavior of a function close to ∞ by inverting the independent variable. Therefore, as the independent variable $\bar{\omega}$ tends to ∞, its inverse transform z tends to 0. More specifically the points lying outside the unit circle centered at the origin of the $\bar{\omega}$ complex plane are mapped inside the circle, while the opposite is true for the points initially inside the unit circle. The points lying on the unit circle remain on the circle.

When a point $\bar{\omega} = \bar{\omega}_r + \bar{\omega}_i i$ is the image of a nonzero point $z = z_r + z_i i$ under the transformation $\bar{\omega} = 1/z$, the relationship between the real and imaginary parts in original $\bar{\omega}$ and transformed z complex planes respectively are given as:

$$z_r = \frac{\bar{\omega}_r}{\bar{\omega}_r^2 + \bar{\omega}_i^2} \text{ and } z_i = -\frac{\bar{\omega}_i}{\bar{\omega}_r^2 + \bar{\omega}_i^2}, \tag{B.1.1}$$

$$\bar{\omega}_r = \frac{z_r}{z_r^2 + z_i^2} \text{ and } \bar{\omega}_i = -\frac{z_i}{z_r^2 + z_i}. \tag{B.1.2}$$

When A,B,C,D $\in \mathbb{R}$ are real numbers satisfying the condition $\mathrm{B}^2 + \mathrm{C}^2 > 4\mathrm{AD}$, the equation

$$\mathrm{A}(z_r^2 + z_i^2) + \mathrm{B}z_r + \mathrm{C}z_i + \mathrm{D} = 0 \tag{B.1.3}$$

represents a circle or a line on the complex plane z. In particular, when A $= 0$ the equation of a line is returned while when $\mathrm{A} \neq 0$ by completing the squares we get:

$$\left(z_r + \frac{\mathrm{B}}{2\mathrm{A}}\right)^2 + \left(z_i + \frac{\mathrm{C}}{2\mathrm{A}}\right)^2 = \left(\frac{\sqrt{\mathrm{B}^2 + \mathrm{C}^2 - 4\mathrm{AD}}}{2\mathrm{A}}\right). \tag{B.1.4}$$

The above equation represents a circle under the condition mentioned previously. Similarly by substitution of z_r, z_i we find:

$$\mathrm{D}(\bar{\omega}_r^2 + \bar{\omega}_i^2) + \mathrm{B}\bar{\omega}_r - \mathrm{C}\bar{\omega}_i + \mathrm{A} = 0. \tag{B.1.5}$$

From the equations (B.1.3),(B.1.5) above it is clear that:

— A circle in the z-plane ($\mathrm{A} \neq 0$) not passing through the origin ($\mathrm{D} \neq 0$) is transformed into a circle not passing through the origin in the $\bar{\omega}$-plane.

— A circle in the z-plane ($\mathrm{A} \neq 0$) passing through the origin ($\mathrm{D} = 0$) is transformed into a line not passing through the origin in the $\bar{\omega}$-plane.

— A line in the z-plane ($\mathrm{A} = 0$) not passing through the origin ($\mathrm{D} \neq 0$) is transformed into a circle passing through the origin in the $\bar{\omega}$-plane.

— A line in the z-plane ($\mathrm{A} \neq 0$) passing through the origin ($\mathrm{D} = 0$) is transformed into a line passing through the origin in the $\bar{\omega}$-plane.

From the above remarks we conclude that in the two complex planes the directions of the real and imaginary axes coincide. Furthermore every line passing from the origin retains its direction.

For our analyses we need to examine the behavior of $\bar{k}_{1,2}(\bar{\omega})$ along lines of constant $\bar{\omega}_r = c_1, \bar{\omega}_i = c_2$. The geometrical loci on the complex z-plane are given by equations:

$$\left(z_r - \frac{1}{2c_1}\right)^2 + z_i^2 = \left(\frac{1}{c_1}\right)^2, \tag{B.1.6}$$

$$z_r^2 + \left(z_i + \frac{1}{2c_2}\right)^2 = \left(\frac{1}{c_2}\right)^2. \tag{B.1.7}$$

We notice that due to the inverse transform properties, lines parallel to the real axis Re, lying in one half of the complex $\bar{\omega}$-plane are transformed into circles passing through the origin, whose center lies on the opposite imaginary half of the z-plane.

B.1.2 Application of the inverse mapping describing the point at complex infinity.

Applying this mapping in equation (4.25) yields:

$$\bar{k}_1(z) = V\frac{1}{z}\left(\frac{3+\bar{h}}{iT} - \frac{1}{z}\right)^{\frac{1}{2}}\left(\frac{\bar{h}}{iT} - \frac{1}{z}\right)^{-\frac{1}{2}}, \tag{B.1.8}$$

where the following relations hold between the components of $\bar{\omega}, z$ in their respective complex plane:

$$z_r = \frac{\bar{\omega}_r}{\bar{\omega}_r^2 + \bar{\omega}_i^2}\ ,\ z_i = \frac{-\bar{\omega}_i}{\bar{\omega}_r^2 + \bar{\omega}_i^2}. \tag{B.1.9}$$

Taking the limit as $z \to 0$ and expanding the root terms as Taylor series around $z \to 0$ we obtain:

$$\lim_{z\to 0} \bar{k}_1\left(\frac{1}{z}\right) = V\frac{1}{z}\left(1 - \frac{1}{2}\frac{3+\bar{h}}{iT}z + \frac{1}{8}\left(\frac{3+\bar{h}}{iT}\right)^2 z^2 + ...\right)\frac{1}{1-\left(\frac{1}{2}\frac{3+\bar{h}}{iT}z - \frac{1}{8}\left(\frac{3+\bar{h}}{iT}\right)^2 z^2 + ...\right)}. \tag{B.1.10}$$

We notice the pattern in the denominator of the last term that we can replace with the Taylor series of $\frac{1}{1-x}$ around $x \to 0$ leading to:

$$\begin{aligned}\lim_{z\to 0} \bar{k}_1(z) =& V\frac{1}{z}\left(1 - \frac{1}{2}\frac{3+\bar{h}}{iT}z + \frac{1}{8}\left(\frac{3+\bar{h}}{iT}\right)^2 z^2 + ...\right)\left(1 + \left(\frac{1}{2}\frac{3+\bar{h}}{iT}z + \frac{1}{8}\left(\frac{3+\bar{h}}{iT}\right)^2 z^2 + ...\right)\right. \\ &\left. + \left(\frac{1}{2}\frac{3+\bar{h}}{iT}z + \frac{1}{8}\left(\frac{3+\bar{h}}{iT}\right)^2 z^2 + ...\right)^2 + ...\right).\end{aligned} \tag{B.1.11}$$

From the above polynomial only the factor $\frac{1}{z}$ tends to ∞, therefore $z = 0 \Leftrightarrow \bar{\omega}^{P2} \to \infty$ is a pole of first order Brown, Churchill, et al., 2009.

For the real part of $\bar{k}$ at the pole $\bar{\omega}^{P2}$ as z_r tends to ∞ applying de l' Hopital rule we can prove:

$$\lim_{\bar{z}_r \to 0^+} \mathrm{Re}\left[\bar{k}_{1,2}(\bar{z}_r + \beta i)\right] = \lim_{\bar{z}_r \to 0^+} \left[\pm V1 \sqrt[4]{\frac{(3+h)^2 + \frac{T1^2}{z_r^2}}{h^2 + \frac{T1^2}{\bar{z}_r^2}}} \frac{\cos\left(\frac{1}{2}\arg\left(\frac{3+h-\frac{iT1}{\bar{z}_r}}{h-\frac{iT1}{\bar{z}_r}}\right)\right)}{\bar{z}_r} \right] = \pm\infty, \tag{B.1.12}$$

where $\beta = 0$ in the case of traveling waves.
Furthermore, for the imaginary part of $\bar{k}(z)$ at the pole $\bar{\omega}^{P2}$ as z_r tends to ∞ we can prove that $\bar{k}_i \to \pm c \ \in \mathbb{R}$ using the de l' Hôpital rule:

$$\lim_{\bar{z}_r \to 0} \mathrm{Im}\left[\bar{k}_{1,2}(\bar{z}_r + 0i)\right] = \lim_{\bar{z}_r \to 0} \left[\pm V1 \sqrt[4]{\frac{(3+h)^2 + \frac{T1^2}{z_r^2}}{h^2 + \frac{T1^2}{\bar{z}_r^2}}} \frac{\sin\left(\frac{1}{2}\arg\left(\frac{3+h-\frac{iT1}{\bar{z}_r}}{h-\frac{iT1}{\bar{z}_r}}\right)\right)}{\bar{z}_r} \right] = \pm c \tag{B.1.13}$$

The value of $\bar{k}_i(\bar{\omega})$ is independent of whether we move towards the left or the right of the real axis $\bar{\omega}_r$. It only depends on the solution branch $\bar{k}_1(\bar{\omega})$, or $\bar{k}_2(\bar{\omega})$ we follow. (see Figure 4.9).

Appendix C

C.1 Stability and localization of a monochromatic sinusoidal propagating pulse

The stability of the homogeneous deformation for a strain-softening ($h < 0$) strain-rate hardening ($g > 0$) material, was examined based on the amplification (unstable) or attenuation (stable) of an arbitrary perturbation. When looking only at the case of a monochromatic propagating sinusoidal pulse, two velocities could be identified. These are the amplitude velocity, c_i, and the phase velocity, c_f (see section 4.3). Examining equation (4.22) we notice that the amplitude term can be described as an exponential function in $\bar{x}$ traveling along $\bar{x}$-axis with velocity c_i. Similarly, the periodic part which travels with a velocity of c_r. A monochromatic sinusoidal pulse, whose amplitude varies with time and distance, is given as:

$$\bar{p}(\bar{x},\bar{t}) = \Big[H(\bar{k}_r\bar{x} - \bar{\omega}_r\bar{t}) - H(\bar{k}_r\bar{x} - \bar{\omega}_r\bar{t} - 2\pi)\Big]\,\bar{u}\exp\left(-\bar{k}_i\bar{x} + \bar{\omega}_i\bar{t}\right)\exp\left(i(\bar{k}_r\bar{x} - \bar{\omega}_r\bar{t})\right), \tag{C.1.1}$$

$$\bar{p}(\bar{x},\bar{t}) = \Big[H(\bar{x} - c_r\bar{t}) - H(\bar{x} - c_r\bar{t} - 2\pi)\Big]\,\bar{u}\exp\Big(-(\bar{x} - c_i\bar{t})\Big)\exp\left(i(\bar{x} - c_r\bar{t})\right). \tag{C.1.2}$$

The Heaviside terms $H(\,\cdot\,)$ are multiplied to the original monochromatic solution to indicate the start and end of the monochromatic signal. Therefore, they travel with the velocity of the periodic wave. In this way we can describe the amplitude that corresponds to the wavelength of the pulse at a specific time. Based on equation (C.1.2) the relationship between the velocities of the two exponential terms comprising the pulse is indicative of the stability and possible strain localization of the solution. In particular the following cases are possible.

— $c_i < 0, c_r > 0$

— $c_i > 0, c_r > 0$
— $c_i > 0, c_r < 0$
— $c_i < 0, c_r < 0$

The negative signs in c_i, c_r refer to the wave moving opposite to the positive direction defined by the positive $\bar{x}$-axis. In the first case described above $c_i < 0, c_r > 0$ (see left part of Figure C.1), the perturbation is moving towards the positive part of the x-axis while the amplitude towards the negative. Due to the construction of the amplitude function (negative exponential) this has as an effect that every perturbation is attenuating with time. Therefore stability of the reference solution of homogeneous deformation is ensured and strain localization cannot take place.

In the second case both amplitude and phase are moving towards the positive part of the $\bar{x}$-axis as shown on the right part of Figure C.1 and the left part of Figure C.2. In this case the behavior of the perturbation is defined by the relative magnitudes of the velocities $|c_i|, |c_r|$. If $|c_i| < |c_r|$ then the velocity of the negative exponential is lower than that of the perturbation. Therefore, the amplitude of the perturbation is attenuated and the reference solution is stable (see right part of Figure C.1). In the opposite case, where the perturbation travels slower than the amplitude velocity, the perturbation grows, rendering the reference solution unstable (see left part of Figure C.2). Since the amplitude is increasing the fastest at the peak behind the pulse, displacement is localizing close to the tip and localization to the smallest mesh dimension is inevitable.

In the third case when $c_i < 0, c_r < 0$, again the amplitude function and the perturbation are traveling towards the negative direction (see left part of Figure C.2, right part of Figure C.3). Again the question of stability and localization is dependent on the relative magnitudes of the two velocities $|c_i|, |c_r|$. In this case, if the perturbation is traveling slower than the amplitude $|c_r| < |c_i|$ then the amplitude of the perturbation is decreasing and no localization happens (see left part of Figure C.3). When we consider the case where $|c_r| > |c_i|$ then the amplitude of the perturbation is increasing exponentially. The amplitude is increasing the fastest for the tip closer to the front of the pulse and localization to the smallest wavelength cannot be avoided (see right part of Figure C.2.

In the final case $c_i > 0, c_r < 0$, the perturbation is moving towards the negative part of the $\bar{x}$-axis while the amplitude towards the positive (see right part of Figure C.3). Due

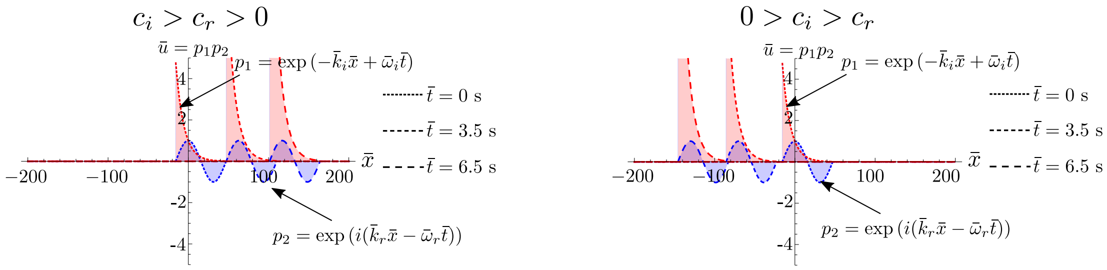

Figure C.2 – Conditions for the growth of the perturbation. Left: Evolution of the perturbation (blue curve) and its amplitude (red curve) at different times for $c_i > c_r > 0$. Right:Evolution of the perturbation (blue curve) and its amplitude (red curve) at different times for $0 > c_i > c_r$. The propagating pulse is the multiplication of the red and blue curves.

to the negative exponential spatial profile of the amplitude function, the amplitude of the perturbation is always increasing the fastest at the tip in front of the pulse. Therefore, in this final case, the solution is unstable and strain localization is possible with the smallest possible wavelength.

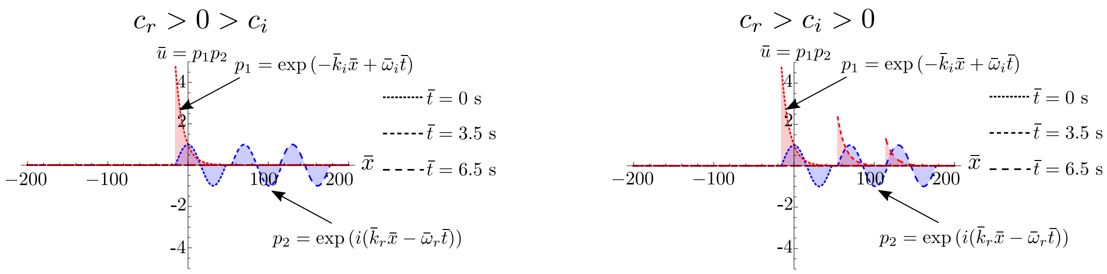

Figure C.1 – Conditions for decaying perturbation. Left: Evolution of the perturbation (blue curve, $\exp\left(i(\bar{(x)} - c_r\bar{t})\right)$ and its amplitude (red curve, $\exp\left(-(\bar{x} - c_i\bar{t})\right)$) at different times for $c_i < 0 < c_r$. Right: Evolution of the perturbation (blue curve) and its amplitude (red curve) at different times for $c_r > c_i > 0$. The propagating pulse is the multiplication of the red and blue curves.

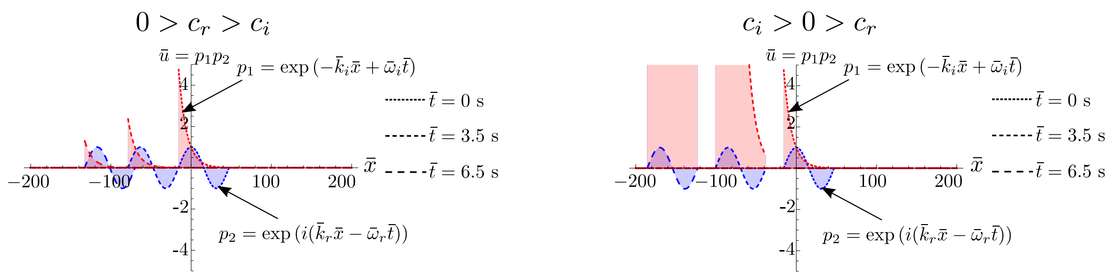

Figure C.3 – Conditions for the decay and growth of the perturbation. Left: Evolution of the perturbation (blue curve) and its amplitude (red curve) at different times for $0 > c_r > c_i$, decay of perturbation. Right: Evolution of the perturbation (blue curve) and its amplitude (red curve) at different times for $c_i > 0 > c_r$, growth of perturbation. The propagating pulse is the multiplication of the red and blue curves.

Appendix D

D.1 Constitutive relations

The devolopement of the thermo-elasto-plastic constitutive ralations that follow is based on J. Sulem et al., 2011 and Rattez, Stefanou, Sulem, Veveakis, et al., 2018b. Since we follow a small strain approach, the strain rate and the curvature rate tensor can be decomposed into their elastic, plastic and thermal parts. Large displacements are then taken into account through an updated Lagrangian approach. In what follows we make the assumption that the curvature tensor stays unaffected by a change of temperature. Therefore strain rate and curvature rate tensors are decomposed as Lemaitre et al., 2020:

$$\begin{aligned}\dot{\gamma}_{ij} =&\dot{\gamma}^e_{ij} + \dot{\gamma}^p_{ij} + \dot{\gamma}^{th}_{ij},\\ \dot{\kappa}_{ij} =&\dot{\kappa}^e_{ij} + \dot{\kappa}^p_{ij}\end{aligned} \tag{D.1.1}$$

Thermal strain rates can be expressed as $\dot{\gamma}^{th}_{ij} = \alpha\dot{T}\delta_{ij}$, where α is the thermal expansion coefficient. For the calculation of the plastic strain rate, we first define a yield function $F = F(\tau_{ij}, \sigma_{ij}, \gamma^p, \epsilon^p_v)$, which we assume to be dependent only on the first and second stress tensor invariants as well as the deviatoric and spherical parts of the accumulated plastic strain tensor $F = F(\tau, \sigma, \gamma^p, \epsilon^p_v)$. A more complete approach in a thermodynamical framework that takes into account grain breakage and the consequent evolution of the internal lengths can be found in Collins-Craft et al., 2020. Following standard arguments of elasto-plasticity and by use of the consistency condition $\dot{F}$ we obtain:

$$\tau_{ij} = C^e_{ijkl}\left(\dot{\gamma}_{ij} - \dot{\gamma}^p_{ij} - \dot{\gamma}^{th}_{ij}\right), \tag{D.1.2}$$

$$\mu_{ij} = M^e_{ijkl}\left(\dot{\kappa}_{ij} - \dot{\kappa}^p_{ij}\right), \tag{D.1.3}$$

$$\dot{\gamma}^p_{ij} = \dot{\gamma}^p \frac{\partial Q}{\partial \tau_{ij}}, \tag{D.1.4}$$

$$\dot{\kappa}^p_{ij} = \dot{\gamma}^p \frac{\partial Q}{\partial \mu_{ij}}, \tag{D.1.5}$$

$$\dot{F} = \frac{\partial F}{\partial \tau_{ij}}\dot{\tau}_{ij} + \frac{\partial F}{\partial \mu_{ij}}\dot{\mu}_{ij} + \frac{\partial F}{\partial \gamma^p}\dot{\gamma}^p + \frac{\partial F}{\partial \epsilon^p_v}\dot{\epsilon}^p_v = 0, \tag{D.1.6}$$

$$\dot{F} = \frac{\partial F}{\partial \tau}\dot{\tau} + \frac{\partial F}{\partial \sigma}\dot{\sigma} + \frac{\partial F}{\partial \gamma^p}\dot{\gamma}^p + \frac{\partial F}{\partial \epsilon^p_v}\dot{\epsilon}^p_v = 0. \tag{D.1.7}$$

Where by $Q, \dot{\gamma}^p$ we denote the plastic potential and the plastic multiplier respectively. We note that in the present context a common criterion for both Cosserat stresses and moments has been assigned to the material. We continue by defining the hardening modulus H_s as:

$$H_s = -\frac{\partial F}{\partial \gamma^p}. \tag{D.1.8}$$

Assuming a linear dependence of the yield and plastic potential functions to τ, σ as is the case in a Drucker-Prager material, which we will later use in the numerical analyses, the following relations hold for the plastic multiplier and the rate of volumetric plastic strain:

$$\dot{\gamma}^p = \dot{\gamma}^p \quad \text{and} \quad \dot{\epsilon}^p_v = \beta\dot{\gamma}^p \tag{D.1.9}$$

where β is the dilatancy angle. Multiplying (D.1.2) by $\frac{\partial F}{\partial \tau_{ij}}$ and (D.1.3) by $\frac{\partial F}{\partial \mu_{ij}}$ then adding together and taking advantage of the fact that $\frac{\partial F}{\partial \tau_{ij}}\dot{\tau}_{ij} + \frac{\partial F}{\partial \mu_{ij}}\dot{\mu}_{ij} = \frac{\partial F}{\partial \tau}\dot{\tau} + \frac{\partial F}{\partial \sigma}\dot{\sigma}$, the consistency condition yields:

$$\dot{\gamma}^p = \frac{<1>}{H_p}\left(\frac{\partial F}{\partial \tau_{ij}}C^e_{ijkl}(\dot{\gamma}_{kl} - \alpha\dot{T}\delta_{kl})\right) + \frac{\partial F}{\partial \mu_{ij}}M^e_{ijkl}\dot{\kappa}_{kl}. \tag{D.1.10}$$

Simplifying the notation we get:

$$\dot{\gamma}^p = \frac{<1>}{H_p}(b^F_{kl}(\dot{\gamma}_{kl} - \alpha\dot{T}\delta_{kl}) + b^F_{kl}\dot{\kappa}_{kl}), \tag{D.1.11}$$

with

$$H_p = \frac{\partial F}{\partial \tau_{ij}} C^e_{ijkl} \frac{\partial Q}{\partial \tau_{kl}} + \frac{\partial F}{\partial \mu_{ij}} M^e_{ijkl} \frac{\partial Q}{\partial \mu_{kl}} + H_s \tag{D.1.12}$$

$$< 1 >= \begin{cases} 1 & \text{if } F = 0 \text{ and } \dot{\gamma}^p > 0 \\ 0 & \text{otherwise} \end{cases} \tag{D.1.13}$$

and

$$b^F_{kl} = \frac{\partial F}{\partial \tau_{ij} C^e_{ijkl}}, \tag{D.1.14}$$

$$b^Q_{ij} = C^e_{ijkl} \frac{\partial Q}{\partial \tau_{kl}}, \tag{D.1.15}$$

$$b^F M_{kl} = \frac{\partial F}{\partial \mu_{ij} M^e_{ijkl}}, \tag{D.1.16}$$

$$b^Q M_{ij} = M^e_{ijkl} \frac{\partial Q}{\partial \mu_{kl}}. \tag{D.1.17}$$

$$\tag{D.1.18}$$

Using (D.1.4),(D.1.5) and (D.1.11) in (D.1.2) we obtain:

$$\dot{\tau}_{ij} = C^{ep}_{ijkl} \dot{\gamma}_{kl} + D^{ep}_{ijkl} \dot{\kappa}_{kl} + E^{ep}_{ijkl} \dot{T} \delta_{kl} \tag{D.1.19}$$

$$\dot{\mu}_{ij} = M^{ep}_{ijkl} \dot{\kappa}_{kl} + L^{ep}_{ijkl} \dot{\gamma}_{kl} + N^{ep}_{ijkl} \dot{T} \delta_{kl} \tag{D.1.20}$$

with

$$\begin{aligned}
C^{ep}_{ijkl} &= C^e_{ijkl} - \frac{< 1 >}{H_p} b^Q_{ij} b^F_{kl}, \\
D^{ep}_{ijkl} &= -\frac{< 1 >}{H_p} b^Q_{ij} b^F M_{kl}, \\
E^{ep}_{ijkl} &= -\left(C^e_{ijkl} - \frac{< 1 >}{H_p} b^Q_{ij} b^F_{kl} \right), \\
L^{ep}_{ijkl} &= -\frac{< 1 >}{H_p} b^Q M_{ij} b^F_{kl}, \\
M^{ep}_{ijkl} &= \left(M^e_{ijkl} - \frac{< 1 >}{H_p} b^Q M_{ij} b^F M_{kl} \right), \\
N^{ep}_{ijkl} &= \frac{< 1 >}{H_p} b^Q M_{ij} b^F_{kl}.
\end{aligned} \tag{D.1.21}$$

Appendix E

E.1 Derivation of the coupled pore fluid pressure diffusion kernel.

In this section we derive the coupled pore fluid pressure diffusion kernel for the cases of a bounded domain subjected to a stationary Dirac load and an unbounded domain under a moving Dirac load. Our procedure follows the discussion in Lee and Delaney, 1987 where the same problem was solved for a stationary Dirac thermal load on an unbounded domain.

E.1.1 Stationary thermal load, coupled pore fluid pressure Green's kernel for a bounded domain.

In the case of the bounded domain we proceed by applying the method of separation of variables and then expanding the solution to a Fourier series. We note here that the coupled system of pressure and temperature diffusion equations have the same form of linear partial differential operators and boundary conditions and therefore their solution belongs to the same space of Sturm-Liouville problems. In essence the two solutions have the same eigenfunctions. In the case of the bounded domain the Temperature diffusion equation has the solution given in Cole et al., 2010:

$$T(x,t) = \sum_{n=1}^{\infty} \frac{2}{\mathrm{H}\rho C} \int_0^t \int_{-\infty}^{\infty} g(x',t') \exp\left[-\lambda^2 c_{th}(t-t')\right] \sin(\lambda_n x) \sin(\lambda_n x') dx' dt', \tag{E.1.1}$$

where λ_n is the Sturm-Liouvile eigenfunction coefficient, $\lambda_n = \frac{n\pi}{\mathrm{H}}$, H is the length of the bounded domain. The eigencondition for the homogeneous Dirichlet boundary condtitions are given by:

$$\sin\left(\frac{n\pi}{\mathrm{H}}\mathrm{H}\right) = 0,\ \lambda_n = \frac{n\pi}{\mathrm{H}},\ n = 1, 2, ... \tag{E.1.2}$$

We note here that the homogeneous pressure diffusion partial deifferential equation on the above bounded domain has the same boundary conditions. Therefore, the pore fluid pressure solution can be written with the same eigenfunctions as above. Replacing the pore fluid pressure eigenfunction expansion $\tilde{p}(x,t) = p(x,t) - p_0 = \sum_{i=n}^{\infty} \tilde{p}_n \sin\frac{n\pi x}{\mathrm{H}}$ into the coupled pressure diffusion partial differential equation,

$$\begin{aligned}
&\frac{\partial \tilde{p}(x,t)}{\partial t} - c_{hy}\frac{\partial^2 \tilde{p}(x,t)}{\partial x^2} = \Lambda\frac{\partial T(x,t)}{\partial t},\\
&\tilde{p}(x,0) = 0,\\
&\tilde{p}(0,t) = \tilde{p}(\mathrm{H},t) = 0,
\end{aligned} \tag{E.1.3}$$

we obtain:

$$\sum_{n=1}^{\infty}\frac{\partial \tilde{p}_n(t)}{\partial t}\sin\lambda_n x + c_{hy}\sum_{n=1}^{\infty}\lambda_n^2\tilde{p}_n(t)\sin\lambda_n x = \frac{2\Lambda}{\mathrm{H}\rho C}\sum_{n=1}^{\infty}\sin\lambda_n x\frac{\partial T_n(t)}{\partial t}, \tag{E.1.4}$$

where $T_n(t)$ is given as:

$$T_n(t) = \int_0^t\int_{-\infty}^{\infty} g(x',t')\exp\left[-\lambda_n^2 c_{th}(t-t')\right]\sin\lambda_n x' dx' dt'.$$

Isolating each eigenfunction $\sin\lambda_n x$ we arrive at the following first order linear differential equations involving the unknown coefficient $\tilde{p}_n(t)$ and the loading coefficient $T_n(t)$ for each particular component of the solution series expansion.

$$\frac{\partial \tilde{p}_n(t)}{\partial t} + c_{hy}\lambda_n^2\tilde{p}_n(t) = \frac{2\Lambda}{\mathrm{H}\rho C}\frac{\partial T_n(t)}{\partial t},\ t \geq 0. \tag{E.1.5}$$

Applying the Laplace transformation in the field of time:

$$s\tilde{P}_n(s) + c_{hy}\lambda_n^2\tilde{P}_n(s) = \frac{2\Lambda}{\mathrm{H}\rho C}\frac{s}{s+\lambda_n^2 c_{th}}\int_{-\infty}^{\infty} G(x',s)\sin\lambda_n x' dx'. \tag{E.1.6}$$

$$\tilde{P}_n(s) = \frac{2\Lambda}{\mathrm{H}\rho C}\frac{s}{(s+\lambda_n^2 c_{th})(s+\lambda_n^2 c_{hy})}\int_{-\infty}^{\infty} G(x',s)\sin\lambda_n x' dx' \tag{E.1.7}$$

Applying the inverse of the Laplace transform gives us:

$$\tilde{p}_n(x,t) = \frac{2\Lambda}{\mathrm{H}\rho C}\int_0^t\int_{-\infty}^{\infty} g(x',t')\frac{c_{hy}\exp\left[-\lambda_n^2 c_{hy}(t-t')\right] - c_{th}\exp\left[-\lambda_n^2 c_{th}(t-t')\right]}{c_{hy}-c_{th}}\sin\lambda_n x' dx' dt' \tag{E.1.8}$$

Finally, in the series expansion $\tilde{p}(x,t) = \sum_{n=1}^{\infty}\tilde{p}_n(t)\sin\lambda_n x$ we move the summation under the integral sign and we obtain:

$$\begin{aligned}\tilde{p}(x,t) = \frac{2\Lambda}{\mathrm{H}\rho C}\int_0^t\int_{-\infty}^{\infty} & g(x',t') \\ & \sum_{n=1}^{\infty}\frac{c_{hy}\exp\left[-\lambda_n^2 c_{hy}(t-t')\right] - c_{th}\exp\left[-\lambda_n^2 c_{th}(t-t')\right]}{c_{hy}-c_{th}}\sin\lambda_n x\sin\lambda_n x' dx' dt'\end{aligned} \tag{E.1.9}$$

We recognize the term in the second line of equation (E.1.9) as the Green's function kernel of the coupled pressure diffusion partial differential equation. This expression has the added advantage that the influence of the thermal load on the pressure $\tilde{p}(x,t) = p(x,t) - p_0$ solution is straightforward. Noticing that for a general diffusion problem on a bounded domain under homogeneous Dirichlet boundary conditions the Green's function kernel is given by:

$$G_{X11}(x,x',t-t',c) = \frac{2}{\mathrm{H}}\sum_{n=1}^{\infty}\exp\left[-\lambda_n^2 c\frac{t-t'}{\mathrm{H}^2}\right]\sin\lambda_n x\sin\lambda_n x'. \tag{E.1.10}$$

The Green's function kernel of the coupled pressure differential equation on the bounded domain is then given as:

$$G_{X11}(x,x',t-t',c_{th},c_{hy}) = \frac{c_{hy}G_{X11}(x,x',t-t',c_{hy}) - c_{th}G_{X11}(x,x',t-t',c_{th})}{c_{hy}-c_{th}}. \tag{E.1.11}$$

Finally, the pressure solution can be given as:

$$p(x,t) - p_0 = \tilde{p}(x,t) = \frac{\Lambda}{\rho C}\int_0^t\int_{-\infty}^{\infty} g(x',t')G_{X11}(x,x',t-t',c_{th},c_{hy})dx'dt' \tag{E.1.12}$$

This result agrees with the formula provided in Lee and Delaney, 1987; Rice, 2006a for the unbounded domain.

E.1.2 Moving thermal load, coupled pore fluid pressure Green's kernel for a unbounded domain.

Here, we present the derivation of the Green's function kernel of the coupled pressure diffusion equation for an unbounded domain under moving thermal load. Note here, that the Green's function kernel is independent of the type of loading (stationary or moving), it depends on the kind of the differential operator and the boundary conditions. What differs here in the form of the Green's function kernel is the velocity dependence, since we want to connect the pressure evolution not with the stationary Green's function but with the moving Dirac thermal load, that can be written as $g(x,t) = \frac{\dot{\delta}}{\rho C}\tau(t)\delta(x-vt)$. In essence we need to only prescribe the velocity dependence of $x' = f(v,t')$ in the Green's function kernel for the unbounded domain under Dirichlet conditions $G_{X00}(x,x',(t-t'),c_{hy},c_{th})$. We provide a full description and then compare the results. The coupled system of temperature and pore fluid pressure diffusion equations in the unbounded domain is given by:

$$\begin{aligned}
&\frac{\partial T(x,t)}{\partial t} - c_{th}\frac{\partial^2 T(x,t)}{\partial x^2} = \frac{\dot{\delta}}{\rho C}\tau(t)\delta(x-vt),\ -\infty < x < \infty,\ 0 < t < \infty\\
&\frac{\partial \tilde{p}(x,t)}{\partial t} - c_{hy}\frac{\partial^2 \tilde{p}(x,t)}{\partial x^2} = \Lambda\frac{\partial T(x,t)}{\partial t},\ -\infty < x < \infty,\ 0 < t < \infty,\\
&T(x,0) = 0,\\
&\lim T(x,t)\|_{x=-\infty,x=\infty} = 0,\\
&\tilde{p}(x,0) = 0,\\
&\lim \tilde{p}(x,t)\|_{x=-\infty,x=\infty} = 0
\end{aligned} \tag{E.1.13}$$

To account for the moving load we perform a change of variables on the original system (E.1.13) where $\xi = x - vt,\ \eta = t$ so that we attach a frame of reference to the moving load. In this case and by suitable application of the chain rule we can write:

$$\begin{aligned}
&\frac{\partial T(\xi,\eta)}{\partial \eta} - v\frac{\partial T}{\partial \xi} - c_{th}\frac{\partial^2 T(\xi,\eta)}{\partial \xi^2} = \frac{1}{\rho C}\tau(t)\delta(\xi),\ -\infty < \xi < \infty,\ 0 < \eta < \infty,\\
&\frac{\partial \tilde{p}(\xi,\eta)}{\partial eta} - v\frac{\partial \tilde{p}(\xi,\eta)}{\partial \xi} - c_{hy}\frac{\partial^2 \tilde{p}(\xi,\eta)}{\partial \xi^2} = \Lambda\frac{\partial T(\xi,\eta)}{\partial \eta},\ -\infty < \xi < \infty,\ 0 < \eta < \infty\\
&T(\xi,0) = 0,
\end{aligned}$$

$$\lim T(\xi,\eta)\|_{\xi=-\infty,\xi=\infty} = 0,$$
$$\tilde{p}(\xi,0) = 0,$$
$$\lim \tilde{p}(\xi,\eta)\|_{\xi=-\infty,\xi=\infty} = 0 \tag{E.1.14}$$

Applying a Fourier transform in space and a Laplace transform in time on the system of partial differential equations (**??**) we obtain:

$$sT(k,s) - v(ik)T(k,s) - c_{th}(ik)^2T(k,s) = \frac{1}{\rho C}\tau(s),$$
$$s\tilde{P}(k,s) - v(ik)\tilde{P}(k,s) - c_{th}(ik)^2\tilde{P}(k,s) = \Lambda sT(k,s). \tag{E.1.15}$$

Solving the above algebraic system (**??**) we obtain:

$$T(k,s) = \frac{1}{\rho C}\frac{\tau(s)}{s - v(ik) + c_{th}k^2}, \tag{E.1.16}$$
$$\tilde{P}(k,s) = \frac{\Lambda\tau(s)}{\rho C}\frac{s}{(s - v(ik) + c_{th}k^2)(s - v(ik) + c_{hy}k^2)} \tag{E.1.17}$$

Inverting the Laplace and then the Fourier transform yields:

$$T(x,t) = \frac{\dot{\delta}}{\rho C}\int_0^t \frac{\tau(t')}{2\sqrt{\pi c_{th}(t-t')}}\exp\left[-\frac{(x-vt')^2}{4c_{th}(t-t')}\right]dt', \tag{E.1.18}$$
$$\tilde{p}(x,t) = \frac{\Lambda\dot{\delta}}{\rho C(c_{hy}-c_{th})}\int_0^t \frac{\tau(t')}{2\sqrt{\pi(t-t')}}\left(\sqrt{c_{hy}}\exp\left[-\frac{(x-vt')^2}{4c_{hy}(t-t')}\right] - \sqrt{c_{th}}\exp\left[-\frac{(x-vt')^2}{4c_{th}(t-t')}\right]\right)$$
$$dt'.$$

By inspection we note that these are the same expressions as the ones presented in (6.17), where x' was replaced by $x' = vt'$ and $c = c_{th}$, or $c = c_{hy}$ respectively.

APPENDIX F

F.1 Frictional behavior for a traveling thermal load on a bounded domain.

We continue our analysis by applying a traveling instability on the bounded domain. Again we assume that the traveling plastic strain localization is wholly contained on a mathematical plane moving with a velocity v. The plastic strain rate is allowed to travel inside the plastified region of the layer h. We note that the plastified region h does not contain the whole layer. This is also the case in the non linear analyses of chapter 5, where due to the influence of the layer's boundary conditions the plastified region is smaller than the fault gouge thickness. The integral equation for the determination of the fault's frictional behavior in this case is given by:

$$\tau(t) = f(\sigma_n - p_0) - \frac{f\Lambda\dot{\delta}}{\rho C(c_{hy} - c_{th})}\int_0^t \tau(t')G_{X11}(x, vt', t-t', c_{th}, c_{hy}))\Big\|_{x=0.5L} dt', \tag{F.1.1}$$

where,

$$\begin{aligned} G_{X11}(x, vt', t-t', c_{th}, c_{hy}) = &\sum_{m=1}^{\infty} c_{hy} \exp\left[-m^2\pi^2 c_{hy}\frac{t-t'}{\mathrm{H}^2}\right]\sin\left(m\pi\frac{vt}{\mathrm{H}}\right)\sin\left(m\pi\frac{vt'}{\mathrm{H}}\right) \\ &-\sum_{m=1}^{\infty} c_{th} \exp\left[-m^2\pi^2 c_{th}\frac{t-t'}{\mathrm{H}^2}\right]\sin\left(m\pi\frac{vt}{\mathrm{H}}\right)\sin\left(m\pi\frac{vt'}{\mathrm{H}}\right). \end{aligned} \tag{F.1.2}$$

We rewrite equation (F.1.1) with the help of $\alpha_m = \frac{m\pi v}{\mathrm{H}}$, replacing the $\sin(\alpha_m t)$,$\sin(\alpha_m t')$ terms, with the help of the exponential trigonometric identity, $\sin\omega = \frac{\exp(i\omega) - \exp(-i\omega)}{2i}$, distributing the exponentials we arrive at:

$$\begin{aligned}\tau(t) &= f(\sigma_n - p_0) \\ &- \frac{f\Lambda\dot{\delta}}{2\mathrm{H}\rho C(c_{hy}-c_{th})}\int_0^t \tau(t')\sum_{m=1}^{\infty} K(v,t-t',m)\exp\left(i\alpha_m(t+t')\right)dt' \\ &- \frac{f\Lambda\dot{\delta}}{2\mathrm{H}\rho C(c_{hy}-c_{th})}\int_0^t \tau(t')\sum_{m=1}^{\infty} K(v,t-t',m)\exp\left(-i\alpha_m(t+t')\right)dt' \\ &- \frac{f\Lambda\dot{\delta}}{2\mathrm{H}\rho C(c_{hy}-c_{th})}\int_0^t \tau(t')\sum_{m=1}^{\infty} K(v,t-t',m)\exp\left(i\alpha_m(t-t')\right)dt' \\ &- \frac{f\Lambda\dot{\delta}}{2\mathrm{H}\rho C(c_{hy}-c_{th})}\int_0^t \tau(t')\sum_{m=1}^{\infty} K(v,t-t',m)\exp\left(-i\alpha_m(t-t')\right)dt'.\end{aligned} \tag{F.1.3}$$

where $K(v,t,m) = c_{hy}\exp\left[-\frac{\alpha_m^2 c_{hy}}{v^2}(t)\right] - c_{th}\exp\left[-\frac{\alpha_m^2 c_{th}}{v^2}(t-t')\right]$, we note here that $t+t'$ can be expressed as $2t-(t-t')$, making use of the exponential identities the above expression can be written as:

$$\begin{aligned}\tau(t) &= f(\sigma_n - p_0) \\ &- \sum_{m=1}^{\infty}\frac{f\Lambda\dot{\delta}\exp\left(2i\alpha_m t\right)}{2\mathrm{H}\rho C(c_{hy}-c_{th})}\int_0^t \sum_{m=1}^{\infty}\tau(t')K_1(v,t-t',m)dt' \\ &- \sum_{m=1}^{\infty}\frac{f\Lambda\dot{\delta}\exp\left(-2i\alpha_m t\right)}{2\mathrm{H}\rho C(c_{hy}-c_{th})}\int_0^t \sum_{m=1}^{\infty}\tau(t')K_2(v,t-t',m)dt' \\ &- \sum_{m=1}^{\infty}\frac{f\Lambda\dot{\delta}}{2\mathrm{H}\rho C(c_{hy}-c_{th})}\int_0^t \sum_{m=1}^{\infty}\tau(t')c_{hy}K_1(v,t-t',m)dt' \\ &- \sum_{m=1}^{\infty}\frac{f\Lambda\dot{\delta}}{2\mathrm{H}\rho C(c_{hy}-c_{th})}\int_0^t \sum_{m=1}^{\infty}\tau(t')c_{hy}K_2(v,t-t',m)dt',\end{aligned} \tag{F.1.4}$$

where:

$$\begin{aligned}K_1(v,t,m) &= c_{hy}\exp\left[-\left(\frac{\alpha_m^2 c_{hy}}{v^2}+i\alpha_m\right)(t)\right] - c_{th}\exp\left[-\left(\frac{\alpha_m^2 c_{th}}{v^2}+i\alpha_m\right)(t)\right], \\ K_2(v,t,m) &= c_{hy}\exp\left[-\left(\frac{\alpha_m^2 c_{hy}}{v^2}-i\alpha_m\right)(t)\right] - c_{th}\exp\left[-\left(\frac{\alpha_m^2 c_{th}}{v^2}-i\alpha_m\right)(t)\right].\end{aligned} \tag{F.1.5}$$

Now every term in the above summations corresponds to a convolution integral and the modified CQM $\mathcal{Z}$-Transform method can be applied. In contrast to previous cases we note that the first two summation terms contain an exponential term to an imaginary power ($\exp 2i\alpha_m t$) that indicates an oscillation in time.

The convolution integrals defined in equation (F.1.4) require a special handling during the application of the CQM method. We start for equation (F.1.4). We start by rewriting the kernel with the help of its inverse Laplace transform.

$$\begin{aligned}\tau(t) &= f(\sigma_n - p_0)\\ &- \frac{f\Lambda\dot{\delta}}{4L\rho C\pi i}\sum_{m=1}^{\infty}\int_{\gamma-i\infty}^{\gamma+i\infty}\int_0^t \tau(t')G_{X11}^1(s,m)\exp\left[-s(t-t')+i\alpha_m 2t\right]dt'ds\\ &- \frac{f\Lambda\dot{\delta}}{4L\rho C\pi i}\sum_{m=1}^{\infty}\int_{\gamma-i\infty}^{\gamma+i\infty}\int_0^t \tau(t')G_{X11}^2(s,m)\exp\left[-s(t-t')-i\alpha_m 2t\right]dt'ds\\ &- \frac{f\Lambda\dot{\delta}}{4L\rho C\pi i}\sum_{m=1}^{\infty}\int_{\gamma-i\infty}^{\gamma+i\infty}\int_0^t \tau(t')G_{X11}^1(s,m)\exp\left[-s(t-t')\right]dt'ds\\ &- \frac{f\Lambda\dot{\delta}}{4L\rho C\pi i}\sum_{m=1}^{\infty}\int_{\gamma-i\infty}^{\gamma+i\infty}\int_0^t \tau(t')G_{X11}^2(s,m)\exp\left[-s(t-t')\right]dt'ds\end{aligned} \tag{F.1.6}$$

where $G_{X11}^1(s,m), G_{X11}^2(s,m), G_{X11}^3(s,m), G_{X11}^4(s,m)$ are given by:

$$G_{X11}^1(s,m) = \frac{1}{c_{hy-c_{th}}}\left(c_{hy}\frac{1}{s+\left(\frac{\alpha_m^2 c_{hy}}{v^2}+i\alpha_m\right)} - c_{th}\frac{1}{s+\left(\frac{\alpha_m^2 c_{th}}{v^2}+i\alpha_m\right)}\right), \tag{F.1.7}$$

$$G_{X11}^2(s,m) = \frac{1}{c_{hy-c_{th}}}\left(c_{hy}\frac{1}{s+\left(\frac{\alpha_m^2 c_{hy}}{v^2}-i\alpha_m\right)} - c_{th}\frac{1}{s+\left(\frac{\alpha_m^2 c_{th}}{v^2}-i\alpha_m\right)}\right). \tag{F.1.8}$$

Here, for the first two terms in equation (F.1.6), we make the observation that the integrals involving the quantities of $(t-t'), t'$ are solutions to the first order linear differential equations:

$$\frac{dh_{1m}(t)}{dt} = (s+2\alpha_m i)h_{1m}(t) + \tau(t)\exp\left[-2\alpha_m it\right],\ h_1(0)=0,\ t\geq 0, \tag{F.1.9}$$

$$\frac{dh_{2m}(t)}{dt} = (s-2\alpha_m i)h_{2m}(t) + \tau(t)\exp\left[2\alpha_m it\right],\ h_2(0)=0,\ t\geq 0, \tag{F.1.10}$$

while the integrals in the last two terms are solutions to the first order linear differential equation (6.25). We apply next the $\mathcal{Z}$-Transform to the sampled linear integral equation

(F.1.6).

$$T(z) = f(\sigma_n - p_0)\frac{z}{z-1} - \frac{f\Lambda\dot{\delta}}{4L\rho C\pi i}\Bigg(\sum_{m=1}^{\infty}\int_{\gamma-i\infty}^{\gamma+i\infty} G^1_{X11}(s,m)H_1(z,m)ds \\ + \int_{\gamma-i\infty}^{\gamma+i\infty} G^2_{X11}(s,m)H_2(z,m)ds \\ + \int_{\gamma-i\infty}^{\gamma+i\infty} G^1_{X11}(s,m)H(z,m)ds \\ + \int_{\gamma-i\infty}^{\gamma+i\infty})G^2_{X11}(s,m)H(z,m)ds\Bigg)$$

To evaluate $T(z)$ we need the expressions of $H_1(z,m), H_2(z,m), H(z,m)$ as functions of $T(z)$. While the expression for $H(z,m)$ remains the same as the one derived in the main text (see equation (6.28)), the sampled differential equations (F.1.9),(F.1.10) at points $t_n = n\Delta t$ are transformed with the help of the $\mathcal{Z}$-Transform properties to:

$$\frac{z-1}{z\Delta t}H_1(z,m) = (s + 2\alpha_m\Delta t\ i)H_1(z,m) + T(\frac{z}{\exp[2\alpha_m\Delta t\ i]}), \tag{F.1.11}$$

$$\frac{z-1}{z\Delta t}H_2(z,m) = (s - 2\alpha_m\Delta t\ i)H_2(z,m) + T(\frac{z}{\exp[-2\alpha_m\Delta t\ i]}). \tag{F.1.12}$$

The transformed auxiliary functions are given as:

$$H_1(z,m) = \frac{T(\frac{z}{\exp[2\alpha_m\Delta t\ i]})}{\frac{z-1}{z\Delta t} - (s + 2\alpha_m\Delta t\ i)}, \tag{F.1.13}$$

$$H_2(z,m) = \frac{T(\frac{z}{\exp[-2\alpha_m\Delta t\ i]})}{\frac{z-1}{z\Delta t} - (s - 2\alpha_m\Delta t\ i)}. \tag{F.1.14}$$

Applying then into equation (F.1.11) we obtain:

$$T(z) = f(\sigma_n - p_0)\frac{z}{z-1} - \frac{f\Lambda\dot{\delta}}{4L\rho C\pi i}\sum_{m=1}^{\infty}\Bigg(\int_{\gamma-i\infty}^{\gamma+i\infty} G^1_{X11}(s,m)\frac{T(\frac{z}{\exp[2\alpha_m\Delta t\ i]})}{\frac{z-1}{z\Delta t} - (s + 2\alpha_m\Delta t\ i)}ds \\ + \int_{\gamma-i\infty}^{\gamma+i\infty} G^2_{X11}(s,m)\frac{T(\frac{z}{\exp[-2\alpha_m\Delta t\ i]})}{\frac{z-1}{z\Delta t} - (s - 2\alpha_m\Delta t\ i)}ds + \int_{\gamma-i\infty}^{\gamma+i\infty} G^1_{X11}(s,m)\frac{T(z)}{\frac{z-1}{z\Delta t} - s}ds \\ + \int_{\gamma-i\infty}^{\gamma+i\infty} G^2_{X11}(s,m)\frac{T(z)}{\frac{z-1}{z\Delta t} - s}ds\Bigg). \tag{F.1.15}$$

Applying the Cauchy residue theorem of complex analysis on equation (F.1.15) we get:

$$T(z)=f(\sigma_n-p_0)\frac{z}{z-1}-\frac{f\Lambda\dot{\delta}}{2\mathrm{H}\rho C}\sum_{m=1}^{\infty}\left(G^1_{X11}\left(\frac{z-1}{z\Delta t}-2\alpha_m\Delta t\; i\right)T\left(\frac{z}{\exp\left[2\alpha_m\Delta t\; i\right]}\right)\right.$$
$$+G^2_{X11}\left(\frac{z-1}{z\Delta t}+2\alpha_m\Delta t\; i\right)T\left(\frac{z}{\exp\left[-2\alpha_m\Delta t\; i\right]}\right)+G^3_{X11}\left(\frac{z-1}{z\Delta t}\right)T(z)$$
$$\left.+G^4_{X11}\left(\frac{z-1}{z\Delta t}\right)T(z)\right). \tag{F.1.16}$$

Contrary to the previous cases examined in the main text, in this case the equation obtained is a functional equation, and the problem is not simplified. We make the following observations:

- According to the value of $\alpha_m=\frac{m\pi v}{\mathrm{H}}$ we note that the denominators of the functional terms lie on the unit circle of the complex z plane. This is a very important information since for finding the inverse of the transformation we need to integrate along a closed contour containing the origin. To simplify our calculations we can take the contour to be a concentric circle to the unit circle in the z plane under the term that we include all the poles of $T(z)$. We can then evaluate the integral by calculating the values of the functional expression at points coincident to the scaled unit circle points used in the expression definition.
- It is always the kernel that controls the poles and branch cuts of $T(z)$, the kernel in this case has not changed from the one used in the bounded case, therefore the same circle with radius of integration 1.1 is valid for the purposes of our analysis.
- By letting m increase, eventually we arrive at repeated values of the denominators in $T(\frac{z}{\exp 2\alpha_m i}), T(\frac{z}{\exp -2\alpha_m i})$. Because the transform has an inverse, the values of $T(\frac{z}{\exp 2\alpha_m i}), T(\frac{z}{\exp -2\alpha_m i})$ have to lie on the same Riemann sheet. Moreover, our kernel presented no branch cuts therefore, we don't need to account for the possibility of double values of T.
- As we apply the values around the unit circle increasing m on the above functional expression, we see that we get extra $m+k, m-k$ terms due to the form of the equation. We note that according to the previous observations, they can safely be neglected since the values on the unit circle constitute a $k\times k$ system of independent unknowns and equations whose determinant is non zero.

- Generalizing even more we can treat each of the different $T(\frac{z}{\exp 2\alpha_m i}), T(\frac{z}{\exp -2\alpha_m i})$ scalings of $T(z)$ as independent functions $T_i(z)$. This way of reasoning produces a system of unknown independent functions. By evaluating at the scaled points to the unit circle the functional system reduces to the algebraic system defined above.

We know that our problem is stable and causal. This means that all of the potential poles of $T(z)$ must lie inside the unit circle, and the region of convergence of $T(z)$ is the whole z complex plain except the region interior to the unit circle. We choose to integrate along a circle centered at the origin of the z plane with radius $R = 1.1$ m. We choose to sample the points on the circle every $\Delta t = 0.0001$ (s). Based on the observations above, we evaluate the functional equation (F.1.16) at the points along the circle $z = 1.1 \exp\left[2\alpha_k \Delta t\, i\right] = 1.1 \exp\left[2k\pi \frac{v\Delta t}{\mathrm{H}} i\right]$. We note that when $\left(k\frac{v\Delta t}{\mathrm{H}}\right)$ is a whole number, our selection process will have traveled around the circle one time. For a first pass around the circle we require that $k_{max} = \frac{\mathrm{H}}{v\Delta t}$. Increasing k more than $k_{max} - 1$ will result in a repetition of the algebraic equations due to the observations established above. In this case the algebraic equations that will be produced by substitution to the functional equation (F.1.16) won't be independent. The following system of unknown points is found:

$$
\begin{aligned}
&k = 0\\
&T\left(1.1\right) = f(\sigma_n - p_0)\frac{z}{z-1}\bigg\|_{z=1.1}\\
&\qquad - \frac{\Lambda\dot{\delta}}{2\mathrm{H}\rho C}\sum_{m=1}^{\infty}\left(G^1_{X11}(z,\beta_m)\bigg\|_{z=1.1} T\left(1.1\exp\left[(\beta_0-\beta_m)i\right]\right)\right.\\
&\qquad + G^2_{X11}(z,\beta_m)\bigg\|_{z=1.1} T\left(1.1\exp\left[(\beta_0+\beta_m)i\right]\right)\\
&\qquad \left. + G^3_{X11}(z,\beta_m)\bigg\|_{z=1.1} T(1.1) + G^4_{X11}(z,\beta_m)\bigg\|_{z=1.1} T(1.1\exp\left[\beta_0 i\right])\right).
\end{aligned}
\tag{F.1.17}
$$

$$
\begin{aligned}
&k = 1\\
&T\left(1.1\exp\left[\beta_1 i\right]\right) = f(\sigma_n - p_0)\frac{z}{z-1}\bigg\|_{z=1.1}\\
&\qquad\qquad - \frac{\Lambda\dot{\delta}}{2\mathrm{H}\rho C}\sum_{m=1}^{\infty}\left(G^1_{X11}(z,\beta_m)\bigg\|_{z=1.1} T\left(1.1\exp\left[(\beta_1-\beta_m)i\right]\right)\right.
\end{aligned}
$$

$$
\begin{aligned}
&+ G^2_{X11}(z,\beta_m)\Big\|_{z=1.1} T\left(1.1\exp\left[(\beta_1+\beta_m)i\right]\right)\\
&+ G^3_{X11}(z,\beta_m)\Big\|_{z=1.1} T(1.1\exp\left[\beta_1 i\right]\\
&+G^4_{X11}(z,\beta_m)\Big\|_{z=1.1} T(1.1\exp\left[\beta_1 i\right])\Bigg) .
\end{aligned}
\tag{F.1.18}
$$

$$
\begin{aligned}
&k = k_{max} - 1\\
&T\left(1.1\exp\left[\beta_k i\right]\right) = f(\sigma_n - p_0)\frac{z}{z-1}\Big\|_{z=1.1\exp\left[\beta_k\ i\right]}\\
&\qquad - \frac{\Lambda\dot{\delta}}{2\mathrm{H}\rho C}\sum_{m=1}^{\infty}\Bigg(G^1_{X11}(z,\beta_m)\Big\|_{z=1.1\exp\left[\beta_k\ i\right]} T\left(1.1\exp\left[(\beta_k-\beta_m)i\right]\right)\\
&\qquad + G^2_{X11}(z,\beta_m)\Big\|_{z=1.1\exp\left[\beta_k i\right]} T\left(1.1\exp\left[(\beta_k+\beta_m)i\right]\right)\\
&\qquad + G^3_{X11}(z,\beta_m)\Big\|_{z=1.1\exp\left[\beta_k\ i\right]} T(1.1\exp\left[\beta_k i\right])\\
&\qquad +G^4_{X11}(z,\beta_m)\Big\|_{z=1.1\exp\left[\beta_k\ i\right]} T(1.1\exp\left[\beta_k i\right])\Bigg) .
\end{aligned}
\tag{F.1.19}
$$

Where $\beta_m = 2m\pi\frac{v\Delta t}{\mathrm{H}}$, $\beta_k = 2k\pi\frac{v\Delta t}{\mathrm{H}}$. We note again that based on our observations that non zero values of T(z) are found when the argument of z lies between $([0, 2\pi))$ which in turn implies that only the values of T(z) whose argument lies between $\beta_k - \beta_m \geq$ and $\beta_k + \beta_m < 2\pi$ are taken into account. Having calculated all the values that are important, we are left with a system that can be solved algebraically for their determination. Therefore, calculating the contour integrals for the numerical inversion of the $\mathcal{Z}$-Transform becomes once again possible.

All this discussion covers only the case, where the strain localization travels to one direction inside the plastified region of the fault gouge. However form chapter 5 we knot that the strain localization travels periodically inside the plastified region of the fault gouge.

We will not pursue this further however, since this solution procedure becomes more involved and it lies outside the scope of this Thesis.

Another way of handling the problem is to use the method of the Adomian Decomposition Wazwaz, 2011. This way the functions needed for the determination of the original unknown are always known based on the previous step of the Adomian method. Since the method is sensitive to the number of terms and the integral calculation we can use the CQM $\mathcal{Z}$-Transform method to handle the successive convolutions. Finally, the collocation method used in chapter 6 of this thesis is in our opinion the most efficient method of solving the problem when periodic loading paths are studied.

Appendix G

G.1 Properties of the $\mathcal{Z}$-Transform

In this appendix we present the properties of the Z-Transform, which we use in the numerical methods of chapter 6.

G.1.0.1 Definition of the Unilateral $\mathcal{Z}$-Transform

We define the discrete time signal $x[n]$ for $n \geq 0$. The single-sided or unilateral $\mathcal{Z}$-transform is defined as:

$$X(z) = \mathcal{Z}\{x[n]\} = \sum_{n=0}^{\infty} x[n] z^{-n}. \tag{G.1.1}$$

G.1.0.2 Definition of the Inverse $\mathcal{Z}^{-1}$-Transform

It's inverse can be calculated via the relation:

$$x[n] = \mathcal{Z}^{-}1\{X(z)\} = \frac{1}{2\pi i} \oint_C X(z) z^{n-1} dz. \tag{G.1.2}$$

We note that C is a counterclockwise closed curve encircling the origin and lying entirely inside the region of convergence. For a causal function $x(t)$ sampled at a sampling period Δt, resulting in the discrete representation $x(t_n) = x[n]$, the curve C must encircle all the poles of the transformed function $X(z)$. The inversion of the $\mathcal{Z}$-Transform can be further simplified as we will see below by making use of the discrete time Fourier transform and (DTFT), which finally can be reduced to the discrete Fourier transform (DFT) assuming the discrete time signal to be part of a periodic function. For numerical reasons we are interested in cases of stable systems, where the $\mathcal{Z}$-Transform contains $|z| = 1$ in its region of convergence. In this case small numerical errors during the calculation do not grow as time progresses.

To handle the inversion of the transformed function $X(z)$ along the closed curve C, we take into account the Cauchy residue theorem of complex analysis and choose to integrate along a circle containing the origin and the poles of the function $X(z)$. The radius of the circle to be used is ρ. The contour integral along the curve C encircling all the poles of the function $X(z)$ can be numerically evaluated by making use of a trapezoidal rule, where since the curve is closed the initial and final positions coincide.

$$x(t_n) = \frac{1}{L}\sum_{p=0}^{L-1} X(z_p) z_p^{n-1},\ \forall n \in [0, M], \tag{G.1.3}$$

where M is the total number of steps. A suitable selection for the parameters L, ρ is discussed in Mavaleix-Marchessoux et al. (2020). Since $z = \rho \exp \frac{2\pi i p}{L}$, the $\mathcal{Z}$-Transform is equivalent to the discrete Fourier transform (DFT) $X(z_n) = \sum_{n=0}^{M} x_n \rho^n \exp \frac{2\pi i p n}{L}$. Calculating the $\mathcal{Z}$-Transform and its Inverse can be done by applying the DFT to the finite sequences $(x_n \rho^n)_{n=0}^{M}$, $X_p \rho^{-p})_{p=0}^{L-1}$ respectively. A high sampling frequency $f_{sample} = \frac{1}{\Delta t}$ is required to counter aliasing based on the Nyquist stability criterion.

G.1.0.3 Properties of the $\mathcal{Z}$-Transform

Here, we provide the properties of the $\mathcal{Z}$-Transform we make use of in chapter 6.

— Linearity:

$$\alpha_1 x_1[n] + \alpha_2 x_2[n] \to \alpha_1 X_1(z) + \alpha_2 X_2(z). \tag{G.1.4}$$

— First difference backward:

$$x[n] - x[n-1] \to (1 - z^{-1})X(z),\ x[n] = 0,\ \forall n < 0. \tag{G.1.5}$$

— Scaling in the $\mathcal{Z}$ domain:

$$\alpha^n x[n] \to X(\alpha^{-1} z). \tag{G.1.6}$$

— Convolution:

$$\int_0^t x_1(t - t')x_2(t')dt' \to X_1(z)X_2(z). \tag{G.1.7}$$

Appendix H

H.1 Collocation Methodology

In order to apply the collocation methodology to the linear Volterra integral equation of the second kind in chapter 6, (6.16), we make use of the collocation methodology described in Tang et al. (2008). The integral equation is given as:

$$\tau(t) = f(\sigma_n - p_0) - C\int_0^t \tau(t')G^\star(t-t', c_{hy}, c_{th})dt',\ t \in [0, T], \tag{H.1.1}$$

where $f(\sigma_n - p_0), G^\star(t, c_{th}, c_{hy})$ are given functions, and $\tau(t)$ is the unknown function. We begin by performing a change of variables from $t \in [0, T]$ to $x \in [-1, 1]$. The change of variables reads:

$$t = T\frac{1+x}{2},\ x = \frac{2t}{T} - 1$$

The Volterra integral equation can then be written:

$$u(x) = f(\sigma_n - p_0) - C\int_0^{T\frac{1+x}{2}} G^\star(T\frac{1+x}{2} - t', c_{hy}, c_{th})dt',\ x \in [-1, 1], \tag{H.1.2}$$

where $u(x) = \tau(T\frac{1+x}{2})$. In order for the collocation method solution to converge exponentially we require that both the integral equation (H.1.2) and the integral inside (H.1.2) are expressed inside the same interval $[-1, 1]$. To do this first we change the integration bounds from $t' \in [0, T\frac{1+x}{2}]$ to $s \in [-1, x]$.

$$u(x) = f(\sigma_n - p_0) - C\int_0^x K(x, s, c_{hy}, c_{th})ds,\ x \in [-1, 1],, \tag{H.1.3}$$

where $K(x, s) = \frac{T}{2}G^\star\frac{T}{2}(x-s), c_{hy}, c_{th})$. Next, we set the $N+1$ collocation points $x_i \in [-1, 1]$ and corresponding weights ω_i according to the Gauss-Legendre quadrature formula.

The integral equation (H.1.3) must hold at each x_i:

$$u(x_i) = f(\sigma_n - p_0) - C\int_0^{x_i} K(x_i, s, c_{hy}, c_{th})ds,\ i \in [0, N],, \tag{H.1.4}$$

The main hindrance in solving equation (**??**) accurately, is the calculation of the integral with variable integration bounds. For small values of x_i, the quadrature provides little information for $u(s)$. We handle this difficulty by yet another variable change where we transfer the integration variable $s \in [-1, x_i]$ to $\theta \in [-1, 1]$ via the transformation:

$$s(x,\theta) = \frac{1+x}{2}\theta + \frac{x-1}{2},\ \theta \in [-1, 1]. \tag{H.1.5}$$

Thus, equation (**??**) is transformed into:

$$u_i + \frac{1+x_i}{2}\sum_{j=0}^{N} u_j \sum_{p=0}^{N} K(x_i, s(x_i,\theta))u(s(x_i,\theta_p))\omega_j = f(\sigma_n - p_0),\ i \in [0, N] \tag{H.1.6}$$

In order to apply the collocation method according to the Gauss Legendre quadrature we express the solution $u(s(x_i,\theta_j))$ with the help of Lagrange interpolation polynomials $F_j(s(x_i,\theta_j))$ as a series: $u(s(x_i,\theta_j)) \sim \sum\limits_{k=0}^{N} u_j F_j(s(x_i,\theta_j))$

$$u_i + \frac{1+x_i}{2}\sum_{j=0}^{N} u_j \left(\sum_{p=0}^{N} K(x_i, s(x_i,\theta))F_j(s(x_i,\theta_p))\omega_p\right) = f(\sigma_n - p_0),\ i \in [0, N]. \tag{H.1.7}$$

In order to assure an exponential degree of convergence we choose that the set of Gauss-Legendre quadrature points for the numerical evaluation of the integral $\{\theta_j\}_{j=0}^{N}$ coincides with the set of collocation points $\{x_j\}$, where the integral equation is evaluated. Rearranging the terms and applying Einstein's summation over repeated indices yields the system of algebraic equations:

$$(\delta_{ij} + A_{ij})u_j = g(x_i), \tag{H.1.8}$$

where, $A_{ij} = \frac{1+x_i}{2}\sum\limits_{j=0}^{N}\left(\sum\limits_{p=0}^{N} K(x_i, s(x_i,\theta))F_j(s(x_i,\theta_p))\omega_p\right)$, $g(x_i) = f(\sigma_n - p_0)$ and u_j the unknown quantities. Since the Gauss-Lagrange quadrature was assumed the interpolation coefficients u_j calculated at each x_j are also the value of the interpolation at x_j.

APPENDIX I

I.1 Proof that the maximum of pressure and the position of the yielding plane (thermal load) coincide

In this appendix we will present the central part of our argument in chapter 6 concerning the applicability of a traveling strain localization mode. I chapter 6 we have argued that in order for the strain localization mode to be applicable to the problem at hand it needs to satisfy the equations of equilibrium and it should warrant that the prescribed localization motion corresponding to the position of the yielding plane inside the layer satisfies also the condition that it coincides with the maximum of the pressure profile inside the layer at all times (see Rice, 2006a).

I.1.1 Proof of pressure Maxima for the traveling strain localization on an bounded domain.

To this end, provided that the function we search for is sufficiently smooth except maybe at a finite number of points, we make use of our tools from calculus that indicate the use of the first and second order derivatives to decide upon the position and the kind of the extremalities of the unknown function. We start our discussion with the case of a traveling localization on a bounded mathematical domain. In this case the derived kernel of the coupled pressure temperature diffusion equation is bounded and smooth at all times $t \in [0, \infty)$. The pressure profile at all times t, for a traveling strain localization mode $\gamma(\dot{x}, t) = \dot{\delta}\delta_{Dirac}(x - vt)$ (and thermal load $\frac{1}{\rho C}\tau t\dot{\delta}\delta_{Dirac}(x - vt)$) at position $x = vt$ is given by the relation:

$$p(x,t) - p_0 = \frac{2\Lambda\dot{\delta}}{\mathrm{H}\rho C(c_{hy} - c_{th})} \int_0^t \tau(t') \sum_{m=0}^{\infty} K(x, t, t', m)dt' \tag{I.1.1}$$

where $K(x,t,t',m) = \left(c_{hy}\exp\left(-m^2\pi^2 c_{hy}\frac{t-t'}{\mathrm{H}^2}\right) - c_{th}\exp\left(-m^2\pi^2 c_{th}\frac{t-t'}{\mathrm{H}^2}\right)\right)\sin\left(m\pi\frac{x}{\mathrm{H}}\right)\sin\left(m\pi\frac{vt'}{\mathrm{H}}\right)$). The first derivative of equation (I.1.1) is given by:

$$\frac{\partial p(x,t)}{\partial x} = \frac{2\Lambda\dot{\delta}m\pi}{\mathrm{H}^2\rho C(c_{hy}-c_{th})}\int_0^t \tau(t')\sum_{m=0}^{\infty}\frac{\partial K(x,t,t',m)}{\partial x}dt' \tag{I.1.2}$$

where $\frac{\partial K(x,t,t',m)}{\partial x} = \left(c_{hy}\exp\left(-m^2\pi^2 c_{hy}\frac{t-t'}{\mathrm{H}^2}\right) - c_{th}\exp\left(-m^2\pi^2 c_{th}\frac{t-t'}{\mathrm{H}^2}\right)\right)\cos\left(m\pi\frac{x}{\mathrm{H}}\right)\sin\left(m\pi\frac{vt'}{\mathrm{H}}\right)$. We note that for $\frac{\partial p}{\partial x} = 0$ we need to find x such that:

$$\Pi(x,t',m) = \mathrm{Re}\left[\cos\left(m\pi\frac{x}{\mathrm{H}}\right)\sin\left(m\pi\frac{vt'}{\mathrm{H}}\right)\right] = 0. \tag{I.1.3}$$

We write the above product with the help of the exponential function.

$$\Pi(x,t',m) = \mathrm{Re}\left[\frac{\exp im\pi\frac{x}{\mathrm{H}} + \exp -im\pi\frac{x}{\mathrm{H}}}{2}\frac{\exp im\pi\frac{vt'}{\mathrm{H}} - \exp -im\pi\frac{vt'}{\mathrm{H}}}{2i}\right] = 0, \tag{I.1.4}$$

$$\begin{aligned}\Pi(x,t',m) = \mathrm{Re}\Bigg[\frac{1}{4i}\Bigg(&\exp\left(im\pi\frac{x+vt'}{\mathrm{H}}\right) + \exp\left(-im\pi\frac{x-vt'}{\mathrm{H}}\right)\\ &-\exp\left(im\pi\frac{x-vt'}{\mathrm{H}}\right) - \exp\left(-im\pi\frac{x+vt'}{\mathrm{H}}\right)\Bigg)\Bigg] = 0.\end{aligned} \tag{I.1.5}$$

Transforming again the above summation with the help of the Euler relations into $\sin(\cdot) + i\cos(\cdot)$ and using the trigonometric equalities between the arguments of the opposite sign we arrive at:

$$\cos\left(m\pi\frac{x-vt'}{\mathrm{H}}\right) - \cos\left(m\pi\frac{-x+vt'}{\mathrm{H}}\right) = 0, \tag{I.1.6}$$

which is true $\forall t \in [0,\infty)$ when $x = vt'$. Thus we know that $p(x,t) - p_0$ presents an extremum an the position of the traveling yielding plane. We need to prove that this extremum is also maximum for every $t > 0$. For this we take the second derivative of equation (I.1.1).

$$\frac{\partial^2 p(x,t)}{\partial x^2} = \frac{2\Lambda\dot{\delta}m^2\pi^2}{\mathrm{H}^3\rho C(c_{hy}-c_{th})}\int_0^t \tau(t')\sum_{m=0}^{\infty}\frac{\partial^2 K(x,t,t',m)}{\partial x^2}dt', \tag{I.1.7}$$

where $\frac{\partial^2 K(x,t,t',m)}{\partial x^2} = -\left(c_{hy}\exp\left(-m^2\pi^2 c_{hy}\frac{t-t'}{\mathrm{H}^2}\right) - c_{th}\exp\left(-m^2\pi^2 c_{th}\frac{t-t'}{\mathrm{H}^2}\right)\right)\sin\left(m\pi\frac{x}{\mathrm{H}}\right)\sin\left(m\pi\frac{vt'}{\mathrm{H}}\right)$. Evaluating the second derivative in equation (I.1.7) with respect to x at the position

$x = vt' \left. \frac{\partial^2 p(x,t)}{\partial x^2} \right\|_{x=vt'}$ we see that for $t > 0$ equation (I.1.7) is always negative. This means that the extremum at $x = vt'$ is also a maximum.

I.1.2 Proof of pressure Maxima for the traveling strain localization on an unbounded domain.

In the case of the unbounded domain due to the form of the coupled temperature and pressure kernel, $G_{T,P}(x, t - t', c_{th}, c_{hy})$, (see Lee & Delaney, 1987) resulting in a weakly singular convolution integral, such a derivation is not trivial. While we can ensure the convergence of the integral in a Riemann sense for the original integral and verify the position of its extremalities we cannot directly calculate its second derivative since the resulting integral corresponds to a hyper singular divergent integral. To answer questions about its convergence we need to apply the notion of Hadamard regularization.

We notice, however, that this question is a special case of the pressure maxima of a traveling strain localization on a bounded domain of height H, when H tends to ∞, see section I.1.1.

Titre : Modelisation des failles sismiques

Mot clés : analyse de stabilite de Lyapunov ; Theorie de bifurcation ; Regularization ; Continuum micromorphe de Cosserat ; Ondes progressives ; Pressurisation thermique

Résumé : Lors d'un glissement sismique, l'énergie libérée par la décharge élastique des blocs de terre adjacente peut être séparée en trois parties principales : L'énergie qui est rayonnée à la surface de la terre ($\sim 5\%$ du budget énergétique total), l'énergie de fracture pour la création de nouvelles surfaces de faille et enfin, l'énergie dissipée à l'intérieur d'une région de la faille, d'épaisseur finie, que l'on appelle le "*fault gouge* ". Cette région accumule la majorité du glissement sismique. Estimer correctement la largeur de *fault gouge* est d'une importance capitale pour calculer l'énergie dissipée pendant le séisme, le comportement frictionnel de la faille et les conditions de nucléation de la faille sous la forme d'un glissement sismique ou asismique.
Dans cette thèse, approches différentes de régularisation ont été explorées pour l'estimation de la largeur de localisation de la zone de glissement principal de la faille pendant le glissement cosmique. Celles-ci comprennent l'application de la viscosité et des couplages multiphasiques dans le continuum classique de Cauchy, et l'introduction d'un continuum micromorphe de Cosserat du premier ordre. Tout d'abord, nous nous concentrons sur le rôle de la régularisation visqueuse dans le contexte des analyses dynamiques, en tant que méthode de régularisation de la localisation des déformations. Nous étudions le cas dynamique d'un continuum de Cauchy classique adoucissant à la déformation et durcissant à la vitesse de déformation. En appliquant l'analyse de stabilité de Lyapunov, nous montrons que l'introduction de la viscosité est incapable d'empêcher la localisation de la déformation sur un plan mathématique et la dépendance de du maillage des éléments finis.
Nous effectuons des analyses non linéaires en utilisant le continuum de Cosserat dans le cas de grands déplacements par glissement sismique de *fault gouge* par rapport à sa largeur. Le continuum de Cosserat nous permet de rendre compte de l'énergie dissipée pendant un séisme et du rôle de la microstructure dans l'évolution de la friction de la faille. Nous nous concentrons sur l'influence de la vitesse de glissement sismique sur le mécanisme d'assidument frictionnel de la pressurisation thermique. Nous remarquons que l'influence des conditions aux limites dans la diffusion du fluide interstitiel à l'intérieur de *fault gouge*, conduit à une reprise du frottement après l'affaiblissement initial. De plus, un mode de localisation de déformation en mouvement est présent pendant le cisaillement de la couche, introduisant des oscillations dans la réponse du frottement. Ces oscillations augmentent le contenu spectral du séisme. L'introduction de la viscosité dans le mode ci-dessus, conduit à un comportement de "*rate and state*" sans l'introduction d'une variable interne. Nos conclusions sur le rôle de la pressurisation thermique pendant le cisaillement de *fault gouge* sont en accord qualitatif avec les nouveaux résultats expérimentaux disponibles.
Enfin, sur la base des résultats numériques, nous étudions les hypothèses du modèle actuel de glissement sur un plan mathématique proposent à la littérature. Le rôle des conditions aux limites et du mode de localisation des déformations dans l'évolution du frottement de la faille pendant le glissement sismique. Le cas d'un domaine délimité et d'un mode de localisation de la déformation en mouvement est examiné dans le contexte d'un glissement sur un plan mathématique sous pressurisation thermique. Nos résultats étoffent le modèle original dans un contexte plus général.

Title: Numerical modeling of earthquake faults

Keywords: Lyapunov stability analysis; Bifurcation theory; Regularization; Cosserat micromorphic continuum; Traveling waves; Thermal pressurization

Abstract: During coseismic slip, the energy released by the elastic unloading of the adjacent earth blocks can be separated in three main parts: The energy that is radiated to the earth's surface ($\sim 5\%$ of the whole energy budget), the fracture energy for the creation of new fault surfaces and finally, the energy dissipated inside a region of the fault, with finite thickness, which is called the fault gauge. This region accumulates the majority of the seismic slip. Estimating correctly the width of the fault gauge is of paramount importance in calculating the energy dissipated during the earthquake, the fault's frictional response, and the conditions for nucleation of the fault in the form of seismic or aseismic slip.
In this thesis different regularization approaches were explored for the estimation of the localization width of the fault's principal slip zone during coseismic slip. These include the application of viscosity and multiphysical couplings in the classical Cauchy continuum, and the introduction of a first order micromorphic Cosserat continuum. First, we focus on the role of viscous regularization in the context of dynamical analyses, as a method for regularizing strain localization. We study the dynamic case for a strain softening strain-rate hardening classical Cauchy continuum, and by applying the Lyapunov stability analysis we show that introduction of viscosity is unable to prevent strain localization on a mathematical plane and mesh dependence.
We perform fully non linear analyses using the Cosserat continuum under large seismic slip displacements of the fault gouge in comparison to its width. Cosserat continuum provides us with a proper account of the energy dissipated during an earthquake and the role of the microstructure in the evolution of the fault's friction. We focus on the influence of the seismic slip velocity to the weakening mechanism of thermal pressurization. We notice that the influence of the boundary conditions in the diffusion of the pore fluid inside the fault gouge, leads to frictional strength regain after initial weakening. Furthermore, a traveling strain localization mode is present during shearing of the layer introducing oscillations in the frictional response. Such oscillations increase the spectral content of the earthquake. Introduction of viscosity in the above mode, leads to a rate and state behavior without the introduction of a specific internal state variable. Our conclusions about the role of thermal pressurization during shearing of the fault gouge, agree qualitatively with newly available experimental results.
Finally, based on the numerical findings we investigate the assumptions of the current model of a slip on a mathematical plane, in particular the role of the boundary conditions and strain localization mode in the evolution of the fault's friction during coseismic slip. The case of a bounded domain and a traveling strain localization mode are examined in the context of slip on a mathematical plane under thermal pressurization. Our results expand the original model in a more general context.